Statistical inference of the relations among air temperature, land-use change, and rockfall hazard

Doctoral Dissertation
Doctoral Program in Environmental Engineering (29th Cycle)

Statistical inference of the relations among air temperature, land-use change, and rockfall hazard

By

Roberta Paranunzio

******

Supervisor(s):
Francesco Laio, Supervisor
Marta Chiarle, Co-Supervisor

Doctoral Examination Committee:
Philip Deline, Referee, Université Savoie Mont Blanc
Andrea Manconi, Referee, ETH Zürich
Serena Ceola, Università di Bologna
Francesco Faccini, Università degli Studi di Genova
Simona Fratianni, Università degli Studi di Torino

Politecnico di Torino
2017

Declaration

I hereby declare that, the contents and organization of this dissertation constitute my own original work and does not compromise in any way the rights of third parties, including those relating to the security of personal data.

Roberta Paranunzio

2017

This dissertation is presented in partial fulfillment of the requirements for **Ph.D. degree** in the Graduate School of Politecnico di Torino (ScuDo).

There is pleasure in the pathless woods, there is rapture in the lonely shore, there is society where none intrudes, by the deep sea, and music in its roar: I love not Man the less, but Nature more.

George Gordon Byron

Acknowledgments

I am extremely grateful to my advisor Francesco Laio, who involved me in his research activities and financed part of my Ph.D. His open-mindedness, enthousiasm and fundamental scientific support have greatly stimulated me in these years. I am sure that the scientific skills and experience I acquired working with him will be extremely helpful for my future.

I would express all my gratitude to my co-advisor Marta Chiarle (CNR IRPI), without whom this adventure would have not started, for her scientific and economical support in the first part of my Ph.D. I warmly thank Guido Nigrelli (CNR IRPI) for his fundamental collaboration and suggestions. Thanks both for the enriching discussions we had during these years of work togheter, and for having shared knowledge and experience on natural hazards and mountain.

I whish to express my gratitude to Serena Ceola (Università di Bologna), who put at my disposal data and helpful suggestions for the second part of my research activity.

Of course, I cannot forget all my friends and colleagues of CNR IRPI and DIATI of the Politecnico di Torino, for having shared with me this adventure and for making these years so great.

Last, but not least, my family, who always believed in me, and strongly encouraged me when I was a step away from giving up.

Abstract

Climate change has widespread impacts on human and natural systems worldwide. The pronounced air temperature warming detected worldwide could explain unusual events, as for example the increment of extreme precipitation events, increased incidence of summer heatwaves and slope instability. The possible presence of non-climatic forcings affecting temperature records, as for example land-use and land-cover changes, could introduce significant bias in the records and uncertainty on global overall temperature trends. This could somehow alterate, on the one hand, the perception of global warming, and on the other hand, all temperature-related analyses and models. Nevertheless, a robust assessment of climate warming patterns entails not only the analysis of all climate variables involved, but also the full understanding of the impacts on the natural systems, as for example the cryosphere, that could be used as terrestrial indicators of climate change.

Chapter 1 shed light on the main scientific question investigated in the thesis, presenting the proposed investigation strategy, and the techniques applied. After an introduction on the issue of increasing air temperature vaiability in the current context of climate change, the two macrotopics of the thesis are presented and briefly outlined (Chapter 2 and 3).

In Chapter 2, we investigate the nexus between temperature variations and urbanization trends, by analysing data recorded from weather instruments worldwide. After an extended introduction on the Urban Heat Island effect and its implications for climate warming trends at regional and global scale, we propose several methods to investigate the presence of a possible relation between air temperature variations and urbanizations dynamics with time, based on nightlights satellite measurements as proxy of urbanization. We applied a global scale analysis on more than 5000 temperature stations from the Berkeley Earth dataset

in the period 1992-2013. Results highlight the tendency of urbanization to affect temperature trend at continental and regional scales. Significant positive concordant trends in temperature and nightlights variations have been detected, especially in developing and emerging regions, where the effects of growing urbanization are more evident.

In Chapter 3 we turn to investigate the effects of air temperature variations on the hydrogeological hazard risk in those environments that are among the most sensitive to climate change, i.e. the high elevation sites. In alpine areas, and in particular in high mountain areas, the potential effects of environmental changes on air temperature data are minimum, since these areas are only slightly affected by urbanization dynamics and land-use changes. More in detail, in Chapter 3, we propose a statistical-based tool for the detection of the role of temperature, in association with other climate-related variables (as precipitation), in the triggering of slope stability. This approach is aimed to point out the potential climatic triggering climate factors for the slope failure. It has thought up as a tool for a better comprehension of the possible effects of air temperature variations on environmental dynamics, also in the presence of sparse and poor-quality data. We performed this method on a catalogue of 41 rockfalls in the Italian Alps, focusing on the role of temperature on slope instability preparation and initiation, and on cryosphere-related dynamics. The final purpose is detecting a possible linkage between slope failures and meteorological anomalies, and results suggest a major role of temperature as a preparatory/triggering factor. Rockfalls occurred in association with significant temperature anomalies in 83% of our case studies, and different regional patterns emerge from the data. Based on these results, temperature can be considered as a key factor contributing to slope failure occurrence in different ways, in presence of both warm and cool temperature anomalies.

Chapter 4 presents a critical analysis in terms of how much it could be really answered of the main scientific questions with this work, what are the limitations encountered, which questions remain open and the possible further developments.

Contents

List of figures

List of tables

Chapter 1

1 Introduction

1.1 The context: increasing air temperature in the framework of global warming

With the terms “global warming” and “climate change”, we refer to the observed increment in the global average temperatures and related implications for the Earth’climate system. More in detail, we refer to a change in the long-term statistical properties of the climate system. In this context, surface air temperature represents an important summary measure for the state of global climate. According to the Fifth Assessment Report of the Intergovernmental Panel on Climate Change (IPCC), land and ocean surface temperature displayed an average global increase of about 0.85 °C over the period 1880-2012. Moreover, the first decade of the 21st century has resulted to be the warmest one since 1850 (Stocker et al., 2013) and 2015 and 2016 are the warmest years on record.

As can be seen in Figure 1-1, warming in the last three decades has been on average more intense over land than over the oceans, the former increasing at a double rate than records over sea, based on 1880-2014 records (NOAA, 2015b). The larger effect of ocean heat capacity contributes to increase the difference between land and sea temperatures. High latitudes in the Northern Hemisphere are characterized by an amplification of temperature increase, while warming is less pronounced over the southern oceans and North Atlantic (Hansen et al., 2006).

In consideration of the growing evidence of climate change in the last decades, one of the main goals of the scientific community is the understanding and quantification of uncertainty in the observed records, as a key point in the development of global and regional long-term climate quality data (Merlone et al., 2015). This is a crucial issue at all scale of analysis, since uncertainty affects records from short-term weather analysis to climate model simulations, limiting and altering critical observations of environmental climate-induced problems. The use of several different measurement approaches and data could contribute to a better characterization of bias in the observed records.

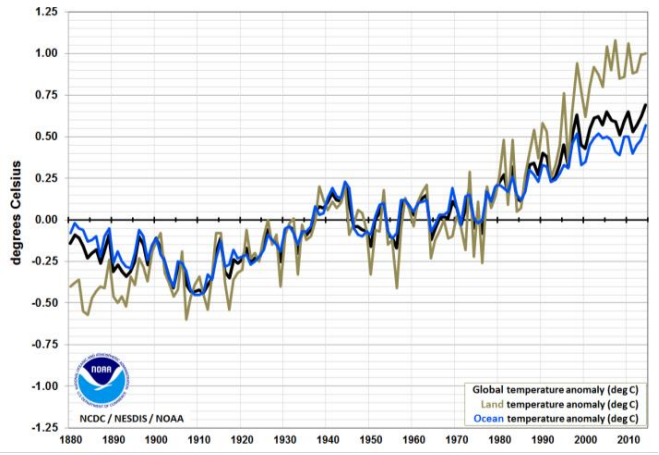

Figure 1-1 Mean annual global temperature anomalies over land, oceans and combined based on NOAA National Geophysical Data Center (NGDC) analyses from 2014 Global Report Supplemental Information (NOAA, 2015b).

Studies on long-term surface air variations and trends have been carried out by several research teams worldwide, providing a series of data products, for example, the Global Historical Climatology Network (GHCN), CRUTEM4, the Goddard Institute of Space Studies (GISS) and the Berkeley Earth project. Despite the use of several methods and approaches, long-term variations in the last 150 years are in broad agreement among the different datasets (Hansen et al., 2010; Stocker et al., 2013). As can be seen in Figure 1-2, globally averaged surface air temperature has increased during the last 150 years and particularly since 1980. Analyses of temperature trends based on shorter time series are significantly influenced by the starting and ending year of measurement and have a larger uncertainty than large-term trends. Various independent studies have been performed also at regional scale, generally supporting the results from global scale analyses of warming trends (Auer et al., 2007; Schär et al., 2004).

According to the IPCC (Stocker et al., 2013) the problem is even more complex at shorter temporal scales: daily maximum and minimum temperature range seems to have increased since 1980. Changes in climate extremes have been detected since about the mid-20th century. Studies on this topic highlight a faster rise in minimum temperature extremes compared to maximum ones. The number of warm (>90th percentile) days has increased in concomitance with a decrease in the number of cold (<10th percentile) days and nights at global scale (Figure 1-3). This large-scale warming is substantially confirmed at regional scale, with some exceptions indicating cooling in some areas as central North America, eastern US countries and part of South America, mainly related to changes in maximum values (Stocker et al., 2013).

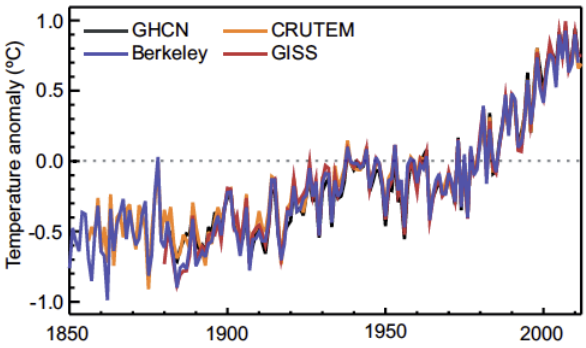

Figure 1-2 Global annual average land-surface air temperature anomalies relative to a 1961-1990 climatological referenced period average from the latest versions of Berkeley, CRUTEM, GHCN and GISS datasets; source: Stocker et al., 2013.

From a statistical point of view, the increased air temperature can be considered as a shift of the distribution. As in Figure 1-3, an horizontal translation of the distribution could lead to changes in the tails, and in the frequency of the extremes (Schär et al., 2004). A similar approach could be of help in the detection of anomalous values in the climate variables and thus in the interpretation of temperature-related natural hazards. Indeed, the pronounced air temperature warming detected worldwide could explain unusual events, as for example the increased incidence of summer heatwaves (Schär et al., 2004) or slope instability at high elevation sites, as occurring in the Alpine region (Gruber et al., 2004a; Huggel et al., 2010).

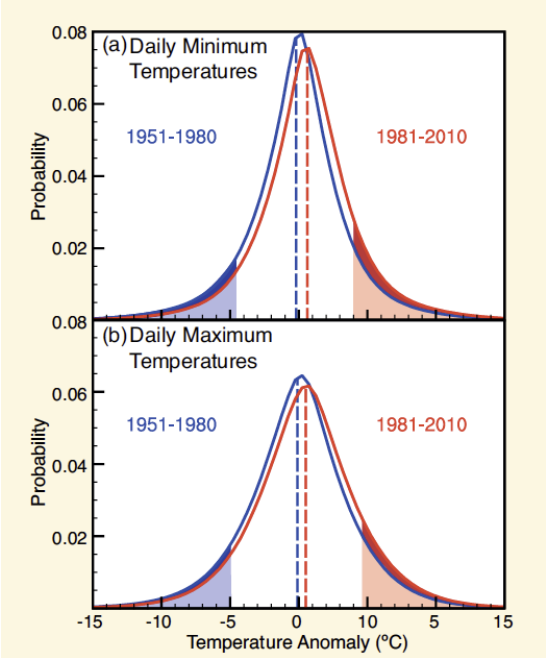

Figure 1-3 Distribution of daily minimum and maximum temperature anomalies relative to a 1961-1990 climatology reference period. Comparison between the two periods (1951-1980 and 1981-2010) is based on HadGHCND dataset; source: (Stocker et al., 2013).

The possible presence of non-climatic forcing affecting temperature records, as for example land-use and land-cover changes, could introduce bias in the records and uncertainty on global overall temperature trends. Urbanization, in particular, may lead to a possible overestimation of temperature values and thus alterate the perception of global warming. Indeed, most part of temperature data used for assessing long-term temperature trends come from weather station localized in widely urbanized areas, possibly influenced by urban warming. Hence, effects due to land-use change rather than to climate variability have to be accounted for in temporal trends detection at all spatial scales of analysis. In the recent past, many studies focused on sources of uncertainty in temperature records and proposed solutions for adjusting and correcting data, thus accounting for local factors contribution to temperature trends, in order to perform more reliable climate analyses and models (Hansen et al., 2010). Biased data give rise to uncertainty about the “true” value of models inputs, resulting in “poor” results, wrong estimates and conclusions. Ensuring the quality and comparability of input

data is critical to reduce uncertainty on the understainding of natural systems, especially in the complex framework of climate change.

1.2 Investigating the interaction between land-use and climate change

Climate change and urbanization are strictly coupled and connected, and changes in one could have considerable impacts on the other one. As the most evident example of land use and land cover change, urban areas play a fundamental role in local to large-scale planetary processes, via modification of heat, moisture, and chemical budgets. With rapid urbanization ramping up globally it is essential to recognize the consequences of landscape conversion to the urban climate. Urban areas represent only a small fraction of the Earth surface (less than 3%), but more than half of the global population lives in urban centres. The maximal increase of urbanized areas is in low and middle income nations, and urbanization is predicted to increase in the next years (Zhou et al., 2015). Beyond the socio-economic implications of growing urbanization, human activities alter the exchange of greenhouse gas between the terrestrial byosphere and the atmosphere through land-use and land-cover changes (IPCC, 2014). This could have considerable consequences on climate change and in particular on temperature variation ranges, in particular at the microscale (Fall et al., 2010). Indeed, most part of cities, independently from global warming, are experiencing a sort of climate change, due to the relative warmth of a city compared with rural neighborhs, which is the so-called Urban Heat Island (UHI) effect (Howard, 1833). As the name suggests, UHI is a localised phenomenon, developping in the nearest kilometers of an urbanized area. So, it refers to a sort of microclimate within cities, leading to higher temperatures than those recorded in the rural surroundings, particularly at night. Urban warming could significantly affect temperature measurements at the local scale, but the understanding of how such process could influence the assessment of global warming trends still is a debated topic (Parker, 2010). As stated in the IPCC report *"the key issue from a climate change standpoint is whether urban-affected temperature records have significantly biased large-scale temporal trends"* (IPCC, 2007). Most part of weather station networks are located in heavily anthropized sites, which result to be overrepresented at the global scale (Parker, 2010; Wickham et al., 2013). Moreover, the rapid urbanization and the expansion of urban centres towards rural neighbourhood could lead to the inclusion of more and more weather instruments

in areas affected by urban heating and, thus, characterized by higher temperatures compared to those of nearby surroundings. Thus, urban heating should be quantified and subtracted from temperature measures as much as possible, in order to guarantee reliable climate observations. For this reason, almost the totality of global adjusted datasets account for UHI effects in measurements (Hansen et al., 2010; Lawrimore et al., 2011; Wickham et al., 2013). The problem can be faced in many ways, for example excluding those sites which experienced urban warming according to climate analyses, or adjusting urban measurements by comparison with records from nearby rural stations (Parker, 2010). New techniques and approaches could be of help in detecting relationships and feedbacks between air temperature and land-use changes. Remote-sensing products, as SAR data, satellite nighttime images or MODIS-500 maps, are widely used to map global urban extent (Marconcini et al., 2014; Zhou et al., 2015) and to identify and geolocalize rural and urban stations (Wickham et al., 2013).

Several studies pointed out that UHI effects and land-use changes are almost negligible at a global scale, since these effects are much smaller than the observed global warming trends, i.e. less than 10% since 1950 (Parker, 2010; Wickham et al., 2013). Nevertheless, UHI could be more impacting than any other factors at smaller scales, particularly in those regions undergoing a rapid development (Stocker et al., 2013). Countries at different developmental stages show very different rates of expansion of urban areas in recent years. In developing regions, characterized by fast evolving urbanization, UHI could be more evident than in well-established urbanized regions. As examples, well-established cities, like London or Tokyo, are characterized by a stable UHI in recent decades (Wickham et al., 2013). On the other hand, Asian countries exhibit more dynamic UHI than European or US countries, where urbanization levels have still been high in past decades (Cui et al., 2016). Urban settlements in Asia, Africa and South America are expected to develop consistently in the future, because of rapid population growth. Meanwhile, the lack of effective mitigation and adaptation strategies in those regions represent a severe problem in the current framework of rising global warming. As can be noticed in Figure 1-4, in most part of those regions, surface air temperature increase has been greater than 1°C. Obviously most part of these regions (Amazonia, Sahara, Arabian Peninsula, Central Asia) are poorly urbanized and even inhabited, but the fact that most part of stations is urban suggest a possible role of population growth and urbanization dynamics in the enhanced climate warming (IPCC, 2014; Parker et al., 2010).

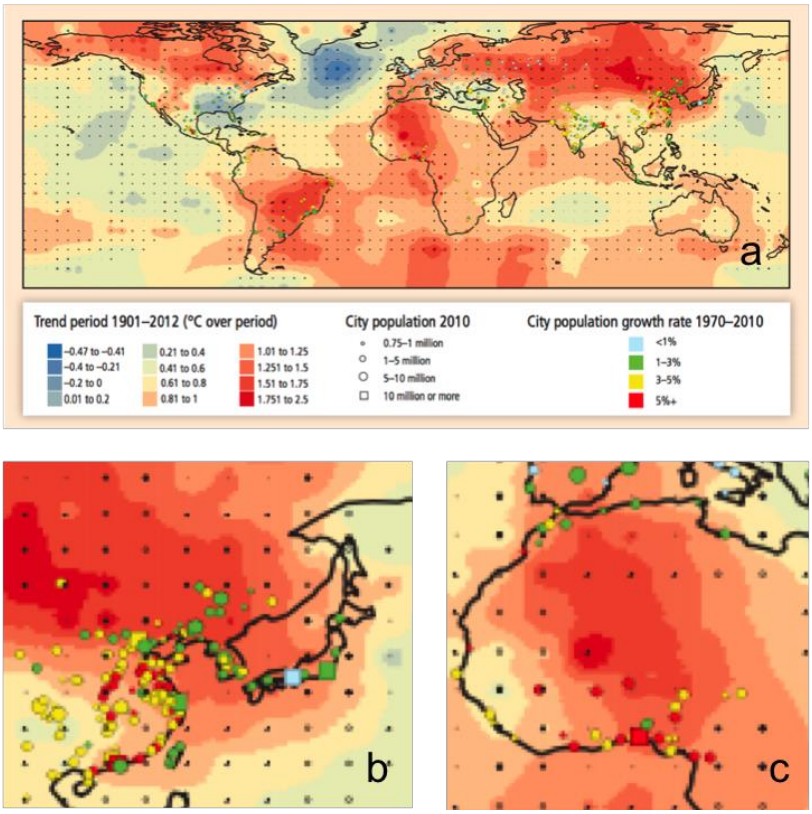

Figure 1-4 Largest urban agglomerations in 2010 against observed temperature trends in the period 1901-2012 (panel a). Urban agglomerations are color-coded based on their population growth between 1970 and 2010. As can be seen, eastern South America, part of North America, Asia (panel b) and western Africa (panel c) are experiencing temperature increase above 1° C. Most of them are also areas of rapid population growth (IPCC, 2014).

1.3 The cryosphere as an indicator of changing climate

A robust assessment of the changing climate requires not only the analysis of all climate variables involved, but also the full understanding of their impact on the natural systems, that could be used as indicators of the occuring changes. The cryosphere is probably the most evident proxy of current global warming (Kääb et al., 2007). We refer to the cryosphere as the part of Earth's surface where water is in solid form, frozen into ice or snow, thus referring e.g. to glaciers, ice sheets, snow and permafrost.

Changes in cryosphere components, as in the snow cover, (sea) ice and glaciers extent and frozen ground features, have direct impacts on multiple

systems, ranging from ecosystems to water resources. As stated in the Fifth Assessment Report of the IPCC, the cryosphere is often considered as a *"natural thermometer"* in the framework of current climate change, and its components could be considered as a sort of natural indicators, since they are among the most sensitive elements to changes in air temperature and related climate variables, as precipitation (Stocker et al., 2013). Studies on the cryosphere show an overall framework of disappearence or degradation of ice almost worldwide, even if important differences have been found at regional scales (Haeberli et al., 2009). High-altitude/latitude regions are among the most sensitive environments to global warming. In most mountain areas, glaciers are shrinking in response to the rise of air temperature in the last decades (Zemp et al., 2015). If focusing on our geographical context, the particular configuration of the Alpine region makes it a site of high scientific interest for climate and environmental issues, as many climate factors interact in this area. Climate in the European Alps is indeed highly complex, depending on the interaction between orography and the general circulation of the atmosphere (Beniston, 2006). As in Figure 1-5, the European alpine region experienced a significant temperature warming in the last century, at a rate faster than the global one (Auer et al., 2007; Beniston, 2006), along with an increase in warm temperature extremes (Allen and Huggel, 2013). In this region, cryosphere degradation is particularly evident, caused by temperature variations affecting the extension of glacial and periglacial belts. Glaciated areas reduced as much as 50 % in the last 150 years over the entire Alps (Zemp et al., 2008). An increase in permafrost temperature has been observed in Europe since 1980s (Harris et al., 2009), and the extent of Northern Hemisphere snow cover has decreased since the midtwentieth century (Stocker et al., 2013). Ice and snow cover and permafrost strictly depend on climate conditions, and changes in their thermal state could affect significantly slope stability (Gruber and Haeberli, 2007). Thus, one of the main issues related to cryosphere degradation at high elevation sites is understanding how temperature-related changes could impact on slope stability.

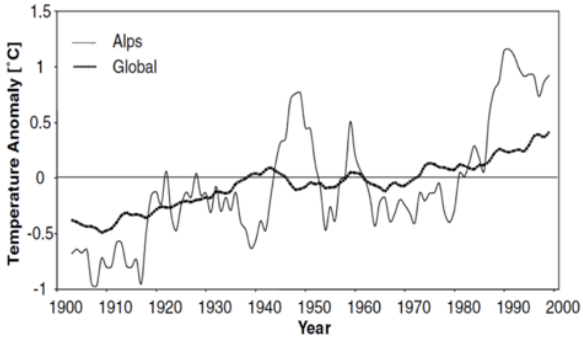

Figure 1-5 Global temperature anomalies compared to anomalies detected in the Alpine region, based on 1961-1990 normal period (modified from Beniston, 2006).

The frequency of rockfalls in the European Alps seems to have increased over the last century (Fischer et al., 2012), and this tendency is expected to increase in the future based on climate projections (Gobiet et al., 2014), even if several studies indicate a more complex response of slope failure activity to climate change (Huggel et al., 2010). Only recently the scientific community started considering temperature variation sensitivity of slope stability at high elevation (Allen and Huggel, 2013). Air temperature variations could have a direct impact on ice falls and avalanches, and indirectly influence landslide triggering, due to changes in the mechanical charateristics of the rock mass and consequent formation of discontinuities or because of changes in the hydraulic and hydrologic-related features (Gariano and Guzzetti, 2016). In this framework, studies related to processes occurring in these remote areas should be based on (as long as possible) unbiased temperature data, in order to perform reliable climate analyses. In alpine areas, the potential effects of land-use/land-cover changes on air temperature data are minimum, since these areas are little affected by urbanization dynamics and by other anthropic-driven changes. Records from mountainous regions could be therefore considered more reliable than those coming from weather stations located in urbanized areas. High elevation sites, being an almost uncontaminated area, are thus among the best environments to be studied for the understanding of the effective natural temperature variations.

1.4 Motivation behind the study

Detecting and attributing the fingerprint of anthropogenic climate change in the observed trends is an active area of research given its scientific relevance.

Moreover, the science is well established for temperature issues, but the study of other climate indicators (as the cryosphere) pose greater challenges due to their inherent complexity.

The main objective of this study is thus discussing and assessing the role of increased air temperature in the current context of global warming.

The red line of this dissertation is the investigation of the mutual interactions and feedbacks among air temperature, environmental changes and impacts on natural systems. For this purpose, we explore a spectrum of techniques and statistical methods aimed to shed light on the aforementioned issues. In this study, we merge various sources of information, derived from remote sensing and climate sciences, and reach across several disciplinary borders (as hydrological, geological and cryospheric sciences), by means of various statistical techniques and methods, to cover new grounds in the understanding of temperature-related effects and feedbacks. Given the complexity and wideness of the problem, we focus on aspects that, in our opinion, can be considered as "hot issues" in the frame of global warming and in our geografical context. The main issues we want to investigate and discuss throughout this work will be developed by focusing on some specific research questions.

Is it possible to disentangle the environmental and climatic factors behind trends in air temperature records at the global scale? More specifically, what is the effect of urbanization dynamics?

In Chapter 2, we investigate the presence of possible bias in temperature records due to factors more related to land-use change rather than to climate change, as the growth of urban areas. In this section, remote-sensing techniques and several statistical approaches have been proposed, aimed to shed light on the relations and feedbacks between urbanization and temperature trends.

Focusing on the temperature-sensitive environments, as the high-elevation sites, is it possible to quantitatively assess the role of temperature rise in the increased slope instability activity reported in recent decades for these environments? Can temperature be considered a key conditioning and/or triggering factor for slope failures at high-elevation sites?

In Chapter 3, we introduce the issue of the impact of temperature variations on natural systems, which can thus be regarded as terrestrial indicators of global

warming. More in detail, we discuss the role of air temperature variations in those environments which are less affected by land-use changes, i.e. mountainous regions. We focus on the growing evidence of slope instabilities in the European (Italian) Alps (Fischer et al., 2012; Gariano and Guzzetti, 2016; Huggel et al., 2010), and on their possible linkage with processes related to cryosphere degradation at high elevation sites. For this purpose, we propose a straightforward statistical-based approach, which allows one to detect anomalies in temperature and other climate variables in the lead-up of a slope failure.

Finally, in Chapter 4, we present a critical analysis in terms of how successful we could be in assessing the scientific questions mentioned above, what are the limitations encountered and which questions remain unanswered.

In order to help the reader to find a connection between the different topics assessed and the methods used, the main steps of the thesis development have been represented in the flowchart below (Figure 1-6).

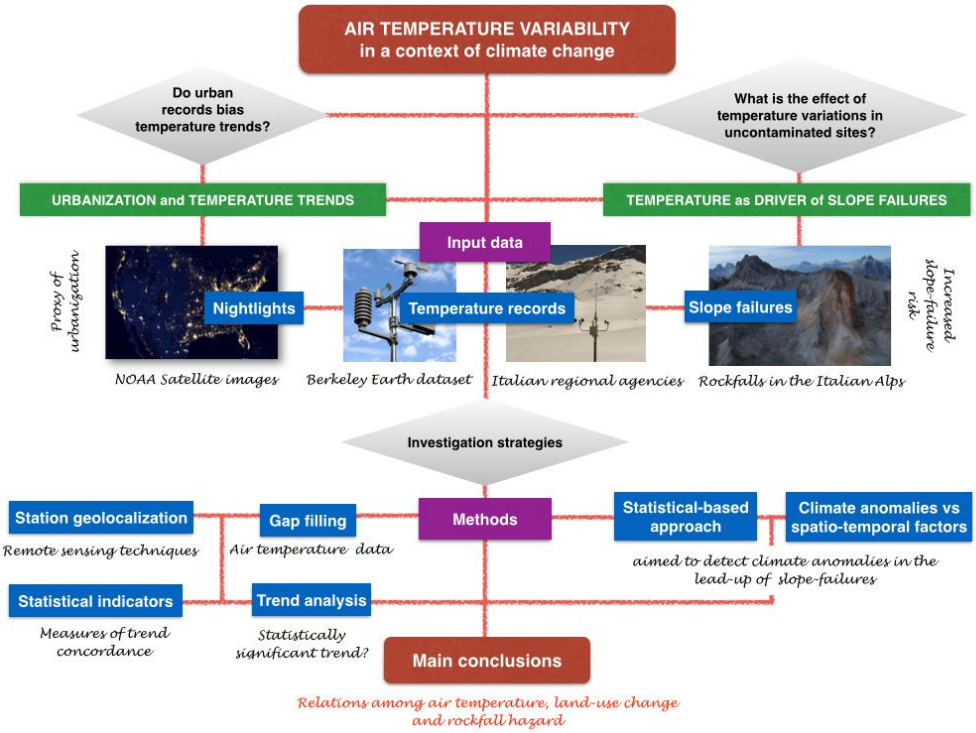

Figure 1-6 Flowchart representing the main topics and steps of the dissertation.

Chapter 2

2 Evaluating the effects of urbanization on air temperature using nightlights satellite data

2.1 Introduction

Urban transition has lead to evident alterations in landscape conditions and to important modifications in urban climate, along with several environmental problems. A rapid and unplanned urbanization growth as occurring in developing countries leads to alterations in demography and economic conditions, increases energy consumption and resources demand and worsens the urban environment (i.e., air and water quality) and the human health (Peng et al., 2012; Santamouris et al., 2015; Zhou et al., 2015). Understanding the complex relationships between urbanization and its consequences is thus a great challenge and concern for our times. In the context of climate change, it is of critical importance to understand if urban growth could affect temperature record trends and estimates and how it could effectively contribute to global warming (Arnfield, 2003; Hansen et al., 2010; Hausfather et al., 2013; Kalnay and Cai, 2003; McCarthy et al., 2010; Parker, 2010; Wickham et al., 2013).

The influence of urbanization on global and regional warming has been investigated since the 1980s (Jones et al., 1990; Oke, 1982). As defined in the previous chapter, many cities and towns are experiencing a sort of microclimate,

which is commonly called Urban Heat Island (UHI from now on). UHIs are the result of the presence of buildings and impervious areas (i.e., artificial structures covered by any impenetrable material as asphalt, concrete, rooftops), which cause the absorption of solar heat in the urban structures and ground surfaces, resulting in warmer temperatures.

Urban heat island effects could be mainly ascribed to (Environmental Protection Agency, 2008):

- solar heat retention by building materials, which have a lower albedo and higher heat capacity than those in the rural surroundings;
- obstruction of nighttime long-wave radiation by buildings;
- changes in land cover e.g., reduced vegetation in urban areas, causing a generalized reduced evapotranspiration;
- urban geometries e.g., urban canyons (streets lying between adjacent buildings walls);
- anthropogenic heat emissions e.g., from air conditioners, industrial facilities and cars.

Many other factors could contribute, including weather and local topographical characteristics (Environmental Protection Agency, 2008; Imhoff et al., 2010; Parker, 2010). Proximity to water bodies or mountainous land surface could influence air circulation and local wind patterns (Arnfield, 2003). Cloudy and windy climates decrease urban heat island effects, while calm wind conditions and low humidity under anticyclonic conditions minimize heat convection; as a consequence, for example, coastal cities may be less affected by urban warming than inland ones.

In the last years, many mitigation strategies have been adopted in order to reduce urban heat island effects e.g., green roofs (vegetative layers grown on a rooftop), cool roofs and pavements (coverages with highly reflective and emissive materials which are cooler than traditional ones), revegetation with trees and grass, and so on (Akbari et al., 2012; Environmental Protection Agency, 2008). Anyway, the methods available to reduce and mitigate UHI differ to some degree to the type of considered urban heat island, i.e. surface and atmospheric UHI. Surface UHI is quantified from remote-sensing data using airborne or satellite-borne sensors, as the parameter studied is the land surface temperature (LST) difference between urban and surrounding non-urban areas (Peng et al., 2012). Atmospheric UHI refers to warmer land air temperature in urban settlements

compared to cooler air in the surrounding rural areas and it is measured by fixed weather stations or mobile traverses. The two UHI could differ significantly from each other, including the maximum peak of UHI, in terms of timing and season of occurrence (Arnfield, 2003). Surface UHI show greatest temporal variability during the day, while atmospheric UHI is most intense after sunset. Because of changes in the sun's intensity, land cover and weather with seasons, surface UHI is more evident in summer, while air UHI in the winter (Figure 2-1).

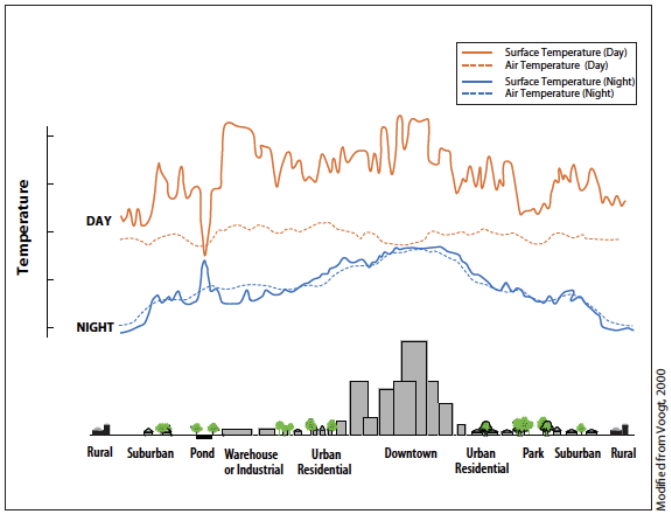

Figure 2-1 Surface and atmospheric temperatures variations, source: Environmental Protection Agency, 2008.

UHI studies have been performed for a large number of cities in the last decades in Europe and worldwide (Imhoff et al., 2010; Peng et al., 2012; Santamouris, 2007), thus highlighting the growing concern about this issue. Indeed, understanding what are the drivers of UHI and impacts on environmental dynamics is of primary importance for urban planning (Arnfield, 2003; Peng et al., 2012).

According to the purposes of this work, studies on the urbanization could be performed in different ways: indirect measurements as satellite remote sensing could provide surface temperature records (thus referring to surface UHI) with high spatial resolution, but the use of air temperature measured at weather stations networks allow a higher temporal resolution and the availability of longer data series (Tran et al., 2006). Air temperatures are commonly used in climate warming analysis of UHI (Wickham et al., 2013). In this study, we will concentrate on this aspect i.e., on the mutual relations and feedbacks between

variations of air temperature and urbanization dynamics. Thus, from now on, we will refer to UHI as atmospheric UHI only.

2.1.1 Urban Heat Island and temperature measurements

In the last years, interest on this topic has grown and several studies on the quantification of the effect of urban growth and Urban Heat Island effects on air and surface temperature have been performed worldwide (Hansen et al., 2010; Hausfather et al., 2013; Wickham et al., 2013). As outlined in Section 1.2, urban developments could have a great impact on temperature measurments, especially in those regions experiencing growing urbanization in time. This means that, in such a scenario, urbanization is expected to influence the climate at microscale, i.e. on the order of a few kilometers around the weather station, thus introducing bias and overestimation in the data (Parker, 2010). This work is thus based on the idea that a relation between temperature variation and urbanization trends could exist. Several studies have been performed in order to avoid or at least compensate for the effect of urban warming on large-scale trends estimate (Hansen et al., 2010; Hausfather et al., 2013; Wickham et al., 2013). NASA Goddard Institute for Space Science (GISS), Hadley Centre of the UK Met Office and the Climatic Research Unit of the University of East Anglia (HadCRU), National Oceanic and Atmospheric Administration (NOAA) and recently Berkeley Earth are only some of the teams that are approaching the problem. Global warming trend analyses have been conducted for example using adjusted urban temperature data, comparing data to sea surface temperature (Hansen et al., 2010), comparing temperature values in different weather conditions (Kassomenos and Katsoulis, 2006) or removing sites with suspected urban warming from global warming trend analysis (Hansen et al., 2010). Note that, often, the poor spatial coverage of the weather stations network does not guarantee the possibility to compare urban stations with the corresponding rural ones (Zhou et al., 2004). Moreover, in this context, another difficulty is to define if a station is rural or not. Rapid urbanization makes the classification between urban and rural difficult, because of the inclusion of several stations in urban areas in the last years. Information on human settlements or on land-use could be of help in this. The problem in the past has been approached for example using census data or population metadata, but such informations are generally out-of date, and thus recently map-based metadata and satellite observed nighttime lights have been introduced. Indeed, UHI and in general soil anthropization detection are closely related to the type of metadata used (Peterson et al., 2005).

2.1.2 Nightlights as a proxy of urbanization

Remote sensing data as satellite nightlights maps (also abbreviated as "nightlights" from now on) allow tracking the spatiotemporal dynamics of the population much better than traditional census and administrative data. The fine spatial resolution of nightlights (nearly 1 km at the equator) makes them a valuable proxy for the human presence, widely used in many research fields (Cauwels et al., 2014).

In the late 90s the scientific community started considering nightlights as a valuable proxy for e.g., assess population density (Imhoff et al., 1997). Many studies followed, focusing mainly on economic activity (Chen and Nordhaus, 2011), electric power consumption patterns (Chand et al., 2009) or on demographic issues e.g., on the production of a global Poverty Index (Elvidge et al., 2009). Nightlights imagery have been largely employed to map and measure urban extent (Imhoff et al., 1997; Small et al., 2005; Zhou et al., 2015) and to address environmental topics e.g., light pollution in Europe (Bennie et al., 2014).

Recently, nightlights data have been employed to relate the flood risk to increasing human pressure near rivers at global scale (Ceola et al., 2014). The same approach has been adopted to study human exposure to hydrogeological risk at local scale e.g., mapping population exposure to natural hazards (Soto Gómez et al., 2015) and more in general, to assess the interaction between water resources and human dynamical systems (Ceola et al., 2015).

In this work, we explore the possibility to relate the temperature variations in recent years to the incorporation of the weather stations in more and more urbanized areas, using nightlights as a proxy of human presence and urbanization. The main idea is to assess if there is a relation between temperature trend and nightlights trend in the last 25 years, thus investigating how urban growth (i.e., Urban Heat Island) could contribute to climate warming not only at local, but also at regional and global scale. In this light, nightlights may offer interesting insights to better understand the impact of urbanization on increasing temperatures trends. Nevertheless, caution must be paid in interpreting the results of such analysis, due to the presence of disturbing factors as policies against nightlight pollution, like those already implemented in USA, UK and and Northern Europe (Cauwels et al., 2014; Ceola et al., 2014).

As confirmed by several studies (Imhoff et al., 2010; Peng et al., 2012; Santamouris, 2007), urban warming could have significant effects on temperature

records at microscale, but the understanding of how these data could bias temporal trends at broader scales still be a crucial point (Parker et al., 2010). This issue could be particularly problematic in developing and emerging countries, where urban areas are growing fast and the lack of urban heat island strategies could enhance the problem.

2.2 Data and methods

2.2.1 Air temperature datasets

Several different archives have been considered. As said before, the main organizations keeping and assembling temperature records, providing data and analyzing global temperatures are NASA Goddard Institute for Space Science (GISS, 2016), Hadley Centre of the UK Met Office and the Climatic Research Unit of the University of East Anglia (HadCRUT4, 2016), National Oceanic and Atmospheric Administration (NOAA, 2016). Also FAO datasets have been investigated (FAOClim-NET, 2016) since they guarantee a good spatial coverage also on developing regions e.g., Africa and most part of Asia. Strict requirements are considered for this work, due to the need of ensuring that temperature data have the same spatial and temporal coverage of nighttime lights imagery:

- the coordinates of air temperature stations should have a spatial precision of 30 arcsec as nightlights images i.e., the cent of a degree in latitude and longitude;
- data should be available from 1992 to 2013 i.e., the same temporal coverage of nightlights data;
- a good spatial coverage at the global scale and in developing countries should be ensured.

Unfortunately, all the datasets listed above show potential limitations. Global Historical Climatology Network-Monthly (GHCN-M) land air temperature dataset, compiled and merged by NOAA's National Climatic Data Center (NCDC), has been internationally considered as the main source of data for climate studies and monitoring activities since the early 1990s. The last version, v3, was released in 2011 and includes mean daily and monthly temperature data for more than 7000 stations. Nevertheless, it does not guarantee a good spatial coverage on developing countries. GISS Surface Temperature Analysis uses stations from GHCN-M v3, augmented with SCAR (Antarctic stations) temperature stations, thus showing the same limitations of GHCN-M as discussed

above. HadCRU has developed another extensively used dataset. The new database (CRUTEM4) consists of 5583 stations from various datasets, which are updated at roughly monthly intervals. Unfortunately, most stations are reported to the nearest tenth of a degree in latitude and longitude, which makes it impossible to perform additional analyses using nightlights. FAO data are used by technical divisions for worldwide food security and climate-related studies; FAO offers free access to data for 245 territories, providing data also on many remote areas and third world regions. For our purposes, we considered the FAOClim-NET dataset, which covers a significant number of data with respect to the previous considered datasets i.e., monthly data for 28100 stations, for up to 14 observed and computed agroclimatic parameters, including rainfall and temperature. Nevertheless, temperature data are available only up to the first semester of 2009, while nightlights temporal evolution is along the years from 1992 to 2013.

The source of mean monthly station measurements for our current analysis is Berkeley Earth database (Berkeley Earth, 2016), which shows the best compromise between spatial and temporal availability. Berkeley Earth dataset combines data and metadata from16 previous existing datasets including:

- GHCN-M
- Global Historical Climatology Network – Daily (GHCN-D)
- US Historical Climatology Network – Monthly (USHCN-M)
- World Monthly Surface Station Climatology
- Hadley Centre / Climate Research Unit Data Collection
- US Cooperative Summary of the Month
- US Cooperative Summary of the Day
- US First Order Summary of the Day
- Scientific Committee on Antarctic Research
- GSN Monthly Summaries from NOAA
- Monthly Climatic Data of the World
- GCOS Monthly Summaries from DWD
- World Weather Records (only those published since 1961)
- Colonial Era Weather Archives
- Multi-network Metadata System (from NOAA)
- World Meteorological Organization Station Metadata

The current dataset, after removing duplicate records, consists of 39000 stations, thus is five times more extended than GCHN-M archive, which is

extensively used at the global scale (Figure 2-2). In general, the best spatial coverage is in North America, Europe, Australia, and Asia.

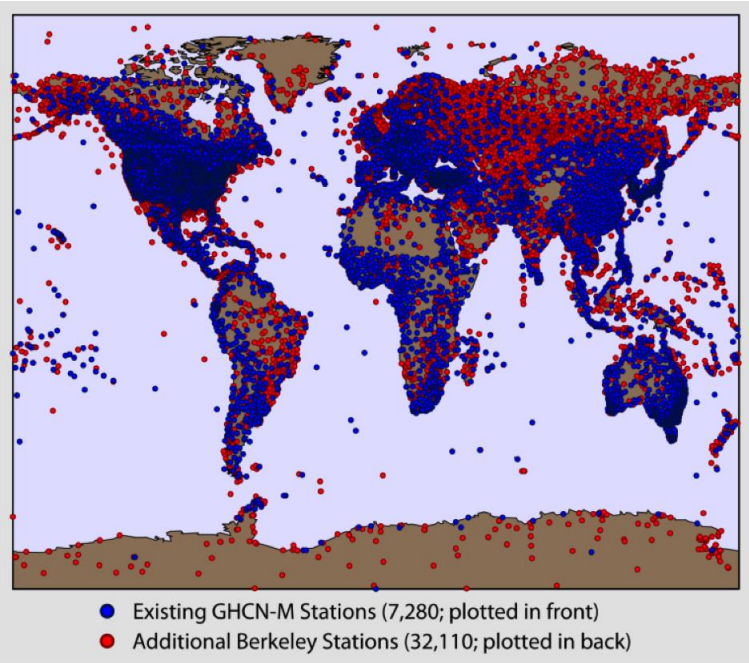

Figure 2-2 Spatial coverage of GHCN-M and Berkeley land air temperature stations, source: Berkeley Earth.

The dataset consists of three categories, as outlined below:

- Source data

Source data include raw temperature data as originally reported from the original agencies mentioned above. They could contain many different quality controls and redundancies.

- Intermediate data

Intermediate data combines all data from original sources and may contain redundancy records ("Multi-valued"). In the next step, duplicate records have been filtered and merged, thus only one time series per location is provided ("Single Valued"). At this point, data are quality checked and flagged and any poor quality data have been removed. Bad quality data include values that had pre-existing indicators of data quality problems associated with instrumental error, post-hoc manipulations and/or in-filling of missing data. Values that exceeded

global climate extremes have been further removed (further details at http://berkeleyearth.org/about-data-set/). In the input file data, flags are used as indicators of how the data has been processed and any quality control issues that are known to be present. When data flagged as bad from a quality point of view have been deleted, clean quality controlled data are obtained ("Quality Controlled"). Nevertheless, this product has not been fully checked for the presence of biasing events and no adjustments related to eventual discontinuities and long-term inhomogeneities have been made. In this context, if a station exhibits severe heating due to urban heat island effect, this could result in a bias in temperature measurements. Global temperature trends created partly from urban stations records could thus show urban warming contamination.

- Output data ("Breakpoint Adjusted Monthly Station data")

These data received a post-processing homogenization step. Series are compared to their neighbors and any discontinuity and/or heterogeneity is detected and corrected (Rohde et al., 2013). Indeed, stations showing significant differences compared to local nearby ones could be affected by local systematic effects (e.g., UHI effects as mentioned above) or could show large discontinuities and inhomogeneities due e.g., to station moves, different observing times, different siting practices and changes in measurement instrumentation (Peterson et al., 1999; Rohde et al., 2013). Seasonality in this dataset has been removed, but this does not affect the analysis in this work, since we considered the multi-year average temperature, as better described below.

For the purposes of this study, three output files have been used: two intermediate products, Single Valued and Quality Controlled datasets, and Breakpoint Adjusted Monthly Station data (Breakpoint Adjusted from now on). Breakpoint Adjusted data could have been also corrected for the presence of local systematic bias as urban heating. An averaging weighting procedure has been applied to this dataset, i.e. weights have been applied to the stations contributions affecting Kriginig averages (the contributions made by individual stations towards the estimate of temperature at a given site). Further details are included in Rohde et al. (2013). This entails that, for the purposes of this work, these data could be misleading in the study of UHI effect in global warming dynamics. Thus, the Breakpoint Adjusted dataset has to be compared to raw values (Single Valued) and to relatively clean data (Quality Controlled), which potentially preserve urban warming biasing effect. In this way, eventual differences in the temperature trends at local and global scale may be detected.

The multi-year average temperatures have been derived from the available mean monthly data. First, average monthly temperatures have been considered, since they are straightforwardly available. Nevertheless, since UHI is more evident on nights with calm, free-cloud and dry skies (Kassomenos and Katsoulis, 2006), it is useful to also evaluate minimum monthly temperatures.

2.2.2 Satellite nightlights time series

Annual time series of nightlights imagery are freely provided from the NOAA National Geophysical Data Center (NGDC) as satellite images (NOAA, 2015a), collected under the Defense Meteorological Satellite Program (DMSP), which currently manages four satellites equipped of Operational Linescan System (OLS) sensors (Figure 2-3). OLS consists of two sensors operating respectively in the near-infrared (400 to 1100 nm) and in the thermal infrared (10.5 to 12.6 μm) spectrums. The field of view is approximately 3000 km and images resolution is about 0.56 km (Cauwels et al., 2014).

Figure 2-3 NASA Visible Earth: Earth's City Lights (source: http://visibleearth.nasa.gov/).

Satellite images are collected on a yearly basis for a 22-year period from 1992 to 2013 and six satellites have been used, with a total of 34 composite images, generating a product called stable light (Table 2-1). In case of years presenting overlapped dataset, we considered a new nightlight product generated by Ceola et al. (2014), which represents the average nighttime brightness. Original satellite images are not onboard calibrated, thus they have been previously intercalibrated in order to compare among years, according to yet known procedures in the

literature (Chen and Nordhaus, 2011; Elvidge et al., 2009). Indeed, the redundacy created by two products generated by overlapped orbiting satellites could be used to intercalibrate images, averaging pixel by pixel in order to take into account all the existing images of the area and thus using adjusted values (Ceola et al., 2014). Each pixel in the final product represents the stable light yearly average in a 6-bit format and it is expressed as a Digital Number (denoted as *DN*). In other words, it is a dimensionless numerical integer number, which represents the brightness on Earth's surface in each cell. Sensors could identify cloud-free nighttime lights from e.g., human settlements, fires and gas flares.

Table 2-1 Satellites number and observation year; modified from Ceola et al. (2015).

	F10	**F12**	**F14**	**F15**	**F16**	**F18**
1992	F101992					
1993	F101993					
1994	F101994	F121994				
1995		F121995				
1996		F121996				
1997		F121997	F141997			
1998		F121998	F141998			
1999		F121999	F141999			
2000			F142000	F152000		
2001			F142001	F152001		
2002			F142002	F152002		
2003			F142003	F152003		
2004				F152004	F162004	
2005				F152005	F162005	
2006				F152006	F162006	
2007				F152007	F162007	
2008					F162008	
2009					F162009	
2010						F182010
2011						F182011
2012						F182012
2013						F182013

Gas flares are combustion devices used mainly in industrial plants to burn gas (e.g., methane) released during petroleum extraction. In this analysis, they have been removed, along with fires, since they are not of interest in studying urbanization and human settlements dynamics. *DN* values are proportional to

radiance and range from 0 (pitch dark areas) to 63 (bright areas). Images are provided as raster products with a spatial resolution of 30 arc seconds (0.00833°), i.e. nearly 1 km resolution at the equator, with a spatial extension between 75°N and 65°S latitude and 180°W and 180°E longitude. Some parts of Alaska, Antarctica, Canada, Greenland, and Scandinavia are missing, but this does not affect our analysis, since only 0.0002% of the global population lives in these areas (Cauwels et al., 2014).

2.2.3 Empirical evidence

The basic idea behind this work is to assess the hypothesis that temperature records could be significantly affected by urbanization dynamics close to measurement stations. For this reason, the mean annual temperature of each station has been plotted against the mean annual luminosity of the station site in order to assess if a relation exists between the response variable temperature *T* and the predictive one *DN*. This is a preliminary step in order to test the relation between trends afterwards (Figure 2-4).

A positive increase of *T* with *DN* can be detected at a global scale from Figure 2-4. Left side cluster mainly corresponds to stations located in extreme darkness areas, with night light radiance less than 1 $\mu Wm^{-2}\ sr^{-1}\ \mu m^{-1}$. As in Hansen et al. (2010), these are regions with luminosity below the satellite's detectability limits.

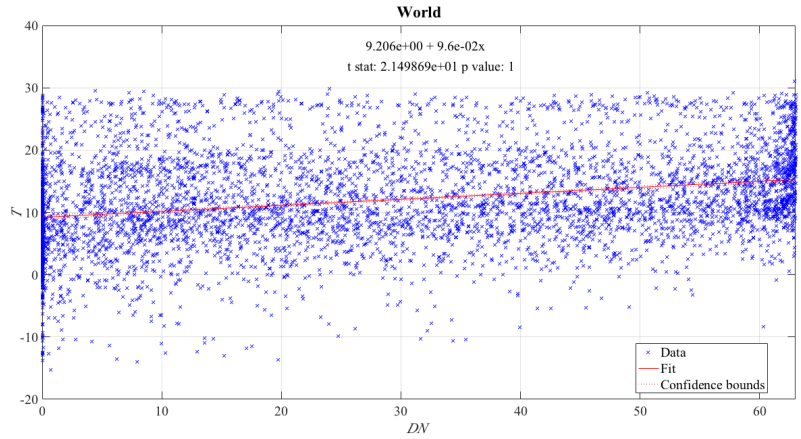

Figure 2-4 Mean annual temperatures against luminosity values in correspondence of stations sites at global scale.

Right side cluster refers to instruments located in bright areas (above 60 DN approximately), which correspond to high-urbanized regions (Zhou et al., 2015).

However, the presence of eventual confounding effects could prevent the correct assessment of the relation between temperature and brightness. As well known, altitude is an important driver for air temperature. In this context, the feature of major interest is the presence of an eventual secondary effect of elevation on anthropization perception. The elevation of the measuring instruments may represent a confounding factor, due to the fact that luminosity is generally more intense at lower altitudes, where most part of considered stations are localized. The relation in Figure 2-4 may derive from a tendency of T to decrease with elevation z, combined with a tendency of DN to decrease with z. Moreover, air is more rare at high altitude, and this entails effects on the refraction of light. Therefore, elevation could prevent the correct assessment of urbanization feedback on air temperature. Thus, a bivariate linear regression has been performed, in order to verify the initial hypothesis i.e., that urban effect could influence temperature data, and to capture an eventual confounding effect of elevation in this relation. The bivariate relation is

$$T(DN, z) = a + b \cdot DN + c \cdot z \tag{2.1}$$

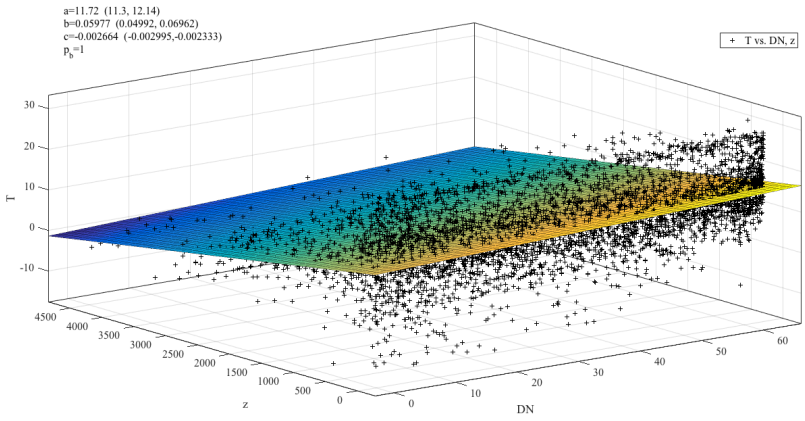

Figure 2-5 Multivariate linear regression at global scale between the response variable T and predictive variable DN and elevation z (dataset: Quality Controlled, average monthly temperature). Coefficients with 95 % confidence bounds and p value of the DN coefficient (b) i.e. p_{DN} at global scale are shown.

Temperature has been regressed against the luminosity in the station pixel (DN) and the station altitude (z) as in Eq. (2.1). The p value of a Student's t distribution has been computed to test if the predictive variable T is still significantly dependent on DN, i.e. b is significantly different from zero. Also after having eliminated the confounding factor z, the p value is nearly 1 for the b

coefficient, demonstrating that a relevant effect is still visible (Figure 2-5). More details are included in Section 2.3.1.

2.2.4 Methods

The main goal of this work is to assess whether a significant relationship exists between trends of temperature and luminosity in the investigated period 1992-2013. Given the complexity of the studied phenomenon, more than one method has been thought up and performed. With this aim, a suitable temperature dataset has been detected and a method for gap filling in air temperature data has been applied (Section 2.2.4.1). Then, the selected stations have been correctly localized, in order to get reasonable nightlights estimates close to the measuring place (Section 2.2.4.2). A simple linear regression analysis has thus been used (Section 2.2.4.3) and more than one approach has been proposed to measure the degree of concordance of the two variables and related statistics (Section 2.2.4.4) For the sake of clarity, examples of application have been included throughout the text.

2.2.4.1 Procedure for gap filling in air temperature data

First, a survey of the available stations from 1992 to 2013 in the Berkeley Earth dataset considering both average and minimum monthly temperatures data has been performed. We first consider some statistics about the number of times when it is possible to derive the temperature T using the available data records i.e., how many stations have the entire data series and, if they are incomplete, how many months per year are available per each station. Figure 2-6 is an example of consistency analysis 3D bar plot, which allows a rapid assessment of the number of available temperature records. As an example in Figure 2-6, we can see that, from 1992 to 1999, we have 12 months of recorded data for nearly 12000 stations (the sample size ranges between 12115 and 12613), while from 2001 to 2005 we have 12 months of recorded data for nearly 13000 stations (the sample size ranges between 12935 and 13801). In 2013 we have 10 months of recorded data for 11754 stations, but no instrument has recorded 12 months of data, probably due to the fact that data acquisition from Berkeley Earth stopped in October 2013.

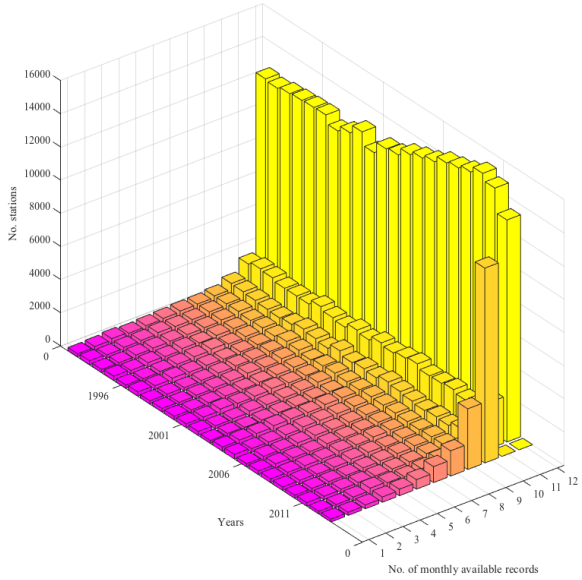

Figure 2-6 Example of a consistency analysis, based on the number of available Berkeley Earth stations per month and per year in the period 1992-2013.

A very common problem in meteorological and climatological data analyses is the presence of gaps in the time series. Indeed, failures in the measuring instruments as, for example, breaking or the interruption of data transmission, may cause gaps in the record observations. In this work, most part of the considered stations shows lacks in the temperature series in the monitoring period 1992-2013. This is particularly evident in developing and emerging continents, where the poor thermometers coverage enhances the problem. These shortcomings could be overcome using methods to reconstruct missing data. In this work we used a statistical-based approach for temperature data reconstruction in order to (i) fill the gaps in the series of monthly temperature data obtained from the Berkeley Earth dataset and (ii) increase the sample size in poorly instrumented areas as Africa and South America.

In order to test the accuracy of the method, the gap filling procedure has been previously tested on a continuous time series by excluding a-priori some values. Then, the reconstructed values have been compared to the data excluded at the beginning. The method proved to be able to predict the values and it has been applied to the entire sample. For the sake of clarity, Figure 2-7 shows an example of application of the gap filling procedure on a selected station.

Months j	Years i																							
	1	2	3	4	5	6	7	8	9	10	11	12	13	14	15	16	17	18	19	20	21	22	Ny_j	$\overline{T_j}$	S_{ij} (i=22)	$\hat{T}_{ij}$(i=22)
1	0.8	1.9	3.5	1.6	2.7	3.3	2.5	4.2	1.7	2.8	0.4	1.4	1.4	1.3	0.8	4.4	3.6	0.5	0.0	1.6	2.5	2.9	22	2.1	0.8	-
2	3.9	3.2	2.2	5.7	2.1	6.1	7.1	3.9	5.8	6.0	5.2	1.2	3.4	1.6	3.1	5.8	5.3	4.4	2.8	5.2	0.9	2.2	22	4.0	-1.7	-
3	8.1	6.9	10.6	6.8	6.6	11.6	9.1	8.3	9.3	9.7	9.9	8.8	7.0	7.6	7.3	9.2	9.4	9.3	7.4	8.6	11.9	6.5	22	8.6	-2.1	-
4	11.2	11.0	10.3	12.3	12.6	12.2	11.2	11.9	11.9	11.0	11.5	11.2	11.3	11.2	12.9	15.7	11.2	12.7	12.6	15.6	11.4	12.4	22	12.1	0.3	-
5	16.8	16.3	15.5	16.1	16.1	17.3	17.4	17.2	17.6	17.6	15.4	18.2	14.7	18.5	16.8	17.3	16.4	19.0	15.8	19.0	17.1	14.7	22	16.9	-2.2	-
6	17.1	20.4	19.5	18.4	21.3	19.4	21.4	19.4	21.3	20.0	21.6	24.2	20.7	22.8	21.5	20.1	20.5	21.4	20.4	20.4	22.1	20.5	22	20.7	-0.1	-
7	21.8	20.6	24.7	24.0	21.5	21.9	23.6	22.5	21.0	22.1	21.3	24.2	22.2	24.0	25.4	22.5	22.3	23.3	24.5	21.5	23.4	23.9	22	22.8	1.1	-
8	23.1	22.3	23.8	21.2	21.1	22.5	23.3	21.4	22.6	23.3	20.5	25.2	21.6	21.7	20.8	20.6	21.9	23.7	21.5	24.0	24.2	22.6	22	22.4	0.2	-
9	17.3	16.2	17.2	15.6	15.4	19.8	17.9	19.1	18.8	16.0	16.6	17.1	18.6	18.8	19.3	17.2	17.2	18.9	17.5	21.2	18.4	18.8	22	17.9	1.0	-
10	10.2	11.2	11.7	13.9	12.9	13.2	12.7	12.6	13.4	15.5	12.4	9.9	13.9	12.9	14.1	13.0	14.1	12.6	11.9	13.3	13.7	13.3	22	12.8	0.5	-
11	6.6	5.4	8.1	6.3	7.6	7.2	5.4	6.2	7.2	6.2	8.3	6.7	7.0	6.5	7.9	6.4	8.0	7.5	7.9	7.6	8.4	NaN	21	7.1	NaN	6.8
12	2.1	2.7	3.5	2.9	3.8	3.8	2.1	2.0	4.8	-0.1	4.3	2.8	3.1	1.2	3.3	2.9	2.6	1.2	1.4	4.0	1.9	NaN	21	2.7	NaN	2.5
Nm_i	12	12	12	12	12	12	12	12	12	12	12	12	12	12	12	12	12	12	12	12	12	10				
$\overline{S_i}$ (i=22)	-	-	-	-	-	-	-	-	-	-	-	-	-	-	-	-	-	-	-	-	-	-0.2				
$\overline{T_j}$	11.6	11.5	12.6	12.1	12.0	13.2	12.8	12.4	12.9	12.5	12.3	12.6	12.1	12.3	12.8	12.9	12.7	12.9	12.0	13.5	13.0	12.3				

Figure 2-7 Example of application of the gap filling procedure described in this section 2.2.4.1. In the selected station Torino Caselle (Berkeley ID 155990) two gaps in November and December 2013 (i=22) have been found.

The temperature station's reported data is identified as T_{ij} i.e., the temperature value of the jth month of the ith year, where j = 1,..,12 and i varies from 1 to 22 according to the temporal coverage of the nightlights (i.e., from 1992 to 2013). Thresholds on the minimum number of months Nm_i and years Ny_j are needed to reconstruct the missing data $\widehat{T_{ij}}$ of the given stations. A minimum threshold of 9 month per year ($Nm_i \geq 9$) and 18 years per series ($Ny_j \geq 18$) is considered as suitable for reconstructing $\widehat{T_{ij}}$. The main steps of the reconstruction method are listed below.

(i) First, the number of available records for the jth month to reconstruct the mean monthly temperature $\overline{T_j}$ is determined. As seen in Figure 2-7, Ny_j = 22 for months January to October, while Ny_j = 21 for November and December 2013. Also in this case, the minimum required threshold $Ny_j \geq 18$ is satisfied and the mean monthly temperature $\overline{T_j}$ can be computed. If for any month $Ny_j \leq 18$, the station is discarded.

(ii) For the year where there is a gap, the deviation S_{ij} is computed for the months where the data are available as

$$S_{ij} = T_{ij} - \overline{T_j} \tag{2.2}$$

The mean deviation in year i is computed as

$$\overline{S_i} = \frac{1}{Nm_i}\sum_{j=1}^{Nm_i} S_{ij} \tag{2.3}$$

(iii)The missing temperature $\widehat{T_{ij}}$ is reconstructed as

$$\widehat{T_{ij}} = \overline{T_j} + \overline{S_i} \tag{2.4}$$

(iv) We can thus compute the mean annual temperature ($\overline{T_i}$) for the year i by averaging the 12 months values.

As in the example of Figure 2-7, for the year i=22 showing missing data in November and December, we can compute the deviation S_{ij} for the months where the data are available (January to October) and, subsequently, the mean deviation $\overline{S_i}$ year i=22 (Eq. (2.2) and (2.3)). At this point, we can reconstruct the missing temperature $\widehat{T_{ij}}$ in year i=22 for months November to December (Eq. (2.4.)). The mean annual temperature ($\overline{T_i}$) is thus computed (Figure 2-8).

Finally, we performed a sensitivity analysis by varying the thresholds through an automatic iterative procedure. In this way, the most efficient threshold combination Nm_i - Ny_j in terms availability of temperature stations could be determined. As seen in Figure 2-9, a good spatial coverage is always guaranteed. The combination $Nm_i \geq 9$ and $Ny_j \geq 18$ is resulted to be the most efficient one, thus it has been selected for further analysis (Figure 2-9).

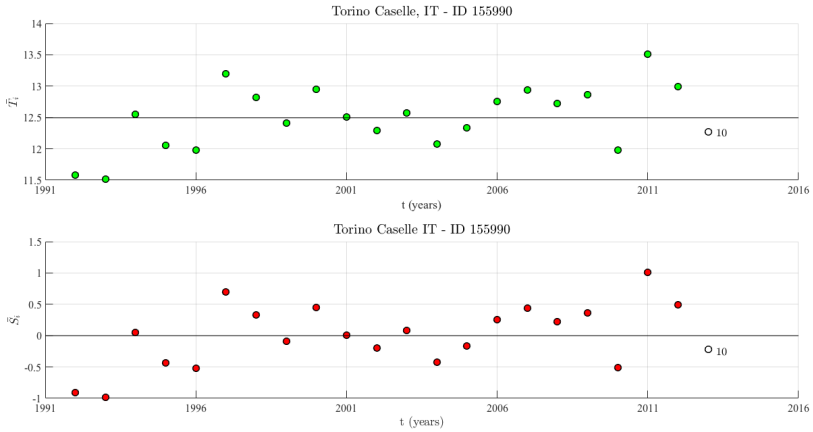

Figure 2-8 Example of gap filling procedure performed on Torino Caselle station (Berkeley Earth ID: 155990); $\overline{T_i}$ is the mean annual temperature, $\overline{S_i}$ is the deviation from the mean temperature in the 22 years (12.5 °C in this case); empty dots refer to temperature values reconstructed with less than 12 months of data ($Nm_i < 12$).

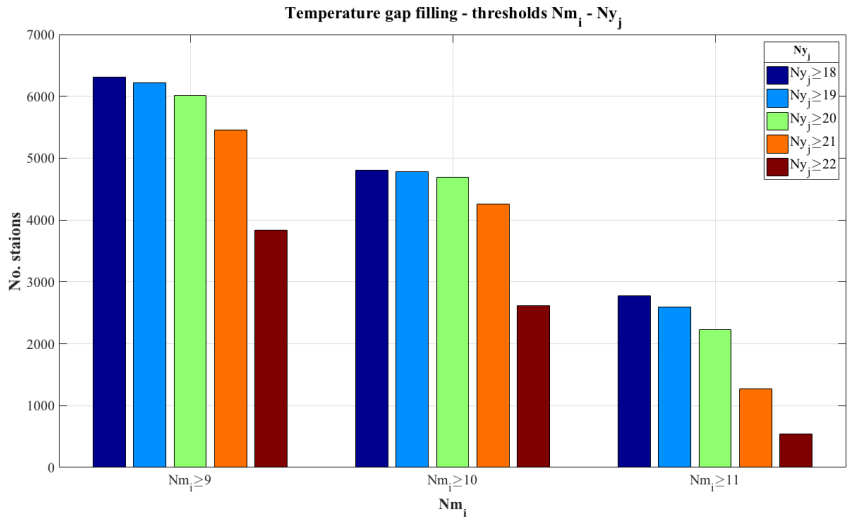

Figure 2-9 Outcomes of the gap filling procedure by iterating the thresholds Nm_i - Ny_j, i.e. the minimum number of months and years needed to reconstruct the mean annual temperature $\overline{T_t}$ of the given stations.

2.2.4.2 Geolocalization of air temperature stations

First, stations localized out of the raster spatial extension have been removed. Air temperature stations selected according to the previous requirements (Sections 2.2.1 and 2.2.4.1) have to be located with a spatial precision of at least 30 arc seconds. Thus, stations underwent a coordinate correction procedure, comparing Berkeley Earth project metadata to those provided by the World Meteorological Organization.

Stations localizations in the dataset are provided along with their uncertainties. As indicated in Berkeley Earth documentation, coordinates uncertainty could be merely based "on the precision with which latitude and longitude are reported", and not on appropriate metadata, thus we could incur in errors in the localization. This could lead to a series of wrong conclusions on the estimation of the mean *DN* value in the surrounding of the stations and, thus, to a wrong estimate of nightlights trends (Figure 2-10). For this reason, it is necessary to perform a further check on metadata of the selected stations. The main steps of the procedure are listed hereinafter and illustrated in the flow chart below (Figure 2-11).

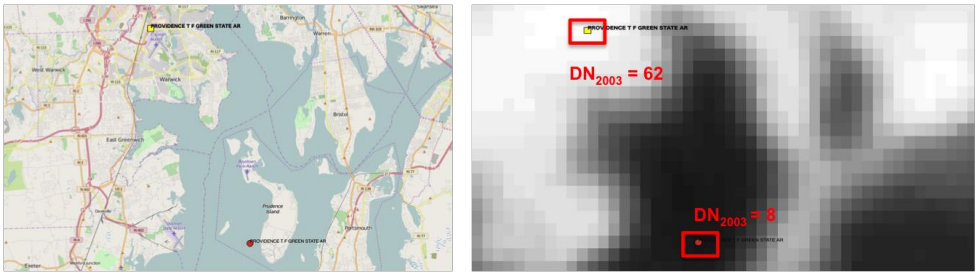

Figure 2-10 Example of different localization of a station by Berkeley Earth and WMO. As shown in the panel at the right, wrong metadata could lead to different estimates of the mean luminosity in the considered buffer.

Once the stations have been selected, we associate the WMO code to the Berkeley ID, whenever available. If this is not possible, it means that the considered stations are not included in the WMO list. In this case, if coordinates provided by Berkeley satisfy the precision of satellite nightlights products, they could be selected; otherwise the station is removed, since it is not possible to compare metadata and make eventual adjustments. If the station is an official WMO one, we further test if the minimum required spatial precision is satisfied. In this case, four situations may occur: (i) if only WMO coordinates satisft the spatial precision requirements of 30 arcseconds, we replace Berkeley coordinates with the WMO ones; (ii) if only Berkeley coordinates are provided at least at 30 arc seconds, the station is included in the final sample; (iii) if both metadata do not satisfy the spatial precision requirements, the station is removed; (iv) both Berkeley and WMO coordinates are reported at 30 arc seconds. Note that, in this last case, a further check on the distance between the two localizations has to be performed, especially if the planimetric distance exceeds 5 km. This means that stations localizations are visually checked on maps and nightlights raster images and further sources are consulted e.g., looking for the metadata station information directly on the first archive of acquisition. The choice of a 5 km threshold is a matter of choosing a reasonable maximum buffer of influence of urban warming. Indeed, even if the Urban Heat Island effect is more evident in the nearest kilometer (Gallo et al., 1993), heat fluxes radiated by anthropogenic sources could be detected up to at least 4–5 km (Corumluoglu and Asri, 2015).

Once the coordinates have been checked, we define a regular squared buffer around the stations, ranging from 1 to 5 km, and the mean annual Digital Number value for the year i ($\overline{DN_i}$) is computed (Eq. (2.5)).

$$\overline{DN_i} = \frac{1}{k_{TOT}} \sum_{k=1}^{k_{tot}} DN_k \tag{2.5}$$

where k is the kth pixel, DN is the value of the kth pixel and k_{tot} is the total number of pixels in the buffer.

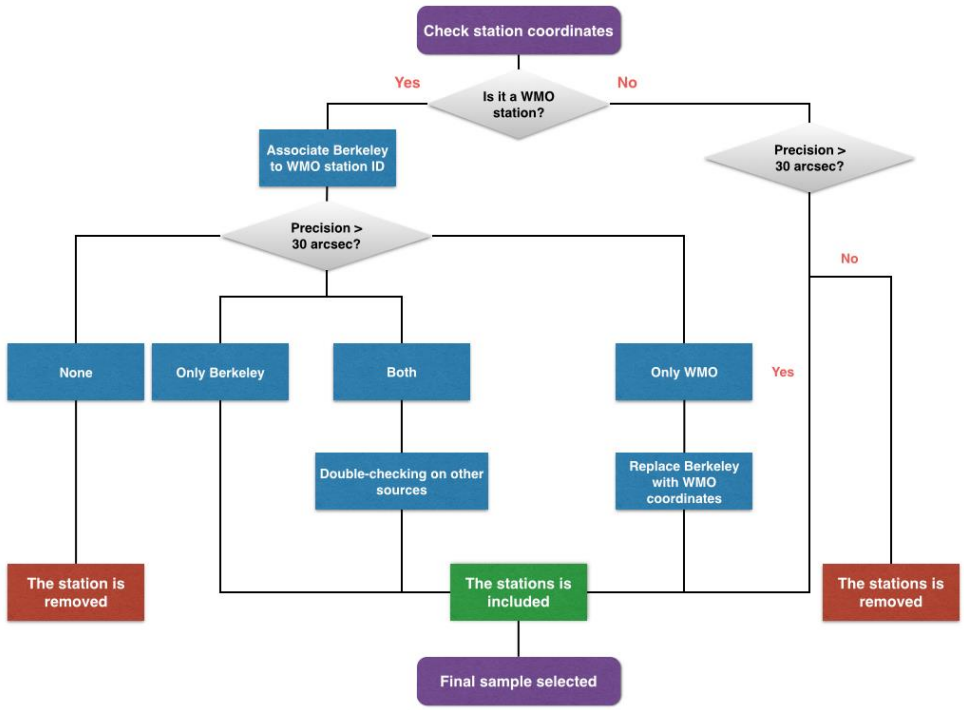

Figure 2-11 Flowchart showing the main steps of the procedure of geolocalization of Berkeley Earth stations.

As an example in Figure 2-12, considering the pixel where the station is located as pixel k=1, we will consider k=9 pixel in the first km buffer (1+8 pixels), k=25 pixel in a 2 km buffer (1+24 pixels) and so on up to a 5 km squared buffer. We considered different buffers ranging from 1 to 5 km in order to detect eventual variations in the DN. As explained before, this choice is due to the fact that effects of urban warming could be detected also some km far from the instrument site, even if the major impact is evident in the first km. For this reason, in the next paragraph, we will show and discuss the outcomes of the analysis in the first km buffer (1+8 pixels), and we will refer to the Appendix for the results on larger spatial buffer. The use of a small spatial buffer is somehow risky, since eventual errors in the localization of weather stations could lead to erroneous DN computations. As we can see in the example of Figure 2-12, we detect a brightness of 48 DN at the station scale, and values tend to decrease far away from the instruments. We could overcome this problem using larger spatial buffer,

in order to attenuate the spatial noise created by a not accurate localization. However, by averaging a higher number of pixels, we risk to lose the information related to eventual peak of luminosity at the station scale.

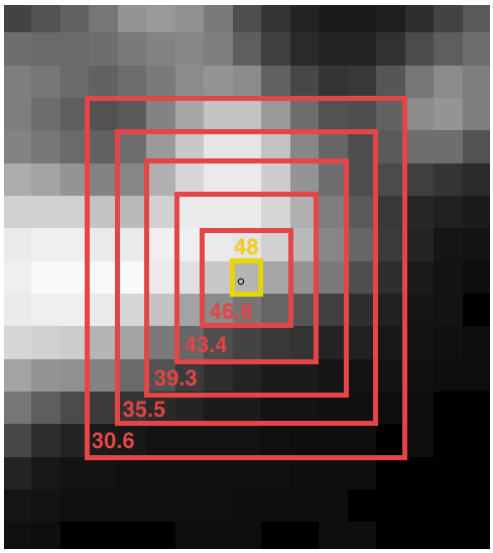

Figure 2-12 Example of the difference in the $\overline{DN}_i$ value for the year 2013 (i=22) with increasing spatial buffer from 1 to 5 km for Tenerife Sur station (Berkeley ID 159095); $\overline{DN}_i$ is in red bold, $\overline{DN}_i$ of the pixel where the station is located is in yellow bold.

2.2.4.3 Trend analysis

Temperature and nightlights data trends are analyzed through a linear regression model to examine the variation of temperature and nightlights with time. Regression coefficients are estimated with the ordinary least squares method. The slope of the regression line represents the percentage of variation of temperature or nightlights records per year (Figure 2-13). We fitted T values versus time by using

$$T(t) = a_T + b_T \cdot t \tag{2.6}$$

where b_T identifies the slope of the temperature regression line, a_T is the intercept and t the time. Positive temperature trends define an air temperature warming. Similarly, positive nightlights trends define an increase of luminosity in the considered buffer. The linear regression model to fit DN values versus time is

$$DN(t) = a_{DN} + b_{DN} \cdot t \tag{2.7}$$

where b_{DN} identifies the slope of the nightlights regression line and a_{DN} is the intercept.

In order to make inferences about the presence of significant trends, we evaluate the significance of the coefficients of the regression lines, by computing the probability value p corresponding to the empirically determined b value on a two-tailed Student's t distribution function. The threshold value for p is denoted as the significance level of the test α. The significance level is the probability α to reject the null hypothesis given that it is true (type I error). The null hypothesis is that there is no trend. In this work, α is equal to 0.1, i.e. a 0.05 significance level on each tail of the distribution. Thus, in our hypothesis, p values exceeding 0.95 detect positive significant trends, p values below or equal to 0.05 are negative significant trends while intermediate p values correspond respectively to positive ($0.05 < p$ value < 0.95) and negative ($0 < p$ value < 0.05) trends, but they are not significant from a statistical point of view. Stations with *DN* systematically equal to zero correspond to pitch dark areas and have been excluded in the following analysis. In this way, one can define four classes of significance c for the regression coefficients of both temperature and nightlights data (Table 2-2). Throughout the text, p values of the slopes of the regression trend lines are reported as p_T for temperature and p_{DN} for nightlights respectively.

Table 2-2 Classes of significance c based on p values of temperature (p_T) and nightlights (p_{DN}) linear regression trend lines.

Class *c*	***p* values**
1 (++)	p value ≥ 0.95
2 (+)	$0.5 < p$ value < 0.95
3 (-)	$0.05 < p$ value < 0.5
4 (--)	p value ≤ 0.05

As an example, we applied a linear regression model on a selected station in a 1 km spatial buffer (Figure 2-13). In this case, we detected increasing variations with time for both *T* and *DN*. *P* values of the slope regression lines are 0.9846 and 0.9998 respectively. Since both p_T and p_{DN} are in class 1, this means that significant temperature variations occur in concomitance with a significant luminosity trend in the considered buffer.

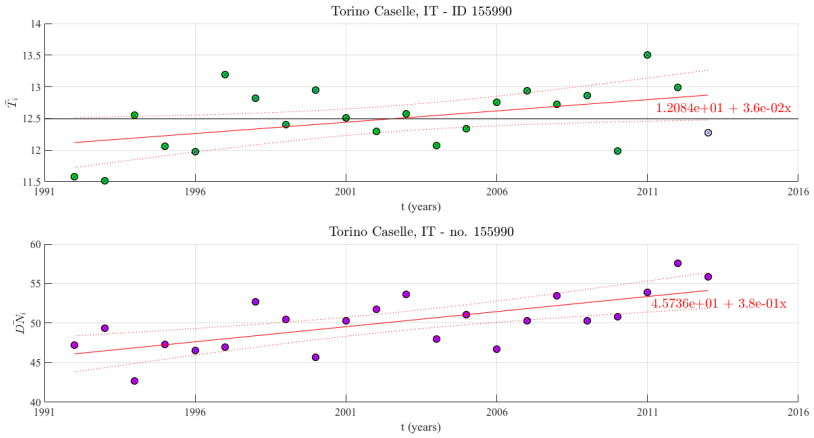

Figure 2-13 Example of linear regression trend lines of T (°C) and DN (-) for the air temperature station of Torino Caselle, IT (Berkeley Earth ID: 155990). The linear regression equation is reported in red. Empty dots refer to temperature values reconstructed with less than 12 months of data ($Nm_i < 12$).

2.2.4.4 Statistical indicators to measure agreement

A statistical indicator is a summary measure related to some issue of interest and derived from a series of data. In other words, it allows representing key features of statistical data so as to allow for comparison and better comprehension of a specifi issue. We now define suitable indicators, which allow measuring the degree of concordance between the variations in time of temperatures and nightlights. For a better characterization of such complex phenomenon, more than one method has been proposed and applied, denoted as methods 1 to 4. In the following paragraphs the Asian (Methods 1 to 3) and European continents (Method 4) are used as examples, in order to clearly illustrate the application of the methods.

2.2.4.4.1 Method 1

Method 1 provides information about the distribution of temperature and nightlights trends based on global and regional features. We first describe the computation of the measure of class agreement based on continental characteristics and then assuming a global distribution everywhere. The main steps are listed hereinafter.

(i) We first assess how p_T and p_{DN} distribute in the four class of significance c with respect to the total sample size. In other words, we compute the percentage of stations indicating significant (or non-significant) increasing (or decreasing) trends based on observed p values. We denote these relative frequencies as $w_{T(c)}$ and $w_{DN(c)}$, with c=1,…,4 (Eqs. (2.8) – (2.9)).

As outlined above, stations located in pitch-dark areas (i.e. slope of the nightlights regression line equal to zero), have been excluded in the following analysis.

$$w_{T(c)} = \frac{n_{T(c)}}{n_{TOT}} \tag{2.8}$$

$$w_{DN(c)} = \frac{n_{DN(c)}}{n_{TOT}} \tag{2.9}$$

$n_{T(c)}$ *and* $n_{DN(c)}$ represent the number of p_T and p_{DN} values occurring in the *c*th class of significance and n_{TOT} the total sample size in the study area.

Considering Asia as an example, given a total sample size n_{TOT} of 1153 stations, the probability of occurring in class *c* has been computed as in Table 2-3.

Table 2-3 Percentage of stations at continental scale (in this case, Asia) indicating significant increasing (*c*=1, ++), non-significant increasing (*c*=2, +), non significant decreasing (*c*=3, -) and significant decreasing trends (*c*=4, --) based on observed p_T *and* p_{DN} values.

c	$\mathbf{n_T}$	$\mathbf{w_T}$	$\mathbf{n_{DN}}$	$\mathbf{w_{DN}}$
1 (++)	471	40.8 %	646	56 %
2 (+)	388	33.7 %	178	15.4 %
3 (-)	233	20.2 %	170	14.7 %
4 (--)	61	5.3 %	159	13.8 %

We assign to each class of significance *c* special values, ranging from -1 to 1, and denoted as V_T and V_{DN} (see Table 2-4).

Table 2-4 Classes of significance of the temperature *T* and nightlight *DN* linear regression trend lines.

c	$V_{T,DN}$	***p* values**
1 (++)	1	p value ≥ 0.95
2 (+)	0.5	0.5 < p value < 0.95
3 (-)	-0.5	0.05 < p value< 0.5
4 (--)	-1	p value ≤0.05

We thus compute the expected values E(V_T) and E(V_{DN}) as follows

$$\mathrm{E}(V_T) = w_{T1} - w_{T4} + \frac{1}{2}(w_{T2} - w_{T3}) \quad (2.10)$$

$$\mathrm{E}(V_{DN}) = w_{DN1} - w_{DN4} + \frac{1}{2}(w_{DN2} - w_{DN3}) \quad (2.11)$$

and the corresponding variances as

$$\sigma^2(V_T) = w_{T1} + w_{T4} + \frac{1}{4}(w_{T2} + w_{T3}) - \mathrm{E}^2(V_T) \quad (2.12)$$

$$\sigma^2(V_{DN}) = w_{DN1} + w_{DN4} + \frac{1}{4}(w_{DN2} + w_{DN3}) - \mathrm{E}^2(V_{DN}) \quad (2.13)$$

In the case of Asia, the expected values and corresponding variances computed as in Eqs. (2.10) to (2.13) are

$$\mathrm{E}(V_T) = 1 \cdot 0.4085 - 1 \cdot 0.0529 + \frac{1}{2} \cdot 0.1344 = 0.4228$$

$$\mathrm{E}(V_{DN}) = 1 \cdot 0.5603 - 1 \cdot 0.1474 + \frac{1}{2} \cdot 0.007 = 0.4258$$

$$\sigma^2(V_T) = 0.4085 + 0.0529 + \frac{1}{4} \cdot 0.5386 - (0.4228^2) = 0.4173$$

$$\sigma^2(V_{DN}) = 0.5603 + 0.1474 + \frac{1}{4} \cdot 0.3018 - (0.4258^2) = 0.5923$$

(ii) A concordance index (CI) allows one to assess the degree of agreement between the two considered variables; it measures a sort of inter-rater agreement among variables, giving a score of the degree of existing homogeneity. The final score assigned to the station is based on V_T and V_{DN} as follows (Eq. (2.14)).

$$\mathrm{CI} = \frac{1}{n_{TOT}} \sum_{i=1}^{n_{TOT}} V_T \cdot V_{\overline{DN}} \quad (2.14)$$

As in Table 2-5, the matrix of weights V_T and V_{DN} is symmetric. A negative index is thus related to a disagreement between p_T and p_{DN}, which means increasing temperature T (c=1,2) and decreasing nightlights trends DN (c=3,4) or vice versa. A positive index is instead associated to increasing degrees of concordance between the two variables. More specifically, stations with significant increasing trends, i.e. p_T and p_{DN} occurring in class c=1 (++), are assigned the maximum value 1 (Table 2-5).

Table 2-5 Weights assigned to p_T *and* p_{DN} based on the class of significance c. The product of V_T and V_{DN} define the final score assigned to the station.

V_{DN} | V_T	++	+	-	--
++	1	0.5	-0.5	1
+	0.5	0.25	-0.25	-0.5
-	-0.5	-0.25	0.25	0.5
--	-1	-0.5	0.5	1

In the case of Asia, the concordance index CI computed as in Eq. (2.14) is equal to 0.2231.

(iii)Assuming that variables are statistically independent, i.e. if the occurrence of one does not affect the probability distribution of the other one, the estimated mean and variance of CI could be computed (Eqs. (2.15)-(2.16)).

$$\mathrm{E(CI)} = \mathrm{E}(V_T \cdot V_{DN}) \tag{2.15}$$

$$\sigma^2(\mathrm{CI}) = \frac{1}{n_{TOT}}[\sigma^2(V_T) \cdot \mathrm{E}^2(V_{DN}) + \sigma^2(V_{DN}) \cdot \mathrm{E}^2(V_T) + \sigma^2(V_T) \cdot \sigma^2(V_{DN})] \tag{2.16}$$

At this point, we can perform a standardization, in order to make norm-referenced interpretations and compare among different distributions. We thus compute a standardized score z as in Eq. (2.17).

$$\mathrm{z} = \frac{\mathrm{CI} - \mathrm{E(C)}}{\sigma} \tag{2.17}$$

Ordinary z scores are two standard deviation away from the mean. More in detail if:

- z<-2, *T* and *DN* variations are strongly discordant;
- -2<z<-1, *T* and *DN* variations are discordant;
- -1<z<0, the discordance is weak;
- 0<z<1 the concordance is weak;
- 1<z<2, *T* and *DN* variations are concordant.
- z>2, *T* and *DN* variations are strongly concordant.

In the case of Asia, as in Eqs. (2.15) to (2.17), we obtain

$$\mathrm{E(CI)} = 0.1801$$

$$\sigma^2(\mathrm{CI}) = \frac{1}{1153}[0.4173 \cdot 0.4258^2 + 0.5923 \cdot 0.4228^2 + 0.2472] = 0.0004$$

$$\mathrm{z} = \frac{0.2231 - 0.1801}{0.0196} = 2.2$$

We can thus derive how much the observed value is above the mean and assess how off-target the process is operating. In other words, we can assess the distance of the observed data from the mean.

2.2.4.4.2 Method 2

The method could be also applied assuming that brightness and temperature trends are the same everywhere, i.e. by assuming a global distribution of p_T and p_{DN} and ignoring continental features driving the distributions. For the sake of clarity, we repeat the procedure as before.

(i) As in Eqs. (2.8) – (2.9), we compute the percentages of p_T and p_{DN} occurring in class c ($w_{T(c)}$ and $w_{DN(c)}$) at global scale (Table 2-6); since in this method we assumed that *T* and *DN* trends are a global feature, we applied the same distribution to the continental scale.

We assign weights, ranging from -1 to 1 and denoted as V_T and V_{DN}, to each class of significance *c* as before (Table 2-4).

(ii) The expected values and variances at a global scale are computed (Eqs. (2.10) to (2.13)). Thus, we force somehow the distribution of temperature and nightlights trends, to be the same everywhere, without considering continental specific features.

$$\mathrm{E}(V_T) = 1 \cdot 0.3506 - 1 \cdot 0.0603 + \frac{1}{2}(0.3943 - 0.1942) = 0.391$$

$$\mathrm{E}(V_{DN}) = 1 \cdot 0.2706 - 1 \cdot 0.3144 + \frac{1}{2}(0.1737 - 0.2443) = -0.076$$

$$\sigma^2(V_T) = 0.3506 + 0.0603 + \frac{1}{4} \cdot 0.2001 - (0.391^2) = 0.4056$$

$$\sigma^2(V_{DN}) = 0.2706 + 0.3144 + \frac{1}{4} \cdot (-0.0706) - (-0.076^2) = 0.6807$$

Table 2-6 Percentage of stations at global scale indicating significant increasing (c=1, ++), non-significant increasing (c=2, +), non significant decreasing (c=3, -) and significant decreasing trends (c=4, --) based on observed p_T *and* p_{DN} values.

c	n_T	w_T	n_{DN}	w_{DN}
1 (++)	1942	35.1 %	1346	27.1 %
2 (+)	2218	39.5 %	864	17.4 %
3 (-)	1058	19.4 %	1215	24.4 %
4 (--)	312	6 %	1549	31.1 %

(iii) The concordance index is computed as in Eq. (2.14), being n_{TOT} the number of stations included in each continent. Thus, CI is the same obtained before (in the case of Asia, CI = 0.2231).

(iv) E(CI) is the expected value of CI, based on the weights V_T and V_{DN} computed at global scale, thus it is the same worldwide (Eq. (2.15)). In the case of Asia, we obtain the following results.

$$\mathrm{E(CI)} = -0.00297$$

$$\sigma^2(\mathrm{CI}) = \frac{1}{4974}[0.391 \cdot 0.6807^2 - 0.076 \cdot 0.4056^2 + 0.2761] = 0.0003$$

$$\mathrm{z} = \frac{0.2231 + 0.0297}{0.0182} = 13.9$$

We refer to the Section 5 for further examples.

2.2.4.4.3 Method 3

We assume a global distribution of temperature trends, while nightlights vary depending on the considered continent. Temperature variation is thus considered as a global feature, thus ignoring an eventual continental forcing that could impact on the distribution. Following the same approach used in Method 1, we list the main steps hereinafter.

(i) As in the first step of Method 1, we compute the relative frequencies of p_T and p_{DN} (Eqs. (2.8) – (2.9)). Here, $w_{T(c)}$ is computed only at the global scale, while $w_{DN(c)}$ varies based on the considered continent. In the case of Asia, the probability of occurring in class c has been summarized in Table 2-7.

Table 2-7 Percentage of stations indicating significant increasing (c=1, ++), non-significant increasing (c=2, +), non significant decreasing (c=3, -) and significant decreasing trends (c=4, --) based on observed p_T at global scale and p_{DN} values at continentally scale (in this case, Asia).

c	w_T	w_{DN}
1 (++)	35.1 %	56 %
2 (+)	39.5 %	15.4 %
3 (-)	19.4 %	14.7 %
4 (--)	6 %	13.8 %

As in Method 1, we assign a weight, ranging from -1 to 1, to each class of significance c (We assign to each class of significance c special values, ranging from -1 to 1, and denoted as V_T and V_{DN} (see Table 2-4).

Table 2-4).

(ii) The expected value E(V_T) and variance are computed assuming the same temperature distribution worldwide, while E(V_{DN}) and its variance change according to the considered scale (Eqs. (2.10) to (2.13)). In the case of Asia, we obtain

$$\mathrm{E}(V_T) = 1 \cdot 0.3506 - 1 \cdot 0.0603 + \frac{1}{2}(0.3943 - 0.1942) = 0.3906$$

$$\mathrm{E}(V_{DN}) = 1 \cdot 0.5603 - 1 \cdot 0.1379 + \frac{1}{2}(0.1544 - 0.1474) = 0.4258$$

$$\sigma^2(V_T) = 0.3506 + 0.0603 + \frac{1}{4} \cdot 0.5885 - (0.3906^2) = 0.4056$$

$$\sigma^2(V_{DN}) = 0.5603 + 0.1379 + \frac{1}{4} \cdot 0.3018 - (0.4258^2) = 0.5923$$

(iii) The concordance index is computed as in Eq. (2.14). In the case of Asia, the concordance index CI is equal to 0.2231 as in Method 1 and 2.

(iv) The expected value of CI, its variance and standardized value have been computed as in Method 1 (Eqs. (2.15) to (2.17)). We obtain the following results for the Asian continent.

$$\mathrm{E}(\mathrm{CI}) = 0.1663$$

$$\sigma^2(\mathrm{CI}) = \frac{1}{1153}[0.4056 \cdot 0.4258^2 + 0.5923 \cdot 0.391^2 + 0.2401] = 0.0004$$

$$\mathrm{z} = \frac{0.2231 - 0.1663}{0.0004} = 3.03$$

We refer to the Section 5 for further examples.

2.2.4.4.4 Method 4

In this further test, the goal is to assess how temperature trends distribute based on different nightlights configurations. In other words, nightlights trends are divided in three ranges based on *p* values, so as to discern between stations showing relevant trends and those where nighttime lighting could be considered almost stable. This last group is thus considered as a sort of baseline to be compared to, representing a situation without any important modification in the nightlight trend, i.e. p_{DN} values in the range 25 % - 75 %. More details on the procedure are reported hereinafter.

(i) As in the first step of Methods 1 and 2, we compute the relative frequencies in class *c* of p_T and p_{DN}, i.e. $w_{DN(c)}$ and $w_{T(c)}$. We first compute $w_{DN(c)}$ as in Eq. (2.9). At this point, we hypothesize three different luminosity configurations:

- $p_{DN} \leq 0.25$ (group A)
- $0.25 < p_{DN} < 0.75$ (baseline, group B)
- $p_{DN} \geq 0.75$ (group C)

Group B with p_{DN} values in the range 0.25-0.75 represents the baseline including stable nightlights trends. We assess how p_T distribute in these three groups, computing $w_{T(c)}$ for each configuration (Eq. (2.8)). The results for the European continent are listed in Table 2-8.

(ii) The cumulative distribution functions (CDF) of p_T are computed. More in detail, a sample with n_{tot} values, $p_{T(j)}$, j=1,…, n_{TOT} is collected, where $p_{T(j)}$ is the jth value in the ordered sample. We thus estimate the CDF as $P(p_T)=j/n_{TOT}$. Multiple CDF have been performed i.e., one for each class A to C. We reported in a graph the cumulative distribution function as in the example of Europe in Figure 2-14. Temperature *p* values p_T are plotted on the horizontal axis, while j/n_{TOT} on the vertical axis allowing a comparison between different distributions. These graphs have been reported from global to continental scale (see Section 2.3.4.2).

Table 2-8 Percentage of stations at continental scale (in this case, Europe) indicating significant increasing (c=1, ++), non-significant increasing (c=2, +), non significant decreasing (c=3, -) and significant decreasing trends (c=4, --) based on observed p_{DN} and p_T in the three nightlights trend configurations (A = $p_{DN} \leq 0.25$; B = $0.25 < p_{DN} < 0.75$; C = $p_{DN} \geq 0.75$).

	w_{DN}		w_T	
c		**A**	**B**	**C**
1 (++)	27.3 %	30.4 %	26.5 %	32.9 %
2 (+)	24.6 %	45.8 %	51.2 %	50.2 %
3 (-)	23.7 %	22.5 %	20.0 %	15.4 %
4 (--)	24.3 %	1.4 %	2.3 %	1.5 %

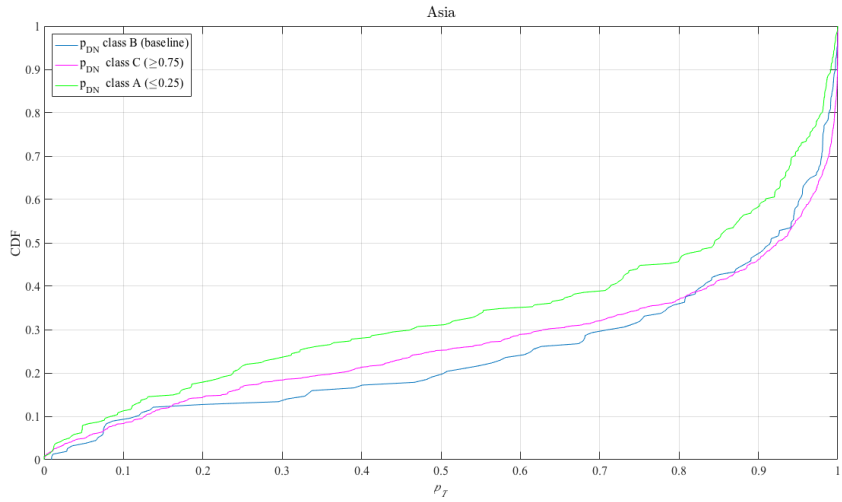

Figure 2-14 Example of a cumulative distribution function plot (CDF) in the case of Europe, as described in Section 2.2.4.4. Considering a fixed probability value, we incur in higher p_T values in occurrence of significant p_{DN} values positive trends than "stable" ones (i.e. the baseline CDF).

In our hypothesis, given a non-exceedance probability associated with p_{T*}, temperature trend should increase faster in the presence of statistically significant *DN* trends, i.e. those included in group C. As in the example of the European continent, if we consider for example the non-exceedance probability associated with $p_{T*} = 0.95$, we obtain a probability $P(p_T < p_{T*}) = 0.732$ for the baseline group, while $P(p_T < p_{T*}) = 0.671$ for group C (Figure 2-14). In other words, this means that 32.9 % of p_T values in group C are statistical significant against 26.5 % of p_T

values in the baseline group. Thus, we incur in a higher percentage of significant p_T values occurring in concomitance with increasing p_{DN} values rather than stable ones. In this case, *DN* is of value in explaining the *T* variations i.e., the variation of temperature could be related to the entity of urbanization, which we associate with a relevant UHI effect.

2.3 Results and discussion

The outcomes of this work will be shown and discussed in the following paragraphs. The methods as explained in Section 2.2 have been applied to all available Berkeley Earth datasets, i.e. Single valued (raw data), Quality Controlled (intermediate data) and Breakpoint Corrected (fully quality checked data), and to both variables involved, i.e. average monthly temperature and minimum monthly temperature. Given the amount of data, only the results of the analysis on average monthly temperature of the Quality Controlled dataset will be shown hereinafter. Analysis on the other datasets leads to similar results, as mentioned throughout the text; we refer to the Appendix A for these further outcomes. Hereinafter, we will denote temperature as *T* and nightlights as *DN*.

2.3.1 Empirical evidence

Figure 2-15 shows the relation between the response variable temperature *T* and the predictive one *DN* in a 1 km buffer (1+8 pixels) for the considered stations. Analyses have been conducted considering the multi-year average temperature and luminosity. At continental scale, all trends are significantly positive, with the exception of Africa, where a negative trend is detected. Note that, while developed continents are characterized by a high concentration of stations located in areas of intense luminosity (i.e., above 50 DN), light intensity in Africa is relatively low. Eventual further divergences could be related to problems as saturation and blooming effects, potentially affecting nightlight data. Light saturation occurred primarly in developed countries and highly populated urban areas, where the intensity of lights is high (Chen and Nordhaus, 2011). Nevertheless, we based our analysis on calibrated images, having the advantage of not being saturated at the highest intensities, and adjusted DN values are used. In poor and developing countries, blooming effect (i.e. the overestimation of lit areas), is more evident, because of the presence of broad pitch dark areas (Huang et al., 2014). Moreover, poor regions are also characterized by a remarkable regional inequality in light intensity (Mveyange, 2015). For these reasons, in the following analyses, we account for this factor by controlling for unlit cells (i.e.,

pitch dark areas showing a stable DN equal to zero along the whole period of analysis). As we can see in Figure 2-15, brightness emerges as an interesting indicator of temperature increment along with urban expansion almost wordlwide, while not already implying the existence of a clear statistical dependence of temperature with luminosity variations.

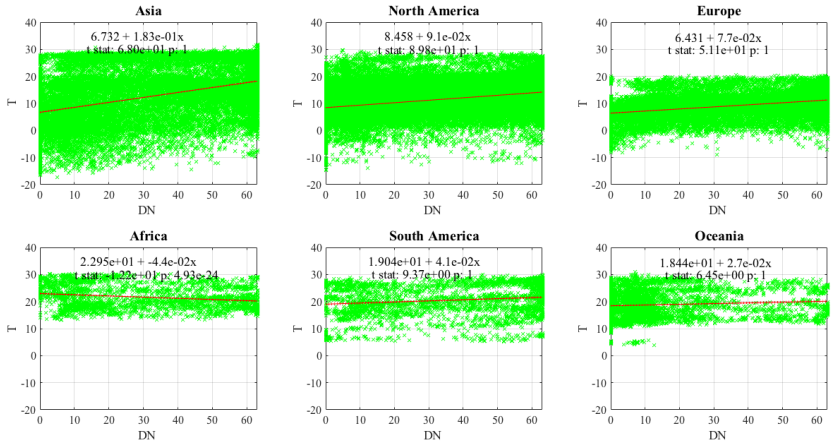

Figure 2-15 Mean annual temperature and mean annual nightlights value at continental scale. Linear regression trend equations, *t* Student and *p* values have been reported (dataset: average monthly temperatures, Quality Controlled).

2.3.2 Confounding effect of elevation

As outlined in Section 2.2.3, elevation may represent a confounding factor, which could prevent the correct assessment of anthropization feedback on temperature. The influence of altitude on nighttime luminosity could be relevant if considering that higher at site locations brightness is typically less intense at high elevations. A general model formalized as a bivariate linear regression accounting also for station altitude (z) may be of help in order to eventually confirm the initial hypothesis i.e., that the predictive variable T could be significantly dependent on DN. This model could be formalized as in Eq. (2.1). As outlined in Section 2.2.3, after having removed the confounding factor z, the p value computation of a Student's t distribution at global scale reveals that temperature is significantly dependent on nightlight values (Table 2-9). This is also confirmed at the continental scale almost everywhere, except for Africa, where a negative trend has been detected as in Figure 2-15, and Oceania, where a not significant positive tendency has been noticed (Figure 2-16). This could be related to the fact that, in both continents, we have a high percentage of stations located in dark or almost-

dark areas. Moreover, as we can see also in Figure 2-15, stations in Africa are few if compared to the other continents, and luminosity values distributed all over the entire range. Results of this analysis are summarized in Table 2-9.

Table 2-9 Coefficients with 95 % confidence bounds and *p* value of the *DN* coefficient (*b*) i.e. p_{DN} at global and continental scale (dataset: average monthly temperatures, Quality Controlled).

Localization	a	b	c	p_{DN}
Asia	9.018(7.955,10.08)	0.1575(0.1322,0.1829)	-0.002402(-0.003093,-0.00171)	1
North America	11.3(10.83,11.78)	0.05329(0.04281,0.06377)	-0.002584(-0.002892,-0.002276)	1
Europe	7.735(7.201,8.269)	0.0627(0.0495,0.0759)	-0.00281(-0.00346,-0.00216)	1
Africa	24.96(23.78,26.13)	-0.0612(-0.0908,-0.0317)	-0.0037(-0.00491,-0.00249)	0
South America	19.46(17.87,21.05)	0.065(0.0282,0.102)	-0.00295(-0.00401,-0.0019)	0.9997
Oceania	19.94(19.03,20.86)	0.01567(-0.0194,0.0507)	-0.0072(-0.00957,-0.00481)	0.8096
World	11.72(11.3,12.14)	0.05977(0.04992,0.06962)	-0.002664(-0.002995,-0.002333)	1

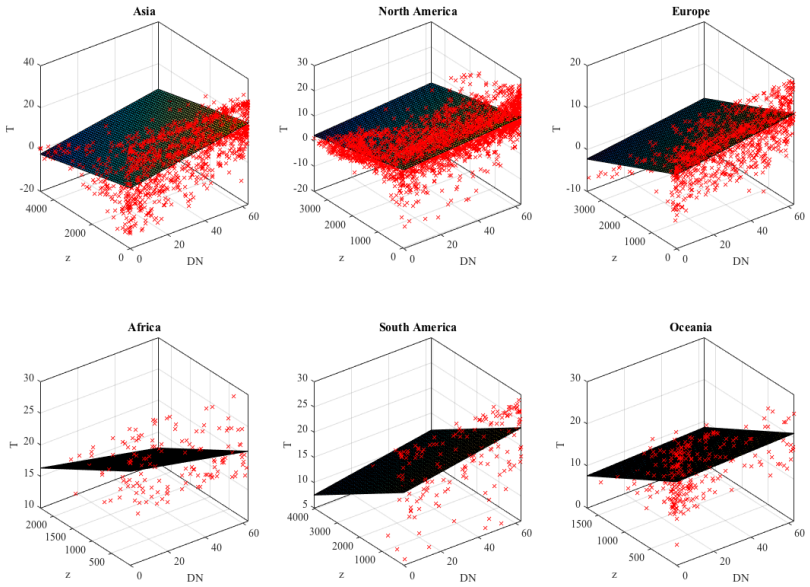

Figure 2-16 Multivariate linear regression at continental scale between the response variable *T* and predictive variable *DN* and elevation *z* (dataset: average monthly temperatures, Quality Controlled).

2.3.3 Gap filling and localization procedures on air temperature stations

2.3.3.1 Gap filling in air temperature data

The first focus is on the availability of air temperature station worldwide based on Berkeley Earth dataset. Synthetic consistency diagrams have been drafted considering the three different types of output dataset, as mentioned in Sect. 2.2.1. Generally, a good temporal coverage is guaranteed since many active stations between 1992 and 2013 have 12 months of data (Figure 2-17). As an example in Figure 2-17, from 1992 to 1999, we have 12 months of recorded data for nearly 12000 stations (the sample size ranges between 12115 and 12613), while in 2013 we have 10 months of recorded data for 11754 stations, but no instrument has recorded 12 months of data. Note that, for example, the 12318 air temperature stations having 12 months of record in 1993 are not necessary included in the in 12472 stations available in 1994 and in the following years. As in The main steps of the procedure have been listed in Table 2-11, along with the number of stations passing the further step up to the final selected sample, as in the flowchart of Figure 2-11.

Out of a total of 6308 stations, a half is included in the list of official WMO stations, while the other half includes unofficial stations selected by Berkeley Earth project; so, for this last group, a comparison is not possible. Finally, stations that have been correctly localized at, at least, 30 arcseconds, are 5547. Note that some of the selected instruments are localized outside the grid of nightlights data and have been excluded from the following analysis. For this reason the final sample includes 5530 stations (Table 2-11).

Table 2-10, the number of active air temperature stations in the period 1992-2013 is 28679, guaranteeing a good spatial coverage everywhere and also in generally poorly represented continents as Africa and South America. With the term “active”, we refer to those stations that have at least one year of data in the period 1992-2013.

The consistency plots as Figure 2-17 could only provide information about the availability of records in the year i and month j, but not on the length of the data series in the investigated period 1992-2013. Indeed, several gaps have been detected in the time series, thus justifying the need of reconstructing missing data.

The gap filling procedure for the Quality Controlled dataset on T allowed computing the mean annual temperature T_i, i=1,…,22, for 6308 stations worldwide, using a threshold combination $Nm_i \geq 9$ and $Ny_j \geq 18$ as mentioned in Section 2.2.4.1. The choice of such combination is the result of an attempt to find the best compromise between a suitable sample size and a good quality of reconstructed data. The outcomes of the gap filling procedure using all possible combinations have been reported before in Figure 2-9.

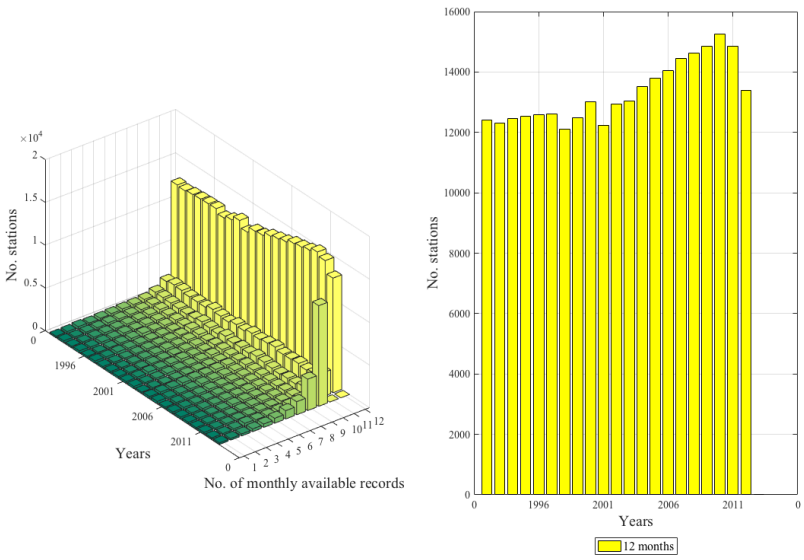

Figure 2-17 Consistency analysis based on the number of available Berkeley Earth stations per month and per year in the period 1992 – 2013 (dataset: average monthly temperatures, Quality Controlled); left panel: 3D general overview of the full dataset; right panel: 2D plot limited at stations having at 12 months of records per year.

2.3.3.2 Geolocalization procedure

Stations coordinates have been checked performing the localization procedure outlined in Section 2.2.4.2. Berkeley ID codes have been compared to WMO metadata and coordinates have been corrected. As explained in Section 2.2.4.2, in some cases coordinates provided by the datasets do not coincide at all, even if both at 30 arcseconds precision (see Figure 2-18 as an example), and this make it necessary to perform a further check on stations metadata. The main steps of the procedure have been listed in Table 2-11, along with the number of stations passing the further step up to the final selected sample, as in the flowchart of Figure 2-11.

Out of a total of 6308 stations, a half is included in the list of official WMO stations, while the other half includes unofficial stations selected by Berkeley Earth project; so, for this last group, a comparison is not possible. Finally, stations that have been correctly localized at, at least, 30 arcseconds, are 5547. Note that some of the selected instruments are localized outside the grid of nightlights data and have been excluded from the following analysis. For this reason the final sample includes 5530 stations (Table 2-11).

Table 2-10 Comparison between the number of active Berkeley Earth air temperature stations from 1992 to 2013 at global and continental scale for the considered dataset (dataset: average monthly temperatures, Quality Controlled).

Localization	Active station 1992-2013
Asia	3862 (13.5 %)
North America	16667 (58.1 %)
Europe	4811 (16.8 %)
Africa	976 (13.4 %)
South America	657 (2.3 %)
Oceania	1462 (5.1 %)
Others	243 (0.8 %)
World	28679 (100 %)

Table 2-11 Main steps and partial outputs of the procedure of localization (dataset: average monthly temperatures, Quality Controlled, 1 km buffer). The final sample includes 5547 stations, but 17 are localized in areas outside the spatial extension of the nightlight raster, so we obtain 5530 stations. In the ID comparison step, we listed the stations included in the WMO dataset ("Stations included in the WMO list") and the unofficial stations included in the Berkeley dataset ("Stations not included in the WMO list").

Step	No. stations
Initial sample	6308
Comparing Berkeley and WMO ID	
Stations not included in the WMO list	3108
Stations included in the WMO list	3200
Removed stations	761
Final sample selected	5547
Point outside grid	17
Final sample	5530

We can thus state that the procedures of temperature reconstruction and localization lead to a remarkable loss of records, in terms of number of stations with respect to the initial sample, but at the same time it could guarantee more robust results. Indeed, this procedure leads to a 84% mean loss of stations data. This could be related, on the one hand, to the high quantity of incomplete historical data series, and on the other hand the poor spatial resolution of most part of available metadata (Figure 2-19). As an example, in the case of North America, this loss does not influence significantly our analysis given both the high station density and deeply extended spatial coverage in this continent. Instead, the consistent number of gaps in the temperature datasets detected in the African region, along with the scarce network coverage, could limit significantly the outcomes of the analysis, as for South America (Table 2-12). Analyses computed on the other datasets have led to similar results (see Appendix A). We can thus expect that highly represented continents, as Asia and North America, will have a considerable weight on the final outcomes.

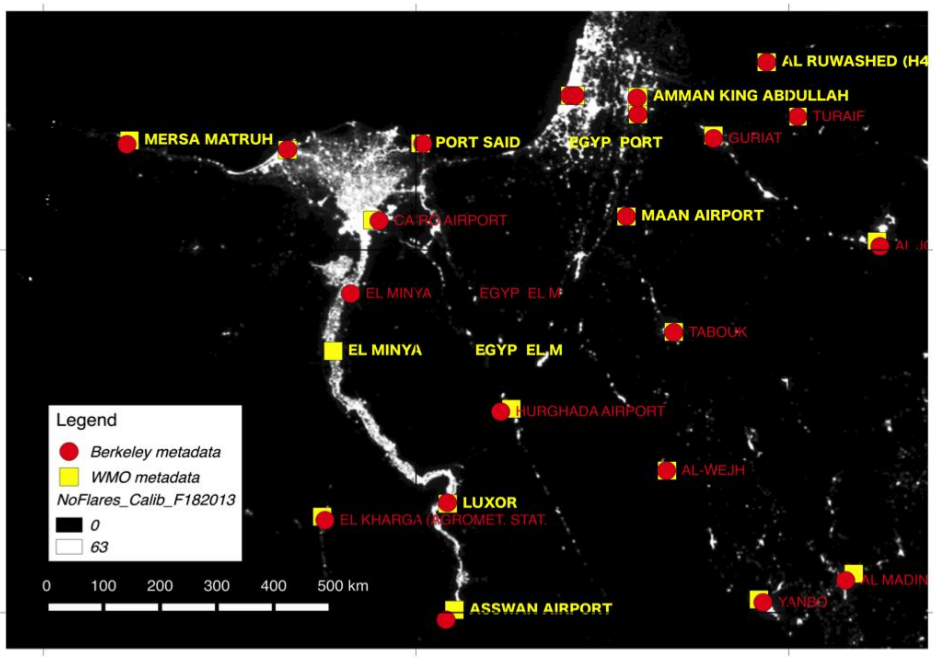

Figure 2-18 Example of application of the localization procedure in the Nile Delta region by comparing the metadata provided by WMO and Berkeley datasets. In some cases coordinates do not coincide at all, for example in the case of El Minya station.

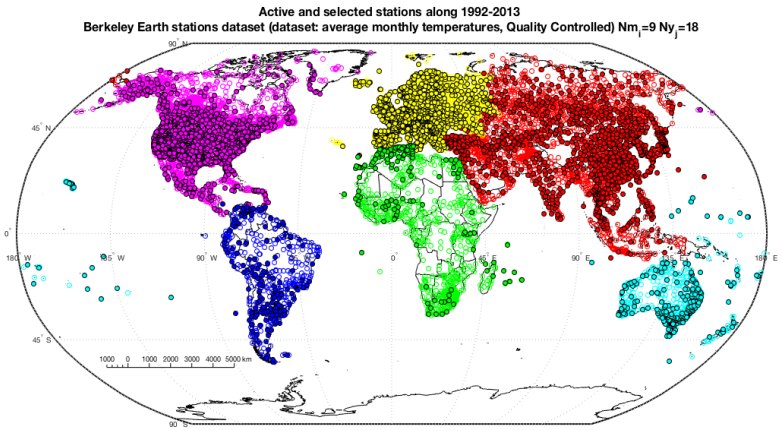

Figure 2-19 Locations of the active Berkeley Earth air temperature stations dataset (dataset: average monthly temperatures, Quality Controlled) between 1992 and 2013 (empty dots) and selected stations after the gap filling and localization procedures (filled dots). The stations are color coded based on the five regions considered.

Table 2-12 Number of active stations from 1992 to 2013 and available stations after the application of thresholds for the reconstruction of mean annual temperature from the mean monthly data (dataset: average monthly temperatures, Quality Controlled) and spatial localization. The selected thresholds are $Nm_i \geq 9$ and $Ny_j \geq 18$.

Localization	**Active station 1992-2013**	**Selected stations $Nm_i \geq 9$ $Ny_j \geq 18$**
Asia	3862 (13.5 %)	1219 (22 %)
North America	16667 (58.1 %)	2673 (48.3 %)
Europe	4811 (16.8 %)	1033 (18.7%)
Africa	976 (13.4 %)	146 (2.6%)
South America	657 (2.3 %)	175 (3.1 %)
Oceania	1462 (5.1 %)	268 (5 %)
Others	243 (0.8 %)	16 (0.3 %)
World	28679 (100 %)	5530 (100%)

2.3.4 Application of statistical methods at global and continental scales

The mean temperature of the selected stations in the 22 years, denoted as $\overline{T}$, and the mean value of luminosity in the 22 years in a 1 km spatial buffer around the instruments, denoted as $\overline{DN}$, have been mapped in Figure 2-20 and Figure

2-21. Looking at Figure 2-20 and at the spatial localization of stations, most part of the African landmass, the central part of South America, Australia inland and the sparsely populated areas of Asia are particularly poorly represented. In Figure 2-21 we represent the spatial distribution of nightlights in the immediate proximity of the weather stations (in this case, the nearest km). Major clusters of intense luminosity have been detected in North-eastern U.S. countries, Central America and Brazilian coastline, India, Japan and Arabian Peninsula. These areas of high artificial luminosity mainly correspond to high population density regions. Hot spots as in the North-eastern U.S., showing nightlights values above 60 DN, could also refer to centres of well-established cities and to large light agglomeration areas, which have not experienced an evident brightness increment along the investigated period 1992-2013, so they are expected to be areas of stable light trends. As confirm of the empirical evidence of Figure 2-15, mean luminosity in Africa is relatively low. There, a clear tendence towards high values (as an example, in the range 50-60 DN) is not detectable as in the other continents, and brightness values are distributed all over the entire range. Considering for example the largest spatial buffer (5 km), we obtain very similar results to those referred to the nearest km (see Appendix A).

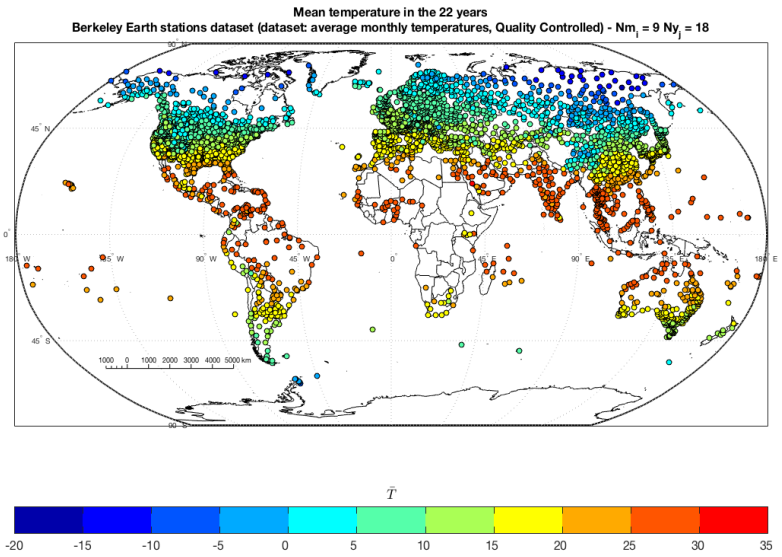

Figure 2-20 Mean annual temperature in the 22 years $\bar{T}$ for the selected air temperature stations (dataset: average monthly temperatures, Quality Controlled, 1 km buffer).

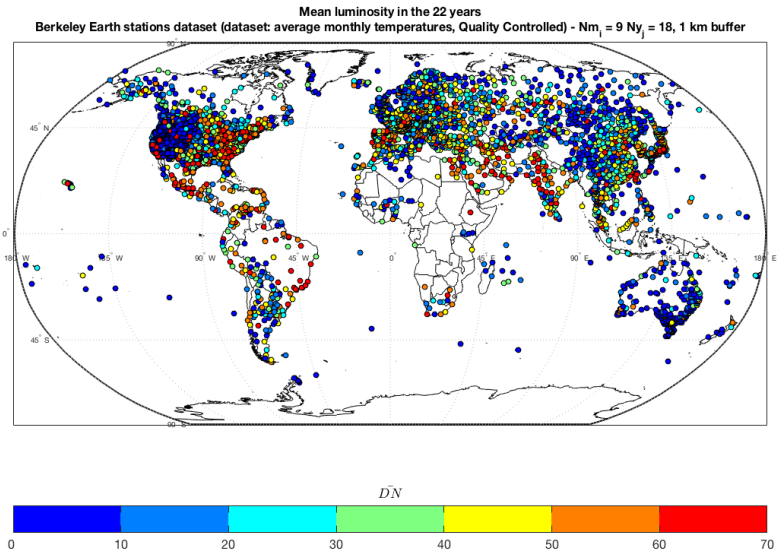

Figure 2-21 Mean Digital Number value in the 22 years ($\overline{DN}$) in a 1 km buffer around the selected stations (dataset: average monthly temperatures, Quality Controlled, 1 km buffer).

2.3.4.1 Relation between nightlights and temperature trends

Regression analyses on mean annual *T* and *DN* have been carried out for each station as outlined in Sect. 2.2.4.3. The results are shown in Figure 2-22. Slopes of *T* regression lines are plotted on the horizontal axis, while slopes of *DN* ones on the vertical axis. Sectors 1 and 3 represent positive and negative concordant trends respectively, while sectors 2 and 4 refer to discordant trends e.g., a rise in temperature in correspondence of a decreasing nightlights trend (sector 4) and vice versa (sector 2). Interesting differences emerge from the continental scale analysis. In more than 50 %, 65 % and 43 % of, respectively, the Asian, African and South American stations positive concordance is detected. This could mean that, in those regions, most part of stations located in more and more anthropized areas have experienced an increase of temperature in the period 1992-2013. An interesting pattern can be noticed in South America, where 30 % of stations are located in areas with increasing nightlights but in concomitance with decreasing temperature trends. Other different and complex patterns have been detected in the rest of the world. In Europe, concordant and discordant patterns are almost balanced, since on the one hand 41 % of stations show positive concordance, but on the other hand 36 % of stations with warming temperature trends are located in decreasing nightlights areas. In Oceania most stations are experiencing warming i.e., 60 % out of the total, in concomitance of nightlights trend. Here, a

considerable percentage of stations are located in pitch-dark areas i.e., areas where the slope of the *DN* regression line is zero (more than 10 %), and this is even more evident in North America (15 %). Surprisingly, more than 62 % of North American stations show negative luminosity tendency, more than 49 % in conjunction with warming trends.

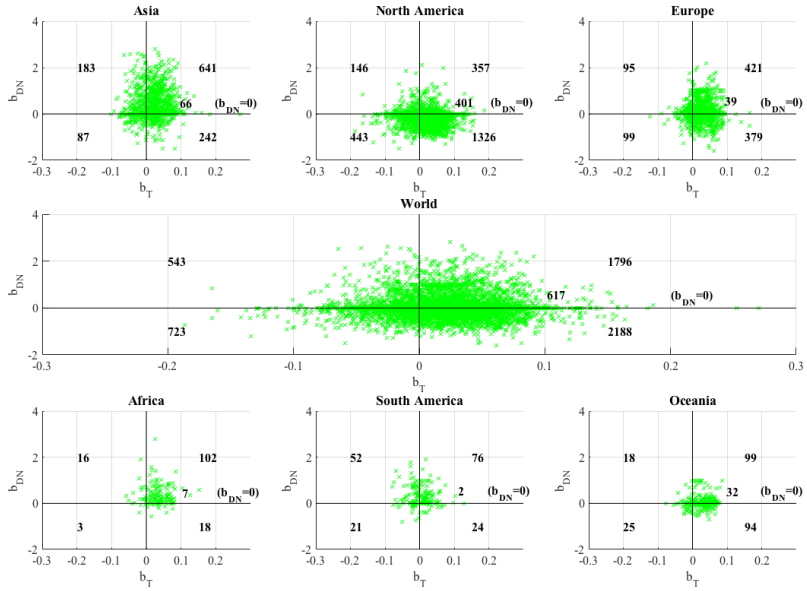

Figure 2-22 Slope of *T* (b_T) and *DN* (b_{DN}) regression trend lines. Sectors 1 and 3 correspond to concordant trends, while sectors 2 and 4 refer to discordant trends. The number of stations included in each sector is in bold, as well as the number of stations with *DN* systematically equal to zero (b_{DN} = 0) on the horizontal axis (dataset: average monthly temperatures, Quality Controlled, 1 km buffer).

As illustrated in Section 2.2.4.3, *p* values have been computed in order to assess the presence of significant variations in temperature/nightlights values. Thus, we tested the significance of the slope of the regression lines for the two considered variables, assuming a level of significance α = 10 %, i.e. 5 % on each tail of the distribution. We mapped the *p* values spatial distribution for temperature trends (Figure 2-23) and for luminosity variations (Figure 2-24). A joint distribution of p_T and p_{DN} values has been represented in density plots such as those in Figure 2-25.

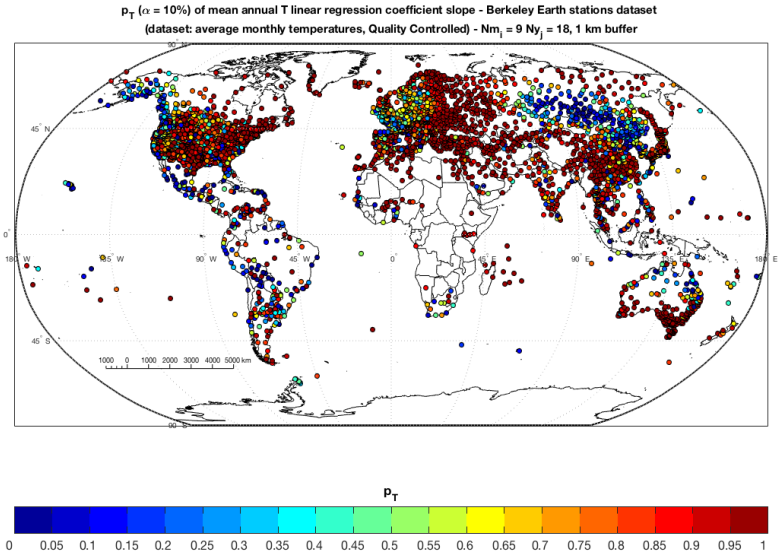

Figure 2-23 Spatial distribution of the p value (p_T) of the slope of the temperature regression line for the selected Berkeley Earth stations (dataset: average monthly temperatures, Quality Controlled, 1 km buffer).

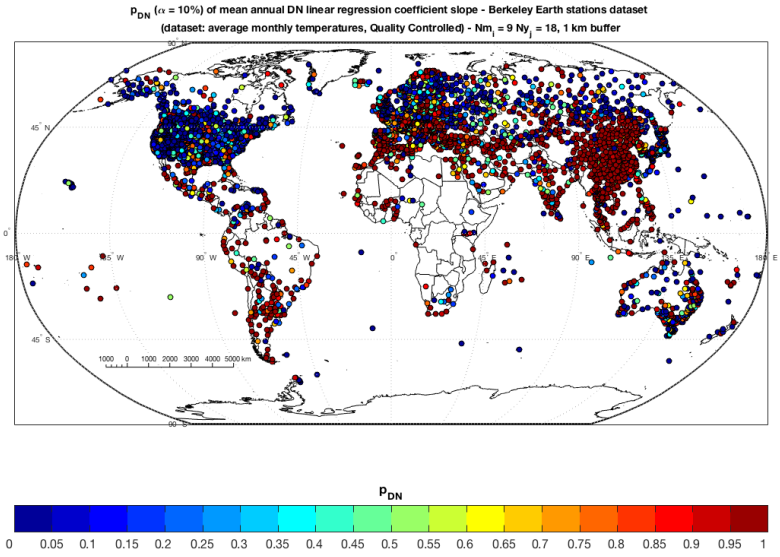

Figure 2-24 Spatial distribution of the p value (p_{DN}) of the slope of the nightlights regression line for the selected Berkeley Earth stations (dataset: average monthly temperatures, Quality Controlled, 1 km buffer).

Density plots are smoothed colour scatterplots obtained by calculating the point density; they are useful where there are many data points. With the same approach of Figure 2-22, in Figure 2-25 p_T values are plotted on the horizontal axis while p_{DN} values on the vertical axis. Asia and Africa show appreciably positive trends, slight positive trends have been detected in South America while North America is strongly balanced towards significant discordant trends, as clearly visible in Figure 2-24. Europe and Oceania instead show the same patterns detected at global scale. In South America we can also notice the presence of discordant patterns, i.e. significant increasing p_{DN} values occurring in concomitance with negative temperature tendency. This is even more evident looking at Figure 2-24 and considering the minimum monthly temperatures dataset (see Appendix A). The high number of American stations included in the sample leads to a decoupled trend at a global scale, with high-points density in the upper and lower right sectors of the *p* value plots related to increasing temperature in concomitance with both significant positive and negative nightlights trends (Figure 2-25).

In Figure 2-26, as an alternative way to discern between classes of trends, we mapped only those stations showing significant trends for both temperature and nightlights. This allows a better visualization of areas characterized by significant trends for both temperature and nightlights, by avoiding unsignificant ones. As can be seen in Figure 2-26, discordant trend with positive p_T and negative p_{DN} values are concentrated not only in North America, but also in Eastern Europe and Japan, while fully positive trends are distributed over Asia and Africa. The U.S. West Coast and Central America are characterized by negative temperature trends in concomitance with decreasing/increasing luminosity. South America is generally characterized by increasing brightness with variable temperature trends, as seen in the previous plot (Figure 2-25).

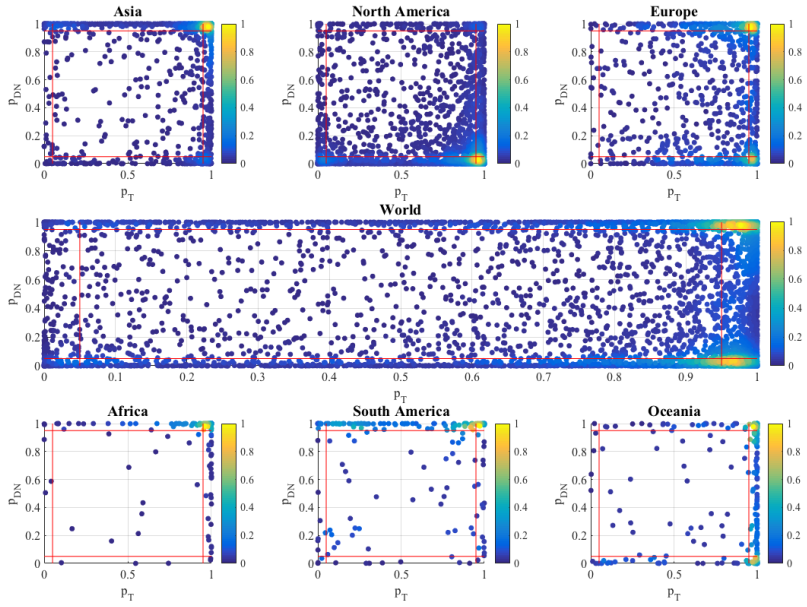

Figure 2-25 *P* values density plots at global and continental scale (dataset: average monthly temperatures, Quality Controlled, 1 km buffer). Red lines, corresponding to 0.05 and 0.95 *p* values, delimitate the different areas of significance.

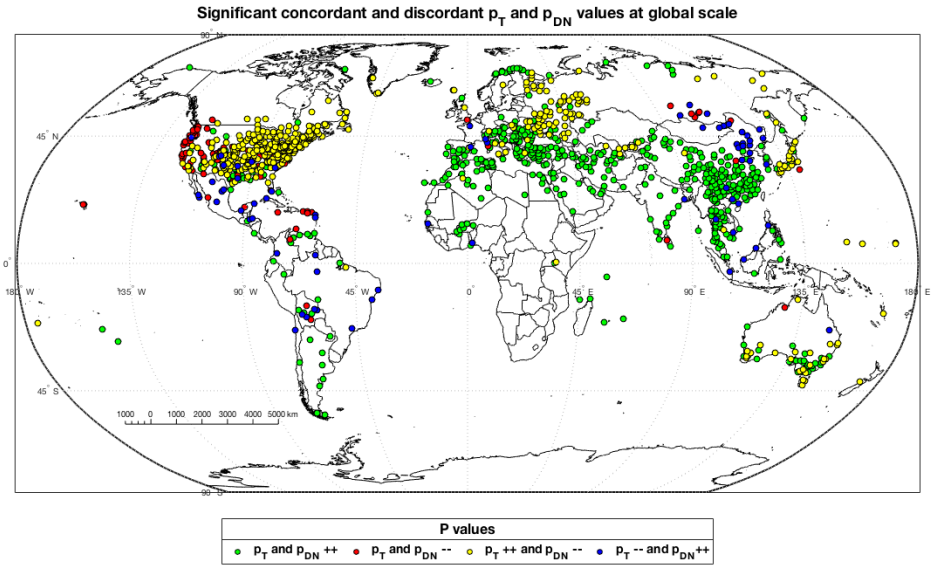

Figure 2-26 Selected stations showing significant values for both temperature and nightlights trends (dataset: average monthly temperatures, Quality Controlled, 1 km buffer).

Results on the other datasets, i.e. raw (Single-valued) and fully-quality checked data (Breakpoint Corrected) on the average monthly temperatures datasets are similar to those presented in this Section. The analyses with increasing buffers from 2 to 5 km confirm the trends detected at global and regional scale in the nearest. This could entail that in some regions, a high percentage of significant temperatures are expected to occur in areas of increasing luminosity not only close to the stations but also considering larger spatial buffer (see Appendix A).

2.3.4.2 Degree of concordance between temperature and nightlights variations in time

After the identification of statistically significant linkage between temperature and luminosity trends, we assessed the level of agreement among the different classes of significance of temperature and nightlights trends. To this aim, four methods have been performed as described before (in Section 2.2.4.4) and results are synthetized in Figure 2-27 to Figure 2-30.

As previously described, we assessed how p_T and p_{DN} distributed in four classes of significance, denoted as c=1,…,4. Then, we computed the percentage of stations in each class based on p values, and we denoted these relative frequencies as $w_{T(c)}$. We refer to Section 2.2.4.4 for further details.

Figure 2-27 summarizes the outcomes of Method 1. In Method 1, we assessed the distribution of temperature and nightlights trends based at global and continental scale. As further confirmation of the results of Figure 2-22 and Figure 2-25, most part of stations is experiencing warming trends: p_T for more than 70 % of the selected stations occur in class c 1 and 2 ($w_{T(1)}$, $w_{T(2)}$), with the solely exception of South America, where negative and positive temperature trends are almost balanced. Here, the expected value $E(V_T)$ is significantly low if compared to the other continents. In Africa and Asia, stations experiencing significant warming are more than 61 % and 40 %, respectively. In these continents, as well as in South America, more than 56 % are located in areas of significant increasing luminosity. Positive and negative trends are almost balanced (~ 25 % in each class of significance), in Europe and Oceania, this last one showing a slightly negative tendency. While in Europe increasing temperatures trends are weak, up to 60 % of stations located in Oceania are experiencing significant temperature rise. The most complex pattern has been detected in North America. There, the tendence of temperature to increase is confirmed as at global scale, but negative luminosity trends are definitely more frequent than those with positive trends: here, p_{DN} for almost 80 % of the selected stations occur in class c 3 and 4 ($w_{T(3)}$, $w_{T(4)}$).

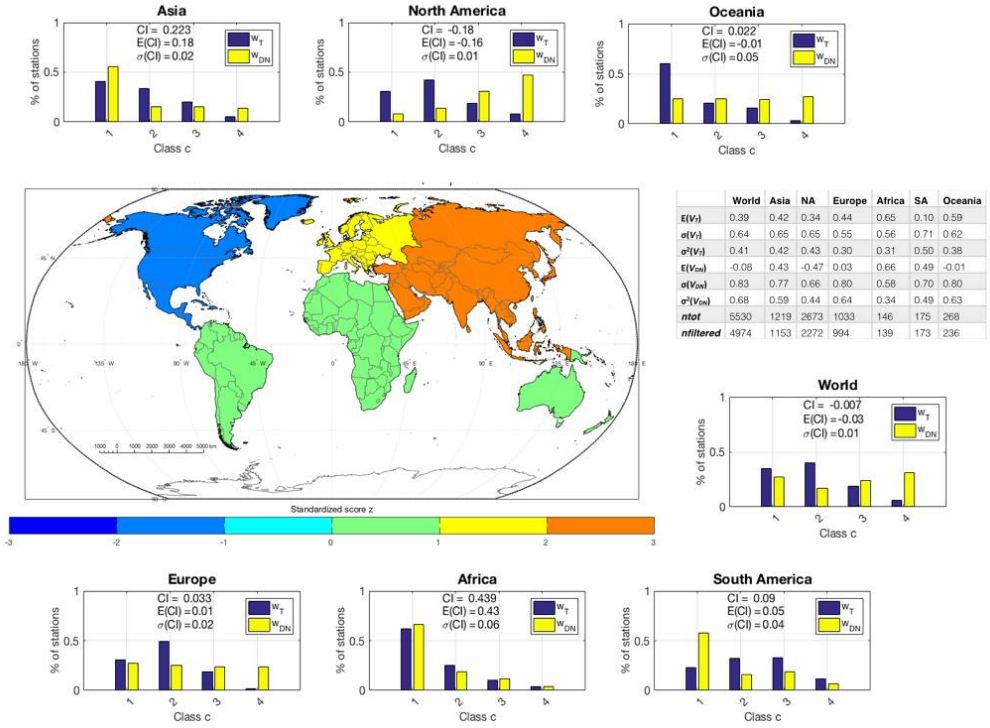

	World	Asia	NA	Europe	Africa	SA	Oceania
$E(V_T)$	0.39	0.42	0.34	0.44	0.65	0.10	0.59
$\sigma(V_T)$	0.64	0.65	0.65	0.55	0.56	0.71	0.62
$\sigma^2(V_T)$	0.41	0.42	0.43	0.30	0.31	0.50	0.38
$E(V_{DN})$	-0.08	0.43	-0.47	0.03	0.66	0.49	-0.01
$\sigma(V_{DN})$	0.83	0.77	0.66	0.80	0.58	0.70	0.80
$\sigma^2(V_{DN})$	0.68	0.59	0.44	0.64	0.34	0.49	0.63
ntot	5530	1219	2673	1033	146	175	268
nfiltered	4974	1153	2272	994	139	173	236

Figure 2-27 Method 1 statistics; *w* refers to the probability of occurrence of classes of significance from 1 (++) to 4 (--); V_T: variable temperature *T*; V_{DN}: variable nightlights *DN*; CI: concordance index; E(CI): expected mean of CI; σ(CI): standard deviation of CI; z: standardized value; E(V_T), E(V_{DN}), σ(V_T) and σ(V_{DN}) refer to expected mean and standard deviation; *n*: total number of stations; $n_{filtered}$: same as *n* excluding stations with *DN* trend equal to 0 (dataset: average monthly temperatures, Quality Controlled, 1 km buffer).

The computation of the concordance index CI (Eq. (2.14)) reveals an appreciable degree of agreement between *T* and *DN* trends in Africa and Asia and a slightly positive index in Oceania and South America. The discordance detected in North America moves the CI towards a negative value at global scale. The standardized *z* value provides information about the distance, measured as the number of standard deviations, between the concordance index and the mean value (Eq. (2.15) to (2.17)). The standardized scores vary in the range ±2σ, as in Asia (about +2σ) and North America (about -2σ), entailing strong concordance and discordance, respectively.

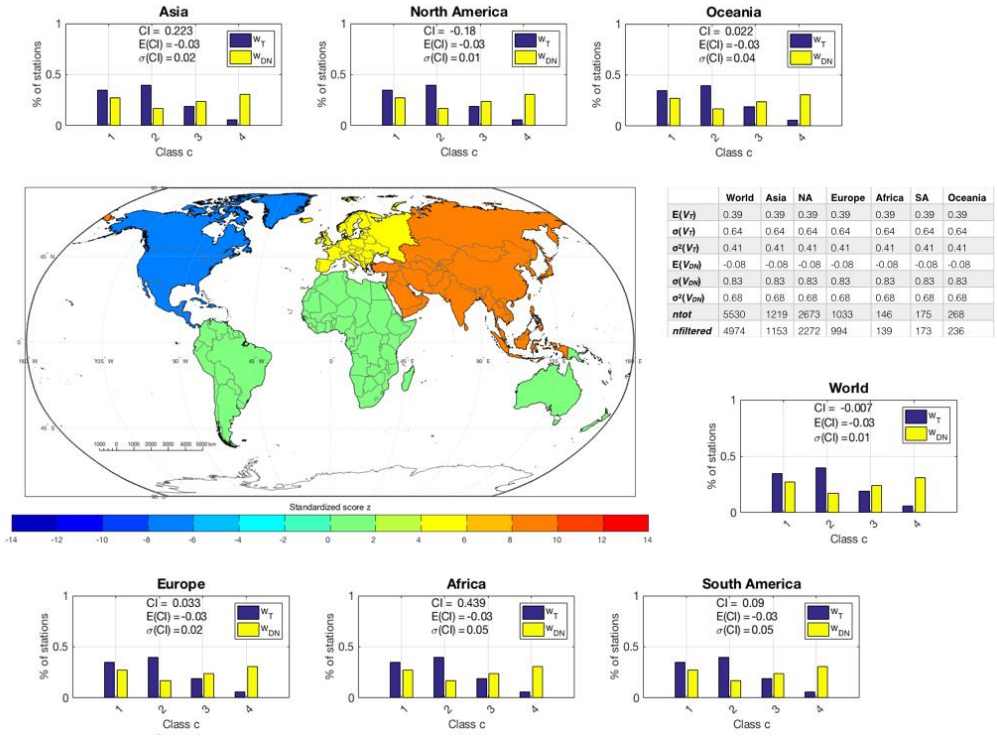

	World	Asia	NA	Europe	Africa	SA	Oceania
$E(V_T)$	0.39	0.39	0.39	0.39	0.39	0.39	0.39
$\sigma(V_T)$	0.64	0.64	0.64	0.64	0.64	0.64	0.64
$\sigma^2(V_T)$	0.41	0.41	0.41	0.41	0.41	0.41	0.41
$E(V_{DN})$	-0.08	-0.08	-0.08	-0.08	-0.08	-0.08	-0.08
$\sigma(V_{DN})$	0.83	0.83	0.83	0.83	0.83	0.83	0.83
$\sigma^2(V_{DN})$	0.68	0.68	0.68	0.68	0.68	0.68	0.68
ntot	5530	1219	2673	1033	146	175	268
nfiltered	4974	1153	2272	994	139	173	236

Figure 2-28 Method 2 statistics, legend as in Method 1 (dataset: average monthly temperatures, Quality Controlled, 1 km buffer).

Results derived from Method 2 are included in Figure 2-28. In Method 2, we hypothesized a unique global-scale base distribution of temperature and nightlights everywhere. This means that expected values and variances related to T and DN, as well as frequency distributions $w_{T(c)}$, are assumed as global distributed, regardless of regional features (Figure 2-28). As a consequence, also expected CI mean are constant worldwide, based on Eq. (2.15). As evident, the assumption of a global distribution of temperature and luminosity could be somehow misleading, since standardized values can be very far from the mean, as in the case of Asia and North America (around ±13σ).

In Method 3, we hypothesized that nightlights distribute based on continental features, while temperature distribution is assumed constant worldwide. Results are listed in Figure 2-29. As can be seen, this hypothesis leads to important differences in the expected value E(CI) in North and South America if compared to Method 1. Indeed, as outlined in previous analyses (Figure 2-22 and Figure 2-25), South America is characterized by an unexpected decrement of temperature for most part of considered stations and the assumption of a global temperature

increasing trend distribution may appreciably force the trends, as confirmed by the negative score *z*. In the same way, in North America, the hypothesis of Method 3 moves the standardized *z* value towards a slight positive value, in spite of the other methods, that clearly shed light on the significant discordance detected in the North American region.

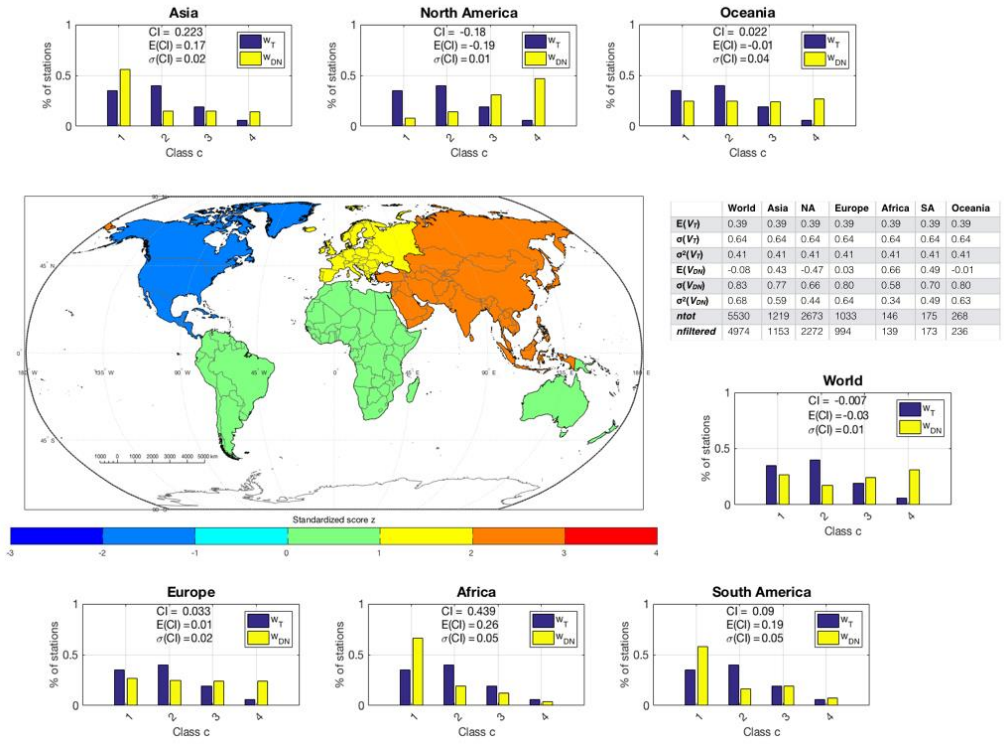

	World	Asia	NA	Europe	Africa	SA	Oceania
$E(V_T)$	0.39	0.39	0.39	0.39	0.39	0.39	0.39
$\sigma(V_T)$	0.64	0.64	0.64	0.64	0.64	0.64	0.64
$\sigma^2(V_T)$	0.41	0.41	0.41	0.41	0.41	0.41	0.41
$E(V_{DN})$	-0.08	0.43	-0.47	0.03	0.66	0.49	-0.01
$\sigma(V_{DN})$	0.83	0.77	0.66	0.80	0.58	0.70	0.80
$\sigma^2(V_{DN})$	0.68	0.59	0.44	0.64	0.34	0.49	0.63
ntot	5530	1219	2673	1033	146	175	268
nfiltered	4974	1153	2272	994	139	173	236

Figure 2-29 Method 3 statistics, legend as in Method 1 (dataset: average monthly temperatures, Quality Controlled, 1 km buffer).

The application of a global temperature distribution does not impact particularly, Asia, Europe and Oceania in terms of standardized score *z*, while tend to influence significantly trend distributions in Africa, and North America. These divergences could be in part explained by comparing Figure 2-29 (Method 3) and Figure 2-27 (Method 1). Based on a global distribution, most part of p_T values (~ 40 % out of the total) are included in the second class, which refers to positive but not significant trends (c=2, $w_{T(2)}$). Based on a continental distribution of p_T values, as in Method 1, we can see that the percentage of stations in class 2 decrease significantly in North America (from 40 % to 18 % of Method 1) and Africa (from 40 % to 25 % of Method 1), respectively. This tends to alter the distribution in the other class of significance and, thus, the information enclosed

in the standardized score z, that means that perception of how off-target the process is operating.

Method 4 allows assessing temperature tendencies across different nightlight configurations (Figure 2-30). As explained before, this means p_{DN} values are divided in three ranges, in order to distinguish between remarkable increasing (and decreasing) luminosity trends and stable ones. More in details, nightlights configurations are the following:

- $p_{DN} \leq 0.25$ (group A)
- $0.25 < p_{DN} < 0.75$ (baseline, group B)
- $p_{DN} \geq 0.75$ (group C)

We refer to Section 2.2.4.4.4 for further details.

As explained before, in the best-case scenario, we should incur in a higher percentage of significant p_T values occurring in concomitance with increasing p_{DN} values rather than stable ones. As can be seen in Figure 2-30, this is true in the most part of investigated areas, and it is substiantially confirmed by fully-quality data (see Appendix A). More in detail, as can be derived from Figure 2-30, this pattern is particularly evident with $p_{T*} < 0.90$ in Africa and Europe. The distributions tend to be similar with significant increasing p_{T*} values (i.e., above 0.95). In other words, the percentage of significant p_T values occurring in concomitance with increasing (group C) and stable (group B) p_{DN} values is almost balanced, and this latter tendence is confirmed almost everywhere.

In North America we detected a modest reverse tendency: there, temperature records show more significant trends in concomitance of almost stable nightlights (p_{DN} values between 0.25 and 0.75) instead of increasing luminosity (p_{DN} values above 0.75). This could be somehow related to the high percentage of air temperature stations located in areas of decreasing luminosity. We detected anomalies in the expected configuration also in South America: there, as in North America, we observe a reverse tendency between stable and increasing p_{DN} values. This could be somehow related to the fact that we observed a consistent number of stations with cooling trends and significant increasing brightness. The tendence of North and South America has been also confirmed by raw data (Single-valued). In Oceania something similar to South America seems to happen, but, differently from the latter, the analysis based on fully-quality data (Breakpoint Corrected) agree with the best-case scenario illustrated in Section 2.2.4.4 (see Appendix A).

Results on minimum monthly values for the Quality-Controlled dataset highlight similar divergences in North America and Oceania.

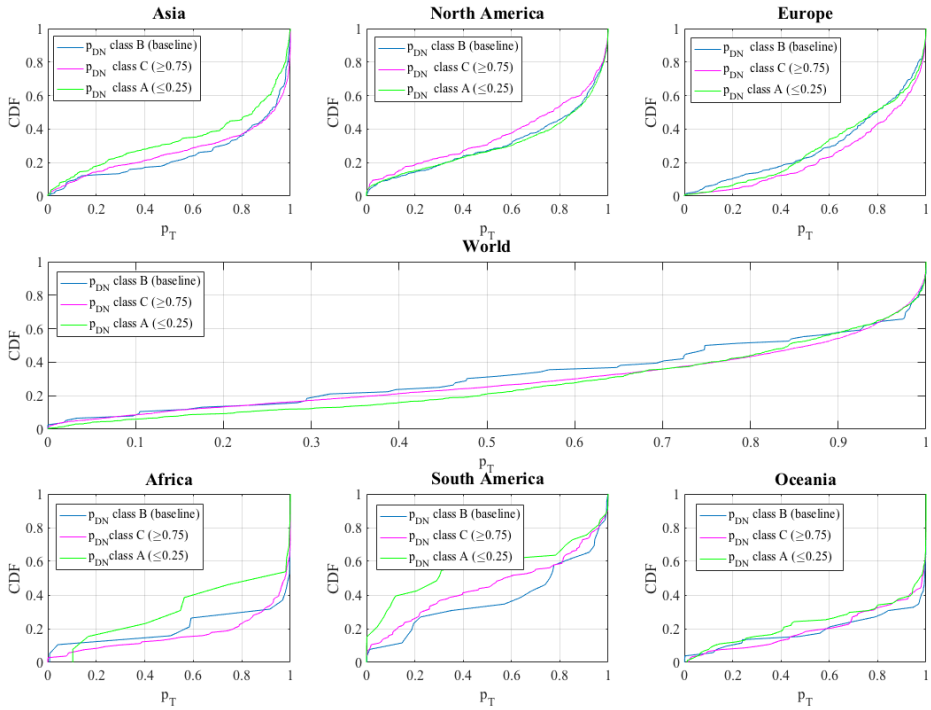

Figure 2-30 Cumulative distribution function CDF of p_T based on the three different nightlights configurations i.e., class A: $p_{DN} \leq 0.25$, class B: $0.25 < p_{DN} < 0.75$, class C: $p_{DN} \geq 0.75$ (dataset: average monthly temperatures, Quality Controlled, 1 km buffer).

Analyses with larger spatial buffers tend to amplify the difference between the baseline (group B) and p_{DN} values in the upper-class (group C), and this is particularly evident in Africa and South America (Figure 2-31). Thus, enlarging the study area, up to 5 km far from the weather station, we find similar patterns to those detected in the nearest km, confirming the results of Section 2.3.4.1.

Further outcomes on Methods 1 to 4 and results on increasing buffers are provided in Appendix A.

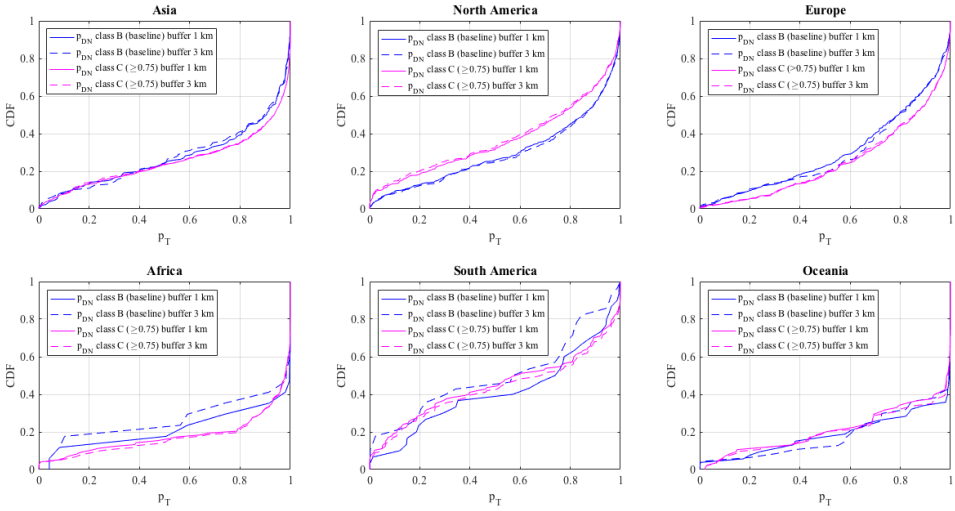

Figure 2-31 Cumulative distribution function CDF of p_T based on the three different nightlights configurations i.e., class A: $p_{DN} \leq 0.25$, class B: $0.25 < p_{DN} < 0.75$, class C: $p_{DN} \geq 0.75$ with increasing buffer from 1 (solid line) to 3 km (dashed line) from the six considered regions the sake of clarity, only results of class B and C configurations are shown on the graph (dataset: average monthly temperatures, Quality Controlled, 1 km buffer).

2.3.5 Discussion

The proposed analysis can be useful to quantify the increase of human presence across urbanized regions and within urban areas and to identify a possible relationship with temperature trends. By applying innovative remote sensed databases, our outcomes provide insights on future trends of temperature controlled by human activities. The use of several statistical based approaches is of help in estimating and verifying temperature-nightlights trend relationship from different perspectives, as well as integrating the shortcomings resulting from the application of a single methodology.

The obtained results confirm the overall tendency of urbanization to affect temperature data, even if the associated uncertainty is rather large, and a fully clear outcome has not been obtained. Indeed, though the results show an overall enhancement of temperature across urbanized regions, some interesting differences could be found among the considered regions. As anticipated in Section 2.1, this is in part due to the presence of some disturbing factors, as better outlined below. Significant increment of temperature in concomitance with increasing luminosity variations have been detected worldwide, and regional-scale

results are generally in agreement with this overall trend. This concordance is significantly evident for both average and minimum temperatures, and results are substantially similar ranging from raw to quality-checked data (see Appendix A).

We assessed quantitatively the degree of concordance among the four classes of trend significance, by means of a series of methods. As outlined in Section 2.2.4.4, we first computed the percentage of stations included in each class of significance, based on temperature and luminosity trends. All methods show that most part of stations is experiencing warming trends, since p_T values are mainly included in the first two class ($w_{T(1)}$, $w_{T(2)}$). South America shows a balanced coexistence of cooling and warming trends, whereas Africa and Asia show the highest degree of concordance, being the percentage of stations experiencing warming in increasing brightness areas rather higher than the other regions. The discordant pattern detected in North America is a common point of all methods, and is ascribable to external policy-driven factors.

The application of global and regional-based forcing nightlights and temperature distributions, and the comparison between the different methods, highlight substantial differences. While Method 1 and 4 lead to similar results, the assumption of a unique temperature distribution worldwide as in Method 3 constrains somehow the continental distribution. This is even more evident if assuming a global distribution for both *T* and *DN* trends, that means a unique distribution applied at all regional and continental scales, as we did in Method 2. Therefore, it is likely that ignoring the presence of regional and local factors forcing temperature records could lead to misleading conclusions. Moreover, Method 3 allows, with a sort of reverse approach, to assess if temperature is effectively driven by anthropization and thus by the spatiotemporal distribution and intensity of nighttime luminosity, revealing that regional effects could significantly influence climate warming trends. Method 4 well highlights the divergencies detected in North and South America with respect to the rest of the world. In South America divergencies can be related to the fact that many stations are experiencing cooling although localized in urbanized areas. Analyses with larger spatial buffers tend to confirm the patterns detected in the first kilometer (see Appendix A), as the results of Section 2.3.4.1.

The analyses on the concordance of temperatures and luminosity variations at continental scale could provide interesting insight on economic features of single continents. As examples, Africa and Asia reveal significant increasing temperature trends along with nocturnal lights increment in recent years, which reflects the fast-evolving and uncontrolled urbanization in these areas. Increasing

temperature along with slightly positive or negative nightlight trends mainly correspond to developed continents. The significant decrement of nighttime luminosity detected in North America could be the result of policy-driven initiatives as light pollution abatement programs promoted in these last years in Canada and in several U.S. countries (Cauwels et al., 2014). The same initiative has been undertaken in many North Europe countries as United Kingdom and Netherlands (Bennie et al., 2014; Ceola et al., 2015). In a recent study, we performed the same analysis illustrated in the previous paragraphs on the Mediterranean area (Paranunzio and Laio, 2016). Indeed, in arid and Mediterranean climates, urban warming represents a major concern in the context of climate change. We applied the same approach described in the previous paragraphs to a limited dataset including only stations located in the Mediterranean countries. The results of this analysis showed that Mediterranean European countries reveal a clear significant positive concordance between trends, while results on the whole European scale show more complex patterns, as illustrated before. We thus put in evidence that, when analyses on Central-Northern and Southern countries are performed separately, the Mediterranean area countries reveal a clear tendence toward a significant positive concordance, while other factors, as light pollution abatement programs, could be responsible for the discordance detected in Northern Europe.

Decreasing temperature trends detected in South America could instead related to mesoscale effects. Indeed, recent findings proposed that the intensification of the South Pacific Anticyclone during these last years, which is a consequence of global warming, could contribute to the coastal cooling and warming in the continental Chile and Andes (Falvey and Garreaud, 2009; Stocker et al., 2013).

Although satellite data provide an information that is not directly related to the quantitative rise of temperature records, we proved how these data can support both global and local analyses of urban and global warming-related issues. At this point of the study, nothing could be stated on the effective reliability of urban temperature records, but analysis over a wide range of spatial scales provides the ground for future discussion on the effect of urban heating on climate data. Further advances in this direction could benefit from the perspectives offered by new approaches and techinques. Merging high-resolution data as nightlights, made available by new advances in remote-sensing, and statistical models and concepts, derived from the hydrological field, could represent the opportunity for an unconventional strategy of study of such issues.

Chapter 3

3 Climate anomalies responsible for slope failure occurrence at high-elevation sites in the Italian Alps

The work described in this chapter has been previously published in two research articles appeared in peer-reviewed international journals, Paranunzio et al. (2015) and Paranunzio et al. (2016).

3.1 Introduction

The recent decades have seen a pronounced warming in global climate, primarily at high elevations and high latitudes (Schär et al., 2004). Temperature across European Alps has increased of about 1.4 K per century over the period 1906-2005, which is more than double the global average (Brunetti et al., 2009) and further increases are expected according to global and regional climate models (Beniston, 2006; Stocker et al., 2013). At the same time, precipitation patterns are suffering remarkable modifications. A general increase in annual rainfall was observed in the northern hemisphere, with significant regional variations (Auer et al., 2007). In the European Alps, precipitations increased in the northern sub-region and decreased in the southern sub-region, both of about 10 % (Brunetti et

al., 2009). Almost everywhere, the cryosphere is degrading rapidly in response to air temperature warming (Stocker et al., 2013).

Glacier shrinkage and permafrost degradation, i.e., the decrease in the thickness/areal extension of permafrost (Stocker et al., 2013), are expected to significantly worsen the geotechnical and mechanical properties of rock, debris and soils in high mountain areas (Harris et al., 2009; Kääb et al., 2007; Noetzli et al., 2006). Permafrost degradation is also warming/thawing permafrost, of which the control on rock slope stability is strong (Davies et al., 2001) although not fully understood (Krautblatter et al., 2013). In particular, permafrost climate-induced degradation affects the stability of steep rock walls at different timing, magnitude and depths, affecting the thermal and hydraulic conditions of the rock mass (Gruber and Haeberli, 2007), e.g., by altering the active layer thickness and fractures conditions by reducing the shear strength (Davies et al., 2001). Permafrost and in general cryosphere degradation might play a role for the growing number of slope failures at high elevation that has been documented since the beginning of the 21st century (Chiarle and Mortara, 2008; Stoffel et al., 2014). However, the exact role of climate parameters and of their influence on the preparation and initiation of slope failure remains poorly understood. While many studies focus on rainfall-induced landslides, which have been performed for different geographic settings and elevation ranges (Guzzetti et al., 2008; Brunetti et al., 2015), the link between landslide occurrence and temperature, in combination or not with precipitation, has been little explored. Only recently, following the summer 2003 heat wave in Europe, the role of temperature in the occurrence of slope failures has been considered thoughtfully (Gruber et al., 2004b; Huggel et al., 2010; Stoffel et al., 2014). The issue of climate change impact on geohazards has been addressed by several authors who focused on specific processes - e.g., debris flows (Jomelli et al., 2004), shallow spring landslides (Saez et al., 2013) - or on specific parameters - e.g., mean air temperatures (Ravanel and Deline, 2011) or daily maximum air temperatures (Allen and Huggel, 2013). However, the use of different definitions of “unusual” or “extreme climate”, based on different percentiles or climatic parameters, makes it difficult to compare results from different studies. In addition, the focus on specific processes, or on specific hypothesis, may lead to an only partial understanding of conditions and processes leading up to slope failure.

One of the main purpose of this work was to try to overcome the specificities related to individual processes, to data availability and to geographic peculiarities

by proposing a statistically based, systematic approach aimed at providing a first assessment of the role of climatic factors on slope failure preparation and initiation. We developped and validated a multi-purpose tool which could be applied to any kind of slope instability, regardless of timing, location, geographic and climatic setting. We focused on daily climate variables, including air temperature, the variation in the air temperature, and precipitation (liquid and solid). In this way, we tried to verify the hypothesis that climate warming can be deemed responsible for increased slope instability in recent years, highlighting the role of temperature, in association or not with precipitation. We tested this methodology on different types of slope instabilities occurred in the Western Italian Alps (Paranunzio et al., 2015). In the following pargraphs, we refer to this group of events as "Case study 1".

Subsequently, we used an advanced version of the method proposed to analyse a catalogue of 41 landslides occurred from 1997 to 2013 at high elevation in the Italian Alps (Paranunzio et al., 2016). In the following pargraphs, we refer to this group of events as "Case study 2". Since our focus is on temperature, which plays an important role in cryosphere dynamics, we concentrated on those events not triggered by rainfall, earthquakes, or anthropic activities. Our catalogue includes rockfalls and rock avalanches, with volume in the range 10^2 – 10^6 m^3. At this point, we also performed a bivariate analysis that includes the climate anomalies identified and the spatiotemporal characteristics of the rockfalls in the catalogue (including elevation, aspect, volume, and season of occurrence). Finally, we discussed the results in a context of climate warming, speculating on the possible causes of rockfall occurrence (Paranunzio et al., 2016).

3.2 Methods

3.2.1.1 First version of the method

The approach proposed consists in a bottom-up statistical method for the identification of possible anomalous values of one or more climate variables (V) on the occasion of slope instability events (Paranunzio et al., 2015). The idea behind the method is to compare the climate conditions in the period preceding the failure, to the climate conditions typical for the area where the failure has occurred. Eventual outliers of the climate variables prior to the occurrence of a slope failure may be considered related to (and possibly responsible for) the preparation and/or the initiation of the slope instability. More details are reported in the steps listed hereinafter. Please note that, hereinafter, the term "date" is used

to refer to the exact date of failure (e.g., 15 May 2004), while "day" is used for the calendar date i.e., the date without the year (e.g., 15 May).

(i) Choosing the climatic variable. Since we aim at proposing a multipurpose method to be used in rather different situations, we extend our analysis to include any easily available climatic variable that can play a role in slope failure events in glacial and periglacial environments. The list of potential descriptors includes temperature T, precipitation R and temperature variation ΔT, i.e., difference between the temperature in the day when the failure occurred and temperature recorded in one or more antecedent days; however, other available variables could be included in the analysis.

(ii) Selecting the aggregation scale. We will call V the time-aggregated variable. Since it is not fully clear if the investigated slope failures are determined by processes with a fast or slow temporal evolution, we will consider for the sake of generality all variables at a daily, weekly, monthly and quarterly scale. This entails, for example, considering as possible triggering factors both precipitation of the day before the event and in the 3 months before the event. Only for the variable ΔT, it would be meaningless to refer to aggregated scales, while it is of interest to consider different time delays (1, 3 and 6 days, in this study) to investigate the possible effect of extraordinary temperature excursions (Table 3-3). As an example, if the failure occurred on 15 May, ΔT_1 will be the difference in daily air temperature between 15 and 14 May, ΔT_3 will be the difference in daily air temperature between 15 and 12 May, and ΔT_6 will be the difference in daily air temperature between 15 and 9 May.

(iii) Identifying the weather stations for data collecting. The closest available stations should be identified. Among these, stations with large data availability are preferred. In order to transpose the V value at the place and date when the failure occurred, we follow a very simple approach where the relevant variables are considered not to significantly vary in space except for the dependence of temperature on elevation, which is modeled through a linear lapse rate approach. Note that the application of a constant lapse rate allows one to determine V directly at the station, provided that also the reference sample is not transposed. In fact, application of a constant lapse rate would merely entail a translation of all values, without affecting the estimate of the probability associated with V. For these reasons in our work, we decided to use the data as they were recorded at the station, without transposing the values to the failure zone.

(iv) Choosing the reference sample, i.e., the record whereon comparing V to understand the severity of the problem. The value of V for the date of the failure was then compared with a reference sample including n values, measured at the same reference meteorological station(s): we considered that a sample to be adequate for such a comparison if $n \geq 10$. In the ordered sample, $V_{(i)}$ is the ith value, $i=1 \ldots n$. When selecting the most suitable reference sample, we need to consider the seasonality of the climate variable. In our study area, seasonality is particularly important for the air temperature T, and we thus compared the temperature recorded before the rockfall event with the temperature of a reference sample that included the same period of the year. As an example, if a rockfall occurring at a given site on 15 September 2014, when we consider the average air temperature (T) in the week before the failure (i.e., the average value of T from 9 to 15 September 2014), the reference sample will include all temperature data aggregated at the weekly scale for the same period of the year i.e., the average value of T in the period from 9 to 15 September for each year in the available historical record for the same reference meteorological station. For the sake of completeness, further tests were performed by considering the day before and after the date/day of the event, in order to see how probability values could change. For precipitation (R) and the variation in the daily air temperature (ΔT), the reference sample is extended to include data registered in the 90-day period centred on the day of the failure (e.g., if the failure occurred on 22 November, we consider data in the previous and following 45 days, this means from 8 October to 6 January). This procedure allows obtaining a larger reference sample, and thus increases the robustness of the obtained results. This is particularly important for R, since precipitation is an intermittent process and not all years in the record necessarily have an R value recorded for the period of interest.

(v) Identifying the potential triggering factors of failure. The last step concerns the estimation of $P(V)$, i.e., the non-exceedance probability associated with the variable V. We will estimate $P(V)$ in a nonparametric way, i.e., without invoking any distributional hypothesis. Thus, we determine the cumulative probability associated with V as $P(V)=i/(n+1)$, if $V>V_{(i)}$. The variable V is assumed to be a significant triggering factor at the a level if $P(V) \leq \alpha/2$ (negative anomaly) or $P(V) \geq 1-\alpha/2$ (positive anomaly). We report the $P(V)$ for any considered variable and time-aggregation scale

in a summary table. Only for variables characterized by $P(V) \leq \alpha/2$ or $P(V) \geq 1-\alpha/2$ (the significance level a is 0.10 here), we also report in a graph the empirical distribution function of the $V_{(i)}$ values in the reference sample, and the V value for comparison. These graphs can be a valuable tool to have a clearer picture of how far from standard values the V value lies, and thus to interpret the role of V as a triggering factor for the failure.

3.2.1.2 Advanced version of the method

In this paragraph we give special attention to the variations and improvements introduced in the method (Paranunzio et al., 2016).

(i) Choosing the climatic variable to be considered in the analysis. In this advanced version of the method, we also considered the minimum (T_{min}) and the maximum (T_{max}) air temperatures to obtain a more comprehensive picture of air temperature conditions before the slope failure.

(ii) Selecting the appropriate temporal-aggregation scale (as in Section 3.2.1.1).

(iii) Identifying the relevant weather stations for the analysis and the rule to suitably transpose the selected variable from the measurement place to the detachment site (as in Section 3.2.1.1).

(iv) Choosing the reference sample to be used as a benchmark (as in Section 3.2.1.1).

(v) Identifying the potential triggering meteorological factors for the failure (as in Section 3.2.1.1). We estimate $P(V)$, i.e. the non-exceedance probability associated to the climate variable V, at a significance level α. The choice of the significance level α is a matter of finding the best compromise between the necessity to reduce the probability to incur in a type I error (the probability to reject the null hypotesis given that is true) and a type II error (the failure to reject a false null hypothesis). In this case, the null hypothesis could be formalized as "the variable V did not influence the rockfall triggering". Given that the former probability increases with increasing significance levels, while the latter decreases and considering that in the present case, in our opinion, type I error is less impacting that type II error, we decided to increase the significance level to 0.2. Thus, in this way, we perform a standard 10% significance test on each of the tails of the distribution (negative or positive anomalies).

(vi) In addition to these analyses, for this work we performed a bivariate analysis to take into account additional factors that, in combination with

climate anomalies, can help understanding the processes leading to slope failure. Here we give a synthetic description of the main steps of the procedure.

- To describe the spatial and temporal distribution of the rockfalls listed in the inventory, we considered the following factors: (i) season of occurrence, (ii) mean elevation of the detachment zone, (iii) probability of permafrost occurrence, and (iv) magnitude of the event.
- The temporal distribution of the events was analyzed considering the season of occurrence. Rockfall events were divided in four seasonal classes i.e., Spring, Summer, Autumn, Winter. In relation to the elevation of the detachment zones, the events were divided into three classes i.e., 1500-2400 m a.s.l., 2400-3300 m a.s.l., and 3300-4200 m a.s.l. Rockfall volumes were ranked in two classes: rockfalls in the range 10^2-10^4 m^3 were classified as small events, and rockfalls in the range 10^4-10^6 m^3 were considered large events. The probability of permafrost occurrence in the detachment zone was derived from the Alpine Permafrost Index Map-APIM (Boeckli et al., 2012). APIM is defined as "a first resource to estimate permafrost conditions at any given location in the European Alps", and it represents a static snapshot of potential permafrost distribution. In rock, the maximal uncertainty in the elevation of the lower permafrost limit is estimated to be ±360 m. In this map, the likelihood of permafrost occurrence is classified in three classes, (i) permafrost "in nearly all conditions", (ii) "mostly in cold conditions", and (iii) "only in very favourable conditions", corresponding to a decreasing probability of permafrost occurrence. We have added the class "no permafrost" and we divided into four classes rockfall events with regard to the probability of permafrost occurrence in the detachment zone.
- Climate anomalies were grouped into five classes: (i) short-term temperature anomaly (ST) i.e., positive and negative temperature anomaly at the daily and/or weekly scale; (ii) long-term temperature anomaly (LT) i.e., positive and negative temperature anomaly at the monthly and/or quarterly scale; (iii) widespread temperature anomaly (WT) i.e, temperature anomaly distributed from the daily to the quarterly temporal range; (iv) precipitation anomaly (RT) i.e., precipitation anomaly from the weekly to the quarterly scale and (v) no climate anomaly detected (NO).

- A joint assessment of frequency distribution of climate anomalies in relation to spatio-temporal characteristics of rockfall events was performed.

3.3 Case study 1

3.3.1 Background

As anticipated in Section 3.1, we first tested this methodology on different types of slope instabilities occurred in the Western Italian Alps. For the purposes of our study, we selected five events of slope instability occurred in glacial/periglacial areas at high elevation in the Piedmont Alps in the years 1989–2008 (Figure 3-1). The choice of the case studies was based on several requirements: the exact knowledge of the location and time of occurrence; the availability of long-term climatic data; good quality of the time series; the conditions of occurrence or characteristics of the event that could be considered anomalous. With the term "anomalous" we refer to a departure from a reference sample, i.e. the record whereon comparing our variables to understand the severity of the issue. The selection of the case studies aimed to represent the different types of slope failures that are characteristic of high mountain environments. Three out of five case studies are located in the Belvedere Glacier basin: this basin culminates in one of the highest peaks of the Alps, Monte Rosa, which in the last 20 years has undergone amazing changes, due to the dramatic loss of ice cover and permafrost degradation (Fischer et al., 2013).

Table 3-1 Failure points main characteristics. Types of failure points according to Varnes landslides classification. Alpine sections according to the Comitato Geografico Nazionale Italiano, 1926.

Failure point (No.)	**Type**	**Date** dd mm yyyy	**Time of occurrence** (UTC)	**Centroid location** Elevation (m a.s.l.)	Latitude (N)	Longitude (E)	**Aspect**	**Glacial and periglacial area**	**Alpine section**
FP1	Ice avalanche	6 July 1989	20:45	3195	44°40'38''	07°05'26''	N	Coolidge Glacier, Monviso	Cottian Alps
FP2	Debris flow	24 September 1993	afternoon	2500	45°21'56''	07°10'44'	NE	Mulinet Glacier, Punta Mezzenile	Graian Alps
FP3	Ice avalanche	25 August 2005	2:36	3800	45°56'08''	07°52'48''	E	Belvedere Glacier, Monte Rosa	Pennine Alps
FP4	Rock avalanche	21 April 2007	10:00	4200	45°56'03''	07°52'37''	E	Belvedere Glacier, Monte Rosa	Pennine Alps
FP5	Debris flow	7 September 2008	2:00	3629	45°58'08''	07°53'22''	SE	Castelfranco Glacier, Monte Rosa	Pennine Alps

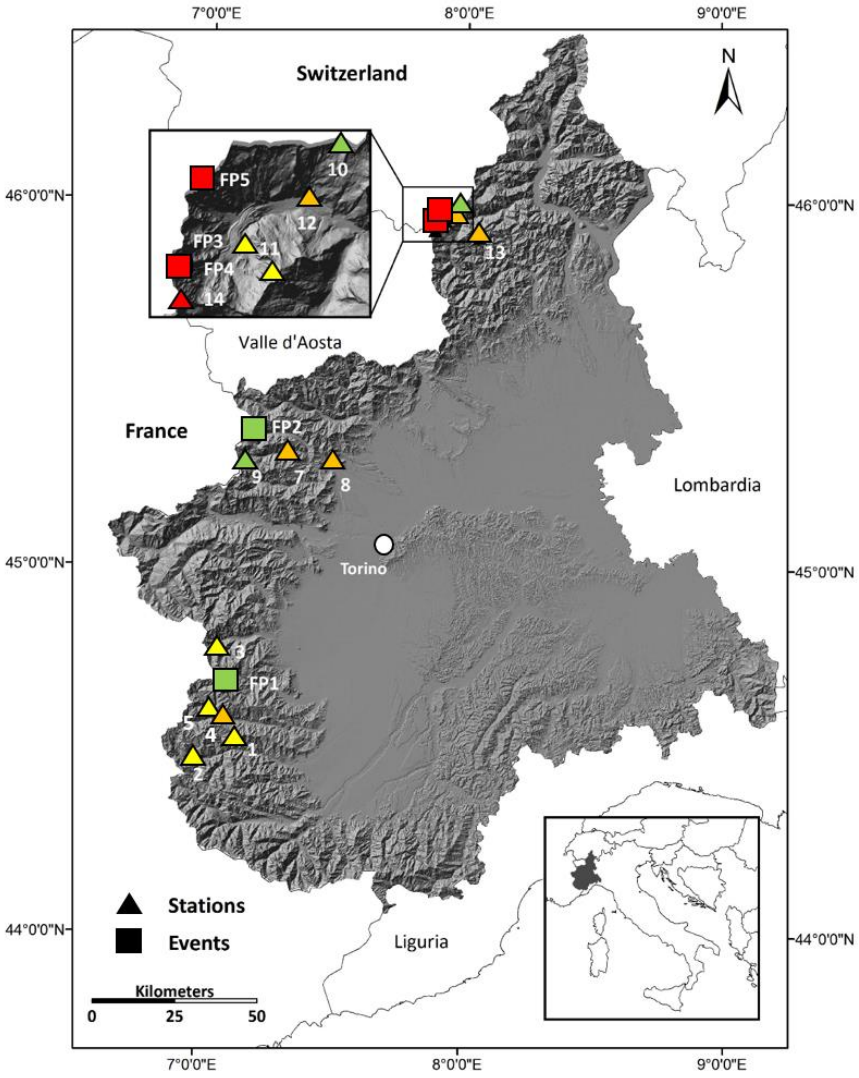

Figure 3-1 Location of the five events (FP) considered in this study (squares) with the corresponding weather stations (triangles). Events and stations are numbered according to Table 3-1and Table 3-2 respectively. Weather stations are associated to the five events FP as follows: 1 to 6 to FP1, 7 to 9 to FP2, 10-12-13-14 to FP3, 10 to 14 to FP4, 10-11-12-14 to FP5. Events and weather stations are coloured differently according to elevation. Yellow squares/traingles represent events/meteorological stations at low elevation (1500-2400 m a.s.l); green squares/traingles represent events/meteorological stations at medium elevation (2400-3300 m a.s.l); red squares/triangles represent events/meteorological stations at high elevation (3300-4200 m a.s.l); weather stations located below 1500 m a.s.l. are in orange. DEM provided by the National Institute of Geophysics and Volcanology (INGV) of Pisa (Tarquini et al., 2012).

3.3.1.1 The Upper Coolidge Glacier 1989 ice avalanche

Two-thirds of the mass of the Upper Coolidge Glacier, located on the northern side of the Monviso massif, suddenly failed on July 6, 1989, at 20:45 UTC (Dutto et al., 1991). The detachment occurred along a crevasse at an altitude of 3195 m a.s.l., which had been identified in 1986 (Figure 3-2). The ice slab (about 2 x 10^5 m^3) slipped along the Canalone Coolidge (about 40°– 60°steep), rapidly evolved in an ice avalanche and finally impacted, 700 m below, the Lower Coolidge Glacier. Along its path, the disintegrating ice mass entrained snow and debris, continued its run down to the Lago Chiaretto depression (2261 m a.s.l.) and 50 m up the opposite side of the lake depression. The event, which induced a visible seismic signature on nearby seismographs (Bovo et al., 1990), produced relevant geomorphic effects: the frontal moraine of the Lower Coolidge Glacier suffered a 50-m lowering; the Chiaretto Lake was partially filled, and more than 2.5 x 10^5 m^2 were covered with a mixture of ice, snow and debris, up to a thickness of 8 – 10 m. It was very fortunate that the event occurred at night, because during the summer the Chiaretto Lake is a very popular destination for family hiking. The 1989 Coolidge ice avalanche has few equals in the European Alps, and no similar event has been recorded in the area before or after it (Chiarle and Mortara, 2008; Dutto and Mortara, 1992).

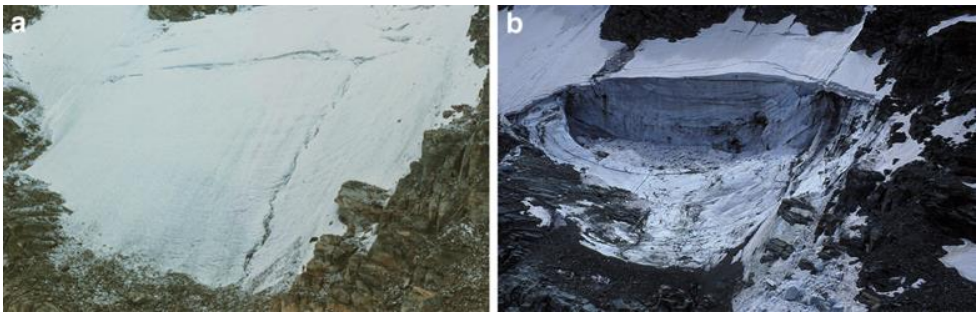

Figure 3-2 Upper Coolidge Glacier ice avalanche (FP1), 6 July 1989: a) the crevasse in 1986; b) the glacier failure in 1989 (source: CNR-IRPI archive).

3.3.1.2 The Mulinet 1993 debris flow

On September 24, 1993, a heavy rainstorm triggered a deep incision of the Little Ice Age moraine of the Mulinet Glacier (15 – 50 m deep, 450 m long and up to 200 m wide), at an elevation of 2525 m a.s.l. (Mortara et al., 1995). Stagnant ice was observed in the moraine cut (Figure 3-3a). The resulting debris flow travelled 4.5 km downvalley before striking the village of Forno Alpi Graie, located 1300 m below, in the Val Grande di Lanzo. The flow caused heavy damage to the

village, but luckily no one was injured. A photogrammetric study allowed a volume of mobilized debris of about 8 x 10^5 m^3 to be estimated. This value, among the largest volumes ever mobilized in the Alps (Marchi and Tecca, 1996), is due to the deep downcutting that affected the moraine ridge (Chiarle et al., 2007). The hydrographic network was also seriously modified, with the incision of new channels and the disappearance of pre-existing ones; the Forno Alpi Graie alluvial plain was buried under 1.5 – 2 m of debris, mainly represented by pebbles and blocks in a sandy matrix, over an area of 4 x 10^5 m^2. Mortara et al., (1995) suggested a possible role of melting ground ice in the moraine body to account for the extreme downcutting.

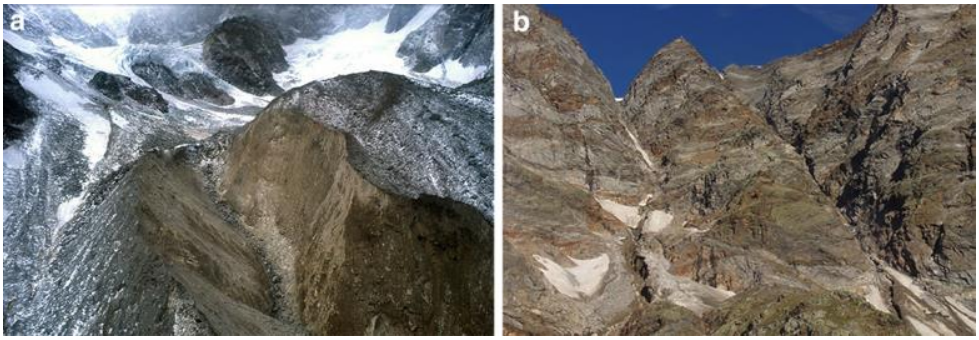

Figure 3-3 a) Upper Lanzo Valley debris flow (FP2), 24 September 1993; b) Castelfranco Glacier basin debris flow (FP5), 7 September 2008 (source: CNR-IRPI archive).

3.3.1.3 The Monte Rosa 2005 ice avalanche

On 25 August 2005, at 02:36 UTC, a huge ice slab (1.1 x 10^6 m^3) detached from the Monte Rosa east face, which overhangs the Belvedere Glacier, at an elevation between 3820 m and 3580 m a.s.l. (Tamburini et al., 2013). The ice slab, up to 50 m thick, detached at the contact with the bedrock and rapidly evolved in an ice-avalanche which ran into the Canalone Imseng, entraining snow, ice and debris along its path (Figure 3-4a). The flowing mass stopped at the foot of the slope, at an elevation of about 2200 m, partially filling the large depression formed in summer 2002 that hosted the "Lago Effimero", a supraglacial lake of more than 3 x 10^6 m^3 that drained in summer 2003 (Kääb et al., 2004). The main part of the accumulation was composed by ice blocks with a diameter up to 50 cm, in a fine matrix made of a mixture of ice powder, clay and silt: the deposit reached a maximum thickness of about 32 m. The avalanche flow reached the Zamboni hut, located more than 3 km downstream, luckily without any casualty or damage. Aerial photo analysis showed a deep fracture located along the right side of the

detached ice mass, since at least 2001. The event, registered by Italian and Swiss seismic stations, is one of the largest of this type documented in the European Alps over the past 100 years (Mortara and Tamburini, 2009).

3.3.1.4 The Monte Rosa 2007 rock avalanche

Two years later, on 21 April 2007, at about 10:00 UTC, a huge rock mass failed at an elevation between 4200 m and 4000 m a.s.l, on the same slope where the 2005 ice-avalanche had detached (Tamburini et al., 2013). A few days earlier, a skier descending along the Canalone Marinelli reported a deposit of a ice/rock fall probably originated from the same source area of the main event. The failed rock mass entrained a consistent volume of ice and debris along the path, evolving into a rock-avalanche that reached the foot of the slope in correspondence with the Belvedere Glacier, and invaded nearly the same area covered by the accumulation of the 2005 ice-avalanche (Figure 3-4b). A comparison of two lidar surveys, taken respectively in 2005 and 2007, allowed a volume estimate of about 1.5 x 10^5 m^3 for the detached mass (Fischer et al., 2011). A comparison of DHM from Lidar data (data acquisition in 2005 and 2007) allowed to quantify the accumulation volume (3 x 10^5 m^3) and mean thickness (5 m).

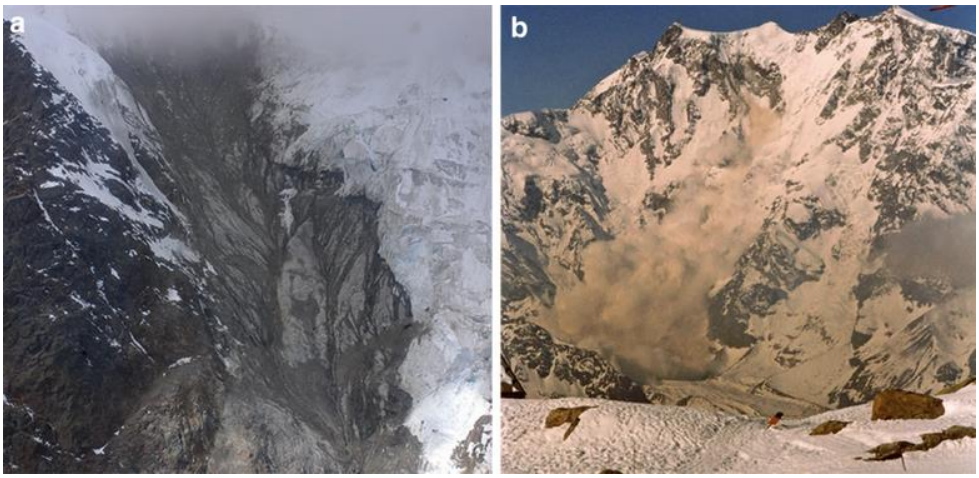

Figure 3-4 a) Belvedere Glacier basin ice avalanche (FP3), 25 August 2005; b) Belvedere Glacier basin rock avalanche (FP4), 21 April 2007 (source: CNR-IRPI archive).

Rockfalls are quite a common occurrence on steep slopes. Nevertheless, this event can be considered as quite exceptional, both for the elevation of the detachment area and the period of the year in which it occurred. The 2005 ice-avalanche, which detached immediately below the 2007 rock-avalanche, was

probably one of the predisposing factors to slope instability, due to loss of support at the foot of the failed rock spur. Other remarkable causes of instability have certainly been the high slope angle and a drastic ice cover reduction in the basin (Mortara and Tamburini, 2009).

3.3.1.5 The Castelfranco 2008 debris flow

A debris flow occurred on 7 September 2008 in the Castelfranco Glacier basin, a tributary basin on the left side of the Belvedere Glacier. The process initiated at an elevation of about 3600 m a.s.l., flowed along the Canalone Tuckett and Canalone Tyndall, and flooded the left side of the proglacial alluvial fan (Figure 3-3b). At the junction with the Belvedere Glacier, part of the flow continued its path beneath the ice mass: after 3 hours from the initiation of the process, the debris reached the mouth of the Belvedere Glacier and the Torrente Anza. The accumulation volume was estimated to be as much as a few thousands of cubic meters (Mortara and Giuliano, 2009).

This event can be considered anomalous for several reasons: the detachment zone was unusually high for debris flow initiation in the Alps; the amount and duration of precipitation were not exceptional; unusual was also the dynamics of the event, which continued through a series of pulses several hours after the end of the rainfalls. The remnants of the Castelfranco Glacier, along with snow avalanche accumulations, are thought to have played a critical role in the initiation and dynamics of the event, acting as temporary dams for the flow (Mortara and Giuliano, 2009).

3.3.2 Climate data

Two different types of climatological data have been used: (a) mean daily air temperature and total daily precipitation; (b) hourly and every ten minutes mean air temperature and total rainfall. The data were collected from a network of automatic and manual weather stations (ARPA, 2013; UIPO, 1913-1994).

Initially, all the stations located in the Alps close to the failure sites were considered. Some of these stations were discarded later on because they supplied a non-continuous data series. The climate datasets from the remaining stations underwent a quality control procedure, to check for the possible presence of erroneous and/or anomalous values. For this purpose, computer programs that generate lists of potential errors were used and all the data were double-checked by a analyst (WMO, 2011). Based on the results from the quality control

procedures, and in order to reach the best compromise between the altitudinal, topographic distance from the considered failure points and data availability, three manual stations and eleven automatic weather stations were considered for the present work (Table 3-2).

Table 3-2 Main characteristics of the meteorological stations considered in this study. Only meteorological stations representing the best compromise between the requirements mentioned in Sect. 3.2 (i.e., covering the failure date, long-term dataset, low distance from the failure area) are displayed. Reference stations, whose results are shown in the following sections, are in italic. No.: failure point numbers (from Table 1) associated to the meteorological stations; variables recorded at the stations: *T* (temperature), *ΔT* (temperature variation between the day of the failure and the days before) and *R* (precipitation). Data source: ARPA Piemonte, 2014 (PIE); ARPA Veneto, 2014 (VEN); Centro Funzionale – Regione Autonoma Valle d'Aosta, 2014 (VDA); Ufficio Idrografico - Provincia Autonoma di Bolzano, 2014 (BUI); Meteotrentino, 2014 (MET).

Failure point	**Station name and no.**	**Variables**	**Location**			**Observation period**	**Distance**	**Elevation difference**
			Elevation	**Latitude**	**Longitude**		**D**	**Δz**
(No.)			**(m a.s.l.)**	**(N)**	**(E)**	**(Years)**	**(km)**	**(m)**
FP1	1.Pian delle Baracche	*T-ΔT*	2135	44°32'59''	07°08'04''	1988-2011	~14	1060
	2.Acceglio	*T-ΔT*	1610	44°29'10''	06°58'57''	1989-2011	~21	1585
	3.Colle Barant	*T-ΔT*	2294	44°46'32''	07°03'42''	*1988-2011*	*~12*	*901*
	4.Casteldelfino	*R*	1296	44°34'56.5''	7°04'06.1''	1913-1989	*~10*	1899
	5.Castello Diga	*R*	1650	44°36'45.7''	7°02'57.5''	1951-1989	*~7*	1545
	6.Crissolo	*R*	1410	44°41'56.5"	07°09'06.1"	*1913-1989*	*~7*	*1785*
FP2	*7.Ala di Stura*	*T-ΔT–R*	1006	45°18'48''	07°18'41"	*1993-2011*	*~12*	*1494*
	8.Lanzo	*T-ΔT–R*	580	45°17'23''	07°29'38''	1989-2011	~26	1920
	9.Rifugio Gastaldi	*T-ΔT*	*2659*	*45°17'57''*	*07°08'40''*	*1988-2011*	*~8*	*-159*
FP3	*10.Passo del Moro*	*T-ΔT-R*	*2820*	*45°59'53''*	*07°58'39''*	*1991-2011*	*~10*	*980*
	14.Capanna Margherita	*T-ΔT*	4560	45°55'37''	07°52'37''	2002-2011	~1	-560
	12.Macugnaga Pecetto	*T-ΔT–R*	1360	45°58'23''	07°57'32''	1999-2011	~8	2440
	13.Carcòforo	*R*	1290	45°54'29''	08°03'06''	1996-2011	~13	2510
FP4	14.Capanna Margherita	*T-ΔT*	4560	45°55'37''	07°52'37''	2002-2011	~1	-360
	10.Passo del Moro	*T-ΔT–R*	*2820*	*45°59'53''*	*08°10'44''*	*1991-2011*	*~10*	*1380*

	11.Rifugio Zamboni	*T-ΔT–R*	2075	45°57’08’’	07°55’05’’	2007-2011	~4	2125
	12.Macunaga Pecetto	*T-ΔT–R*	1360	45°58’23’’	07°57’32’’	1999-2011	~8	2840
	13.Carcòforo	*R*	1290	45°54'29’’	08°03'06’’	1996-2011	~13	2910
FP5	14.Capanna Margherita	*T-ΔT*	4560	45°55’37’’	07°52’37’’	2002-2011	~5	-931
	10.Passo del Moro	*T-ΔT–R*	*2820*	*45°59’53’’*	*08°10’44’’*	*1991-2011*	*~7*	*809*
	11.Rifugio Zamboni	*T-ΔT–R*	2075	45°57’08’’	07°55’05’’	2007-2011	~3	1554
	12.Macugnaga Pecetto	*T–R*	1360	45°58’23’’	07°57’32’’	1999-2011	~5	2269

3.3.3 Results and discussion

The following sections illustrate the results of our analyses. Table 3-4 summarizes the $P(V)$ for any considered variable and time-aggregation scale. For each case study we first describe the results of our analysis, we then compare with previous studies and finally discuss the possible mechanisms of initiation. Steps i, ii and iv of the method are common to all the case studies while the weather stations selected as the most representative of the meteorological conditions (step iii) are shown in Table 3-2. The Upper Coolidge Glacier is fully described, in order to clearly illustrate the application of our method and all available graphs are provided (Figures 2-5, 2-6, 2-7). For the other case studies, only the most significant graphs are shown, according to the probability values associated with V.

Table 3-3 The methodology was applied to the following variables: temperatures (T) and precipitation (R) using different aggregation scales (from daily to quarterly scale) and temperature variation (ΔT) in different time delays (one day, three days and six days). We compared the reference sample with: T recorded during the same period of the year; R with the values recorded in the three months surrounding the failure date; ΔT with the values recorded in the three months surrounding the failure date.

Variable	Aggregation scale	Reference sample
T	**d**	same period of the year
T	**7 d**	same period of the year
T	**30 d**	same period of the year
T	**90 d**	same period of the year
ΔT	**1 d**	3-months surrounding the failure date
ΔT	**3 d**	3-months surrounding the failure date
ΔT	**6 d**	3-months surrounding the failure date
R	**d**	3-months surrounding the failure date
R	**7 d**	3-months surrounding the failure date
R	**30 d**	3-months surrounding the failure date
R	**90 d**	3-months surrounding the failure date

Table 3-4 Estimation of the probability P(*V*) associated with the variable *V*, where *V* is temperature (*T*), precipitation (*R*) or temperature variation between the day of the failure and the days before (*ΔT*), and *V* is the correspondent value recorded when the failure occurred. *T* and *R* analysis were performed considering different aggregation scales: daily scale (d), weekly scale (7 d), monthly scale (30 d) and quarterly scale (90 d). *ΔT* analysis was performed considering the previous day (1 d), three (3 d) and six days (6 d). Variables in bold are characterized by P(*V*)<α/2 or P(*V*)>1-α/2 (α= 0.10). The symbol ">" was used when the value was extrapolated.

Variables	***T***	***T***	***T***	***T***	***ΔT***	***ΔT***	***ΔT***	***R***	***R***	***R***	***R***
Aggregation scale	**d**	**7 d**	**30 d**	**90 d**	**1 d**	**3 d**	**6 d**	**d**	**7 d**	**30 d**	**90 d**
FP1	0.85	0.27	0.36	0.14	**0.97**	**0.99**	0.92	/	0.44	0.54	0.94
FP2	0.45	0.82	0.14	0.11	0.57	0.12	0.52	**0.99**	**0.96**	0.82	0.25
FP3	0.35	0.08	0.08	0.62	0.85	0.87	0.29	/	**0.97**	**0.98**	0.65
FP4	**>0.96**	**>0.96**	0.92	0.83	0.81	0.41	0.77	/	/	0.54	0.40
FP5	0.43	0.57	0.42	0.61	0.70	0.60	0.18	0.73	0.79	0.77	0.73

3.3.3.1 The Upper Coolidge Glacier, ice-avalanche, 6 July 1989

Our main source of results was Colle Barant weather station, due to its lower distance from the failure point, the smaller difference in elevation, and the larger availability of data (Table 3-2). Since precipitation records (from these automatic weather stations) were not available for the period of the year when the failure occurred, precipitation data from three manual stations had to be considered: in this case, the best compromise between proximity and data availability was represented by the Crissolo station (Table 3-3).

First, we analyzed the variable *T*. In Figure 3-5 we show: (a) the daily mean *T* measured in the day of the event (July 6, 1989), compared with a reference sample including the July 6 values recorded in other years when data are available; (b) the weekly mean *T* registered in the seven days before the ice-avalanche detachment, compared with the mean *T* of the intervals 30 June – 6 July of the recorded time series; (c) the monthly mean *T* measured during the 30 days before the event, compared with the mean *T* of the intervals 7 June – 6 July of the recorded time series; (d) the three months mean *T* registered during the 90 days before the event, compared with the mean *T* of all the intervals 7 April – 6 July of the recorded time series. Analysis of temperature data detected lower than usual *T* values, at the weekly, monthly, and quarterly scales (Table 3-4). The daily value on the other hand is quite high, even though P*(V)* is not extraordinary (0.85). We then

considered the difference between the daily mean T of the day of the event and the daily mean T values measured one, three and seven days before the event (ΔT), compared to all ΔT values for the same time intervals recorded in the three months surrounding the failure date (i.e. the variation of T between 6 July and 5 July 1989 compared to all differences between T_k and T_{k-1} of the recorded time series, where k is the k-th day in the three months surrounding the failure date). T underwent a sudden rise in the days before the event, in particular during the three days before the failure, when ΔT reached the 99th percentile at Colle Barant station (Figure 3-6). Data from Pian delle Baracche and Acceglio stations showed a similar trend. After that, we compared daily, weekly, monthly and quarterly precipitation with analogue values registered in the three months window centered on the failure date (Figure 3-7). High precipitation values were detected at quarterly scale (486.6 mm), plotting on the 94th percentile (Table 3-4).

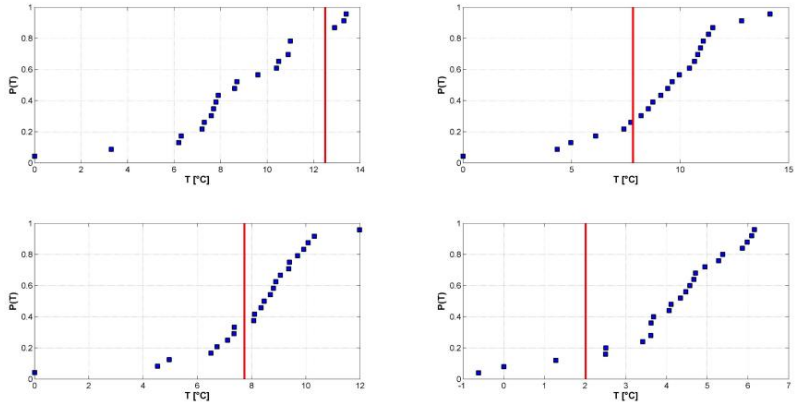

Figure 3-5 Empirical distribution function for temperatures (T) recorded at Colle Barant weather station (Upper Coolidge Glacier ice avalanche, 1989). The long-term series (1988–2011) is represented by squares, while the line is the value recorded at the time of the failure: a) daily scale; b) weekly scale; c) monthly scale; d) quarterly scale.

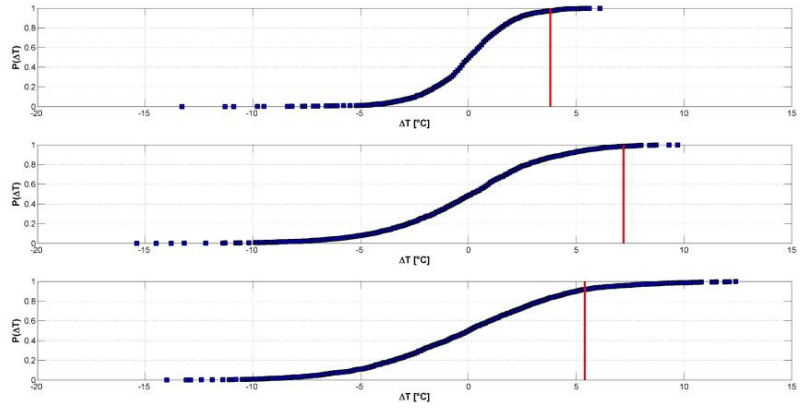

Figure 3-6 Empirical distribution function for the differences of temperature (ΔT) recorded at Colle Barant weather station (Upper Coolidge Glacier ice avalanche, 1989). The long-term series (1988–2011) is represented by squares, while the line is the value recorded at the time of the failure: a) ΔT between 6 July and 5 July comparedwith all $T_{(i)}$ - $T_{(i-1)}$ values in the 3 months surrounding the failure date; b) ΔT between 6 July and 3 July compared with all $T_{(i)}$ - $T_{(i-3)}$ values in the 3 months surrounding the failure date; c) ΔT between 6 July and 29 June compared with all $T_{(i)}$ - $T_{(i-7)}$ values in the 3 months surrounding the failure date.

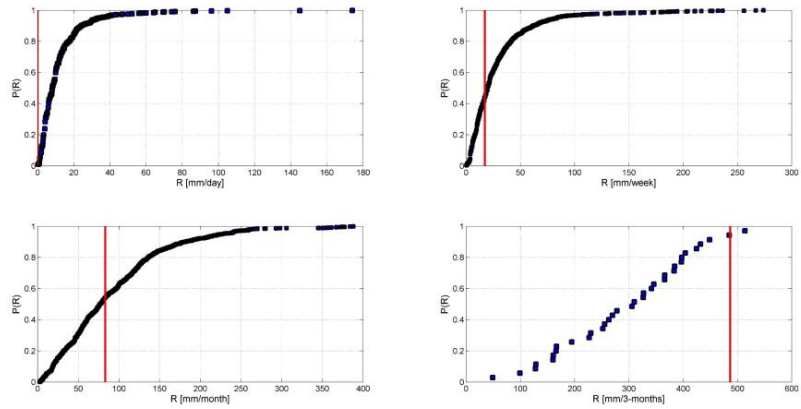

Figure 3-7 Empirical distribution function for precipitations (R) recorded at Crissolo weather station (Upper Coolidge Glacier ice avalanche, 1989). The long-term series (1913–1989) is represented by squares, while the line is the value recorded at the time of the failure: a) daily scale; b) weekly scale; c) monthly scale; d) quarterly scale.

Speculating on the triggering causes, Dutto et al. (1991) explained the occurrence of the glacier failure through a combination of unfavorable

geomorphological and meteorological factors. In particular, daily temperatures above the typical seasonal values may have caused the precipitation of the days immediately before the event to occur as rainfall instead of snowfall (Mortara and Palomba, 2009). According to Dutto et al. (1991), precipitation and melt water may have leaked down to the glacier bottom through a large crevasse, which had been identified since 1986 in the upper part of the glacier (Figure 3-2), causing the decoupling of the glacier from the bed.

If we consider the development of meteorological conditions highlighted by our analysis (Table 3-4), we observe very abundant precipitation in the three months before the event, together with temperatures that remained well below the average up to a week before the event. Temperature rose abruptly from the week before the event, and in particular from three days before the failure (ΔT = 7.2°C). According to these data, we can speculate that the sudden increase of temperature in the days before the event has accelerated the melting of the thick snow cover accumulated on the glacier in the previous months, which had been limited until that moment by the low temperatures. The large crevasse at the head of the glacier may have represented a preferential entrance for melt water that was "trapped" in the glacial system, giving rise to a hydraulic thrust. The rainfall that occurred in the days immediately before the event may have further increased water pressure at the glacier bed, triggering the final failure.

3.3.3.2 The Mulinet debris flow, 24 September 1993

The Rifugio Gastaldi station was taken as the most representative weather station, because of its proximity to the failure zone. However, since it provides only temperature records, we used precipitation data from the Ala di Stura station (Table 3-2). The outcomes of our analyses are summarized in Table 3-4.

Temperature analysis did not reveal any significant anomaly. The most remarkable results relate to precipitations, which are believed to have been rainfall during the pluviometric event, since the calculated zero-degree isotherm was above the failure zone. On 24 September 1993, the freezing level was around 3000 m a.s.l., whereas the debris flow originated at 2500 m a.s.l. (Mortara et al., 1995). The Ala di Stura pluviometer registered 110.8 mm of rain on 24 September and 164.4 mm during the preceding week (Figure 3-8), which plotted respectively on the 99th and 96th percentile (Table 3-4).

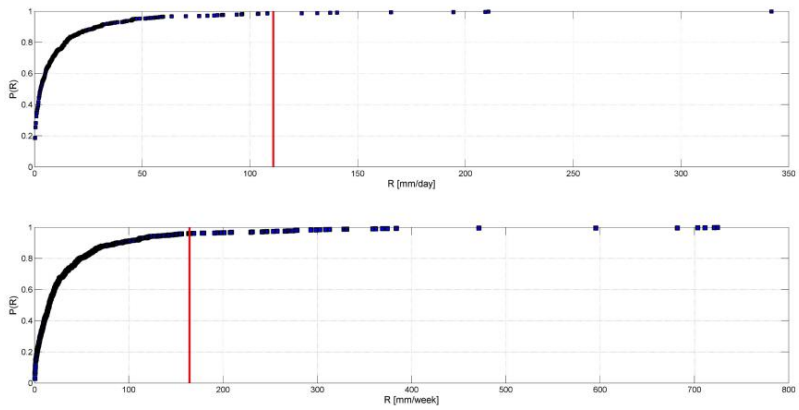

Figure 3-8 Empirical distribution function for precipitations (*R*) recorded at Ala di Stura weather station (Upper Lanzo Valley debris flow, 1993). The long-term series (1993–2011) is represented by squares, while the line is the value recorded at the time of the failure: a) daily scale; b) weekly scale.

Based on the outcomes of our analysis, we can infer that the Mulinet moraine downcutting that initiated the 1993 debris flow was most likely triggered by heavy rainfall. The huge size reached by the failed mass, along with the buried ice observed in the scar, led previous studies to consider ground ice melting as the possible trigger in initiating the downcutting process (Chiarle et al., 2007). However, according to our analyses, temperature values did not show relevant anomalies for any of the considered periods of observation. We would thus tend to exclude that thawing of the moraine ice-core had a relevant role in triggering the failure, even though ground ice degradation may have occurred in previous years; this would have contribute to predispose the moraine to collapse. Nevertheless, temperature may have played a role during the meteorological event, as the elevation of the zero-degree isotherm was well above the main failure: as a consequence, the Mulinet moraine and a wide proglacial area upstream received heavy liquid precipitation. In our opinion, the 1993 moraine failure can thus be considered the result of the combination of ground saturation and heavy runoff from the proglacial area above the moraine.

3.3.3.3 The Monte Rosa ice-avalanche, 25 August 2005

The most suitable stations for the analysis of the events occurred on the east face of Monte Rosa are Capanna Margherita and Passo del Moro. Since the Passo del Moro station has a longer-term data series and both precipitation and temperature records, we primarily used the results from this station.

Temperatures during the week and month prior to the ice-avalanche were extremely low with respect to the reference sample, and close to the median considering the quarterly scale. However, temperature rose consistently in the three days before the event, as shown by ΔT values in Table 3-4. No precipitation was measured during the day of the failure, whereas weekly and monthly total precipitation reached very high values, respectively around the 97th and the 98th percentile (Figure 3-9).

Temperature fluctuations in the 40 days prior to the failure have been analysed by Huggel et al., (2010). The authors highlighted several warm periods lasting 5-10 days in June-July 2005, followed by a cooler period in the 20 days before the event, with several freeze-thaw cycles. They also noticed that four days prior to the failure temperature rose again, reaching 5°C on the day of the event. The observations of Huggel et al., (2010) can in part be found in the results of our analyses. These highlighted very low (even if not extraordinarily low) temperatures in week and month prior to the failure (P(T) = 0.08), and a marked temperature rise in the 3 days before the failure (P(ΔT) = 0.87). On the other hand, the warm periods lasting 5-10 days in June and July mentioned by Huggel et al. 2010, have not been highlighted by our method, as we only considered the P(T) in the previous three months, which had a value of 0.62. However, Huggel et al., (2010) do not take into account precipitations in the period prior to the event, which our analysis identifies as the most anomalous parameter associated to the event (P(R) = 0.98 in the previous 30 days).

Speculating on the mechanisms of initiation, Huggel et al., (2010) explain failure occurrence as triggered by penetration to the base of the glacier of melt water produced during the warm periods, while the repeated cycles of freeze-thaw may have destabilized the bedrock. We reconstructed the processes that triggered the ice avalanche on the basis of the outcomes of our analysis, and taking into account the study by Huggel et al., (2010). As in Table 3-4, temperature values recorded on the day of the event were not particularly significant (P(T)=0.35), whereas the thermic excursion between this day and the previous ones has been anomalous. In this context, since the event occurred at 4 am, also the probability associated to the previous day should be particularly taken into account, and the use of ΔT could be of help in integrating this gap. Considering the sudden rise in temperature between the failure date and the previous days (ΔT = 4°C) and the large amount of precipitation registered during the previous month (Figure 3-9), we can hypothesize that enhanced snowmelt occurred in the days before the event,

which had been limited by low temperatures in the previous weeks. The presence of an existing fracture (documented since 2001) could have represented a predisposing factor to failure, as well as a preferential way for melt water to reach the glacier bed. The increase in pore water pressure may have led to effective stress reduction, mainly due to melt water that had seeped into the glacial system. This event shows many similarities with other failures reported in the literature (Huggel et al., 2010) and in particular to the 1991 Mount Cook rock-ice avalanche. In this last case, a few days of warm temperatures were followed by a temperature drop to freezing conditions 24 hours before failure. The 2005 Monte Rosa event occurred during the night: we can speculate that the final trigger of both events was an increase of pore water pressure inside the unstable masses, caused by blockage of melt water movement, as suggested by McSaveney (2002) for the Mount Cook 1991 event and by Fischer et al. (2010) for the 1988 Tschierva rock avalanche.

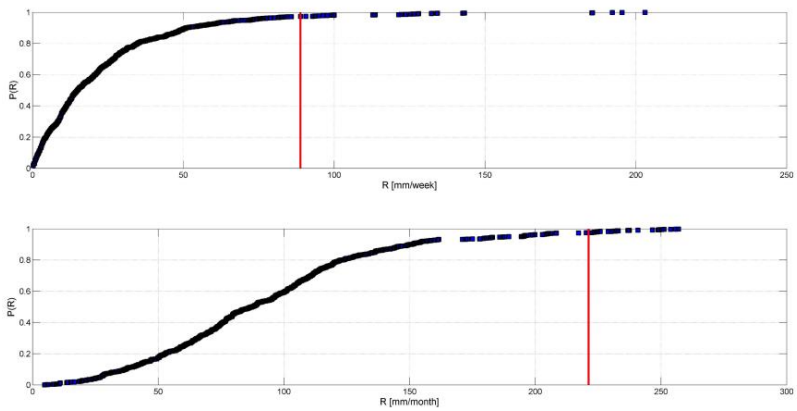

Figure 3-9 Empirical distribution function for precipitation (*R*) recorded at Passo del Moro weather station (Belvedere Glacier basin ice avalanche, 2005). The long-term series (1991–2011) is represented by squares, while the line is the value recorded at the time of the failure: a) weekly scale; b) monthly scale.

3.3.3.4 The Monte Rosa rock-avalanche, 21 April 2007

April 2007 was the warmest month in the last 150 years (Mortara and Tamburini, 2009). The outcomes of our analyses of daily, weekly and monthly data registered by the Passo del Moro station before the event are in agreement with this finding, since all the reference values are well above the average (Table 3-4). The other considered weather stations showed a similar behavior. The most significant results come from daily and weekly temperature distributions registered before the

rock-avalanche, which plot over the 96th percentile (Figure 3-10). A similar anomaly is reported by Huggel et al. (2010), who found that the temperature of the day before the event at the Jungfraujoch station (3580 m a.s.l.) was in the 98th-99th percentile of the long-term April record (available from 1958). Precipitations, instead, did not show any significant anomaly, since they occurred only during the thirty days and three months before the failure, with no remarkable values (Table 3-4).

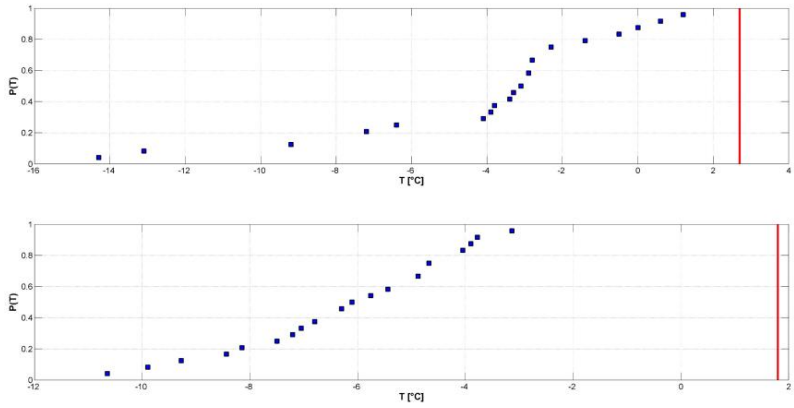

Figure 3-10 Empirical distribution function for temperature (*T*) recorded at Passo del Moro weather station (Belvedere Glacier basin rock avalanche, 2007). The long-term series (1991-2011) is represented by squares, while the line is the value recorded at the time of the failure: a) daily scale; b) weekly scale.

Speculating on the mechanisms of initiation, we can infer from the results of our analyses that the unusually warm temperatures occurring in the days before the event were the triggering factor of the rock-avalanche. According to Huggel et al., (2010), air temperature, even though much higher than usual, in the days prior to the event was about -5°C at the scar elevation. However, the authors suggest that radiation on the east face of Monte Rosa was high and cloud cover was generally low in April 2007: in their opinion, these conditions may have allowed snow and ice melting at the surface, in spite of the subfreezing air temperature. Based on data recorded by Capanna Margherita station (4560 m a.s.l.), total solar radiation in the week before 21 April 2007 was above 28 MJ/m^2, with an associated probability above the 91th percentile, thus confirming Huggel et al. (2010) hypothesis. According to (Gruber and Haeberli, 2007), melt water can leak in the rock slope and rapidly lead to the development of thaw corridors along fractures in permafrost, and potentially destabilize large rock volumes. In

conclusion, in our opinion infiltration of water from snow and ice melting at the surface into the bedrock fractures might thus have reduced the shear strength of the rock mass, causing the collapse: warm conditions in fall 2006 might have contributed by warming the bedrock to a few meters depth (Fischer et al., 2013).

3.3.3.5 Castelfranco Glacier debris flow, 7 September 2008

Rifugio Zamboni would be the most representative station for this case study, because of its proximity to the failure area: unfortunately, the data-series are very short and we have thus to rely once more on data registered by the Passo del Moro station.

Our analyses did not reveal any anomalies in daily, weekly and monthly and quarterly values of temperature, since reference values range between the 42^{th} and 61^{th} percentile (Table 3-4). Similarly, the analysis of ΔT and R did not produce any clear evidence of the possible triggering factor in this case (Table 3-4).

A significant hint of what may have occurred comes out comparing daily R values registered at Passo del Moro and Rifugio Zamboni: as shown in Figure 3-11, precipitation data registered on 7 September 2008 at Passo del Moro widely differed from those at Rifugio Zamboni (6.6 mm versus 41.4 mm) even though the two stations are quite close to each other. A further analysis on hourly values pointed out the same trend. Marked spatial variability of precipitation is a quite usual feature of summer storms, in particular in mountain areas: in order to assess the role of precipitation as a triggering factor, we needed to assess which registration was more representative of precipitation conditions in the failure zone. In order to comprehend if Rifugio Zamboni area could have been affected by a storm cell unlike the Passo del Moro one, an additional analysis using data from a weather radar was carried out. The most suitable instrument for the considered area was the Monte Lema station, since its position ensures good visibility over south-western Alps regions. Data were measured at a 5 minutes time step. We compared data registered by Rifugio Zamboni and Passo del Moro instruments (from 6 September 2008, 00:00 UTC to 8 September 2008, 00:00 UTC) with those estimated using radar, but they differed a lot, possibly due to the distance and irregular terrain between the failure point and the radar. Radar data analysis was thus not decisive to interpret the causes behind this event.

On the basis of the above results, we think that an interpretation of the event triggering factors and mechanisms is still ambiguous. According to Mortara and Giuliano (2009), the remnants of the Castelfranco Glacier, along with snow

avalanche accumulations, played a critical role in the initiation and dynamics of the event, acting as temporary dams for the flow. This interpretation might explain why temperature and precipitation data analysis did not provide any significant anomaly, since the meteorological conditions alone are not able to justify debris flow initiation.

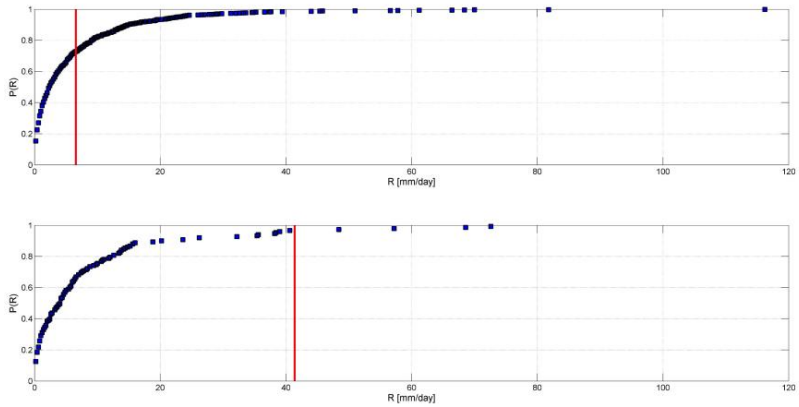

Figure 3-11 Empirical distribution function for precipitation (R) at a daily time scale, recorded at Passo del Moro and Rifugio Zamboni weather stations (Castelfranco Glacier basin debris flow, 2008). The long-term series (respectively, 1991–2011 and 2007–2011) is represented by squares, while the line is the value recorded at the time of the failure: a) Passo del Moro weather station b) Rifugio Zamboni weather station.

3.3.4 Considerations and basis for further developments

The methodology proposed is a simple procedure for relating meteorological factors to the initiation of slope failures and can thus be a valid tool for a better comprehension of the possible effects of climate change on environmental dynamics, with a particular focus on glacial and periglacial areas, which are particularly sensitive to temperature variations.

Based on the results of this preliminary phase, out of the five case studies analysed, four can be ascribed to meteorological anomalies, such as the rise of temperature or heavy precipitation, while the method did not provide any significant result about the debris flow in the Castelfranco Glacier basin. The examination of meteorological conditions prior to each failure highlighted some thermal patterns for the case of the Upper Coolidge Glacier ice-avalanche in 1989 and the Belvedere Glacier rock-avalanche in 2007, since the anomaly is correlated

to a sudden thermometric rise in the days before the failure. On the other hand, precipitation anomalies were evident for the Mulinet Glacier debris flow in September 1993 and the Belvedere Glacier ice-avalanche in August 2005, with a possible contribution for this latter temperature rise in the few days before the event.

Thus, the general approach presented here proved to be able to discriminate between slope failures triggered by meteorological factors and those triggered by other factors, and to eventually identify the most relevant meteorological driver (e.g., temperature or precipitation). The inclusion of more climatic parameters (e.g., maximum/ minimum daily temperatures) for selected case studies could allow to further investigate processes leading to slope failure, and eventual relationships to climate change.

3.4 Case study 2

After having tested our method on a sample of five different processes of slope instability, we validated it on a larger sample, including 41 rock-slope failures occurred in the last two decades at high elevation sites in the Italian Alps. The catalogue includes both rockfalls and rock avalanches occurred in the absence of an evident rainfall, seismic, or anthropic trigger. Hereinafter, for the sake of clarity, “rockfall” is used to refer to both rockfalls and rock avalanches.

As explained in Section 3.2 ,our main purpose was to provide a statistically based analysis of the main climate variables in the period preceding the rockfalls, aimed to detect anomalous values that can be deemed responsible for slope failure. We thus improved the method, on one hand, considering more parameters than before (i.e., mean, maximum and minimum daily temperature values), and on the other hand, associating the identified climate anomalies to spatiotemporal features of the events (characteristics of rockfalls, in terms for example of magnitude and temporal collocation), in order to have a more detailed overview of the processes behind rockfall initiation.

3.4.1 Study area

We focused on the whole Italian side of the European Alps. The Italian Alps extend for about 1200 km and cover 5200 km^2, 27.3 % of the European Alps. The tectonic units of the European Alps results in four parts: Helvetic, Penninic, Eastern and Southern Alpine. Western Alps result to be more compressed than the

eastern sector due to the collision between the African and European Plates. As a consequence, the western sector hosts the highest peaks, while the eastern sector has the greatest diameter. The Periadriatic Fault divides the Southern Alpine from the other three sectors. Permian volcanic rocks and Mesozoic sediments (limestones, dolomites, and volcano-detritic facies) overlap the crystalline basement. The Dolomites relief, dominated by mountain ridges up to 3400 m a.s.l., is mainly composed by Mesozoic sediments. The Western Italian Alps are mainly characterized by Penninic nappes; here, limestones, gneiss and granites predominate (Fitzsimons and Veit, 2001).

Glaciers on the Italian flank of the Alps are located mainly in the western and central regions. From the Little Ice Age (LIA) to 2000s, glaciers on the Alpine relief suffered a reduction of almost 50% (Zemp et al., 2006) with a significant peak on the western Italian side (Nigrelli et al., 2014).

According to the Alpine Permafrost Index Map, that shows a qualitative index describing how likely is permafrost to exist in the European Alps (Boeckli et al., 2012), Thirteen rockfalls occurred where permafrost is expected in nearly all conditions, while 18 occurred in areas where we expect permafrost only in cold (7) and favorable conditions (11). From studies carried out in the European Alps, permafrost on shaded slopes is present above 2500 m, whereas on S-facing slopes it is found above 3500 m (Fischer et al., 2012; Gruber et al., 2004b). Indeed, distribution of permafrost in high-elevated rockwalls is more complex, as shown by Magnin et al (2015b, 2015c) in the Mont Blanc massif. Climate in the European Alps depends on the complex interaction between orography and the general circulation of the atmosphere (Beniston, 2006). As a result, the Italian Alps show a high variability in the spatial distribution of temperature and precipitation, at regional and local scales (Auer et al., 2007; Brunetti et al., 2009). Referring to the regional scale, the climate regimes of the Western and Eastern Italian Alps differ significantly.

In relation to the 30-Year Climate Normals (1981-2010), the total annual precipitation that occurs in mountain areas of the Western and Eastern Italian Alps is about 850 and 1050 mm, respectively. Minimum (maximum) annual temperature is respectively -3 °C (5 °C) in the Western and -1 °C (8 °C) in the Eastern Italian Alps (Esposito et al., 2014). These temperatures refer to areal values, extrapolated using known observations recorded from the weather stations located in the area of interest.

3.4.2 Data

3.4.2.1 Rockfall catalogue

Our catalogue lists 41 rockfalls occurred in the 17-year period between 1997 and 2013 at high elevation (above 1500 m a.s.l.) in the Italian Alps (Table 3-5). The 41 rockfall events concentrate in two main geographical clusters. A first cluster corresponds to rockfalls occurred in the Western Italian Alps; a second cluster includes the rockfalls occurred in the Eastern Italian Alps. Only one case (the Thurwieser rockfall of 18 September 2004) is located in the Central Italian Alps (Figure 3-12). More specifically, the rockfalls concentrate in four mountain areas, including (i) the Mont Blanc Massif (4808 m a.s.l.), (ii) the Matterhorn Peak (4478 m a.s.l.), (iii) the Monte Rosa Massif (4637 m a.s.l.), and (iv) the Dolomites (maximum elevation: 3348 m a.s.l., Marmolada mountain group).

We constructed the catalogue consulting different sources, including national and local newspapers, journal articles, technical reports, and CNR IRPI archives (Figure 3-13). For most of the events (25) information on the slope failures was obtained in the framework of a national project aimed to collect information on slope failures in the period from 2000 and 2013 (Brunetti et al., 2015). Information on the magnitude is available for 26 rockfalls (63 %), which range in volume between 10^2 and 2 x 10^6 m^3 (Figure 3-12). The information on the volume comes from different sources, thus it is inhomogeneous for accuracy and level of detail. This is crucial, given the hankering for estimating rockfalls magnitude. In most cases, we do not know how volumes have been estimated. Nonetheless, a prevalence of large volume events, i.e. above or equal to 10^4 m^3, is detected in the western while small events, i.e. below 10^4 m^3, prevail in the eastern sector (respectively eight out of 14 and eight of 12 events with available magnitude data). All the events were located geographically using *Google Earth*. To select the events listed in the catalogue, we considered the availability of accurate information on the location and the time of occurrence of the failure, and the availability of a long-term record of climate data covering the date of the event.

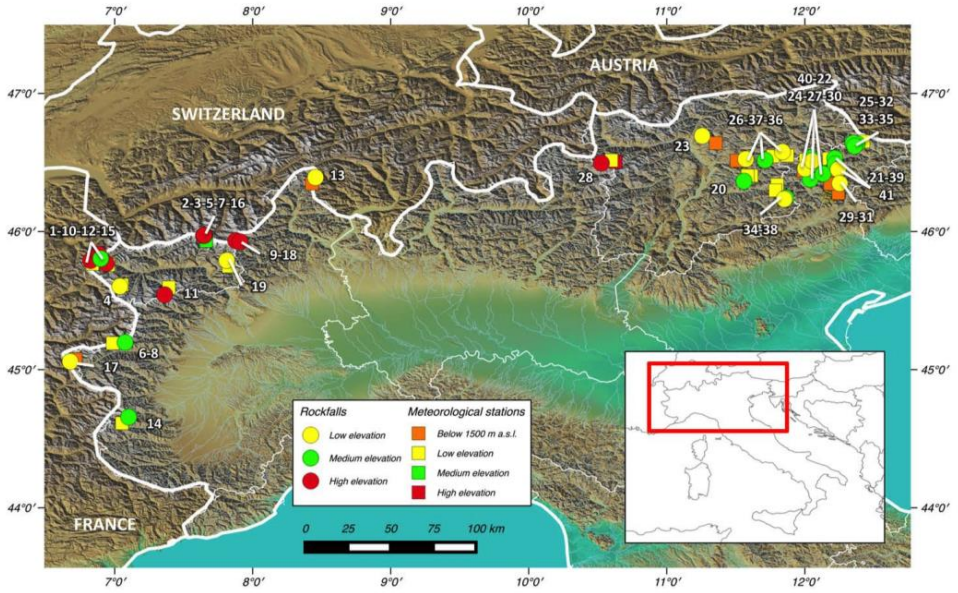

Figure 3-12 Map showing 41 events included in the inventory (dots) and of the 27 meteorological stations used in the study (squares). Events and meteorological stations are coloured differently according to elevation. Yellow dots/squares represent events/meteorological stations at low elevation (1500-2400 m a.s.l); green dots/squares represent events/meteorological stations at medium elevation (2400-3300 m a.s.l); red dots/squares represent events/meteorological stations at high elevation (3300-4200 m a.s.l); meteorological stations located below 1500 m a.s.l. are in orange. Events are numbered according to Table 3-5.

The sample size that we used for this work is relatively limited. This is due in part to the fact that the landslides that we are looking at i.e., rockfalls occurring at high elevation and not triggered by rainfall, earthquakes or human activities, are only a small subset of all landslides occurring in the Italian Alps (see e.g., Brunetti et al., 2015 and Stoffel et al., 2014). In addition, the acquisition of information about slope failures in remote areas such as high mountains is often difficult. Moreover, we are aware of the fact that our dataset may include inhomogeneities. Small-volume events are usually reported only if they caused some relevant damage and, for this reason, they are probably underrepresented in the dataset. Summer events are documented more easily than those occurring in the other seasons. Many of the documented rockfalls occurred in the most famous mountain ranges (Mont-Blanc, Monte Rosa, Dolomites), and this is due in part to the high frequentation and to increased media attention in these mountains.

Table 3-5 Main characteristics of the rockfalls and rock-avalanches considered in this inventory. Events are listed in chronological order. Lithology information are based on the Geological Survey geoportal (ISPRA, Italian National Institute for Environmental Protection and Research, http://sgi.isprambiente.it/GMV2/index.html) scale 1:100000, and on further research paper and reports. Type of failure: rock fall (RF), rock avalanche (RA). Wherever available, references have been reported. Cited references are: Barla et al., 2000 [a], Deline et al., 2011 [b], (Turconi et al., 2010) [c], Fischer et al., 2012 [d], Tamburini et al., 2013 [e], Fischer et al., 2013 [f], Sosio et al., 2008 [g], Chiarle et al., 2014 [h], ARPA, 2009 [i], Deline et al., 2008 [l], Deline et al., 2013 [m], Noetzli et al., 2006 [n], Viero et al., 2013 [m].

No.	Location	Date and time of occurrence (dd month yyyy) (UTC)	Location Elevation (m a.s.l.)	Latitude N	Longitude E	Aspect	Volume (m^3)	Lithology	Type of failure	Reference
	Western Italian Alps									
1	**Brenva**	18 January 1997	-	3725	45°50'10"	6°53'0.76"	SE	$2x10^6$	Granitoid rocks and crystalline schists	RA	[a] [n]
2	**Matterhorn I**	4 August 2003	night	3880	45°58'24.9"	7°38'54.67"	SW	10^2x10^3	Gneiss and micaschists	RF	[b]
3	**Matterhorn II**	18 August 2003	16:00	3770	45°58'22.28"	7°38'48.96"	SW	$2x10^3$	Gneiss and micaschists	RF	[b]
4	**Mont Pelà**	19 July 2004	-	2340	45°36'12.61"	7° 2'12.91"	E	$3x10^2$	Gneiss	RF	-
5	**Matterhorn III**	18 July 2005	15:30	3715	5°58'16.17"	7°38'36.21"	NW	-	Gneiss and micaschists	RF	[b]
6	**Rocciamelone I**	29 June 2006	after midnight	3100-3250	45°11'51"	7°04'30"	W	-	Phyllites and micaschists	RF	[c]

7	**Matterhorn IV**	25 July 2006	16:00	3750	45°58'22.57"	7°38'49.02"	SW	-	Gneiss and micaschists	RF	[b]
8	**Rocciamelone II**	26 December 2006	-	3100-3250	45°11'51"	7°04'30"	W	$>10^4$	Phyllites and micaschists	RF	[c]
9	**Belvedere**	21 April 2007	10:00	4200	45°56'3.05"	7°52'36.96"	E	$1.5x10^5$	Gneiss	RA	[d] [e] [f]
10	**Tré-la-Tête**	11 September 2008	7:00	3470	5°47'27.35"	6°49'29.52"	E	10^4-10^5	Gneiss	RF	[b] [l]
11	**Punta Patrì Nord**	18 September 2008	7:45	3200-3400	45°32'31.72"	7°21'40.22"	E	$1x10^5$	Tabular Gneiss		[b]
12	**Crammont**	24 December 2008	16:21	2400-2450	45°46'6.53"	6°56'16.24"	N	$5x10^5$	Conglomerates and beds of limestones, calceschists, molassic sandstones	RA	[b] [m]
13	**Val Formazza**	19 April 2009	9:00	1950	46°23'31.10"	8°27'16.58"	NW	10^5-10^6	Gneiss, calcshicsts and pelitic schists	RF	[i]
14	**Monviso**	26 July 2009	12:00	3133	44°39'24.21"	7° 6'2.29"	E	$2x10^3$	Phyllites and micaschists	RF	-
15	**Mont Rouge Peuterey**	13 August 2009	13:00	2941	45°48'14.67"	6°53'52.45"	SE	-	Granites	RF	-
16	**Matterhorn V**	28 August 2009	during the day	3880	45°58'24.49"	7°38'54.67"	SW	-	Gneiss and micaschists	RF	-
17	**Melezet**	21 May 2010	18:40	1500	45°3'29.83"	6°40'37.18"	E	$2x10^3$	Dolomitic	RF	-

									limestones and dolomites		
18	**Punta Tre Amici**	26 September 2010	late morning	3425	45°55'31.88"	7°54'27.50"	NE	$1x10^5$	Gneiss	RF	[f]
19	**Gressoney-Saint-Jean**	2 May 2013	late afternoon	2000	45°47'25.44"	7°48'40.37"	E	10^2-10^3	Gneiss	RF	-
	Eastern and Central Italian Alps										
20	**Latemar**	15 August 2000	17:20	2799	46°21'52"	11°33'33"	-	-	Limestones, dolomitic limestones	RF	-
21	**San Vito di Cadore**	30 October 2003	15:00	2460	46°29'24.06"	12°13'13.2"	W	$5x10^3$	Dolomites	RF	-
22	**Colcuc**	2 April 2004	1:30	1700-1800	46°27'18.15"	12°0'9.46"	W	10^3-10^4	Pyroclastics, tuffs, ignimbrites	RF	-
23	**Ivigna**	24 May 2004	afternoon	2050	46°41'33.17"	11°15'24.58"	-	-	Granitoid rocks	RF	-
24	**Torre Trephor**	13 June 2004	-	>2000	46°30'37.81"	12°3'8.83"	NE	-	Dolomites	RF	-
25	**Cima Dodici I**	1 July 2004	night	3094	46°37'6"	12°21'36.96	W	-	Dolomites	RF	-
26	**Forcella dei Ciampei**	1 July 2004	night	2366	46°34'38.22"	11°50'18.64"	N	10^2	Dolimites	RF	-
27	**Monte**	19 August 2004	16:00	2900	46°25'6.75"	12°7'54.95"	-	-	Dolomites	RF	-

	Pelmo										
28	**Thurwieser**	18 September 2004	13:41	3658	46°29'42.81"	10°31'32.23"	S	2-2.5x10^6	Dolomites	RA	[g]
29	**Monte Castelin**	21 September 2004	7:00	1580	46°20'56.00"	12°15'12.00"	W	-	Dolomites	RF	-
30	**Tofana di Rozes**	17 August 2005	13:00	2656	46°32'3.56"	12° 2'32.33"	SE	-	Dolomites	RF	-
31	**Monte Pelf**	23 April 2006	8:00	1400-1500	46°24'56.00"	12°8'9.00"	N	-	Dolomites	RF	-
32	**Cima Dodici II**	20 July 2006	10:00	3094	46°37'6"	12°21'36.96	W	1x10^5	Dolomites	RF	-
33	**Cima Una**	12 October 2007	8:40	2598	46°38'23.63"	12°20'57.70"	N	6x10^4	Dolomites	RF	[m]
34	**Cima Canali**	19 August 2008	11:45	2850	46°14'38.22"	11°51'49.31"	S	3x10^3	Dolomites	RF	-
35	**Cima Undici**	31 August 2008	afternoon	3092	46°38'8.09"	12°22'46.30"	-	3x10^2	Dolomites	RF	-
36	**Plattkofel**	19 August 2010	15:00	2650	46°30'59"	11°42'44"	NE	7x10^2	Dolomites	RF	[b]
37	**Euringer**	11 August 2011	6:30	2394	46°31'28.01"	11°34'19.56"	NE	2x10^3	Dolomites	RF	-
38	**Sass Maor**	21 December 2011	6:23	2200	46°14'5.64"	11°51'4.05"	E	-	Dolomites	RF	-
39	**Sorapiss**	30 September 2013	21:00	3150	46°31'50.90"	12°13'1.14"	N	4.7x10^3	Dolomites	RF	[h]
40	**Monte Civetta**	16 November2013	14:20	2600	46°22'41.18"	12°2'20.26"	NW	5x10^4	Limestones	RF	[h]
41	**Antelao**	22 November 2013	-	2050-2250	46°27'0.13"	12°14'30.52"	SW	-	Dolomites	RF	[h]

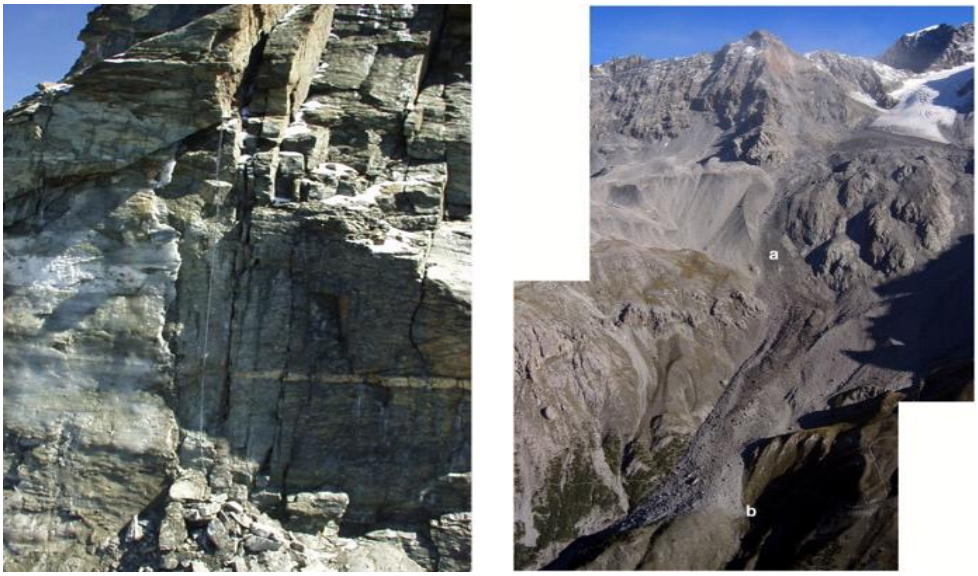

Figure 3-13 Selected examples of rockfall events. Left: Detachment area of the Matterhorn II rockfall (18 August 2003), with the ice lens (on the left) exposed by the collapse of the rock mass; photo source: L. Trucco. Right: Turwieser rock-avalanche (18 September 2004); photo source: Sosio et al., 2008.

3.4.2.2 Climate data

We considered climate data obtained from 87 meteorological stations pertaining to different networks in the Italian Alps, including networks managed by the Regional Environmental Protection Agencies (ARPA) in Piemonte, Lombardia and Veneto regions, the Centro Funzionale of the Regione Autonoma Valle d'Aosta, the Hydrographic Office of the Provincia Autonoma di Bolzano, and Meteotrentino, in the Provincia Autonoma di Trento. We used different types of climate data, including (i) mean, minimum, and maximum daily air temperature, and (ii) daily cumulated precipitation. In the Italian Alps, meteorological stations located above 1500 m a.s.l. are rare, and many of them were installed only recently. Therefore, climate records in high-mountain areas are limited and have a short duration in the study area. The limited geographical and temporal distribution of the climate information is the main constraint for the analysis of the climate conditions associated to the occurrence of slope failures at high elevation in the Italian Alps. For this reason, the first requirement for the selection of the meteorological stations for our analyses was the availability of a climate record covering the date of the failure and 90 days before it. We then considered only meteorological stations with a climate record exceeding 10 years. Since the elevation of the weather station is as important as its distance from the detachment area, weather stations have been selected in order to be close to it in terms of

altitude and planimetric distance. In the end, we used climate data from a total of 27 meteorological stations (Table 3-6); we checked the quality of all the climate data, to identify and remove possible erroneous values (WMO, 2011).

Table 3-6 Main characteristics of the meteorological stations considered in this study. Only meteorological stations representing the best compromise between the requirements mentioned in Sect. 3.2 (i.e., covering the failure date, long-term dataset, low distance from the failure area) are displayed. No.: failure point numbers (from Table 1) associated to the meteorological stations; variables recorded at the stations: *T* (temperature), *ΔT* (temperature variation between the day of the failure and the days before) and *R* (precipitation). Data source: ARPA Piemonte, 2014 (PIE); ARPA Veneto, 2014 (VEN); Centro Funzionale – Regione Autonoma Valle d'Aosta, 2014 (VDA); Ufficio Idrografico - Provincia Autonoma di Bolzano, 2014 (BUI); Meteotrentino, 2014 (MET).

Station name	**Location**	**Observation period**	**Data source**	**Failure point**	**Data source**	
	Elevation (m a.s.l.)	**Latitude (N)**	**Longitude (E)**	**(years)**		**(No.)**
Western Italian Alps						
Barcenisio	1525	45°11'30.34"	6°59'6.05"	1994-2013	PIE	6-8
Formazza-Bruggi	1226	46°20'51.60"	8°25'43.67"	1999-2013	PIE	13
Gressoney-Saint-Jean-Weissmatten	2038	45°44'54.41"	7°49'30.26"	2003-2013	VDA	19
Cogne-Lillaz	1613	45°35'43.03"	7°23'29.19"	2002-2012	VDA	11
Lex Blanche	2162	45°45'58.86"	6°50'17.84"	2002-2012	VDA	15
Passo del Moro	2820	45°59'53"	7°58'39	1988-2014	PIE	9-18
Pontechianale	1575	44°36'43.02"	7°03'9.07"	1993-2013	PIE	14
Prerichard	1353	45°4'29.91"	6°42'59.17"	1990-2013	PIE	17
Pré-Saint-Didier-Plan Praz	2044	45°45'28.76"	6°57'9.71"	1993-2012	VDA	1-10-12
Valgrisenche-Menthieu	1859	45°34'0.24"	7°12'30.19"	2001-2012	VDA	4
Valtournenche-Lago Goillet	2526	45°55'53.52"	7°39'45.46"	1942-2012	VDA	2-3-5-7-16
Eastern Italian Alps						
Campo di Zoldo	884	46°20'47.68"	12°11'3.14"	1993-2013	VEN	29

Caprile	1008	46°26’25.35”	11°59’24.13”	1993-2013	VEN	22-40
Corvara in Badia	1558	46°33’1.48”	11°52’23.71”	1956-2013	BUI	26
Faloria	2240	46°31’38.53”	12°10’30.22”	1993-2013	VEN	21-39-41
Fié allo Sciliar	840	46°30’48.24”	11°30’21.60”	1980-2013	BUI	37
Passo Falzarego	2090	46°31’7.20”	12°00’24.51”	1993-2013	VEN	24-26-30
Passo Rolle	2012	46°17’52.70”	11°47’13.10”	1980-2013	MET	34-38
Passo Costalunga	1750	46°24’18.27”	11°35’9.16”	1991-2012	MET	20
Passo Monte Croce Comelico	2150	44°41’21.99”	07°07’42.93”	1993-2013	VEN	25-32-33-35
Passo Valles	2032	46°20’18.20”	11°47’59.20”	1985-2013	MET	36-37
Sarentino	966	46°38’26.16”	11°21’18.36”	1977-2013	BUI	23
Selva Gardena	1570	46°32’44.16”	11°46’6.24”	1991-2013	BUI	36
Soffranco	605	46°16’41.03”	12°14’33.74”	1993-2013	VEN	31
Solda	1907	46°30’55.03”	10°35’52.53”	1971-2013	BUI	23-28
Solda Cima Beltovo	3328	46°30’10.37”	10°37’42.91”	1998-2013	BUI	28
Villanova (Borca di Cadore)	968	46°26’35.58”	12°12’22.52"	1993-2013	VEN	27

3.4.3 Results and discussion

3.4.3.1 Statistical analysis of climate variables

Results of the analysis of the climate variables considered for this work are presented in Figure 3-14 and in Table B-1. For the sake of clarity, Figure 3-14 reports only the climate anomalies detected for each event, while all probability values are fully reported in Table B-1. There, one can see that 34 (83 %) of 41 rockfalls considered in this work were associated to air temperature anomalies. For six rockfalls, a precipitation anomaly was detected, usually in combination with a temperature anomaly. The Brenva rockfall of 18 January 1997 is the only event in our catalogue that was associated solely to a precipitation anomaly. In six cases, the climate variables revealed no anomaly.

Temperature anomalies associated to rockfall occurrence were more frequently hot (53 %) than cold (35 %). In a few cases, both warm and cold temperature anomalies, at different temporal scales, were detected (12 %). Short-term temperature anomalies (ST) predominate (50 % of case studies) over long-term (LT) anomalies (15 %), but in many cases widespread temperature anomalies (WT) were detected (35 %).

Of the six rockfall events associated to a precipitation anomaly, three events were associated only to a long-term precipitation anomaly, and three events were associated to precipitation anomalies both at the weekly and at the monthly/quarterly scale.

Regarding the regional distribution of our case studies, we notice that four of the six events with no detected anomaly occurred in the Eastern Italian Alps. In the Western Italian Alps, 11 out of 19 rockfall events (58 %) were associated to warm temperature anomalies (in the short-term and/or long-term range), whereas in the Eastern Italian Alps only nine out of 21 events (43 %) were associated to warm temperature anomalies. Conversely, only five out of 19 rockfalls (26 %) were associated to cold temperature anomalies in the Western Italian Alps, and eleven out of 21 events (52 %) in the Eastern Italian Alps. Finally, four of the six rockfall events associated with a precipitation anomaly were located in the Western Italian Alps.

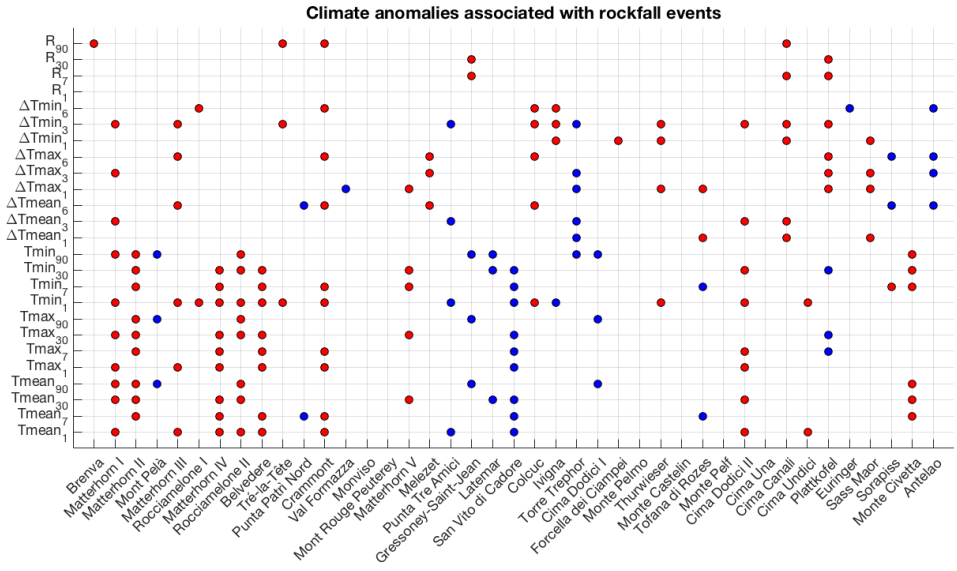

Figure 3-14 Estimation of the non-exceedance probability P(V) associated with the variable V, for each considered event. V may be temperature (T), precipitation (R) or temperature variation between the day of the failure and the days before (ΔT), and V is the correspondent value recorded when the failure occurred. The aggregation range is reported, i.e. daily range (1), weekly range (7), monthly range (30) and quarterly range (90) for T and R, while ΔT refers to the previous day (-1), three (-3) and 6 days (-6) before failure. Mean, max and min refer to mean, maximum and minimum average temperatures. Warm anomalies (P(V)≥1-α/2) are in red, whereas cold anomalies are in blue (P(V)≤α/2). Here, α=0.2. For precipitation, only probability values exceeding P(V)≥ 1-α/2 have been reported (in red).

3.4.3.2 Spatial and temporal distribution of rockfalls

The main characteristics of the spatial and temporal distributions of the considered events are listed in Table B-2 (Appendix B). Looking at the elevation of the detachment areas, we note that the events are evenly distributed among all elevation classes. As regards the season of occurrence, the summer events predominate and occurred mostly at elevation higher than 2400 m. All the spring events occurring at lower elevations, with the only exception of the Belvedere rockfall in April 2007. Both spring and summer events are equally distributed in the Western and Eastern sectors. Autumn events occurred mainly in the elevation range 2400-3300 m, and all have occurred in the Eastern Alps, except for the Punta Tre Amici rockfall on September 2010. Winter rockfalls are the less numerous group, they occurred all between mid-December and mid-January, and most of them are located in the Western sector of the study area.

While analysing the seasonal distribution of the events according to their volume, consider that information on the detached volume was available only for 26 rockfalls out of 41 (63 %). This is because the selected events often occurred in remote areas and caused no damage. It is likely that most of the processes for which we do not have this type of information are small-volume events ($<10^4$ m^3). Therefore, the number of small events is probably underestimated. Most of the small-volume events occurred during the summer, and none in the winter. Conversely, the large magnitude events show a quite homogeneous seasonal distribution. It is likely that the seasonal distribution of small events is influenced by the wider frequentation of mountain areas during the summer, which causes a higher probability of events and/or reporting. Finally, if we consider rockfall volumes versus elevation, we notice that small-volume events concentrate in the lower and intermediate elevation classes, while large rockfalls occurred mainly above 2400 m a.s.l.. The Val Formazza event of April 2009 is the only large event documented in the lower elevation class. If we analyse the case studies according to the probability of permafrost occurrence in the detachment zone, we get an information similar to that provided by the terrain elevation: small-volume events occurred in non-permafrost areas or where permafrost is expected only in favorable conditions, while larger events mainly concentrate in areas where permafrost is expected in nearly all conditions.

3.4.3.3 Climate anomalies and spatio-temporal distribution of rockfalls

Results of the bivariate statistical analysis are shown in Figure 3-15. The climate anomalies are grouped in the five types described in 3.2.1.2. Note that case studies showing both *R* and *T* anomalies were counted only once, in the RT group.

Results shown in Figure 3-15a highlight that half of the spring and autumn events are associated to a ST anomaly. Summer events occurred mainly in the presence of ST or WT anomalies. ST anomalies are both warm and cold, while WT anomalies are always warm. Conversely, LT anomalies, which were found only on occasion of summer events, are cold and are at the quarterly range. Winter events are associated to ST (Sass Maor, December 2011) or WT (Rocciamelone II, December 2006) anomalies, and/or to long-term *R* anomalies (Brenva, January 1997, Crammont, December 2008).

Considering to the elevation of the rockfall detachment zone (Figure 3-15b), low elevation failures occurred mainly in combination with ST anomalies. Events occurred in the mid-range class (2400-3300 m a.s.l.) are homogeneously distributed among all types of anomaly. However, they are also the most numerous group of events for which no anomaly was detected (four out of six

events). Most of the events that occurring at the highest elevations are associated to ST or WT anomalies, with warm anomalies that significantly outweigh cold ones. Interestingly, none of the failures that occurred in the highest range of elevation is exclusively associated to long-term T anomalies, or no anomaly.

With regard to the magnitude of the events (Figure 3-15c), there is no strong indication of a preferential distribution of small and large events among the different climate anomalies, even though small events are more numerous in the ST group, while large events are quite evenly distributed among ST, WT, and RT groups.

As for the probability of occurrence of permafrost conditions in the detachment zone, Figure 3-15d shows that eight events associated to WT anomalies occurred in areas where permafrost occurrence is likely. Conversely, in non-permafrost areas events mainly concentrate across ST anomalies.

Focusing on the type of climate anomaly, we can summarize the results illustrated in Figure 3-15 as follows. ST anomalies (both warm and cold) are preferentially associated to small-volume failures, occurring in any season at lower elevations (where no permafrost is expected). Only few events are associated uniquely to LT anomalies, which resulted to be always cold and at the quarterly range, and occurred during the summer. These events are located in the lower or medium range of elevation, where permafrost is absent or present only in cold conditions. WT anomalies (mainly of the warm type) are associated in particular to summer events, occurring at high elevation (in particular in the highest altitudes, where permafrost is present in all conditions) and that involve large volumes of rock. RT anomalies are associated to failures occurring in almost any season, of both small and large magnitude, mainly in the medium range of elevation, in variable permafrost conditions. Case studies associated to NO anomaly are mainly reported during the summer, at low or medium elevations.

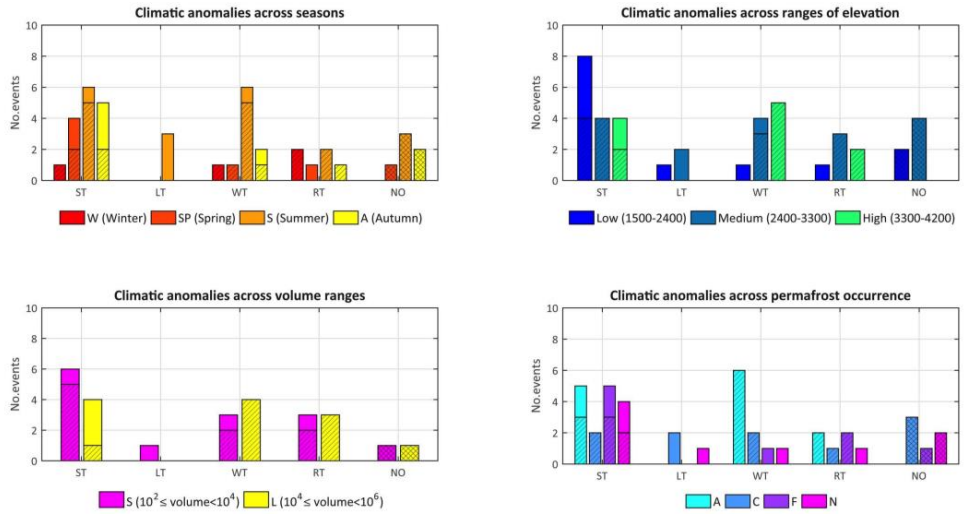

Figure 3-15 Distribution of rockfalls according to the type of climate anomaly, and considering: (a) the season of occurrence: W (winter), SP (spring), S (summer), A (autumn); (b) the elevation: Low (1500-2400 m); Medium (2400-3300 m); High (3300-4200 m); (c) rockfall volume: small-volume events (S, $10^2 \leq$volume$<10^4$ m^3), large-volume events (L, $10^4 \leq$volume$<10^6$ m^3); d) expected permafrost occurrence in the detachment zone: A (permafrost in nearly all conditions), C (mostly in cold conditions), F (only in very favourable conditions), N (no permafrost). Climate anomaly groups: ST: short-term temperature anomaly; LT: long-term temperature anomaly; WT: widespread temperature anomaly; R: precipitation anomaly (at the weekly range or longer) without or in association to temperature anomalies; NO: no anomaly. Warm T anomalies are highlighted with a strikethrough overlay.

3.4.3.4 Discussion

In the second part of this study, we have concentrated on those events that, based on the available documentation, occurred in the absence of evident rainfall. In this way, we tried to assess if temperature could be a key factor in the triggering of slope failures at high elevation sites, where the cryosphere plays a major role in geomorphological dynamics and where temperature trends should be almost unbiased. The most relevant outcomes of the statistical analyses on the considered rockfall inventory, based on the improved version of the method, can be synthetized as follows.

(i) In 85 % of our case studies, one (or more) climate anomaly was identified in association with rockfall occurrence.

(ii) Most of the rockfall events were associated with a temperature anomaly (34 cases out of 41). In most cases (30 out of 34) it was a short-term temperature anomaly, occasionally (12 cases) combined with a long-term temperature anomaly.

(iii) Surprisingly, temperature anomalies associated with rockfall occurrence were positive and/or negative, with only a slight prevalence of the positive anomalies;
(iv) Only six rockfalls (15 %) were associated to exceptional precipitations in the medium/long term (i.e., 7-90 days before the failure).
(v) Timing and conditions of rockfall initiation differ in relation to the elevation altitude. At lower elevation (1500-2400 m), rockfalls occurred mainly in spring, and were mostly associated to negative temperature anomalies. At medium elevation (2400-3300 m), rockfall events concentrated in summer and positive temperature anomalies prevail with the negative anomalies. In this altitudinal range, we find the largest number of events not associated to climate anomaly. Summer events prevail also at the highest elevations (>3300 m), mostly in association with positive temperature anomalies.
(vi) In the Western Alps, rockfalls associated with warm air temperatures predominate, whereas in the Eastern Alps rockfalls are often associated to very cold conditions.

At higher altitude (above 3300 m) rockfalls documented since 2003 were mainly associated to positive temperature anomalies. Thus we can suppose that permafrost and cryosphere degradation induced by climate change could have a major role in the initiation of these events. At lower altitudes, the impact of climate change on slope stability, if it exists, must be sought in more complex processes (e.g., change of the snow/rain ratio, increased temperature variations with more frequent cycles of snowfall/snowmelt and of freeze/thaw in the rock slopes).

Looking to regional differences, the role of different lithology and topographic settings in the rockfall occurrence have to be considered analyzing the results. As can be seen in Table 3-5, most of the events occurred in gneisses and schists in the western sector, while dolomite is the prevalent lithology in the eastern one. We have to note that we refer to lithology maps at 1:100000 scale and, only when specific studies are available, a better level of detail could be provided. Thus, we had to adopt generalizations that could lead to a certain level of error considering that similar lithologies may be characterized by different geotechnical features (Fischer et al., 2012). However, this is not the focus of our study, since we concentrated on climate anomalies potentially leading to failure. Nevertheless, a more detailed study on the lithological and geomorphological features could be of help in the understanding of predisposing factors, which could be useful to explore in future studies.

Keeping in mind this point and considering the different elevation of occurrence of the listed rockfalls, we can suppose that slope failure occurrence in the Eastern Alps could be mainly attributed to water pressure increase inside the slopes; it may be related to freezing of water springs along the slopes, and/or by repeated cycles of snowfall/snowmelt, especially in autumn. In the Western Alps, instead, slope failures could be ascribable to the build-up of water pressure in the rock masses due to accelerated snowmelt and/or permafrost thaw. The differences may be ascribed to the typical topographic settings of the two sectors as well. In particular, the Western Italian Alps host the highest peaks in the study area (e.g., Mont Blanc, 4810 m, Monte Rosa, 4637 m, Matterhorn 4478 m), where we expect permafrost in all conditions. Peak elevation in the Eastern Alps is much lower (Tofana di Mezzo, 3245 m, Sorapiss, 3205 m, Cima Undici, 3092 m) and permafrost is expected only in cold or favourable conditions. Moreover, previous studies highlight that discontinuous permafrost could be found at different elevations, depending on the direction, i.e. at higher locations (around 3500 m a.s.l.) in southern aspects and at lower locations, from about 2500 m a.s.l., on NE, N, NW and W facing slopes (Fischer et al., 2012; Gruber et al., 2004b). This is in agreement with the fact that rockfalls in the Dolomites concentrate mostly on northern aspect (13 out 18 events in the eastern sector with available information on aspect), where permafrost could be found only in cold or favorable conditions.

The type of temperature anomaly detected influence differently the mechanism of failure. Warm temperatures could enhance permafrost thaw and snowmelt at higher altitudes or cause melting of early snowfall at lower elevation. Cold temperature anomalies may cause the blockage of groundwater flow and the build-up of high water pressures inside the rock mass. Some interesting insights could be made on the spatial distribution of the anomalies. Based on the results of the extended dataset, rockfalls in the Eastern Alps are mainly related to cold temperature anomalies, while in the Western Alps slope failures are mainly associated with warm temperature anomalies.

By analysing the type of the detected climate anomaly(ies) in combination with spatio-temporal characteristics of the individual rockfalls, we attempted to provide some possible explanation on the temperature-related processes that may have caused the slope failures. Details on this case-by-case analysis are listed in Table B-2 (Appendix B), below we give general comments:

(i) Permafrost thawing, necessarily related to a long-term (or wide-spread) positive temperature anomaly, seems to contribute to slope failure only at the

highest elevations (>3300 m), and only as a predisposing factor. Our findings are in agreement with previous studies which pointed out that climatic variations over long-term period could destabilize greater depths of the rock mass (Fischer et al., 2012; Gruber and Haeberli, 2007). The linkage between processes at high elevation sites and permafrost degradation has already been highlighted by several authors, who have reconstructed and described the events included in our catalogue e.g., Matterhorn events (Deline et al., 2011), Belvedere and Punta Tre Amici events (Fischer et al., 2013).

(ii) Positive ST anomalies may have contributed to rockfall triggering in multiple ways. In spring and early summer, they may have increased the snow cover melting (Cardinali et al., 2000; Saez et al., 2013). In summer, they may have enhanced the ongoing process of active-layer thickening (Gruber et al., 2004b; Gruber and Haeberli, 2007; Harris et al., 2009). In autumn, warm temperatures may have caused melting of an early snowfall, or precipitation to fall as rain rather than as snow. In particular, infiltration of water into the bedrock fractures due to rainfall or particularly when near-surface ice/snow is available for melt (because of rain-on-snow process or high temperatures melting early snowfall) may reduce the shear strength of the rock mass potentially leading to the failure (Allen and Huggel, 2013; Fischer et al., 2010). These results are in agreement with the outcomes Weber et al. (2017) who investigate the role of thermo-mechanical forcing on displacements in steep fractured bedrock permafrost, by means of a systematical analysis revealing reversible and irreversible deformations. Based on their outcomes, the combination of increased shear stress and decreased shear resistance due to thermo-elastic oscillations could affect significantly slope instability in fractured bedrock in permafrost areas. Based on their systematical analysis, irreversible hydro and cryogenic deformations occur respectively in thawing and freezing periods, resulting in outward deformational peaks. Also Collins and Stock (2016) achieve a similar conclusion, even if in different environments. The authors investigate the role of daily, seasonal and annual temperature fluctuations in driving cyclic and cumulative opening of esfoliated fractures. Their results show that the warmest times and period of the day/year can lead to deformative peaks in the rock mass and that the cyclic thermal stressing could increase the effect of other relevant triggering factors.

(iii) More complex is the interpretation of the role of the positive ST and WT anomalies that are usually associated to winter events. In these cases, it is likely that temperature, though higher than the average, was well below 0 °C at the time of failure. In this case, also winter precipitation values must be

assessed with care, due to rain gauge measure errors mainly related to undercatch bias. As in the case of Brenva rock avalanche, we can hypothesize that the combination of more processes could have a major role in such type of events. As in Magnin et al. (2015a), warm propagation from the rockwall surface to depth (which is maximum in October, because of thermal inertia) and almost concomitant surface refreezing (Gruber and Hoelzle, 2008; 2015a) could be responsible for further groundwater pressure increase, leading finally to failure.

(iv) Negative ST anomalies may have been responsible for rockfall triggering by freezing the water springs along the slope, thus causing the blockage of ground water flow and the build-up of water pressure in the rock masses leading to slope failure (Fischer et al., 2013; Govi et al., 1993; McSaveney and Massey, 2013).

(v) Small volume events are supposed to be more influenced by near-surface dynamics, related to a faster response to climatic variables variations. On the other hand, large-volume events involve greater depths, as a consequence of complex and gradual processes, mainly linked to longer-term climatic anomalies (Allen and Huggel, 2013); in that case, a longer-term analysis (that means decadal/centennial scales) would be necessary.

In order to properly consider the outcomes of this study, some important constraints of our work have to be kept in mind. Our method may not have detected all possible climate anomalies associated with the onset of the slope failures. To refine the results, or to use the method for different purposes or in different geographic settings, the method can be composed and/or integrated with further variables and analysis, e.g. considering different temporal aggregations scales. The use of a fixed temporal aggregation could somehow limit our knowledge on the mechanisms of failure. Indeed, the method as is does not allow to detect possible climate anomalies in periods others than the considered aggregation scales (e.g., 1, 7, 30, 90 or 1 to 6 days depending on the variable *V*). The use of moving windows could be of help in this catching, for example, a possible succession of warm and cold periods in the period prior to the event, that could not be detected using fixed temporal aggregations.

Another relevant advantage of the method is that the uncertainty related to lapse rate assessment could be in part neglected. Data extrapolation to the location of failure occurrence may be very problematic, as lapse rates in high mountain environments are highly variable in space and time (Nigrelli et al., 2017; Kirchner et al., 2013). Even if translated temperatures could be of help as to have an idea

about what sort of temperatures are experienced at the elevation of the slope instability, this could introduce further bias in our records, since the uncertainty in estimates of the thermometric conditions at high-elevation rock fall sites strictly depends on local site characteristics, season and the type of parameter considered. For this reason, we preferred not to base our analyses on translated temperatures, as explained in Section 3.2.

Attention must be also paid to the quantitative estimation of other climate variables in high latitudes and mountain regions. In the currect context of climate change, precipitation is subjected to a larger spatial variability, even more evident for short-duration rainfall. Despite the wide range of new technologies performed worldwide for the characterization of the spatio-temporal distribution of convective systems (Libertino et al., 2016), one of the main issue still is the quantitative detection of extreme rainfall in mountanous regions, where the gauge density is smaller and where the complex topography and morphology reduce the chances of observing extreme rainstorms (Isotta et al., 2013). As in the case of Castelfranco debris flow (FP5), data recorded by Rifugio Zamboni were very different from those of Passo del Moro. Coupling remote sensing data and the discrete information provided by the rain gauges does not allow to determine which one of the two weather stations was representative. Surely further developments are needed and new technologies aimed to overcome the problems related to the estimation of rainfall events in ungauged areas are in progress (Allamano et al., 2015).

Considering winter (e.g., Brenva) and also early spring events, the reliability of winter season precipitations recorded at high elevation stations should be analysed by considering undercatch bias. Rain gauge precipitation measurements, in fact, are prone to undercatch of precipitation, due to wind-induced turbulence (eddies) over the gauge orifice, snow overtopping of the gauge, along with wetting and evaporative losses (Groisman and Legates, 1994). Heated rain gauges, wherever available, are preferred since they can provide more accurate snowfall measures, even if under-catch problems are not totally eliminated. On the other hand, snow depth measurements say little of the snow water equivalent of a snowfall. Other techniques have been developed to overcome problems related to precipitation record errors and in order to gather combined precipitation measures (Allamano and Claps, 2010). As I had occasion to note in the framework of a long experimental campaign aimed to define the Snow Water Equivalent at high-elevation sites, understanding these errors is important for correct interpretation of snowfall and SWE measures and for the successful

assimilation of such data into models and analysis. Thus, further developments of the method will take more into account these limits, in order to better interprate such type of events in the curret context of climate change.

The method is not an operational tool for landslide (rockfall) forecasting (as for example Manconi and Giordan, 2016); i.e. it does not provide thresholds for rockfall initiation. In order to do so, it would need to be further validated on a larger dataset and with a false positive analysis, i.e. the analysis of the number of times that a climate anomaly was detected and no slope instability occurred. However, this validation could prove difficult for high-elevation areas, where slope failures are only seldom reported. The method is instead intended as a tool for assessing the possible role of climate parameters and especially temperature, in slope failure occurrence.

As far as concern the dataset, we are aware that the number of rockfalls included in our catalogue is limited from a statistical point of view. In this light, since our main requirements while collecting data for our study were the knowledge of the failure date and of the (at least indicative) location of the detachment zone, together with the availability of climate records covering the failure date, only part of the rockfall events that we collected could be used for this work. Moreover, we have to keep in mind that inhomogeneities related to data acquisition timing and relevance of the event exist (e.g. summer events are more documented due to tourism increase in summer months as well as large-volume events). Finally, many news come from newspapers and may contain inaccuracies, which are not always simple to identify and connect.

However, we point out that only a few inventories of this type are available in the literature, and their size and systematic nature are comparable to that of our dataset (Allen and Huggel, 2013; Allen et al., 2010; Fischer et al., 2012; Noetzli et al., 2003; Ravanel et al., 2010). Data collected in the inventories are the result of years of documentation, field surveys, and remote sensing. It is unlikely that the number of events listed in the catalogue will increase substantially in the next few years, considering the remoteness and the low frequentation of high mountains, unless new techniques will become available to support this type of studies (e.g. Manconi et al., 2016). The straightest way to overcome these difficulties would be the combination of datasets from different mountain areas of the world, for example including data catalogue of rockfalls in the Mont Blanc massif, where a great number of rockfalls has been surveyed from 2007 (Ravanel et al., 2010), or in the Swiss Alps. This approach would give more strength and robustness to the

statistical analysis, even if one will always inevitably cope with small numbers of case studies, compared to other types of processes or other geographic settings. Moreover, merging catalogues from different sources would require that the collection of geologic and climate data be done according to common standards. Gridded data could be of help in overcoming inconsistencies in the lack of climate data, but the spatial and temporal resolution of the dataset has to be considered, since usually they include data with a large geographic extension and on a long term. Certainly, the creation of shared dataset at European scale would be a crucial and exciting point to be addressed in the future, but it has to be done through the direct involvement of the scientists who worked on such data and not simply combining different inventories. This is not the case at the moment, despite a few attempts in this direction conducted in the framework of international projects (Deline et al., 2007).

Chapter 4

4 Conclusions

The research activity outlined in the present thesis deals with several facets of air temperature variations (Chapter 1). In the first part of this study (Chapter 2), we investigated the role of non-climatic forcing affecting temperature trends at regional and global scale. We concentrated on the potential role of Urban Heat Island and urbanization in affecting temperature records. In the second part (Chapter 3), we focused on those environments where the effects of land-use and land-cover changes are minimum, i.e. the mountainous regions. More in detail, we investigated the possible implications of changes in climate variables on geohazards related to cryosphere degradation. Hereinafter, the main conclusions of this study are presented, by re-connecting to the main research questions that drove this work.

Is it possible to disentangle the environmental and climatic factors behind trends in air temperature records at the global scale? More specifically, what is the effect of urbanization dynamics?

As outlined in Chapter 2, a major concern in the analysis of global and regional temperature trends is the fact that most part of temperature stations are located in or near deeply anthropized areas. Urban stations, which are overrepresented at global scale, could experience local warming as a consequence of land-use/cover changes in the surrounding areas, due to urbanization. From a statistical point of view, this could introduce bias in the temporal trends, affecting temperature analyses. The novelty of the work presented in Chapter 2 is in the fact that the nexus between air temperature variations and land-use changes could be

investigated through the use of nighttime satellite images as proxy of urbanization.

We demonstrated that it is possible to statistically infer a relation between temperature and nightlights trends. For this purpose, an extended dataset of more than 28000 temperature stations in the period 1992-2013 has been considered, in order to achieve the best compromise between the fine spatial and temporal resolution of nightlights images and the availability of suitable temperature long-term series. Trend analyses reflect the tendency of temperature to rise at a faster rate in areas of increasing nightlights, that should be linked to growing urbanization in those sites. The methods proposed to investigate the significance of such trends have shed light on interesting differences on regional distribution of nightlights and temperature trends. Moreover, analyses with larger spatial buffers, including also areas located up to 5 km far from urban weather stations, confirmed this trend. Anthropogenic pressure still grows towards neighbours, and most part of suburbs areas continue to experience warming relative to nearby rural sites (Nel·lo et al., 2017).

Our findings confirm a positive concordance almost worldwide, except for regions where patterns of change in nighttime brightness are more complex, especially in developed countries (Bennie et al., 2014). As already pointed out in recent studies (Ceola et al., 2014; Chen and Nordhaus, 2011), the use of nightlights as proxy of urbanization could provide interesting information on the economic features of the considered continents. Regions underpinning rapid urbanization as Africa and Asia reveal a significant positive concordance, i.e. a significant temperature trend in areas of increasing brightness. In these cases, the inclusion of more and more weather stations from rural surroundings to more anthropized areas, could somehow determine a microscale environment close to the measurements stations, which significantly impact the observed temperature. More developed continents show instead more complex patterns. As an example, in well-established urbanized city centres anthropogenic heat inputs, and thus UHI, could be considered stable in recent decades (Wickham et al., 2013), and thus an evident relation between variations in time of temperature and nightlights is not detectable (Parker, 2010).

What are the main limiting factors of this analysis?

As anticipated in the previous paragraph, a series of factors could somehow influence the final outcomes and thus the perception of UHI. These

are mainly ascribable to economical and environmental strategies undertaken by the different countries. As an example, light reduction policies promoted in many North Europe and North American countries could have influenced nighlitghts trends, making more complex the interpretation of urbanization dynamics on temperature trends (Cauwels et al., 2014). Therefore, if not considering these aspects, these results may lead to the perhaps misleading conclusion that *T* increases independently of the entity of urbanization, thus suggesting a minimum UHI effect in some regions as, for example, North America and part of Europe. This is not confirmed by analyses worldwide, where the increment of nighttime luminosity tendency, and therefore of urbanization, seem to be of value in explaining temperature variations.

Natural mesoscale effects could influence the interpretation of anthropization feedbacks on temperature. As an example, in South America we detected unexpected negative temperature trends in areas of increasing luminosity. This pattern could be somehow related to the intensification of the South Pacific Anticyclone, contributing to the air temperature cooling of the Chilean coast (Falvey and Garreaud, 2009).

What questions remained opened?

In response to the research questions raised at the beginning of this thesis, we can say that implications of urbanization on temperature on a global scale still remain difficult to be fully interpreted, not without controversy. In this study, we basically explored the possibility to relate temperature increase in the last decades to the incorporation of weather stations in urbanized area by means of urbanization proxy as nighttlights. The further step will be a quantitative estimation of the Urban Heat Island contribution to air temperature records, at global and regional scale, by comparing temperature trends in presence/absence of luminosity. We expect that part of temperature increase would be absorbed by effects of urbanization. This could be a further step towards the quantitative assessment of the influence of urban heating on warming trends, and will represent the object of future analyses. Obvously, the comparison with previous studies on this issue will provide us with the basis for further insights. Indeed, several previous works account for UHI effect on their analysis, trying to remove or minimise to the greatest possible extent the influence of such effect on broader scales. Most part of these works came to the conclusion that UHI contamination from urban stations can explain very little of the recent global warming (Hausfather et al., 2013;

Peterson et al., 2005; Wickham et al., 2013), whereas it tends to be crucial at smaller scales (Parker, 2010).

Based on the outcomes of Chapter 2, further developments will be aimed at defining how much of temperature rise is effectively related to global warming and what is due to land-use changes. A wide and a robust assessment of climate warming should not neglect the understanding of the impacts of land-use/cover change worldwide. At this point, we wonder what effectively are the effects of temperature rise regardless of bias due to urban heating. In this light, high-elevation sites offer more than one possibility for our study, since they are i) almost uncontaminated from urbanization and ii) particularly sensitive to temperature variations. There, temperature trends should be almost unbiased from a land-use change point of view.

We thus wonder if is it possible to quantitatively assess the role of temperature rise in the increased slope instability activity documented in recent decades. Can temperature be considered as a potential driver of slope-failures at high-elevation sites?

In Chapter 3, we concentrated on the role of air temperature variations on cryosphere dynamics, in combination or not with precipitation. In this context, the statistical method used proved to be a valuable tool to discriminate whether, and which, climate variables may have contributed to rockfall initiation at high elevation in recent years. The focus is on the initiation phase, i.e. on the comparison between the climate conditions typically occurring in the failure area and those occurring in the period immediately before the event. The method can be applied to a wide range of climate parameters, to any process of instability, and in any geographical context, given its schematic nature and the simplicity. We first analysed only mean air temperatures, because the latter provides a preliminary and general idea about the considered events, and it is easily available even in places where detailed data are scarce. In a second time, we also considered maximum and minimum daily temperatures, in order to deepen our knowledge on the mechanisms that triggered failure. In this work, we focus on the time of occurrence of rockfalls (i.e. “when”) rather than on the characterisation of the failure area (i.e. “where”). The interpretation of failure mechanisms and/or the geological/structural characterisation of the detachment areas go beyond the purposes of this work. We rather aim to catch a possible climatic signal at different timescales, which could be related to rockfall occurrence.

Out of the five case studies whereon the method has been first tested, four can be associated to outliers of climate values prior to the event, with respect to the climate conditions tipically present in source areas. Results obtained on the extended dataset confirm this aspect: in the absence of a clear rainfall trigger, temperature is a key factor controlling rockfall occurrence in the Italian Alps. These results are in agreement with recent studies (Collins and Stock, 2016; Weber et al., 2017), which highlight the role of thermal stressing at different temporal scales in unstable rock masses. Indeed, daily and seasonal cycles of warming-cooling could progressively affect the thermal-mechanical characteristics of steep fractured bedrock, leading to failure. According to the authors, both temperature rise and variations could play a major role in rockfall iniation, representing a possible explanation for those events that does not have a clear trigger, despite the availability of full and detailed documentation.

What are the most critical points in this study?

It should be pointed out that a main constraint when studying processes occurring in the alpine environment is represented by the location of weather stations, as only a few of them are located at high altitude and have only coverage for the last 10 years. Nevertheless, in the last decades, the weather station density at high elevation has significantly increased in the Italian Alps, allowing to increase knowledge about climate observational issues. The issue of the reliability of climate data in the Alpine area is even more complex if considering the heterogeneity of available measurments and the large spatial variation of other associated climate variables as precipitation (Isotta et al., 2013). Moreover, the fragmentation into multiple regional and national datasets and the different methodological approaches performed complicate the climatological overview (Isotta et al., 2013; Merlone et al., 2015). The lack of long-term historical data series could be in part overcome by using climate data recorded by delocalized weather stations, i.e. far from the study area. However, this means, most of times, relying on temperature data that are not fully representative of the climate conditions in the detachment area, thus introducing a degree of uncertainty in the analyses. The capacity of the method proposed in Chapter 3 to provide useful and significant results will of course improve by increasing the data availability, but its ability to work also with short time-series is a crucial feature.

The focus is on the final initiation phase, i.e. on the comparison between the climate conditions typically occurring in the failure area and those occurring in the period immediately before the event. For the sake of clarity, we thus

distinguish between short-term (days/weeks) and long-term (months) analyses. Based on previous studies (Govi and Sorzana, 1980), the choice of a 90 days term is considered as critical for the preparation of rainfall-induced landslides. In a first attempt, since we have no idea of what kind of climate anomalies could have occurred and performing the method as a bottom-up approach, we decided to consider a three-months period as suitable for the temperature parameter, as well. Obviously, the method as is does not allow catching all possible processes taking place in the preparation phase of the slope failure; in that case, a longer-term analysis (that means annual/decadal/centennial scales) is needed.

What are the remaining open questions on this issue?

Our results represent a potential explanation for those failure processes that do not have any clear recognized trigger despite detailed documentation and observation in the lead-up of the slope failure. The method allows one to detect the anomalies in temperature and precipitation values that are associated to the development of these slope instabilities, providing the ground for discussion of possible causes and triggering mechanisms, also in the framework of ongoing climate change. However, how climate anomalies could effectively impact on triggering mechanisms is still an open question. The considerable number of events associated with cold anomalies (in particular in NE Italy) would suggest that the role of global warming is not so evident, but it offers interesting insights in the study of the linkage between climate variables and landslide initiation. Our study also demonstrates that the type of temperature anomaly, and thus how temperature controls rockfall occurrence, was very different from case to case.

Additional developments are needed, as highlighted in Chapter 3, including: i) increasing the catalogue size, aimed to guarantee the robustness of the analysis; ii) improving the method by adding further variables and flexible aggregation scales; iii) paying attention to inhomogeneities related to data acquisition and processing at high-elevation sites. In this light, the method presented here is a preliminary step towards a characterisation and quantification of the impacts of climate change on slope instability in mountain areas and towards a definition of hazard scenarios under the present climate change.

Finally, what we can say about the role of air temperature worldwide and about its interactions with land-use change and natural (rockfall) hazard?

A multifaceted analysis, as we did in this work, allows one to face the problems from different perspectives. On the one hand, the combination of remote

sensing techniques and statistics to investigate the role of increasing human pressure and land-use changes on urban warming dynamics provides interesting insights on the assessment of the effective perception of climate warming worldwide. On the other hand, the study of mass-wasting processes (rockfalls) as terrestrial indicators of climate change reveal that global warming could have a major role in their initiation/preparation, also in the absence of overestimation factors, as UHI. In this context, station location, as well as the quality of records, are fundamental, since the assessment of atmospheric warming effects on natural systems is a matter of having reliable and (as possible) unbiased climate data (Merlone et al., 2015). With a reverse approach, further developments could be focused on the analysis of natural hazards in developing and emerging regions, which are more affected by urbanization dynamics. This could allow one to verify the authenticity of climate data recorded by land-based stations and to guarantee a robust assessment of air temperature variations patterns worldwide.

Appendix

A Further analyses on the effects of urbanization on temperature records

In this section we report all the outcomes for the main dataset, i.e. the Quality Controlled dataset, which includes quality-checked data.

First we include further otucomes of Quality Controlled dataset, more in detail: (i) tabular outcomes of average temperatures with 1 km spatial buffer, referring to graphs from Figure 2-27 to Figure 2-30; the graphical and tabular outcomes of (ii) minimum temperatures with 1 km spatial buffer, (iii) average temperatures with increasing spatial buffers from 2 to 5 km, (iv) minimum temperatures with increasing spatial buffers from 2 to 5 km.

Subsequently, we report the main outcomes of the analysis on the other two analysed dataset, i.e. fully-quality checked (Breakpoint Corrected) and raw (Single-Valued) data. More in detail, we include for both datasets: (iv) average temperatures with 1 km spatial buffer for Breakpoint Corrected data; (v) average temperatures with 1 km spatial buffer for Single-Valued data; (vi) minimum temperatures with 1 km spatial buffer for Breakpoint Corrected data; (vii) minimum temperatures with 1 km spatial buffer for Single-Valued data.

A.1 Results of Quality Controlled dataset – Average Temperatures

Table A-1 Method 1 statistics; *w* refers to the probability of occurrence of classes of significance from 1 (++) to 4 (--); V_T: variable temperature *T*; V_{DN}: variable nightlights *DN*; CI: concordance index; E(CI): expected mean of CI; σ(CI):standard deviation of CI; z: standardized value; $E(V_T)$, $E(V_{DN})$, $\sigma(V_T)$ and $\sigma(V_{DN})$ refer to expected mean and standard deviation; *n*: total number of stations; $n_{filtered}$: same as *n* excluding stations with *DN* trend equal to 0 (dataset: average monthly temperatures, Quality Controlled, 1 km buffer).

	World	**Asia**	**North America**	**Europe**	**Africa**	**South America**	**Oceania**
CI	-0.007	0.223	-0.18	0.033	0.439	0.09	0.022
E(CI)	-0.03	0.18	-0.16	0.01	0.43	0.05	-0.01
σ(CI)	0.01	0.02	0.01	0.02	0.06	0.04	0.05
σ^2(CI)	0.0001	0.0004	0.0001	0.0003	0.0028	0.0022	0.0019
z	2.6	2.2	-1.6	1.1	0.1	0.9	0.7
$E(V_T)$	0.39	0.42	0.34	0.44	0.65	0.10	0.59
$\sigma(V_T)$	0.64	0.65	0.65	0.55	0.56	0.71	0.62
$\sigma^2(V_T)$	0.41	0.42	0.43	0.30	0.31	0.50	0.38
$E(V_{DN})$	-0.08	0.43	-0.47	0.03	0.66	0.49	-0.01
$\sigma(V_{DN})$	0.83	0.77	0.66	0.80	0.58	0.70	0.80
$\sigma^2(V_{DN})$	0.68	0.59	0.44	0.64	0.34	0.49	0.63
$w_{T(1)}$	35.1%	40.8%	30.9%	30.6%	61.9%	22.5%	59.7%
$w_{T(2)}$	39.5%	33.7%	41.9%	48.8%	24.5%	32.4%	20.8%
$w_{T(3)}$	19.4%	20.2%	18.9%	19.0%	10.1%	32.9%	16.1%
$w_{T(4)}$	6.0%	5.3%	8.3%	1.6%	3.6%	12.1%	3.4%
$w_{DN(1)}$	27.1%	56.0%	7.8%	27.3%	66.2%	57.8%	24.6%
$w_{DN(2)}$	17.4%	15.4%	14.3%	24.6%	18.7%	16.2%	25.0%
$w_{DN(3)}$	24.4%	14.7%	31.0%	23.7%	11.5%	19.1%	23.7%
$w_{DN(4)}$	31.1%	13.8%	46.9%	24.3%	3.6%	6.9%	26.7%
n_{tot}	5530	1219	2673	1033	146	175	268
$n_{filtered}$	4974	1153	2272	994	139	173	236

Table A-2 Method 2 statistics, legend as in Method 1 (dataset: average monthly temperatures, Quality Controlled, 1 km buffer).

	World	**Asia**	**North America**	**Europe**	**Africa**	**South America**	**Oceania**
CI	-0.007	0.223	-0.18	0.033	0.439	0.09	0.022
E(CI)	-0.03	-0.03	-0.03	-0.03	-0.03	-0.03	-0.03
σ(CI)	0.01	0.02	0.01	0.02	0.05	0.05	0.04
σ^2(CI)	0.0001	0.0003	0.0002	0.0004	0.0028	0.0022	0.0016
z	2.6	13.9	-12.6	3.3	8.7	2.6	1.2
E(V_T)	0.39	0.39	0.39	0.39	0.39	0.39	0.39
σ(V_T)	0.64	0.64	0.64	0.64	0.64	0.64	0.64
σ^2(V_T)	0.41	0.41	0.41	0.41	0.41	0.41	0.41
E(V_{DN})	-0.08	-0.08	-0.08	-0.08	-0.08	-0.08	-0.08
σ(V_{DN})	0.83	0.83	0.83	0.83	0.83	0.83	0.83
σ^2(V_{DN})	0.68	0.68	0.68	0.68	0.68	0.68	0.68
$w_{T(1)}$	35.1%	35.1%	35.1%	35.1%	35.1%	35.1%	35.1%
$w_{T(2)}$	39.5%	39.5%	39.5%	39.5%	39.5%	39.5%	39.5%
$w_{T(3)}$	19.4%	19.4%	19.4%	19.4%	19.4%	19.4%	19.4%
$w_{T(4)}$	6.0%	6.0%	6.0%	6.0%	6.0%	6.0%	6.0%
$w_{DN(1)}$	27.1%	27.1%	27.1%	27.1%	27.1%	27.1%	27.1%
$w_{DN(2)}$	17.4%	17.4%	17.4%	17.4%	17.4%	17.4%	17.4%
$w_{DN(3)}$	24.4%	24.4%	24.4%	24.4%	24.4%	24.4%	24.4%
$w_{DN(4)}$	31.1%	31.1%	31.1%	31.1%	31.1%	31.1%	31.1%
n_{tot}	5530	1219	2673	1033	146	175	268
$n_{filtered}$	4974	1153	2272	994	139	173	236

Table A-3 Method 3 statistics, legend as in Method 1 (dataset: average monthly temperatures, Quality Controlled, 1 km buffer).

	World	**Asia**	**North America**	**Europe**	**Africa**	**South America**	**Oceania**
CI	-0.007	0.223	-0.180	0.033	0.439	0.090	0,022
E(CI)	-0.03	0.17	-0.19	0.01	0.26	0.19	-0.01
σ(CI)	0.01	0.02	0.01	0.02	0.05	0.05	0.04
σ^2(CI)	0.0001	0.0004	0.0001	0.0004	0.0026	0.0022	0.0015
z	2.6	3	0.4	1.1	3.5	-2.2	0.7
E(V_T)	0.39	0.39	0.39	0.39	0.39	0.39	0.39
σ(V_T)	0.64	0.64	0.64	0.64	0.64	0.64	0.64
σ^2(V_T)	0.41	0.41	0.41	0.41	0.41	0.41	0.41
E(V_{DN})	-0.08	0.43	-0.47	0.03	0.66	0.49	-0.01
σ(V_{DN})	0.83	0.77	0.66	0.80	0.58	0.70	0.80
σ^2(V_{DN})	0.68	0.59	0.44	0.64	0.34	0.49	0.63
$w_{T(1)}$	35.1%	35.1%	35.1%	35.1%	35.1%	35.1%	35.1%
$w_{T(2)}$	39.5%	39.5%	39.5%	39.5%	39.5%	39.5%	39.5%
$w_{T(3)}$	19.4%	19.4%	19.4%	19.4%	19.4%	19.4%	19.4%
$w_{T(4)}$	6.0%	6.0%	6.0%	6.0%	6.0%	6.0%	6.0%
$w_{DN(1)}$	27.1%	56.0%	7.8%	27.3%	66.2%	57.8%	24.6%
$w_{DN(2)}$	17.4%	15.4%	14.3%	24.6%	18.7%	16.2%	25.0%
$w_{DN(3)}$	24.4%	14.7%	31.0%	23.7%	11.5%	19.1%	23.7%
$w_{DN(4)}$	31.1%	13.8%	46.9%	24.3%	3.6%	6.9%	26.7%
n_{tot}	5530	1219	2673	1033	146	175	268
$n_{filtered}$	4974	1153	2272	994	139	173	236

Table A-4 Method 4 statistics, legend as in Method 1; class A: p value $DN \leq 0.25$, class B: $0.25 < p$ value $DN < 0.75$, class C: p value $DN \geq 0.75$ (dataset: average monthly temperatures, Quality Controlled, 1 km buffer). All values are in percentage (%), except for n and $n_{filtered}$.

	World			**Asia**			**North America**			**Europe**			**Africa**			**South America**			**Oceania**		
	A	**B**	**C**	**A**	**B**	**C**	**A**	**B**	**C**	**A**	**B**	**C**	**A**	**B**	**C**	**A**	**B**	**C**	**A**	**B**	**C**
$w_{T(1)}$	35.2	33.7	38.9	29.0	41.4	44.5	32.4	29.3	26.6	30.4	26.5	32.9	53.8	68.4	61.7	21.2	26.9	21.9	56.0	67.3	59.1
$w_{T(2)}$	39.6	42.7	36.7	40.2	39.5	30.3	41.1	43.8	42.8	45.8	51.2	50.2	23.1	21.1	25.2	18.2	42.3	34.2	19.8	17.3	23.7
$w_{T(3)}$	19.4	18.1	19.2	22.8	15.9	20.3	18.5	19.0	20.7	22.5	20.0	15.4	23.1	0.0	10.3	39.4	23.1	33.3	20.9	11.5	14.0
$w_{T(4)}$	5.9	5.6	5.2	7.9	3.2	4.9	8.1	8.0	9.9	1.4	2.3	1.5	0.0	10.5	2.8	21.2	7.7	10.5	3.3	3.8	3.2
$w_{DN(1)}$		27.1			56.0			7.8			27.3			66.2			57.8			24.6	
$w_{DN(2)}$		17.4			15.4			14.3			24.6			18.7			16.2			25.0	
$w_{DN(3)}$		24.4			14.7			31.0			23.7			11.5			19.1			23.7	
$w_{DN(4)}$		31.1			13.8			46.9			24.3			3.6			6.9			26.7	
n_{tot}	2261	897	1816	241	157	755	1511	427	334	369	215	410	13	19	107	33	26	114	91	52	93
$n_{filtered}$		4974			1153			2272			994			139			173			236	

A.2 Results of Quality Controlled dataset – Minimum Temperatures

Table A-5 Number of active stations from 1992 to 2013 and available stations after the application of thresholds for the reconstruction of mean annual temperature from the mean monthly data (dataset: minimum monthly temperatures, Quality Controlled) and spatial localization. The selected thresholds are $Nm_i \geq 9$ and $Ny_j \geq 18$.

Localization	Active station 1992-2013	Selected stations $Nm_i \geq 9$ $Ny_j \geq 18$
Asia	3322 (12.9 %)	1097 (20.9 %)
North America	15642 (60.9 %)	2734 (52.2 %)
Europe	4087 (16 %)	900 (17.2%)
Africa	869 (3.4 %)	105 (2 %)
South America	536 (2.1 %)	104 (2 %)
Oceania	1168 (4.5 %)	290 (5.5 %)
Others	51 (0.2 %)	8 (0.2 %)
World	25675 (100 %)	5238 (100%)

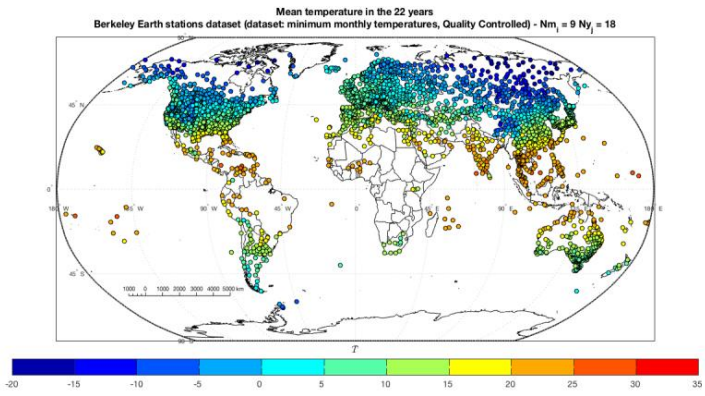

Figure A-1 Mean minimum temperature in the 22 years $\bar{T}$ for the selected air temperature stations (dataset: minimum monthly temperatures, Quality Controlled, 1 km buffer).

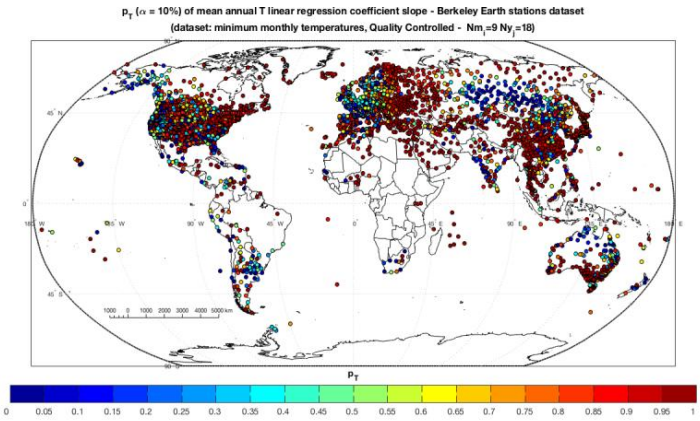

Figure A-2 Spatial distribution of the p value (p_T) of the slope of the temperature regression line for the selected Berkeley Earth stations (dataset: minimum monthly temperatures, Quality Controlled, 1 km buffer).

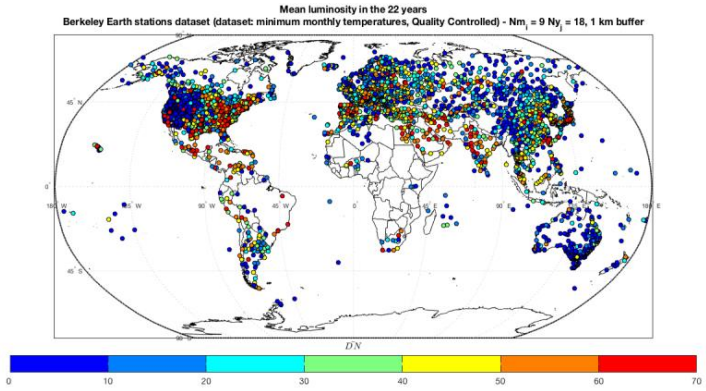

Figure A-3 Mean Digital Number value in the 22 years ($\overline{DN}$) in a 1 km buffer around the selected stations (dataset: minimum monthly temperatures, Quality Controlled, 1 km buffer).

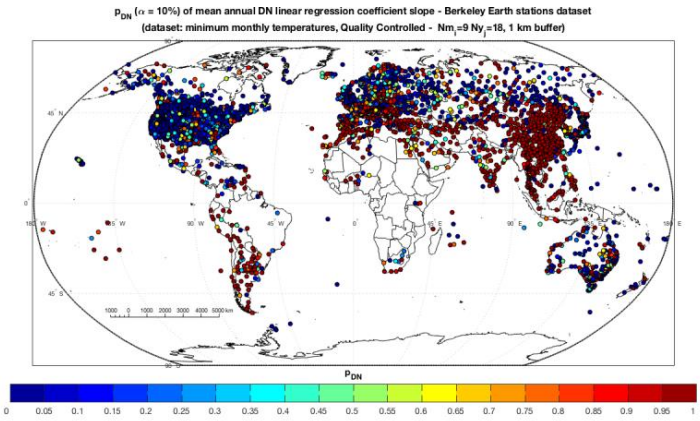

Figure A-4 Spatial distribution of the *p* value (p_{DN}) of the slope of the nightlights regression line for the selected Berkeley Earth stations (dataset: minimum monthly temperatures, Quality Controlled, 1 km buffer).

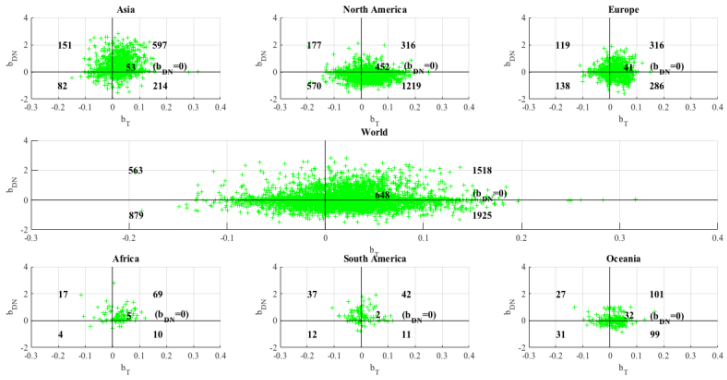

Figure A-5 Slope of *T* (b_T) and *DN* (b_{DN}) regression trend lines. Sectors 1 and 3 correspond to concordant trends, while sectors 2 and 4 refer to discordant trends. The number of stations included in each sector is in bold, as well as the number of stations with *DN* systematically equal to zero (b_{DN} = 0) on the horizontal axis (dataset: minimum monthly temperatures, Quality Controlled, 1 km buffer).

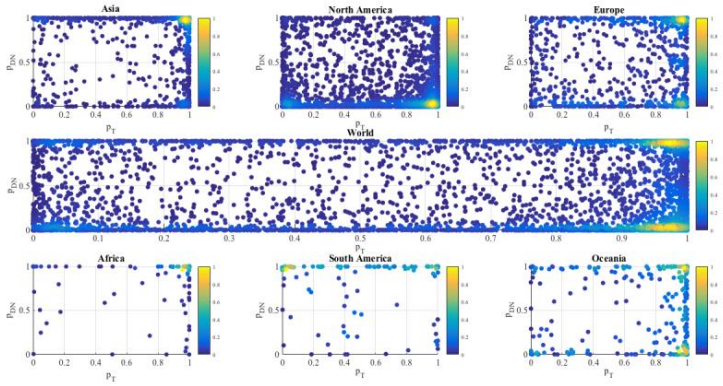

Figure A-6 *P* values density plots at global and continental scale (dataset: minimum monthly temperatures, Quality Controlled, 1 km buffer).

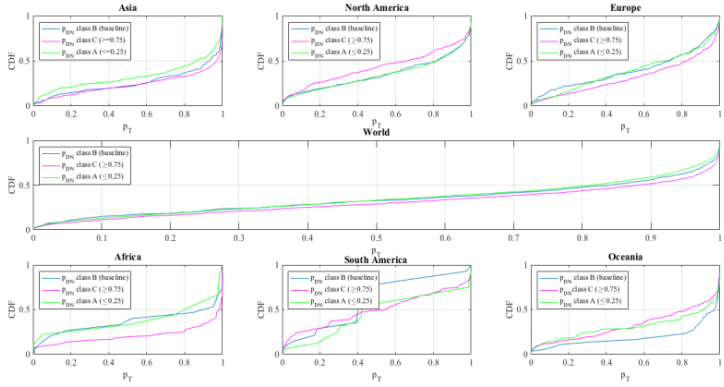

Figure A-7 Method 4: cumulative distribution function CDF of p_T based on the three different nightlights configurations i.e., class A: $p_{DN} \leq 0.25$, class B: $0.25 < p_{DN} < 0.75$, class C: $p_{DN} \geq 0.75$ (dataset: minimum monthly temperatures, Quality Controlled, 1 km buffer).

Table A-6 Method 1 statistics; *w* refers to the probability of occurrence of classes of significance from 1 (++) to 4 (--); V_T: variable temperature *T*; V_{DN}: variable nightlights *DN*; CI: concordance index; E(CI): expected mean of CI; σ(CI):standard deviation of CI; z: standardized value; $E(V_T)$, $E(V_{DN})$, $\sigma(V_T)$ and $\sigma(V_{DN})$ refer to expected mean and standard deviation; *n*: total number of stations; $n_{filtered}$: same as *n* excluding stations with *DN* trend equal to 0 (dataset: minimum monthly temperatures, Quality Controlled, 1 km buffer).

	World	**Asia**	**North America**	**Europe**	**Africa**	**South America**	**Oceania**
CI	0.002	0.266	-0.15	0.049	0.378	0.01	0.022
E(CI)	-0.04	0.21	-0.13	0.004	0.35	0.003	-0.004
σ(CI)	0.01	0.02	0.01	0.02	0.06	0.04	0.05
σ^2(CI)	0.0001	0.0005	0.0002	0.0004	0.0046	0.0039	0.0016
z	4.3	3.05	-1.8	2.6	0.5	0.2	0.6
$E(V_T)$	0.33	0.48	0.27	0.27	0.54	0.00	0.42
$\sigma(V_T)$	0.69	0.66	0.70	0.66	0.69	0.73	0.68
$\sigma^2(V_T)$	0.48	0.44	0.49	0.43	0.48	0.54	0.47
$E(V_{DN})$	-0.12	0.43	-0.49	0.01	0.65	0.55	-0.01
$\sigma(V_{DN})$	0.82	0.78	0.65	0.79	0.58	0.67	0.79
$\sigma^2(V_{DN})$	0.67	0.60	0.42	0.63	0.34	0.45	0.63
$w_{T(1)}$	36.0%	49.8%	31.6%	27.2%	59.0%	22.5%	44.2%
$w_{T(2)}$	33.0%	26.6%	34.5%	40.0%	20.0%	24.5%	30.6%
$w_{T(3)}$	22.2%	17.1%	23.6%	25.6%	11.0%	37.3%	16.3%
$w_{T(4)}$	8.9%	6.4%	10.3%	7.1%	10.0%	15.7%	8.9%
$w_{DN(1)}$	25.1%	57.0%	6.8%	26.0%	63.0%	60.8%	24.8%
$w_{DN(2)}$	17.3%	14.7%	14.8%	24.7%	23.0%	16.7%	24.8%
$w_{DN(3)}$	24.5%	13.8%	30.3%	24.8%	9.0%	16.7%	24.4%
$w_{DN(4)}$	33.1%	14.6%	48.1%	24.6%	5.0%	5.9%	26.0%
n_{tot}	5238	1097	2734	900	105	104	290
$n_{filtered}$	4646	1044	2282	859	100	102	258

Table A-7 Method 2 statistics, legend as in Method 1 (dataset: minimum monthly temperatures, Quality Controlled, 1 km buffer).

	World	**Asia**	**North America**	**Europe**	**Africa**	**South America**	**Oceania**
CI	0.002	0.266	-0.15	0.049	0.378	0.01	0.022
E(CI)	-0.04	-0.04	-0.04	-0.04	-0.04	-0.04	-0.04
σ(CI)	0.01	0.02	0.01	0.02	0.05	0.04	0.04
σ^2(CI)	0.0001	0.0004	0.0002	0.0005	0.0040	0.0039	0.0016
z	4.3	16.4	-9.5	4.5	7.6	1.04	1.4
E(V_T)	0.33	0.33	0.33	0.33	0.33	0.33	0.33
σ(V_T)	0.69	0.69	0.69	0.69	0.69	0.69	0.69
σ^2(V_T)	0.48	0.48	0.48	0.48	0.48	0.48	0.48
E(V_{DN})	-0.12	-0.12	-0.12	-0.12	-0.12	-0.12	-0.12
σ(V_{DN})	0.82	0.82	0.82	0.82	0.82	0.82	0.82
σ^2(V_{DN})	0.67	0.67	0.67	0.67	0.67	0.67	0.67
$w_{T(1)}$	36.0%	36.0%	36.0%	36.0%	36.0%	36.0%	36.0%
$w_{T(2)}$	33.0%	33.0%	33.0%	33.0%	33.0%	33.0%	33.0%
$w_{T(3)}$	22.2%	22.2%	22.2%	22.2%	22.2%	22.2%	22.2%
$w_{T(4)}$	8.9%	8.9%	8.9%	8.9%	8.9%	8.9%	8.9%
$w_{DN(1)}$	25.1%	25.1%	25.1%	25.1%	25.1%	25.1%	25.1%
$w_{DN(2)}$	17.3%	17.3%	17.3%	17.3%	17.3%	17.3%	17.3%
$w_{DN(3)}$	24.5%	24.5%	24.5%	24.5%	24.5%	24.5%	24.5%
$w_{DN(4)}$	33.1%	33.1%	33.1%	33.1%	33.1%	33.1%	33.1%
n_{tot}	5238	1097	2734	900	105	104	290
$n_{filtered}$	4646	1044	2282	859	100	102	258

Table A-8 Method 3 statistics, legend as in Method 1 (dataset: minimum monthly temperatures, Quality Controlled, 1 km buffer).

	World	Asia	North America	Europe	Africa	South America	Oceania
CI	0.002	0.266	-0.151	0.049	0.377	0.010	-0.009
E(CI)	-0.0378	0.1394	-0.1594	0.0044	0.2113	0.1785	-0.0032
σ(CI)	0.01	0.02	0.01	0.02	0.06	0.06	0.04
σ^2(CI)	0.0001	0.0004	0.0002	0.0004	0.0040	0.0040	0.0014
z	4.32	6.16	0.66	2.15	2.62	-2.67	-0.15
E(V_T)	0.325	0.325	0.325	0.325	0.325	0.325	0.325
σ(V_T)	0.693	0.693	0.693	0.693	0.693	0.693	0.693
σ^2(V_T)	0.481	0.481	0.481	0.481	0.481	0.481	0.481
E(V_{DN})	-0.116	0.429	-0.490	0.013	0.650	0.549	-0.010
σ(V_{DN})	0.820	0.776	0.649	0.793	0.581	0.670	0.794
σ^2(V_{DN})	0.673	0.603	0.422	0.629	0.338	0.449	0.631
$w_{T(1)}$	36.0%	36.0%	36.0%	36.0%	36.0%	36.0%	36.0%
$w_{T(2)}$	33.0%	33.0%	33.0%	33.0%	33.0%	33.0%	33.0%
$w_{T(3)}$	22.2%	22.2%	22.2%	22.2%	22.2%	22.2%	22.2%
$w_{T(4)}$	8.9%	8.9%	8.9%	8.9%	8.9%	8.9%	8.9%
$w_{DN(1)}$	25.1%	57.0%	6.8%	26.0%	63.0%	60.8%	24.8%
$w_{DN(2)}$	17.3%	14.7%	14.8%	24.7%	23.0%	16.7%	24.8%
$w_{DN(3)}$	24.5%	13.8%	30.3%	24.8%	9.0%	16.7%	24.4%
$w_{DN(4)}$	33.1%	14.6%	48.1%	24.6%	5.0%	5.9%	26.0%
n_{tot}	5238	1097	2734	900	105	104	290
$n_{filtered}$	4646	1044	2282	859	100	102	258

Table A-9 Method 4 statistics, legend as in Method 1; class A: p value $DN \leq 0.25$, class B: $0.25 < p$ value $DN < 0.75$, class C: p value $DN \geq 0.75$ (dataset: minimum monthly temperatures, Quality Controlled, 1 km buffer). All values are in percentage (%), except for n and $n_{filtered}$.

	World			**Asia**			**North America**			**Europe**			**Africa**			**South America**			**Oceania**		
	A	**B**	**C**	**A**	**B**	**C**	**A**	**B**	**C**	**A**	**B**	**C**	**A**	**B**	**C**	**A**	**B**	**C**	**A**	**B**	**C**
$w_{T(1)}$	32.2	33.5	42.4	38.6	45.5	54.3	32.3	32.6	26.9	23.8	21.1	34.0	44.4	53.3	61.8	31.3	14.3	22.2	43	54.5	39.8
$w_{T(2)}$	34.8	36.4	28.8	31.8	33.6	23.6	34.8	36.3	30.6	39-6	43.7	38.4	33.3	13.3	19.7	12.5	14.3	29.2	29	30.9	32.0
$w_{T(3)}$	23.6	20.4	21.1	18.4	15.7	17.0	23.3	19.8	30.3	29.9	24.7	22.0	0	20.0	10.5	50	64.3	29.2	17	10.9	18.4
$w_{T(4)}$	9.4	9.7	7.7	11.2	5.2	5.1	9.6	11.4	12.2	6.7	10.5	5.6	22.2	13.3	7.9	6.3	7.1	19.4	11	3.6	9.7
$w_{DN(1)}$		25.1			57.0			6.8			26			63			60.8			24.8	
$w_{DN(2)}$		17.3			14.7			14.8			24.7			23			16.7			24.8	
$w_{DN(3)}$		24.5			13.8			30.3			24.8			9			16.7			24.4	
$w_{DN(4)}$		33.1			14.6			48.1			24.6			5			5.9			26.0	
n_{tot}	2208	838	1600	223	134	687	1532	430	320	328	190	341	9	15	76	16	14	72	100	55	103
$n_{filtered}$		4646			1044			2282			859			100			102			258	

A.2 Main results of Quality Controlled dataset with increasing spatial buffers from 2 to 5 km – Average Temperatures

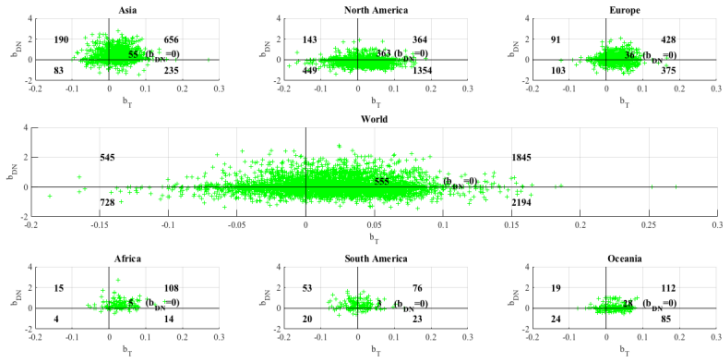

Figure A-8 Slope of *T* (b_T) and *DN* (b_{DN}) regression trend lines. Sectors 1 and 3 correspond to concordant trends, while sectors 2 and 4 refer to discordant trends. The number of stations included in each sector is in bold, as well as the number of stations with *DN* systematically equal to zero (b_{DN} = 0) on the horizontal axis (dataset: average monthly temperatures, Quality Controlled, 2 km buffer).

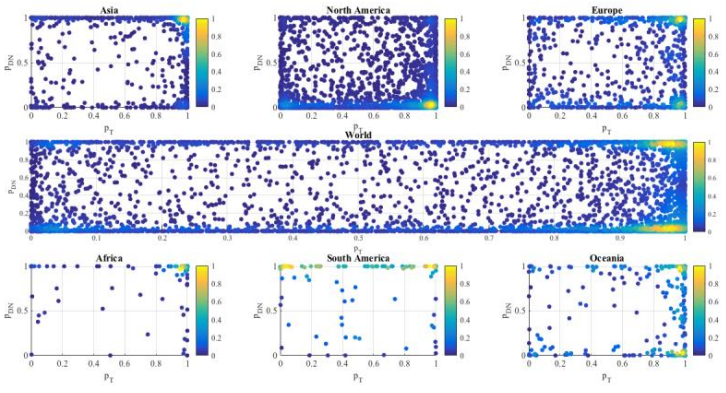

Figure A-9 *P* values density plots at global and continental scale (dataset: average monthly temperatures, Quality Controlled, 2 km buffer).

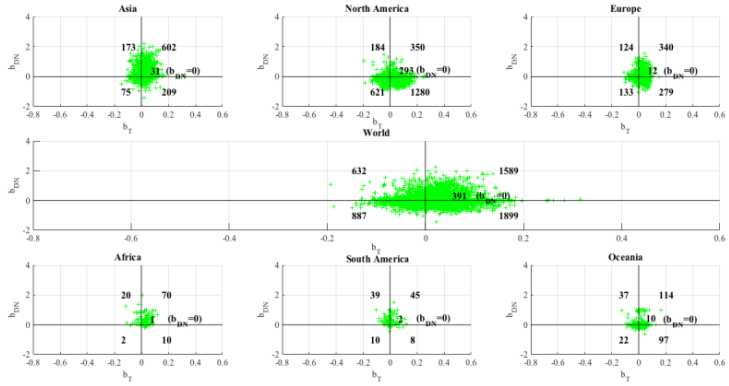

Figure A-10 Slope of *T* (b_T) and *DN* (b_{DN}) regression trend lines. Sectors 1 and 3 correspond to concordant trends, while sectors 2 and 4 refer to discordant trends. The number of stations included in each sector is in bold, as well as the number of stations with *DN* systematically equal to zero (b_{DN} = 0) on the horizontal axis (dataset: average monthly temperatures, Quality Controlled, 3 km buffer).

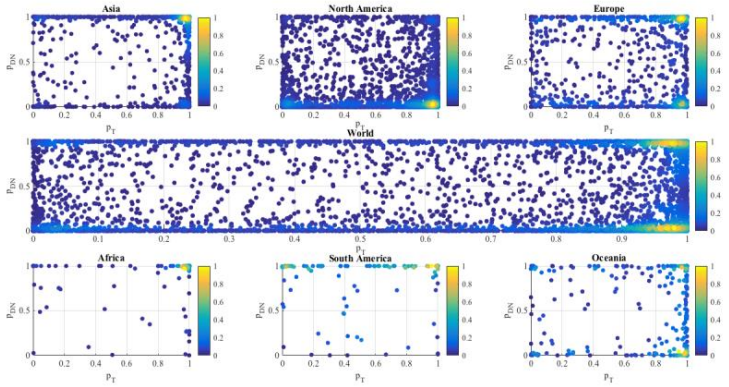

Figure A-11 *P* values density plots at global and continental scale (dataset: average monthly temperatures, Quality Controlled, 3 km buffer).

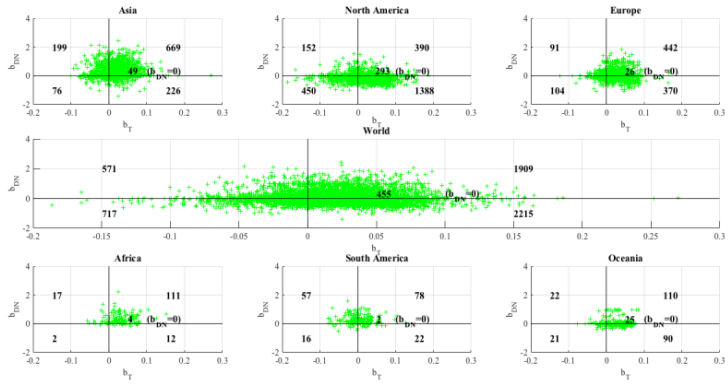

Figure A-12 Slope of *T* (b_T) and *DN* (b_{DN}) regression trend lines. Sectors 1 and 3 correspond to concordant trends, while sectors 2 and 4 refer to discordant trends. The number of stations included in each sector is in bold, as well as the number of stations with *DN* systematically equal to zero (b_{DN} = 0) on the horizontal axis (dataset: average monthly temperatures, Quality Controlled, 4 km buffer).

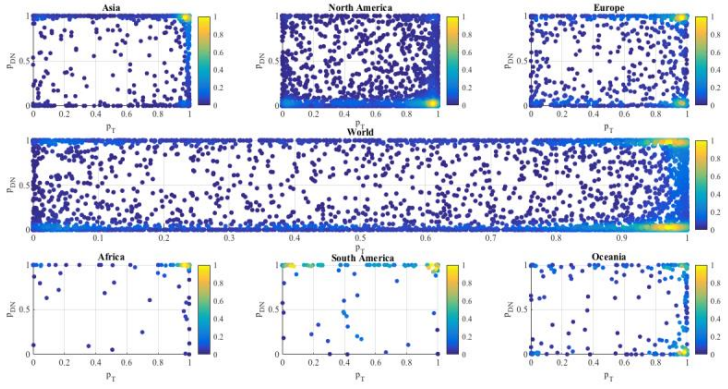

Figure A-13 *P* values density plots at global and continental scale (dataset: average monthly temperatures, Quality Controlled, 4 km buffer).

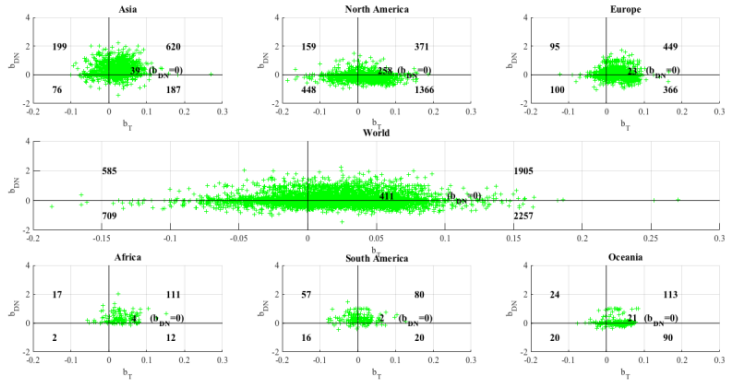

Figure A-14 Slope of *T* (b_T) and *DN* (b_{DN}) regression trend lines. Sectors 1 and 3 correspond to concordant trends, while sectors 2 and 4 refer to discordant trends. The number of stations included in each sector is in bold, as well as the number of stations with *DN* systematically equal to zero (b_{DN} = 0) on the horizontal axis (dataset: average monthly temperatures, Quality Controlled, 5 km buffer).

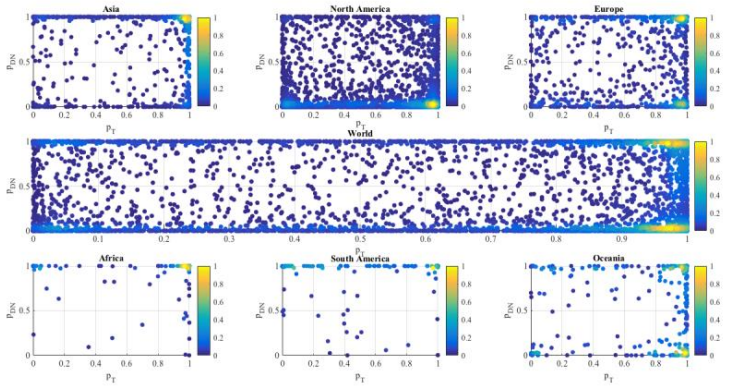

Figure A-15 *P* values density plots at global and continental scale (dataset: average monthly temperatures, Quality Controlled, 5 km buffer).

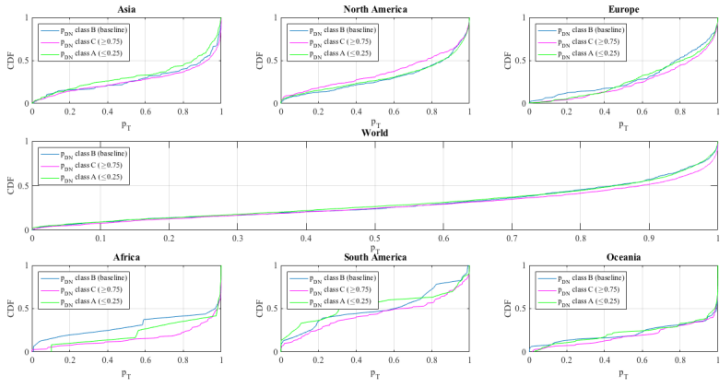

Figure A-16 Method 4: cumulative distribution function CDF of p_T based on the three different nightlights configurations i.e., class A: $p_{DN} \leq 0.25$, class B: $0.25 < p_{DN} < 0.75$, class C: $p_{DN} \geq 0.75$ (dataset: average monthly temperatures, Quality Controlled, 2 km buffer).

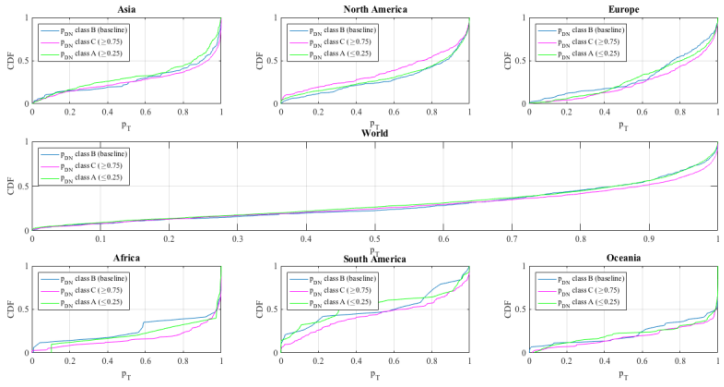

Figure A-17 Method 4: cumulative distribution function CDF of p_T based on the three different nightlights configurations i.e., class A: $p_{DN} \leq 0.25$, class B: $0.25 < p_{DN} < 0.75$, class C: $p_{DN} \geq 0.75$ (dataset: average monthly temperatures, Quality Controlled, 3 km buffer).

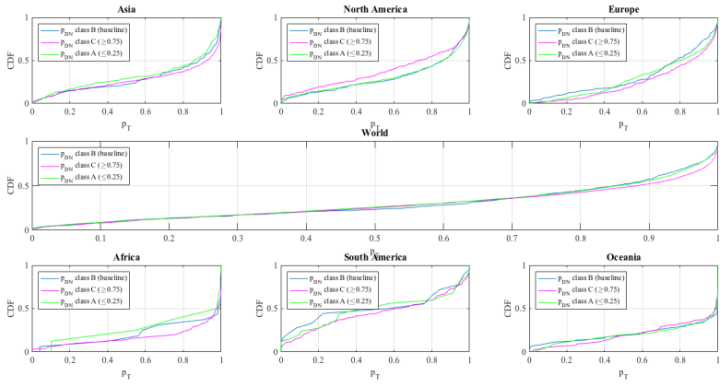

Figure A-18 Method 4: cumulative distribution function CDF of p_T based on the three different nightlights configurations i.e., class A: $p_{DN} \leq 0.25$, class B: $0.25 < p_{DN} < 0.75$, class C: $p_{DN} \geq 0.75$ (dataset: average monthly temperatures, Quality Controlled, 4 km buffer).

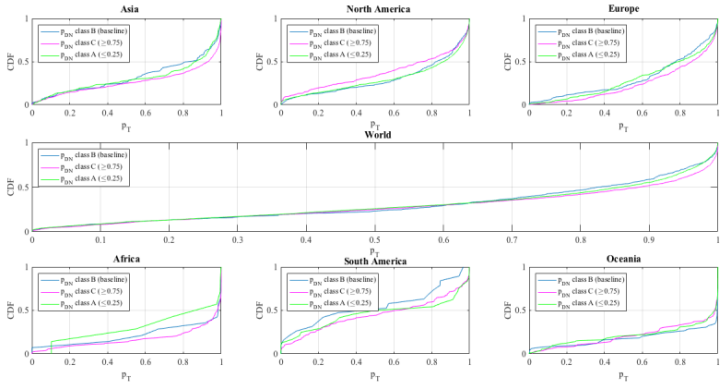

Figure A-19 Method 4: cumulative distribution function CDF of p_T based on the three different nightlights configurations i.e., class A: $p_{DN} \leq 0.25$, class B: $0.25 < p_{DN} < 0.75$, class C: $p_{DN} \geq 0.75$ (dataset: average monthly temperatures, Quality Controlled, 5 km buffer).

A.3 Main results of Quality Controlled dataset with increasing spatial buffers from 2 to 5 km – Minimum Temperatures

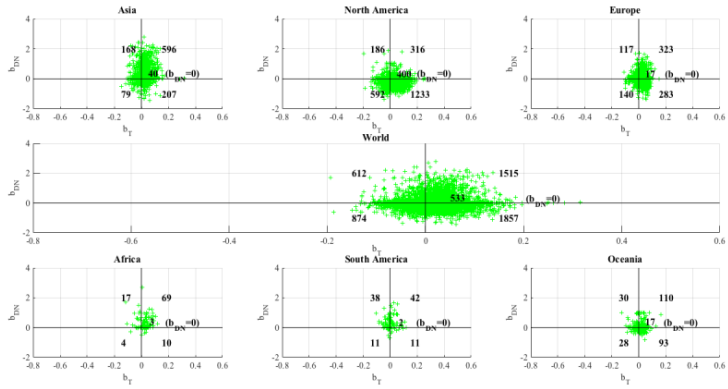

Figure A-20 Slope of *T* (b_T) and *DN* (b_{DN}) regression trend lines. Sectors 1 and 3 correspond to concordant trends, while sectors 2 and 4 refer to discordant trends. The number of stations included in each sector is in bold, as well as the number of stations with *DN* systematically equal to zero ($b_{DN} = 0$) on the horizontal axis (dataset: minimum monthly temperatures, Quality Controlled, 2 km buffer).

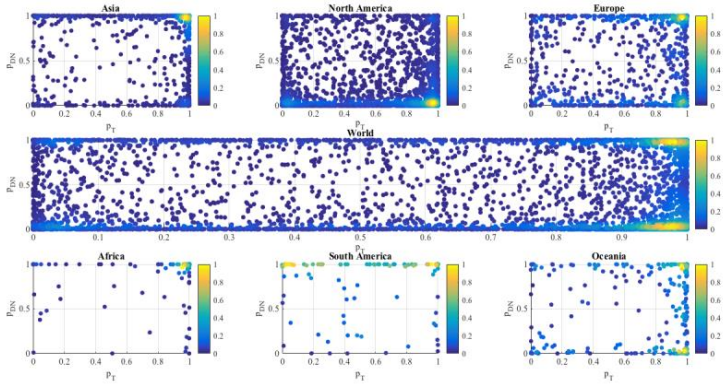

Figure A-21 *P* values density plots at global and continental scale (dataset: minimum monthly temperatures, Quality Controlled, 2 km buffer).

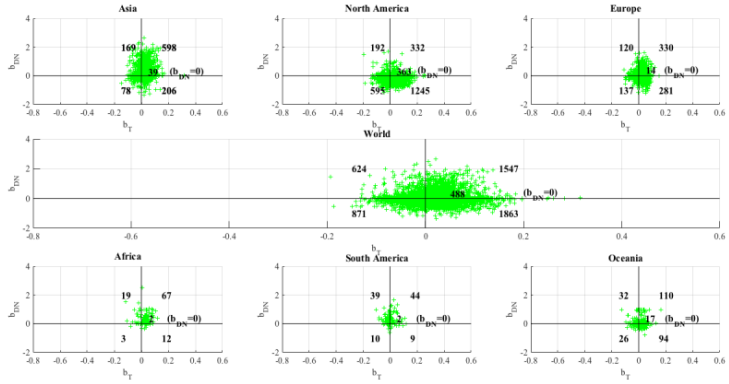

Figure A-22 Slope of *T* (b_T) and *DN* (b_{DN}) regression trend lines. Sectors 1 and 3 correspond to concordant trends, while sectors 2 and 4 refer to discordant trends. The number of stations included in each sector is in bold, as well as the number of stations with *DN* systematically equal to zero ($b_{DN} = 0$) on the horizontal axis (dataset: minimum monthly temperatures, Quality Controlled, 3 km buffer).

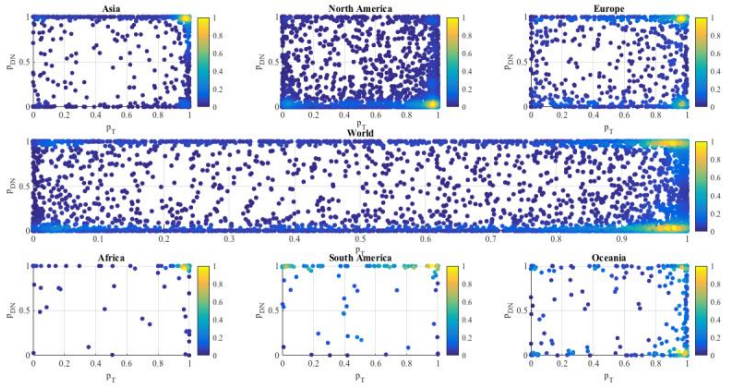

Figure A-23 *P* values density plots at global and continental scale (dataset: minimum monthly temperatures, Quality Controlled, 3 km buffer).

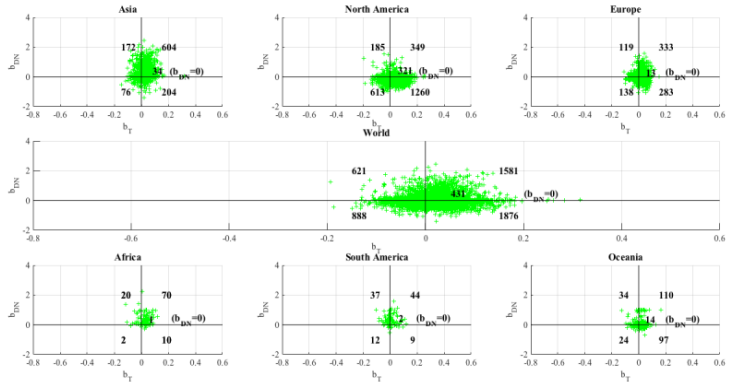

Figure A-24 Slope of *T* (b_T) and *DN* (b_{DN}) regression trend lines. Sectors 1 and 3 correspond to concordant trends, while sectors 2 and 4 refer to discordant trends. The number of stations included in each sector is in bold, as well as the number of stations with *DN* systematically equal to zero ($b_{DN} = 0$) on the horizontal axis (dataset: minimum monthly temperatures, Quality Controlled, 4 km buffer).

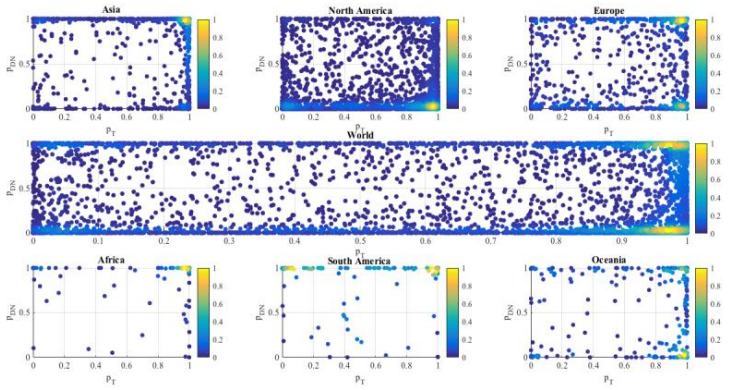

Figure A-25 *P* values density plots at global and continental scale (dataset: minimum monthly temperatures, Quality Controlled, 4 km buffer).

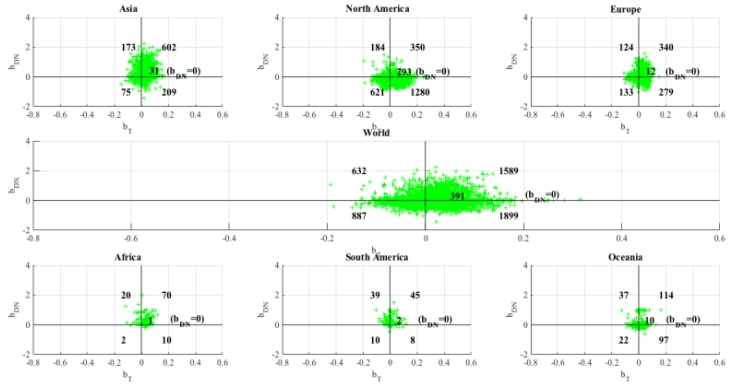

Figure A-26 Slope of *T* (b_T) and *DN* (b_{DN}) regression trend lines. Sectors 1 and 3 correspond to concordant trends, while sectors 2 and 4 refer to discordant trends. The number of stations included in each sector is in bold, as well as the number of stations with *DN* systematically equal to zero ($b_{DN} = 0$) on the horizontal axis (dataset: minimum monthly temperatures, Quality Controlled, 5 km buffer).

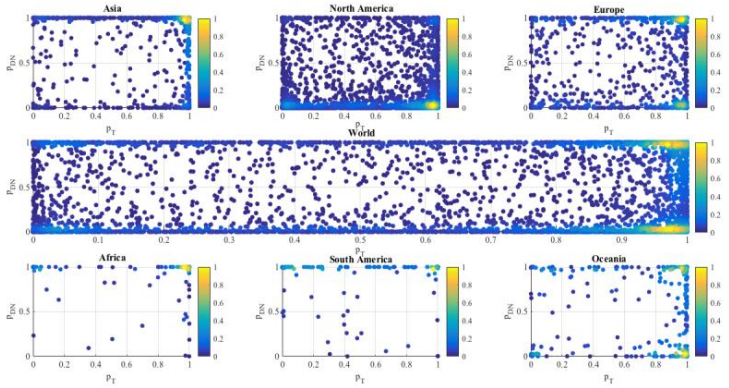

Figure A-27 *P* values density plots at global and continental scale (dataset: minimum monthly temperatures, Quality Controlled, 5 km buffer).

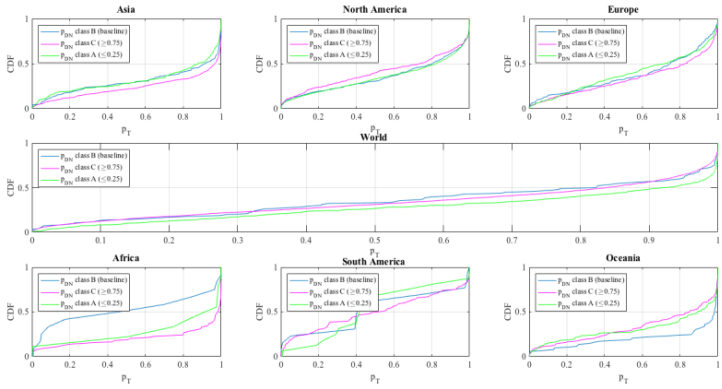

Figure A-28 Method 4: cumulative distribution function CDF of p_T based on the three different nightlights configurations i.e., class A: $p_{DN} \leq 0.25$, class B: $0.25 < p_{DN} < 0.75$, class C: $p_{DN} \geq 0.75$ (dataset: minimum monthly temperatures, Quality Controlled, 2 km buffer).

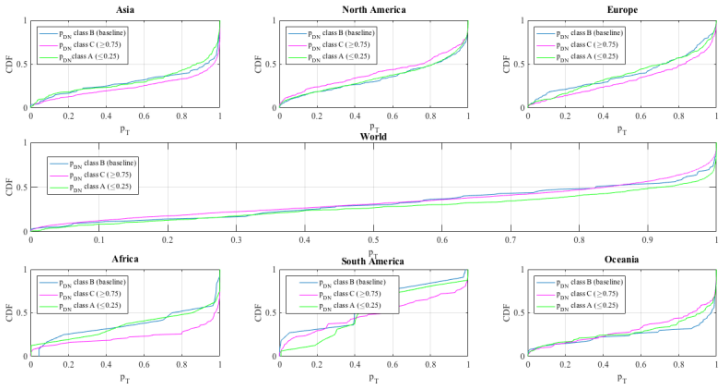

Figure A-29 Method 4: cumulative distribution function CDF of p_T based on the three different nightlights configurations i.e., class A: $p_{DN} \leq 0.25$, class B: $0.25 < p_{DN} < 0.75$, class C: $p_{DN} \geq 0.75$ (dataset: minimum monthly temperatures, Quality Controlled, 3 km buffer).

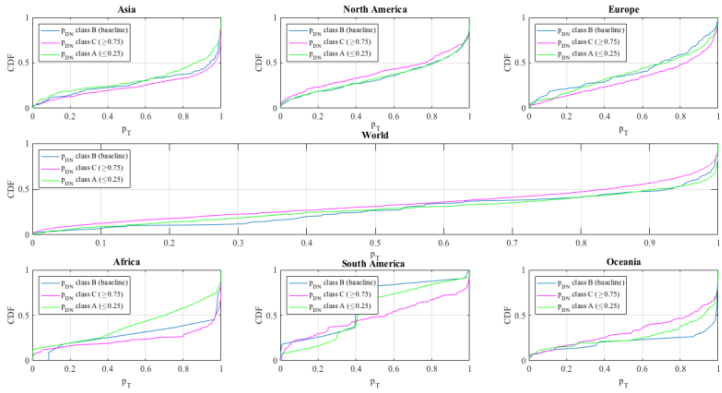

Figure A-30 Method 4: cumulative distribution function CDF of p_T based on the three different nightlights configurations i.e., class A: $p_{DN} \leq 0.25$, class B: $0.25 < p_{DN} < 0.75$, class C: $p_{DN} \geq 0.75$ (dataset: minimum monthly temperatures, Quality Controlled, 4 km buffer).

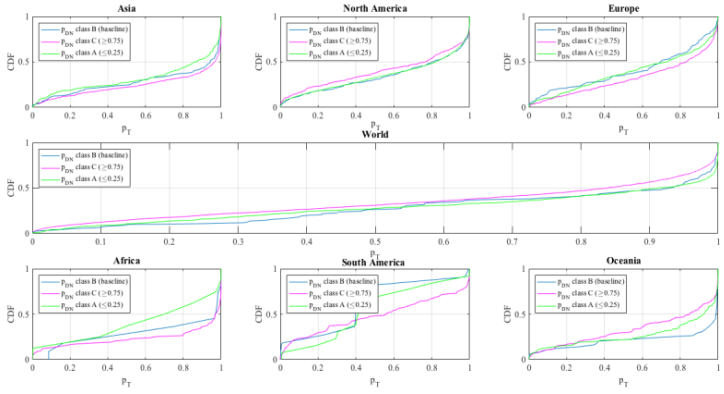

Figure A-31 Method 4: cumulative distribution function CDF of p_T based on the three different nightlights configurations i.e., class A: $p_{DN} \leq 0.25$, class B: $0.25 < p_{DN} < 0.75$, class C: $p_{DN} \geq 0.75$ (dataset: minimum monthly temperatures, Quality Controlled, 5 km buffer).

A.4 Results of Breakpoint Adjusted dataset – Average Temperatures

Table A-10 Number of active stations from 1992 to 2013 and available stations after the application of thresholds for the reconstruction of mean annual temperature from the mean monthly data (dataset: average monthly temperatures, Breakpoint Corrected) and spatial localization. The selected thresholds are $Nm_i \geq 9$ and $Ny_j \geq 18$.

Localization	Active station 1992-2013	Selected stations $Nm_i \geq 9$ $Ny_j \geq 18$
Asia	3862 (13.5 %)	1219 (22 %)
North America	16667 (58.1 %)	2673 (48.3 %)
Europe	4811 (16.8 %)	1033 (18.7%)
Africa	976 (13.4 %)	146 (2.6%)
South America	657 (2.3 %)	175 (3.1 %)
Oceania	1462 (5.1 %)	268 (5 %)
Others	243 (0.8 %)	16 (0.3 %)
World	28679 (100 %)	5530 (100%)

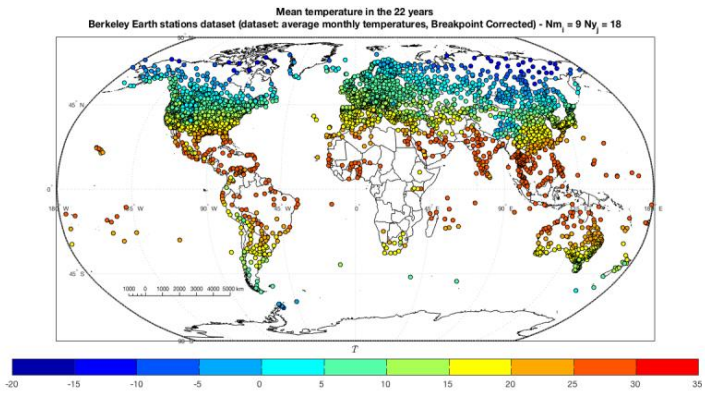

Figure A-32 Mean average temperature in the 22 years $\bar{T}$ for the selected air temperature stations (dataset: average monthly temperatures, Breakpoint Corrected, 1 km buffer).

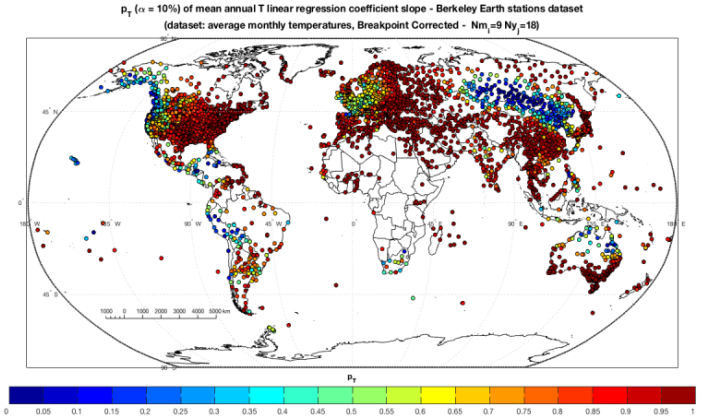

Figure A-33 Spatial distribution of the p value (p_T) of the slope of the temperature regression line for the selected Berkeley Earth stations (dataset: average monthly temperatures, Breakpoint Corrected, 1 km buffer).

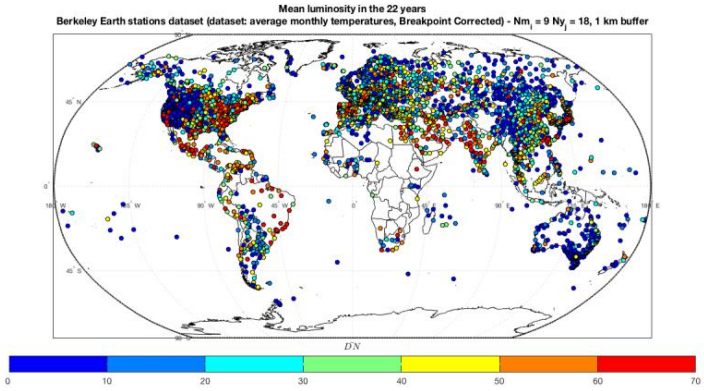

Figure A-34 Mean Digital Number value in the 22 years ($\overline{DN}$) in a 1 km buffer around the selected stations (dataset: average monthly temperatures, Breakpoint Corrected, 1 km buffer).

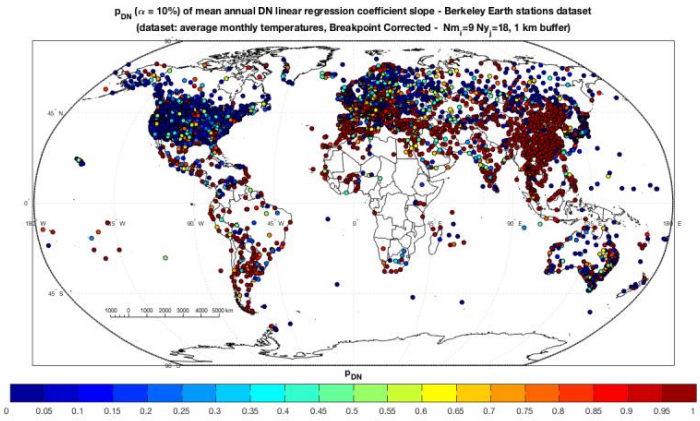

Figure A-35 Spatial distribution of the p value (p_{DN}) of the slope of the nightlights regression line for the selected Berkeley Earth stations (dataset: average monthly temperatures, Breakpoint Corrected, 1 km buffer).

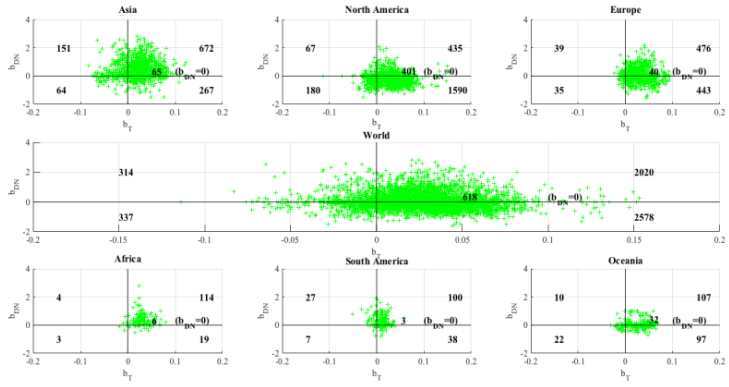

Figure A-36 Slope of T (b_T) and DN (b_{DN}) regression trend lines. Sectors 1 and 3 correspond to concordant trends, while sectors 2 and 4 refer to discordant trends. The number of stations included in each sector is in bold, as well as the number of stations with DN systematically equal to zero (b_{DN} = 0) on the horizontal axis (dataset: average monthly temperatures, Breakpoint Corrected, 1 km buffer).

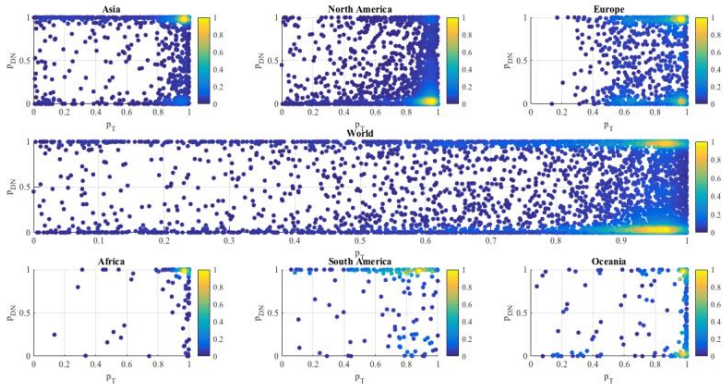

Figure A-37 *P* values density plots at global and continental scale (dataset: average monthly temperatures, Breakpoint Corrected, 1 km buffer).

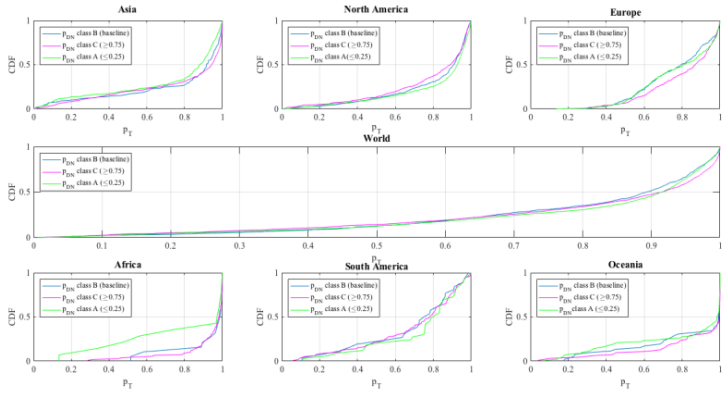

Figure A-38 Method 4: cumulative distribution function CDF of p_T based on the three different nightlights configurations i.e., class A: $p_{DN} \leq 0.25$, class B: $0.25 < p_{DN} < 0.75$, class C: $p_{DN} \geq 0.75$ (dataset: average monthly temperatures, Breakpoint Corrected, 1 km buffer).

Table A-11 Method 1 statistics; *w* refers to the probability of occurrence of classes of significance from 1 (++) to 4 (--); V_T: variable temperature *T*; V_{DN}: variable nightlights *DN*; CI: concordance index; E(CI): expected mean of CI; σ(CI):standard deviation of CI; z: standardized value; $E(V_T)$, $E(V_{DN})$, $\sigma(V_T)$ and $\sigma(V_{DN})$ refer to expected mean and standard deviation; *n*: total number of stations; $n_{filtered}$: same as *n* excluding stations with *DN* trend equal to 0 (dataset: average monthly temperatures, Breakpoint Corrected, 1 km buffer).

	World	**Asia**	**North America**	**Europe**	**Africa**	**South America**	**Oceania**
CI	0.039	0.257	-0.28	0.025	0.543	0.17	0.043
E(CI)	-0.04	0.21	-0.26	0.02	0.52	0.18	-0.01
σ(CI)	0.01	0.02	0.01	0.02	0.05	0.04	0.04
σ^2(CI)	0.0001	0.0004	0.0001	0.0003	0.0023	0.0013	0.0020
z	0.4	2.3	-1.2	0.38	0.57	-0.19	1.2
$E(V_T)$	0.55	0.50	0.56	0.56	0.79	0.36	0.68
$\sigma(V_T)$	0.48	0.57	0.46	0.38	0.37	0.46	0.53
$\sigma^2(V_T)$	0.23	0.33	0.21	0.15	0.14	0.22	0.29
$E(V_{DN})$	-0.08	0.42	-0.48	0.03	0.65	0.49	-0.01
$\sigma(V_{DN})$	0.83	0.77	0.66	0.80	0.59	0.70	0.80
$\sigma^2(V_{DN})$	0.68	0.59	0.44	0.63	0.35	0.49	0.63
$w_{T(1)}$	36.8%	41.9%	35.5%	27.2%	68.6%	12.8%	65.3%
$w_{T(2)}$	50.1%	38.7%	52.7%	64.8%	26.4%	66.9%	19.9%
$w_{T(3)}$	12.1%	17.1%	11.0%	8.1%	5.0%	20.3%	14.4%
$w_{T(4)}$	0.9%	2.3%	0.8%	0.0%	0.0%	0.0%	0.4%
$w_{DN(1)}$	27.0%	56.0%	7.8%	27.2%	65.7%	57.6%	24.6%
$w_{DN(2)}$	17.4%	15.4%	14.3%	24.7%	18.6%	16.3%	25.0%
$w_{DN(3)}$	24.4%	14.7%	30.9%	23.9%	11.4%	19.2%	23.7%
$w_{DN(4)}$	31.2%	13.9%	47.0%	24.3%	4.3%	7.0%	26.7%
n_{tot}	5530	1219	2673	1033	146	175	268
$n_{filtered}$	4974	1153	2272	994	139	173	236

Table A-12 Method 2 statistics, legend as in Method 1 (dataset: average monthly temperatures, Breakpoint Corrected, 1 km buffer).

	World	**Asia**	**North America**	**Europe**	**Africa**	**South America**	**Oceania**
CI	0.039	0.257	-0.28	0.025	0.543	0.17	0.043
E(CI)	-0.04	-0.04	-0.04	-0.04	-0.04	-0.04	-0.04
σ(CI)	0.01	0.02	0.01	0.02	0.05	0.05	0.04
σ^2(CI)	0.0001	0.0003	0.0002	0.0004	0.0026	0.0021	0.0015
z	0.4	16.9	-18.6	3.5	11.5	4.6	2.2
E(V_T)	0.55	0.55	0.55	0.55	0.55	0.55	0.55
σ(V_T)	0.48	0.48	0.48	0.48	0.48	0.48	0.48
σ^2(V_T)	0.23	0.23	0.23	0.23	0.23	0.23	0.23
E(V_{DN})	-0.08	-0.08	-0.08	-0.08	-0.08	-0.08	-0.08
σ(V_{DN})	0.83	0.83	0.83	0.83	0.83	0.83	0.83
σ^2(V_{DN})	0.68	0.68	0.68	0.68	0.68	0.68	0.68
$w_{T(1)}$	36.8%	36.8%	36.8%	36.8%	36.8%	36.8%	36.8%
$w_{T(2)}$	50.1%	50.1%	50.1%	50.1%	50.1%	50.1%	50.1%
$w_{T(3)}$	12.1%	12.1%	12.1%	12.1%	12.1%	12.1%	12.1%
$w_{T(4)}$	0.9%	0.9%	0.9%	0.9%	0.9%	0.9%	0.9%
$w_{DN(1)}$	27.0%	27.0%	27.0%	27.0%	27.0%	27.0%	27.0%
$w_{DN(2)}$	17.4%	17.4%	17.4%	17.4%	17.4%	17.4%	17.4%
$w_{DN(3)}$	24.4%	24.4%	24.4%	24.4%	24.4%	24.4%	24.4%
$w_{DN(4)}$	31.2%	31.2%	31.2%	31.2%	31.2%	31.2%	31.2%
n_{tot}	5530	1219	2673	1033	146	175	268
$n_{filtered}$	4974	1153	2272	994	139	173	236

Table A-13 Method 3 statistics, legend as in Method 1 (dataset: average monthly temperatures, Breakpoint Corrected, 1 km buffer).

	World	Asia	North America	Europe	Africa	South America	Oceania
CI	0.039	0.257	-0.28	0.025	0.543	0.17	0.043
E(CI)	-0.04	0.23	-0.26	0.02	0.36	0.27	-0.01
σ(CI)	0.01	0.02	0.01	0.02	0.05	0.04	0.04
σ^2(CI)	0.0001	0.0003	0.0001	0.0003	0.0020	0.0019	0.0014
z	0.39	1.39	-1.5	0.36	4.12	-2.31	1.36
E(V_T)	0.549	0.549	0.549	0.549	0.549	0.549	0.549
σ(V_T)	0.482	0.482	0.482	0.482	0.482	0.482	0.482
σ^2(V_T)	0.232	0.232	0.232	0.232	0.232	0.232	0.232
E(V_{DN})	-0.078	0.425	-0.475	0.033	0.650	0.491	-0.015
σ(V_{DN})	0.825	0.771	0.660	0.797	0.594	0.702	0.796
σ^2(V_{DN})	0.681	0.594	0.435	0.635	0.353	0.493	0.634
$w_{T(1)}$	36.8%	36.8%	36.8%	36.8%	36.8%	36.8%	36.8%
$w_{T(2)}$	50.1%	50.1%	50.1%	50.1%	50.1%	50.1%	50.1%
$w_{T(3)}$	12.1%	12.1%	12.1%	12.1%	12.1%	12.1%	12.1%
$w_{T(4)}$	0.9%	0.9%	0.9%	0.9%	0.9%	0.9%	0.9%
$w_{DN(1)}$	27.0%	56.0%	7.8%	27.2%	65.7%	57.6%	24.6%
$w_{DN(2)}$	17.4%	15.4%	14.3%	24.7%	18.6%	16.3%	25.0%
$w_{DN(3)}$	24.4%	14.7%	30.9%	23.9%	11.4%	19.2%	23.7%
$w_{DN(4)}$	31.2%	13.9%	47.0%	24.3%	4.3%	7.0%	26.7%
n_{tot}	5530	1219	2673	1033	146	175	268
$n_{filtered}$	4974	1153	2272	994	139	173	236

Table A-14 Method 4 statistics, legend as in Method 1; class A: p value $DN \leq 0.25$, class B: $0.25 < p$ value $DN < 0.75$, class C: p value $DN \geq 0.75$ (dataset: average monthly temperatures, Breakpoint Corrected, 1 km buffer). All values are in percentage (%), except for n and $n_{filtered}$.

	World			**Asia**			**North America**			**Europe**			**Africa**			**South America**			**Oceania**		
	A	**B**	**C**	**A**	**B**	**C**	**A**	**B**	**C**	**A**	**B**	**C**	**A**	**B**	**C**	**A**	**B**	**C**	**A**	**B**	**C**
$w_{T(1)}$	35.2	33.3	40.6	25.5	39.5	47.6	37.1	31.9	32.7	28.7	22.2	28.4	64-3	73.7	68.2	12.1	15.4	12.4	60.4	67.3	68.8
$w_{T(2)}$	52.4	54.1	45.2	54.3	43.9	32.6	51.5	55.9	54.1	62.6	67.6	65.2	14.3	26.3	28.0	69.7	65.4	66.4	18.7	19.2	21.5
$w_{T(3)}$	11.6	11.7	13.1	16.5	13.4	18.0	10.7	11.5	11.4	8.7	10.2	6.4	21.4	0.0	3.7	18.2	19.2	21.2	20.9	13.5	8.6
$w_{T(4)}$	0.8	0.9	1.1	3.7	3.2	1.7	0.7	0.7	1.8	0	0.0	0.0	0.0	0.0	0.0	0	0.0	0.0	0	0.0	1.1
$w_{DN(1)}$		27			56.0			7.8			27.2			65.7			57.6			24.6	
$w_{DN(2)}$		17.4			15.4			14.3			24.7			18.6			16.3			25	
$w_{DN(3)}$		24.4			14.7			30.9			23.9			11.4			19.2			23.7	
$w_{DN(4)}$		31.2			13.9			47			24.3			4.3			7			26.7	
n_{tot}	2208	838	1600	243	134	687	1513	430	320	369	190	341	14	15	76	33	14	72	91	55	103
$n_{filtered}$		4646			1044			2282			859			100			102			258	

A.5 Results of Breakpoint Adjusted dataset – Minimum Temperatures

Table A-15 Number of active stations from 1992 to 2013 and available stations after the application of thresholds for the reconstruction of mean annual temperature from the mean monthly data (dataset: minimum monthly temperatures, Breakpoint Corrected) and spatial localization. The selected thresholds are $Nm_i \geq 9$ and $Ny_j \geq 18$.

Localization	Active station 1992-2013	Selected stations $Nm_i \geq 9$ $Ny_j \geq 18$
Asia	3322 (12.9 %)	1097 (20.9 %)
North America	15642 (60.9 %)	2734 (52.2 %)
Europe	4087 (16 %)	900 (17.2%)
Africa	869 (3.4 %)	105 (2 %)
South America	536 (2.1 %)	104 (2 %)
Oceania	1168 (4.5 %)	290 (5.5 %)
Others	51 (0.2 %)	8 (0.2 %)
World	25675 (100 %)	5238 (100%)

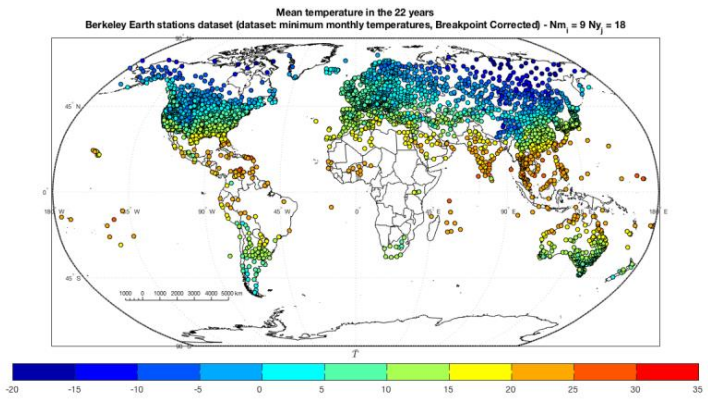

Figure A-39 Mean minimum temperature in the 22 years $\bar{T}$ for the selected air temperature stations (dataset: minimum monthly temperatures, Breakpoint Corrected, 1 km buffer).

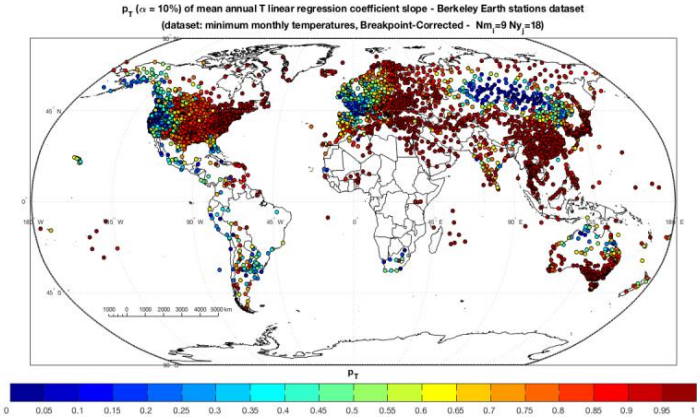

Figure A-40 Spatial distribution of the p value (p_T) of the slope of the temperature regression line for the selected Berkeley Earth stations (dataset: minimum monthly temperatures, Breakpoint Corrected, 1 km buffer).

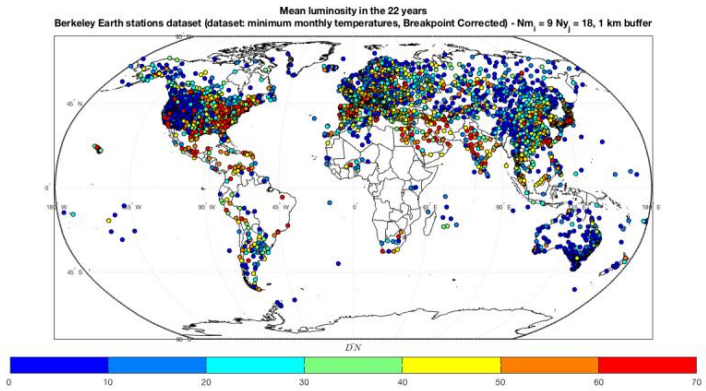

Figure A-41 Mean Digital Number value in the 22 years ($\overline{DN}$) in a 1 km buffer around the selected stations (dataset: minimum monthly temperatures, Breakpoint Corrected, 1 km buffer).

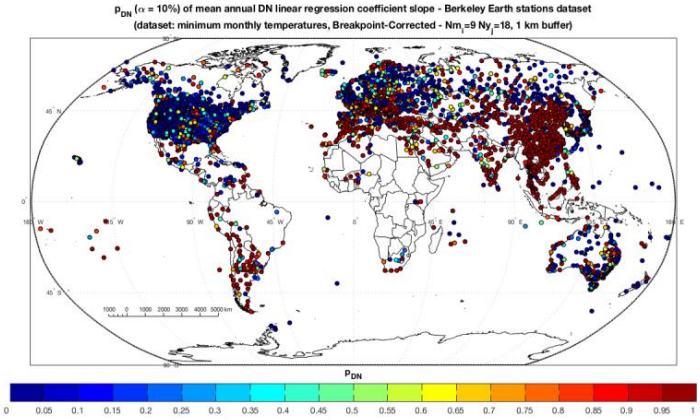

Figure A-42 Spatial distribution of the p value (p_{DN}) of the slope of the nightlights regression line for the selected Berkeley Earth stations (dataset: minimum monthly temperatures, Breakpoint Corrected, 1 km buffer).

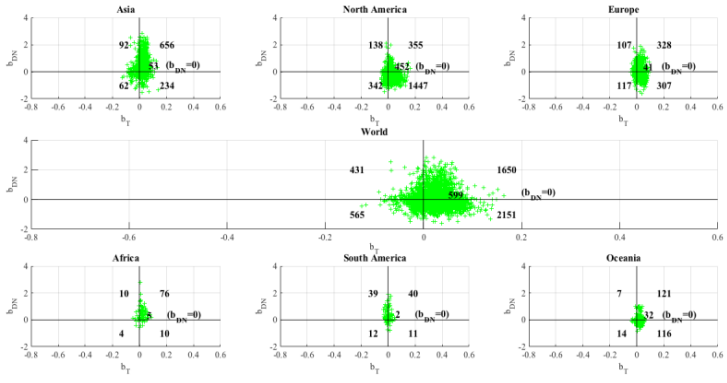

Figure A-43 Slope of T (b_T) and DN (b_{DN}) regression trend lines. Sectors 1 and 3 correspond to concordant trends, while sectors 2 and 4 refer to discordant trends. The number of stations included in each sector is in bold, as well as the number of stations with DN systematically equal to zero (b_{DN} = 0) on the horizontal axis (dataset: minimum monthly temperatures, Breakpoint Corrected, 1 km buffer).

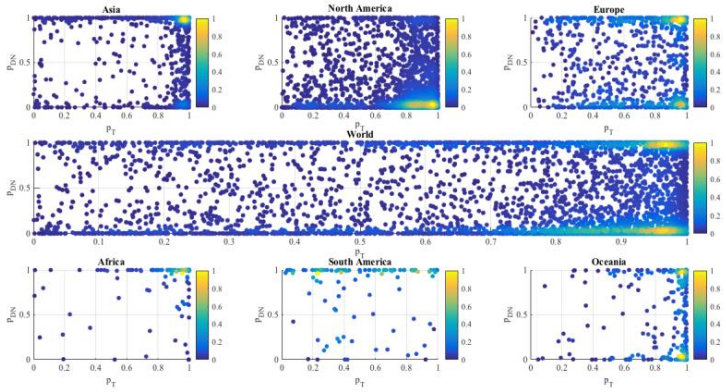

Figure A-44 *P* values density plots at global and continental scale (dataset: minimum monthly temperatures, Breakpoint Corrected, 1 km buffer).

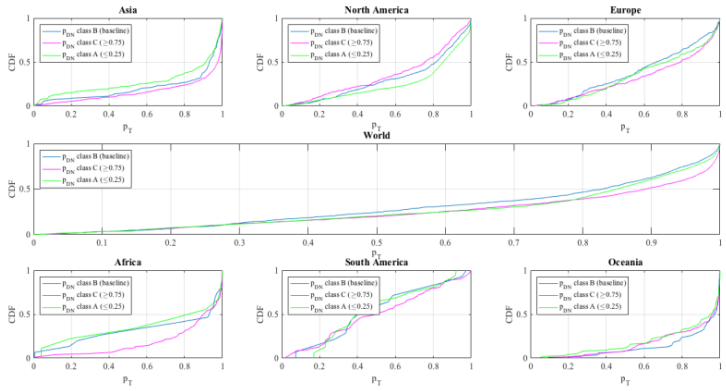

Figure A-45 Method 4: cumulative distribution function CDF of p_T based on the three different nightlights configurations i.e., class A: $p_{DN} \leq 0.25$, class B: $0.25 < p_{DN} < 0.75$, class C: $p_{DN} \geq 0.75$ (dataset: minimum monthly temperatures, Breakpoint Corrected, 1 km buffer).

Table A-16 Method 1 statistics; *w* refers to the probability of occurrence of classes of significance from 1 (++) to 4 (--); V_T: variable temperature *T*; V_{DN}: variable nightlights *DN*; CI: concordance index; E(CI): expected mean of CI; σ(CI):standard deviation of CI; z: standardized value; $E(V_T)$, $E(V_{DN})$, $\sigma(V_T)$ and $\sigma(V_{DN})$ refer to expected mean and standard deviation; *n*: total number of stations; $n_{filtered}$: same as *n* excluding stations with *DN* trend equal to 0 (dataset: minimum monthly temperatures, Breakpoint Corrected, 1 km buffer).

	World	**Asia**	**North America**	**Europe**	**Africa**	**South America**	**Oceania**
CI	-0.026	0.341	-0.239	0.024	0.405	0.022	0.015
E(CI)	-0.05	0.26	-0.2	0.004	0.37	0	-0.006
σ(CI)	0.01	0.02	0.01	0.02	0.06	0.04	0.05
σ^2(CI)	0.0001	0.0001	0.0001	0.0003	0.0032	0.0025	0.0016
z	2.93	4.2	-3.8	1.2	0.7	0.5	0.5
$E(V_T)$	0.44	0.60	0.40	0.32	0.57	0.00	0.67
$\sigma(V_T)$	0.55	0.55	0.52	0.56	0.53	0.58	0.44
$\sigma^2(V_T)$	0.30	0.31	0.27	0.32	0.28	0.34	0.20
$E(V_{DN})$	-0.12	0.43	-0.49	0.01	0.65	0.55	-0.01
$\sigma(V_{DN})$	0.82	0.78	0.65	0.79	0.58	0.67	0.79
$\sigma^2(V_{DN})$	0.67	0.60	0.42	0.63	0.34	0.45	0.63
$w_{T(1)}$	31.4%	53.1%	23.1%	21.7%	44.0%	8.8%	52.7%
$w_{T(2)}$	47.7%	32.2%	55.8%	49.7%	42.0%	38.2%	38.4%
$w_{T(3)}$	19.4%	11.7%	19.9%	28.1%	11.0%	50.0%	8.5%
$w_{T(4)}$	1.5%	3.1%	1.1%	0.6%	3.0%	2.9%	0.4%
$w_{DN(1)}$	25.1%	57.0%	6.8%	26.0%	63.0%	60.8%	24.8%
$w_{DN(2)}$	17.3%	14.7%	14.8%	24.7%	23.0%	16.7%	24.8%
$w_{DN(3)}$	24.5%	13.8%	30.3%	24.8%	9.0%	16.7%	24.4%
$w_{DN(4)}$	33.1%	14.6%	48.1%	24.6%	5.0%	5.9%	26.0%
n_{tot}	5238	1097	2734	900	105	104	290
$n_{filtered}$	4646	1044	2282	859	100	102	258

Table A-17 Method 2 statistics, legend as in Method 1 (dataset: minimum monthly temperatures, Breakpoint Corrected, 1 km buffer).

	World	**Asia**	**North America**	**Europe**	**Africa**	**South America**	**Oceania**
CI	-0.026	0.257	-0.28	0.025	0.543	0.17	0.043
E(CI)	-0.05	-0.05	-0.05	-0.05	-0.05	-0.05	-0.05
σ(CI)	0.01	0.02	0.01	0.02	0.05	0.05	0.04
σ^2(CI)	0.0001	0.0003	0.0001	0.0004	0.0034	0.0033	0.0013
z	2.9	16.9	-18.6	3.5	11.5	4.6	2.2
E(V_T)	0.44	0.44	0.44	0.44	0.44	0.44	0.44
σ(V_T)	0.55	0.55	0.55	0.55	0.55	0.55	0.55
σ^2(V_T)	0.30	0.30	0.30	0.30	0.30	0.30	0.30
E(V_{DN})	-0.12	-0.12	-0.12	-0.12	-0.12	-0.12	-0.12
σ(V_{DN})	0.82	0.82	0.82	0.82	0.82	0.82	0.82
σ^2(V_{DN})	0.67	0.67	0.67	0.67	0.67	0.67	0.67
$w_{T(1)}$	31.4%	31.4%	31.4%	31.4%	31.4%	31.4%	31.4%
$w_{T(2)}$	47.7%	47.7%	47.7%	47.7%	47.7%	47.7%	47.7%
$w_{T(3)}$	19.4%	19.4%	19.4%	19.4%	19.4%	19.4%	19.4%
$w_{T(4)}$	1.5%	1.5%	1.5%	1.5%	1.5%	1.5%	1.5%
$w_{DN(1)}$	25.1%	25.1%	25.1%	25.1%	25.1%	25.1%	25.1%
$w_{DN(2)}$	17.3%	17.3%	17.3%	17.3%	17.3%	17.3%	17.3%
$w_{DN(3)}$	24.5%	24.5%	24.5%	24.5%	24.5%	24.5%	24.5%
$w_{DN(4)}$	33.1%	33.1%	33.1%	33.1%	33.1%	33.1%	33.1%
n_{tot}	5238	1097	2734	900	105	104	290
$n_{filtered}$	4646	1044	2282	859	100	102	258

Table A-18 Method 3 statistics, legend as in Method 1 (dataset: minimum monthly temperatures, Breakpoint Corrected, 1 km buffer).

	World	Asia	North America	Europe	Africa	South America	Oceania
CI	-0.026	0.257	-0.28	0.025	0.543	0.17	0.043
E(CI)	-0.051	0.189	-0.216	0.006	0.286	0.242	-0.004
σ(CI)	0.009	0.018	0.011	0.019	0.054	0.055	0.035
σ^2(CI)	0.0001	0.0003	0.0001	0.0004	0.0030	0.0031	0.0012
z	2.93	8.23	-2.10	0.97	2.18	-3.96	0.54
E(V_T)	0.440	0.440	0.440	0.440	0.440	0.440	0.440
σ(V_T)	0.550	0.550	0.550	0.550	0.550	0.550	0.550
σ^2(V_T)	0.303	0.303	0.303	0.303	0.303	0.303	0.303
E(V_{DN})	-0.116	0.429	-0.490	0.013	0.650	0.549	-0.010
σ(V_{DN})	0.820	0.776	0.649	0.793	0.581	0.670	0.794
σ^2(V_{DN})	0.673	0.603	0.422	0.629	0.338	0.449	0.631
$w_{T(1)}$	31.4%	31.4%	31.4%	31.4%	31.4%	31.4%	31.4%
$w_{T(2)}$	47.7%	47.7%	47.7%	47.7%	47.7%	47.7%	47.7%
$w_{T(3)}$	19.4%	19.4%	19.4%	19.4%	19.4%	19.4%	19.4%
$w_{T(4)}$	1.5%	1.5%	1.5%	1.5%	1.5%	1.5%	1.5%
$w_{DN(1)}$	25.1%	57.0%	6.8%	26.0%	63.0%	60.8%	24.8%
$w_{DN(2)}$	17.3%	14.7%	14.8%	24.7%	23.0%	16.7%	24.8%
$w_{DN(3)}$	24.5%	13.8%	30.3%	24.8%	9.0%	16.7%	24.4%
$w_{DN(4)}$	33.1%	14.6%	48.1%	24.6%	5.0%	5.9%	26.0%
n_{tot}	5238	1097	2734	900	105	104	290
$n_{filtered}$	4646	1044	2282	859	100	102	258

Table A-19 Method 4 statistics, legend as in Method 1; class A: p value $DN \leq 0.25$, class B: $0.25 < p$ value $DN < 0.75$, class C: p value $DN \geq 0.75$ (dataset: minimum monthly temperatures, Breakpoint Corrected, 1 km buffer). All values are in percentage (%), except for n and $n_{filtered}$.

	World			**Asia**			**North America**			**Europe**			**Africa**			**South America**			**Oceania**		
	A	**B**	**C**	**A**	**B**	**C**	**A**	**B**	**C**	**A**	**B**	**C**	**A**	**B**	**C**	**A**	**B**	**C**	**A**	**B**	**C**
$w_{T(1)}$	28	24.7	39.6	38.57	43.3	59.7	0.27	18.1	13.1	0.21	16.8	24.6	0.47	46.7	43.4	0	14.3	9.7	50	54.5	54.4
$w_{T(2)}$	51.5	50.7	40.9	39.46	41.8	27.9	0.55	56.3	59.4	0.48	51.6	49.9	0.27	26.7	46.1	0.38	28.6	40.3	39	38.2	37.9
$w_{T(3)}$	18.8	23.4	18.1	14.35	11.2	10.9	0.17	24.7	26.3	0.3	31.6	24.3	0.2	20.0	9.2	0.63	57.1	45.8	10	7.3	7.8
$w_{T(4)}$	1.7	1.2	1.4	7.62	3.7	1.5	0.01	0.9	1.3	0	0.0	1.2	0.07	6.7	1.3	0	0.0	4.2	1	0.0	0.0
$w_{DN(1)}$		25.1			57.0			6.8			26.0			63.0			60.8			24.8	
$w_{DN(2)}$		17.3			14.7			14.8			24.7			23.0			16.7			24.8	
$w_{DN(3)}$		24.5			13.8			30.3			24.8			9.0			16.7			24.4	
$w_{DN(4)}$		33.1			14.6			48.1			24.6			5.0			5.9			26.0	
n_{tot}	2208	838	1600	243	134	687	1513	430	320	369	190	341	14	15	76	33	14	72	91	55	103
$n_{filtered}$		4646			1044			2282			859			100			102			258	

A.6 Results of Single-Valued dataset – Average Temperatures

Table A-20 Number of active stations from 1992 to 2013 and available stations after the application of thresholds for the reconstruction of mean annual temperature from the mean monthly data (dataset: average monthly temperatures, Single-value, 1 km buffer) and spatial localization. The selected thresholds are $Nm_i \geq 9$ and $Ny_j \geq 18$.

Localization	Active station 1992-2013	Selected stations $Nm_i \geq 9$ $Ny_j \geq 18$
Asia	3918 (14.1 %)	1500 (21.3%)
North America	16242 (58.2 %)	3382 (48.1 %)
Europe	4417 (15.8 %)	1218 (17.3 %)
Africa	1173 (4.2 %)	276 (4 %)
South America	796 (2.8 %)	232 (3.3 %)
Oceania	1218 (4.4 %)	399 (5.7 %)
Others	127 (4.6 %)	22 (0.3 %)
World	27891 (100 %)	7029 (100%)

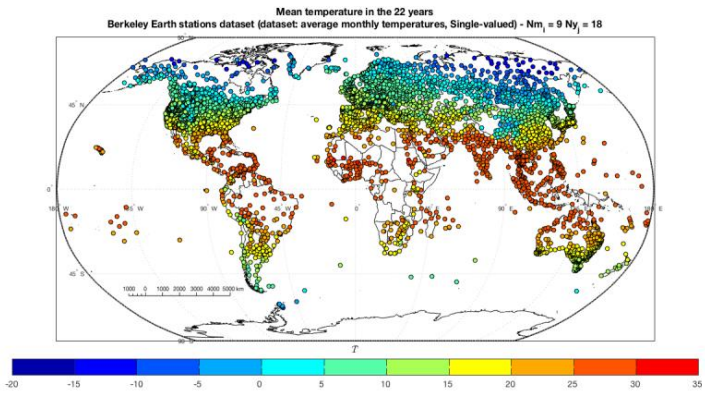

Figure A-46 Mean average temperature in the 22 years $\bar{T}$ for the selected air temperature stations (dataset: average monthly temperatures, Single-valued, 1 km buffer).

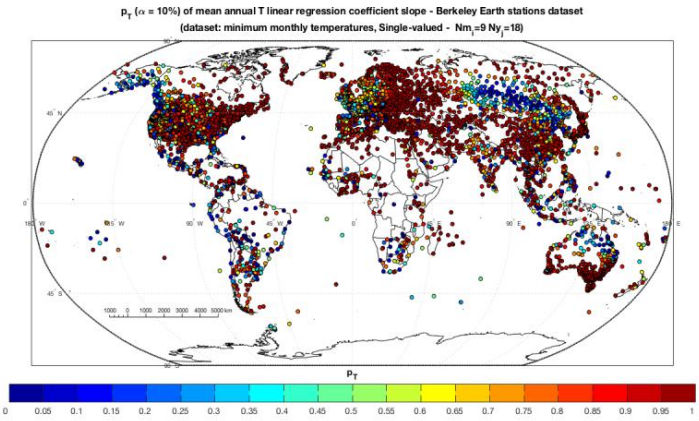

Figure A-47 Spatial distribution of the p value (p_T) of the slope of the temperature regression line for the selected Berkeley Earth stations (dataset: average monthly temperatures, Single-value, 1 km buffer).

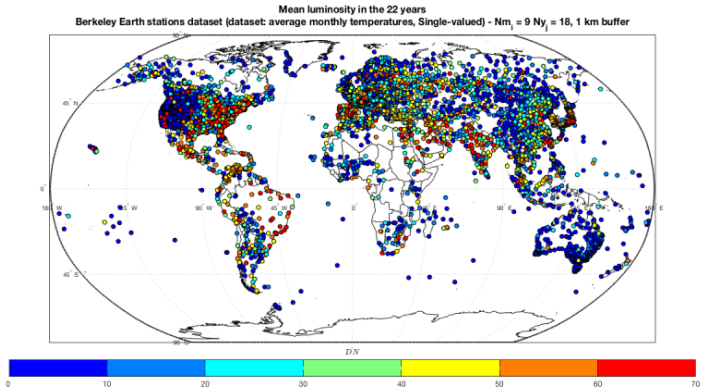

Figure A-48 Mean Digital Number value in the 22 years ($\overline{DN}$) in a 1 km buffer around the selected stations (dataset: average monthly temperatures, Single-valued, 1 km buffer).

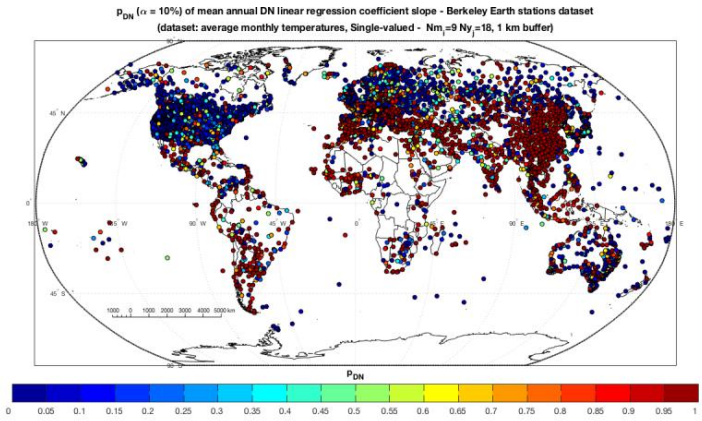

Figure A-49 Spatial distribution of the p value (p_{DN}) of the slope of the nightlights regression line for the selected Berkeley Earth stations (dataset: average monthly temperatures, Single-valued, 1 km buffer).

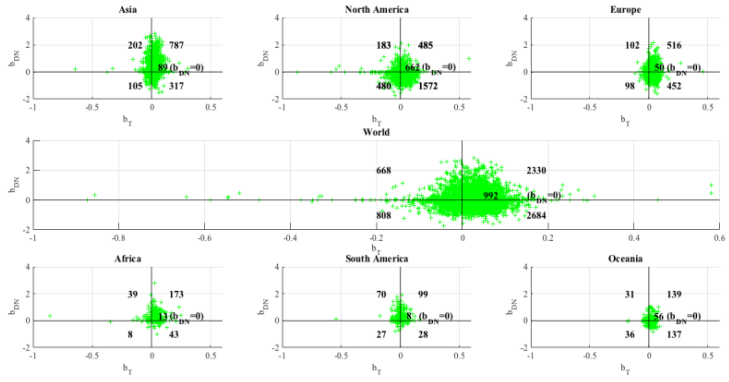

Figure A-50 Slope of T (b_T) and DN (b_{DN}) regression trend lines. Sectors 1 and 3 correspond to concordant trends, while sectors 2 and 4 refer to discordant trends. The number of stations included in each sector is in bold, as well as the number of stations with DN systematically equal to zero (b_{DN} = 0) on the horizontal axis (dataset: average monthly temperatures, Single-Valued, 1 km buffer).

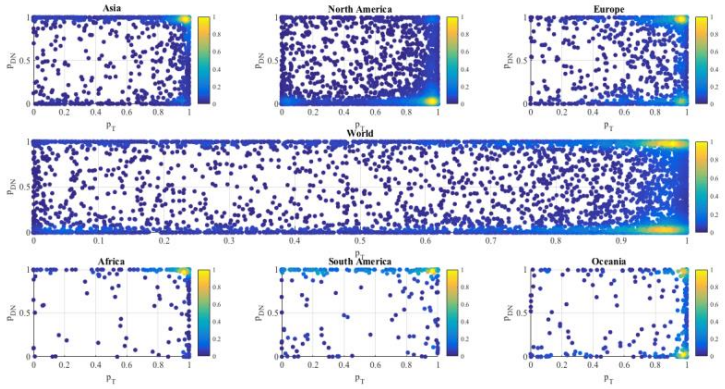

Figure A-51 *P* values density plots at global and continental scale (dataset: average monthly temperatures, Single-Valued, 1 km buffer).

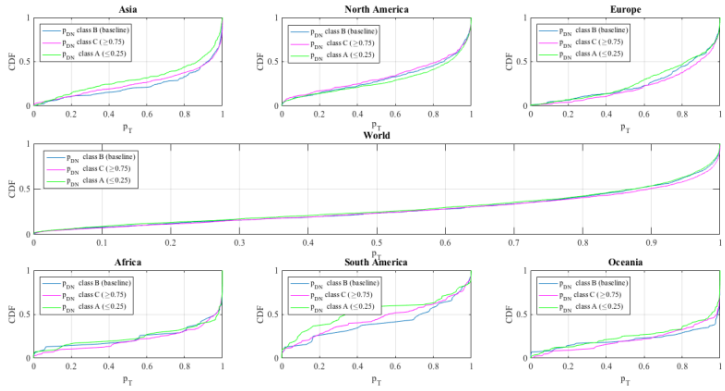

Figure A-52 Method 4: cumulative distribution function CDF of p_T based on the three different nightlights configurations i.e., class A: $p_{DN} \leq 0.25$, class B: $0.25 < p_{DN} < 0.75$, class C: $p_{DN} \geq 0.75$ (dataset: average monthly temperatures, Single-valued, 1 km buffer).

Table A-21 Method 1 statistics; *w* refers to the probability of occurrence of classes of significance from 1 (++) to 4 (--); V_T: variable temperature *T*; V_{DN}: variable nightlights *DN*; CI: concordance index; E(CI): expected mean of CI; σ(CI):standard deviation of CI; z: standardized value; $E(V_T)$, $E(V_{DN})$, $\sigma(V_T)$ and $\sigma(V_{DN})$ refer to expected mean and standard deviation; *n*: total number of stations; $n_{filtered}$: same as *n* excluding stations with *DN* trend equal to 0 (dataset: average monthly temperatures, Single-valued, 1 km buffer).

	World	**Asia**	**North America**	**Europe**	**Africa**	**South America**	**Oceania**
CI	0.008	0.213	-0.184	0.04	0.298	0.09	0.015
E(CI)	-0.01	0.18	-0.17	0.02	0.31	0.05	-0.01
σ(CI)	0.01	0.02	0.01	0.02	0.04	0.04	0.04
σ^2(CI)	0.0001	0.0003	0.0001	0.0003	0.0016	0.0017	0.0013
z	0.2	1.88	-1.5	0.95	-0.4	1	0.7
$E(V_T)$	0.42	0.45	0.38	0.49	0.56	0.10	0.54
$\sigma(V_T)$	0.63	0.63	0.65	0.54	0.63	0.71	0.64
$\sigma^2(V_T)$	0.40	0.39	0.42	0.29	0.40	0.51	0.40
$E(V_{DN})$	-0.05	0.40	-0.44	0.05	0.57	0.51	-0.02
$\sigma(V_{DN})$	0.83	0.63	0.68	0.80	0.65	0.69	0.80
$\sigma^2(V_{DN})$	0.69	0.40	0.47	0.64	0.42	0.48	0.63
$w_{T(1)}$	38.0%	42.4%	34.4%	35.6%	54.0%	23.2%	55.1%
$w_{T(2)}$	37.9%	33.8%	39.8%	46.4%	27.8%	31.3%	23.6%
$w_{T(3)}$	18.4%	19.8%	18.1%	16.4%	11.8%	33.0%	16.9%
$w_{T(4)}$	5.6%	4.0%	7.6%	1.6%	6.5%	12.5%	4.4%
$w_{DN(1)}$	27.7%	54.1%	8.8%	28.3%	58.6%	58.0%	24.2%
$w_{DN(2)}$	18.4%	16.0%	15.8%	24.7%	22.1%	17.4%	25.4%
$w_{DN(3)}$	23.2%	15.2%	29.0%	22.5%	12.9%	17.4%	23.6%
$w_{DN(4)}$	30.7%	14.7%	46.4%	24.6%	6.5%	7.1%	26.8%
n_{tot}	7029	1500	3382	1218	276	232	399
$n_{filtered}$	6138	1411	2720	1168	263	224	343

Table A-22 Method 2 statistics, legend as in Method 1 (dataset: average monthly temperatures, Single-valued, 1 km buffer).

	World	Asia	North America	Europe	Africa	South America	Oceania
CI	0.008	0.213	-0.184	0.04	0.298	0.09	0.015
E(CI)	-0.01	-0.02	-0.02	-0.02	-0.02	-0.02	-0.02
σ(CI)	0.01	0.02	0.01	0.02	0.04	0.04	0.03
σ^2(CI)	0.0001	0.0003	0.0001	0.0003	0.0015	0.0018	0.0012
z	0.2	14.1	-13.3	3.4	8.3	2.7	1.1
E(V_T)	0.42	0.42	0.42	0.42	0.42	0.42	0.42
σ(V_T)	0.63	0.63	0.63	0.63	0.63	0.63	0.63
σ^2(V_T)	0.40	0.40	0.40	0.40	0.40	0.40	0.40
E(V_{DN})	-0.05	-0.05	-0.05	-0.05	-0.05	-0.05	-0.05
σ(V_{DN})	0.83	0.83	0.83	0.83	0.83	0.83	0.83
σ^2(V_{DN})	0.69	0.69	0.69	0.69	0.69	0.69	0.69
$w_{T(1)}$	38.0%	38.0%	38.0%	38.0%	38.0%	38.0%	38.0%
$w_{T(2)}$	37.9%	37.9%	37.9%	37.9%	37.9%	37.9%	37.9%
$w_{T(3)}$	18.4%	18.4%	18.4%	18.4%	18.4%	18.4%	18.4%
$w_{T(4)}$	5.6%	5.6%	5.6%	5.6%	5.6%	5.6%	5.6%
$w_{DN(1)}$	27.7%	27.7%	27.7%	27.7%	27.7%	27.7%	27.7%
$w_{DN(2)}$	18.4%	18.4%	18.4%	18.4%	18.4%	18.4%	18.4%
$w_{DN(3)}$	23.2%	23.2%	23.2%	23.2%	23.2%	23.2%	23.2%
$w_{DN(4)}$	30.7%	30.7%	30.7%	30.7%	30.7%	30.7%	30.7%
n_{tot}	7029	1500	3382	1218	276	232	399
$n_{filtered}$	6138	1411	2720	1168	263	224	343

Table A-23 Method 3 statistics, legend as in Method 1 (dataset: average monthly temperatures, Single-valued, 1 km buffer).

	World	Asia	North America	Europe	Africa	South America	Oceania
CI	-0.008	0.213	-0.184	0.040	0.298	0.092	0.015
E(CI)	-0.01	0.17	-0.19	0.02	0.24	0.21	-0.01
σ(CI)	0.01	0.02	0.01	0.02	0.04	0.04	0.03
σ^2(CI)	0.0001	0.0003	0.0001	0.0003	0.0014	0.0017	0.0011
z	0.2	2.65	0.25	1.1	1.57	-2.99	-0.67
E(V_T)	0.422	0.422	0.422	0.422	0.422	0.422	0.422
σ(V_T)	0.632	0.632	0.632	0.632	0.632	0.632	0.632
σ^2(V_T)	0.399	0.399	0.399	0.399	0.399	0.399	0.399
E(V_{DN})	0.398	0.398	0.398	0.398	0.398	0.398	0.398
σ(V_{DN})	0.779	0.779	0.779	0.779	0.779	0.779	0.779
σ^2(V_{DN})	0.607	0.607	0.607	0.607	0.607	0.607	0.607
$w_{T(1)}$	38.0%	38.0%	38.0%	38.0%	38.0%	38.0%	38.0%
$w_{T(2)}$	37.9%	37.9%	37.9%	37.9%	37.9%	37.9%	37.9%
$w_{T(3)}$	18.4%	18.4%	18.4%	18.4%	18.4%	18.4%	18.4%
$w_{T(4)}$	5.6%	5.6%	5.6%	5.6%	5.6%	5.6%	5.6%
$w_{DN(1)}$	27.7%	54.1%	8.8%	28.3%	58.6%	58.0%	24.2%
$w_{DN(2)}$	18.4%	16.0%	15.8%	24.7%	22.1%	17.4%	25.4%
$w_{DN(3)}$	23.2%	15.2%	29.0%	22.5%	12.9%	17.4%	23.6%
$w_{DN(4)}$	30.7%	14.7%	46.4%	24.6%	6.5%	7.1%	26.8%
n_{tot}	7029	1500	3382	1218	276	232	399
$n_{filtered}$	6138	1411	2720	1168	263	224	343

Table A-24 Method 4 statistics, legend as in Method 1; class A: *p* value $DN \leq 0.25$, class B: $0.25 < p$ value $DN < 0.75$, class C: *p* value $DN \geq 0.75$ (dataset: average monthly temperatures, Single-valued, 1 km buffer). All values are in percentage (%), except for *n* and $n_{filtered}$.

	World			**Asia**			**North America**			**Europe**			**Africa**			**South America**			**Oceania**		
	A	**B**	**C**	**A**	**B**	**C**	**A**	**B**	**C**	**A**	**B**	**C**	**A**	**B**	**C**	**A**	**B**	**C**	**A**	**B**	**C**
$w_{T(1)}$	36.1	36.6	40.9	34.5	42.4	45.1	35.7	32.1	32.1	33.8	33.3	38.3%	58.5	54.8	52.9	19.5	21.9	24.5	51.0	63.4	54.9
$w_{T(2)}$	39.1	40.0	35.5	37	38.2	31.7	39.9	40.7	38.7	46.2	48.1	45.8%	22	29.0	28.8	22	40.6	31.8	23.7	18.3	26.3
$w_{T(3)}$	18.7	18.2	18.2	24.7	17.3	18.6	17.1	20.0	19.9	18.4	16.9%	14.3%	12.2	9.7	12.0	41.5	25.0	32.5	20.1	11.3	16.5
$w_{T(4)}$	6	5.2	5.3	3.8	2.1	4.5	7.3	7.2	9.3	1.6	1.7%	1.6%	7.3	6.5	6.3	17.1	12.5	11.3	5	7.0	2.3
$w_{DN(1)}$		27.7			54.1			8.8			28.3			58.6			58			24.2	
$w_{DN(2)}$		18.4			16			15.8			24.7			22.1			17.4			25.4	
$w_{DN(3)}$		23.2			15.2			29			22.5			12.9			17.4			23.6	
$w_{DN(4)}$		30.7			14.7			46.4			24.6			6.5			7.1			26.8	
n_{tot}	2746	1062	2330	316	191	904	1769	499	452	435	237	496	41	31	191	41	32	151	139	71	133
$n_{filtered}$		6138			1411			2720			1168			263			224			343	

A.7 Results of Single-Valued dataset – Minimum Temperatures

Table A-25 Number of active stations from 1992 to 2013 and available stations after the application of thresholds for the reconstruction of mean annual temperature from the mean monthly data (dataset: minimum monthly temperatures, Single-value, 1 km buffer) and spatial localization. The selected thresholds are $Nm_i \geq 9$ and $Ny_j \geq 18$.

Localization	Active station 1992-2013	Selected stations $Nm_i \geq 9$ $Ny_j \geq 18$
Asia	3966 (13.5 %)	1623 (20.7 %)
North America	17475 (59.4 %)	3775 (48.2 %)
Europe	4537 (15.4 %)	1493 (19.1 %)
Africa	1302 (4.4 %)	259 (3.3 %)
South America	815 (2.8 %)	214 (2.7 %)
Oceania	1222 (4.1 %)	458 (5.8 %)
Others	105 (0.4 %)	14 (0.2 %)
World	29422 (100 %)	7836 (100%)

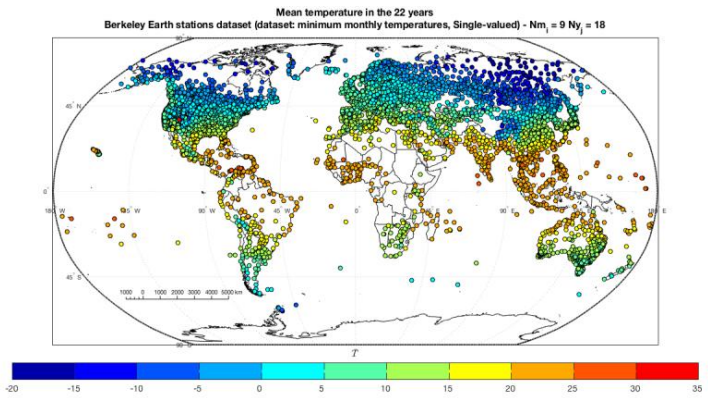

Figure A-53 Mean minimum temperature in the 22 years $\bar{T}$ for the selected air temperature stations (dataset: minimum monthly temperatures, Single-valued, 1 km buffer).

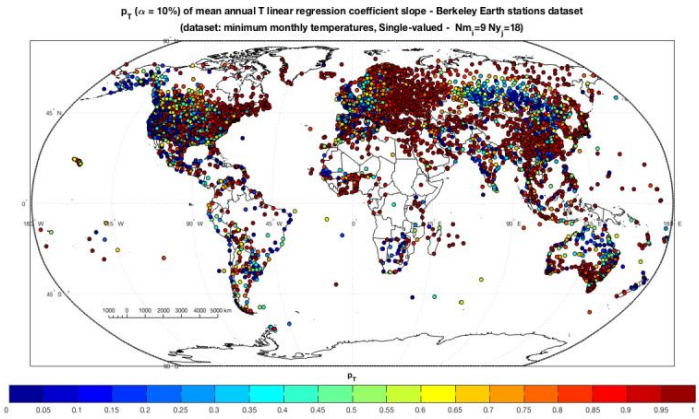

Figure A-54 Spatial distribution of the p value (p_T) of the slope of the temperature regression line for the selected Berkeley Earth stations (dataset: minimum monthly temperatures, Single-value, 1 km buffer).

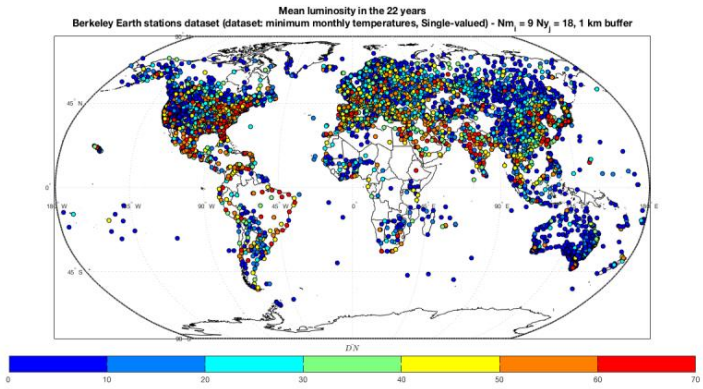

Figure A-55 Mean Digital Number value in the 22 years ($\overline{DN}$) in a 1 km buffer around the selected stations (dataset: minimum monthly temperatures, Single-valued, 1 km buffer).

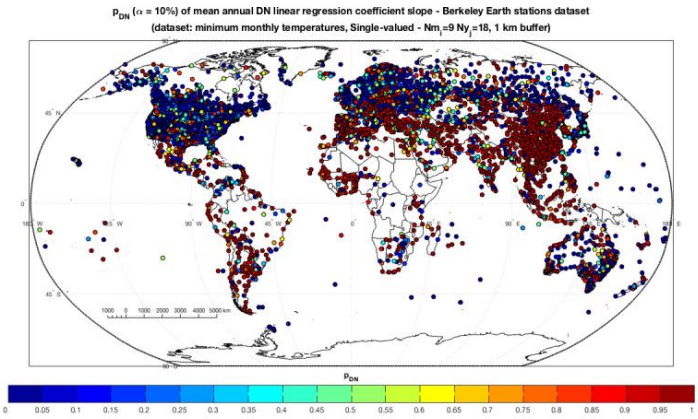

Figure A-56 Spatial distribution of the p value (p_{DN}) of the slope of the nightlights regression line for the selected Berkeley Earth stations (dataset: minimum monthly temperatures, Single-valued, 1 km buffer).

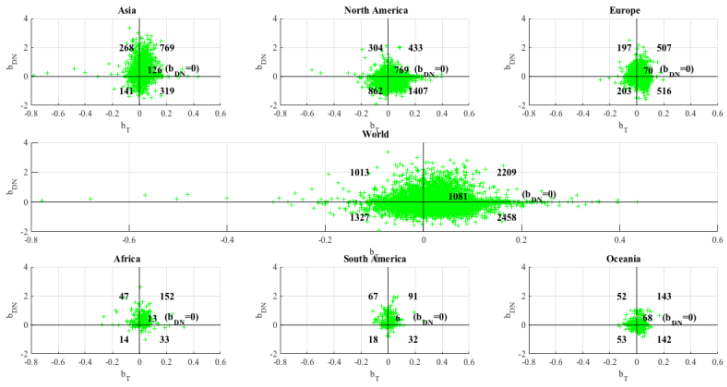

Figure A-57 Slope of T (b_T) and DN (b_{DN}) regression trend lines. Sectors 1 and 3 correspond to concordant trends, while sectors 2 and 4 refer to discordant trends. The number of stations included in each sector is in bold, as well as the number of stations with DN systematically equal to zero (b_{DN} = 0) on the horizontal axis (dataset: minimum monthly temperatures, Single-Valued, 1 km buffer).

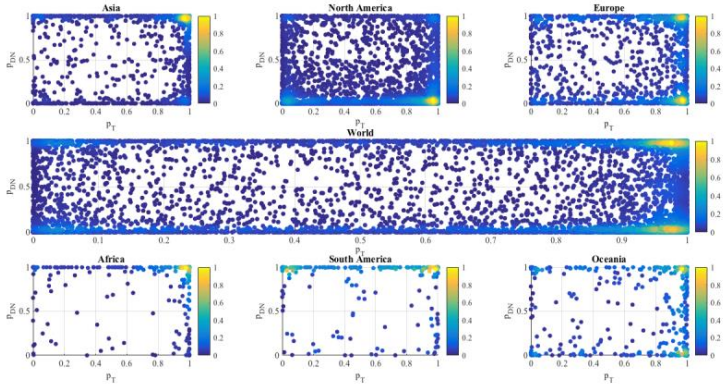

Figure A-58 *P* values density plots at global and continental scale (dataset: minimum monthly temperatures, Single-Valued, 1 km buffer).

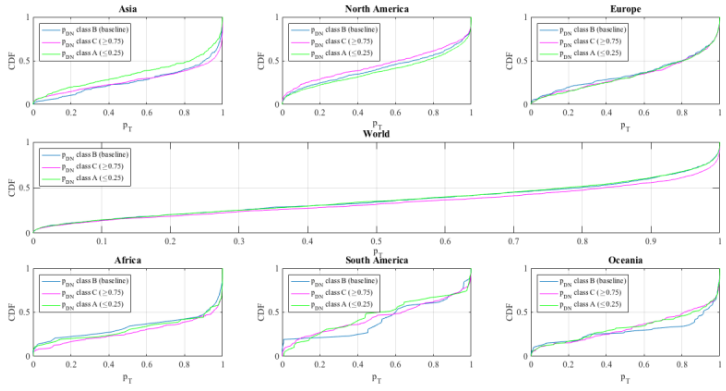

Figure A-59 Method 4: cumulative distribution function CDF of p_T based on the three different nightlights configurations i.e., class A: $p_{DN} \leq 0.25$, class B: $0.25 < p_{DN} < 0.75$, class C: $p_{DN} \geq 0.75$ (dataset: minimum monthly temperatures, Single-valued, 1 km buffer).

Table A-26 Method 1 statistics; *w* refers to the probability of occurrence of classes of significance from 1 (++) to 4 (--); V_T: variable temperature *T*; V_{DN}: variable nightlights *DN*; CI: concordance index; E(CI): expected mean of CI; σ(CI):standard deviation of CI; z: standardized value; $E(V_T)$, $E(V_{DN})$, $\sigma(V_T)$ and $\sigma(V_{DN})$ refer to expected mean and standard deviation; *n*: total number of stations; $n_{filtered}$: same as *n* excluding stations with *DN* trend equal to 0 (dataset: minimum monthly temperatures, Single-valued, 1 km buffer).

	World	**Asia**	**North America**	**Europe**	**Africa**	**South America**	**Oceania**
CI	0.008	0.203	-0.108	0.003	0.27	0.04	-0.006
E(CI)	-0.06	0.15	-0.09	-0.0014	0.25	0.06	-0.004
σ(CI)	0.01	0.02	0.01	0.01	0.04	0.04	0.03
σ^2(CI)	0.0001	0.0003	0.0001	0.0002	0.0018	0.0019	0.001
z	6.80	2.65	-1.80	0.44	0.50	-0.50	-0.07
$E(V_T)$	0.28	0.45	0.19	0.32	0.43	0.12	0.35
$\sigma(V_T)$	0.71	0.68	0.73	0.66	0.70	0.72	0.71
$\sigma^2(V_T)$	0.50	0.46	0.53	0.44	0.49	0.52	0.51
$E(V_{DN})$	-0.22	0.38	-0.44	-0.005	0.58	0.52	-0.01
$\sigma(V_{DN})$	0.93	0.79	0.68	0.80	0.64	0.69	0.80
$\sigma^2(V_{DN})$	0.87	0.63	0.69	0.64	0.41	0.48	0.65
$w_{T(1)}$	34%	43.4%	29.3%	31.2 %	48.4%	25.5%	40%
$w_{T(2)}$	32.3%	29.3%	31.9%	38.4%	25.2%	29.8%	30%
$w_{T(3)}$	23.4%	20.1%	25.8%	22.8%	17.1%	32.2%	19.2%
$w_{T(4)}$	10.3%	7.2%	12.9%	7.5%	9.3%	12.5%	10.8%
$w_{DN(1)}$	33.9%	53.8%	9%	25.9%	61%	59.1%	25.1%
$w_{DN(2)}$	4.8%	15.5%	15.5%	23.5%	19.9%	16.8%	24.9%
$w_{DN(3)}$	5.4%	14.6%	28.6%	24.7%	13.4%	16.3%	22.3%
$w_{DN(4)}$	55.9%	16.2%	46.9%	25.8%	5.7%	7.7%	27.7%
n_{tot}	7836	1623	3755	1493	259	214	458
$n_{filtered}$	6138	1497	3006	1423	246	208	390

Table A-27 Method 2 statistics, legend as in Method 1 (dataset: minimum monthly temperatures, Single-valued, 1 km buffer).

	World	**Asia**	**North America**	**Europe**	**Africa**	**South America**	**Oceania**
CI	0.008	0.203	-0.108	0.003	0.27	0.04	-0.006
E(CI)	-0.06	-0.06	-0.06	-0.06	-0.06	-0.06	-0.06
σ(CI)	0.01	0.04	0.01	0.02	0.05	0.05	0.04
σ^2(CI)	0.0001	0.0015	0.0002	0.0003	0.0022	0.0026	0.0014
z	6.8	6.56	-4.8	3.15	6.6	2	1.35
E(V_T)	0.28	0.28	0.28	0.28	0.28	0.28	0.28
σ(V_T)	0.71	0.71	0.71	0.71	0.71	0.71	0.71
σ^2(V_T)	0.50	0.50	0.50	0.50	0.50	0.50	0.50
E(V_{DN})	-0.22	-0.22	-0.22	-0.22	-0.22	-0.22	-0.22
σ(V_{DN})	0.93	0.93	0.93	0.93	0.93	0.93	0.93
σ^2(V_{DN})	0.87	0.87	0.87	0.87	0.87	0.87	0.87
$w_{T(1)}$	34%	34%	34%	34%	34%	34%	34%
$w_{T(2)}$	32.3%	32.3%	32.3%	32.3%	32.3%	32.3%	32.3%
$w_{T(3)}$	23.4%	23.4%	23.4%	23.4%	23.4%	23.4%	23.4%
$w_{T(4)}$	10.3%	10.3%	10.3%	10.3%	10.3%	10.3%	10.3%
$w_{DN(1)}$	33.9%	33.9%	33.9%	33.9%	33.9%	33.9%	33.9%
$w_{DN(2)}$	4.8%	4.8%	4.8%	4.8%	4.8%	4.8%	4.8%
$w_{DN(3)}$	5.4%	5.4%	5.4%	5.4%	5.4%	5.4%	5.4%
$w_{DN(4)}$	55.9%	55.9%	55.9%	55.9%	55.9%	55.9%	55.9%
n_{tot}	7836	1623	3755	1493	259	214	458
$n_{filtered}$	6138	1497	3006	1423	246	208	390

Table A-28 Method 3 statistics, legend as in Method 1 (dataset: minimum monthly temperatures, Single-valued, 1 km buffer).

	World	**Asia**	**North America**	**Europe**	**Africa**	**South America**	**Oceania**
CI	0.008	0.203	-0.108	0.003	0.27	0.04	-0.006
E(CI)	-0.06	0.10	-0.125	-0.001	0.165	0.146	-0.0036
σ(CI)	0.01	0.01	0.02	0.01	0.02	0.04	0.04
σ^2(CI)	0.0001	0.0003	0.0001	0.0003	0.0017	0.0020	0.0010
z	6.8	10.3	0.85	0.4	5.25	-2.65	-0.06
E(V_T)	0.422	0.422	0.422	0.422	0.422	0.422	0.422
σ(V_T)	0.632	0.632	0.632	0.632	0.632	0.632	0.632
σ^2(V_T)	0.399	0.399	0.399	0.399	0.399	0.399	0.399
E(V_{DN})	-0.22	0.38	-0.44	-0.005	0.58	0.52	-0.01
σ(V_{DN})	0.93	0.79	0.68	0.80	0.64	0.69	0.80
σ^2(V_{DN})	0.87	0.63	0.69	0.64	0.41	0.48	0.65
$w_{T(1)}$	34%	34%	34%	34%	34%	34%	34%
$w_{T(2)}$	32.3%	32.3%	32.3%	32.3%	32.3%	32.3%	32.3%
$w_{T(3)}$	23.4%	23.4%	23.4%	23.4%	23.4%	23.4%	23.4%
$w_{T(4)}$	10.3%	10.3%	10.3%	10.3%	10.3%	10.3%	10.3%
$w_{DN(1)}$	33.9%	53.8%	9%	25.9%	61%	59.1%	25.1%
$w_{DN(2)}$	4.8%	15.5%	15.5%	23.5%	19.9%	16.8%	24.9%
$w_{DN(3)}$	5.4%	14.6%	28.6%	24.7%	13.4%	16.3%	22.3%
$w_{DN(4)}$	55.9%	16.2%	46.9%	25.8%	5.7%	7.7%	27.7%
n_{tot}	7836	1623	3755	1493	259	214	458
$n_{filtered}$	6138	1497	3006	1423	246	208	390

Table A-29 Method 4 statistics, legend as in Method 1; class A: *p* value $DN \leq 0.25$, class B: $0.25 < p$ value $DN < 0.75$, class C: *p* value $DN \geq 0.75$ (dataset: minimum monthly temperatures, Single-valued, 1 km buffer). All values are in percentage (%), except for *n* and $n_{filtered}$.

	World			**Asia**			**North America**			**Europe**			**Africa**			**South America**			**Oceania**		
	A	**B**	**C**	**A**	**B**	**C**	**A**	**B**	**C**	**A**	**B**	**C**	**A**	**B**	**C**	**A**	**B**	**C**	**A**	**B**	**C**
$w_{T(1)}$	31.4	32.2	38	31.8	40.7	48.2	25.8	27.6	25.8	31.4	31.4	30.9	44.4	44.8	49.7	28.2	26.9	24.5	38.5	44.3	39.4
$w_{T(2)}$	33.5	33.4	30.4	35.2	35.4	25.9	30.4	32.4	30.4	38.6	36.4	39.3	27.8	24.1	24.9	23.1	38.5	30.1	29.5	27.8	31.6
$w_{T(3)}$	24.6	23.6	21.9	25.1	20.1	18.3	28.2	26.4	28.2	22.9	23.7	22.4	16.7	17.2	17.1	41	15.4	32.9	21.8	16.5	18.1
$w_{T(4)}$	10.5	10.8	9.7	7.9	3.7	7.7	15.7	13.6	15.7	7.2	8.5	7.4	11.1	13.8	8.3	7.7	19.2	12.6	10.3	11.4	11
$w_{DN(1)}$		33.9			53.8			9			25.9			61			59.1			24.2	
$w_{DN(2)}$		4.8			15.5			15.5			23.5			19.9			16.8			25.4	
$w_{DN(3)}$		5.4			14.6			28.6			24.7			13.4			16.3			23.6	
$w_{DN(4)}$		55.9			16.2			46.9			25.8			5.7			7.7			26.8	
n_{tot}	3098	1171	2504	189	189	953	1937	565	504	573	283	567	36	29	181	39	26	143	156	79	155
$n_{filtered}$		6138			1497			3006			1423			246			208			390	

B Further analyses on the effects of temperature on rockfall hazard

B.1 Characterization of rockfalls and possible processes leading to failure

In this section we fully report the results of the application of the method (summarised in Figure 3-14) and the main details of the case-by-case analysis of the rockfalls included in the inventory described in Chapter 3. In the latter, we include information about the climate anomalies detected, in combination with the spatio-temporal characteristics of each analysed event, i.e. the season and elevation of occurrence, the magnitude (if available) and the possible presence of permafrost in the detachment area. Moreover, we provide some possible explanation on the temperature-related processes that may have caused the slope failures.

Table B-1 Estimation of the non-exceedance probability P(V) associated with the variable V, where V may be temperature (T), precipitation (R) or temperature variation between the day of the failure and the days before (ΔT), and V is the correspondent value recorded when the failure occurred. The aggregation range is reported, i.e. daily range (d), weekly range (7d), monthly range (30d) and quarterly range (90d) for T and R, while ΔT refers to the previous day (-1d), three (-3d) and 6 days (-6d) before failure. Probability values related to T and ΔT are reported in each row referring to the mean, maximum and minimum temperature, in this order. The symbols ">" and "<" have been used when the values have been extrapolated. "NA" refers to an available data. The symbol "/" has been used when no precipitation have been recorded. Variables characterized by P(V)≤α/2 or P(V)≥1-α/2 (here α=0.2) are respectively in bold italic and bold (for R, we only report P(V)≥1-α/2).

No.	**Location**	V	**Temporal aggregation**						
			1d	**7d**	**30d**	**90d**	**-1d**	**-3d**	**-6d**
Western Italian Alps									
1	**Brenva**	T	0.58 0.61 0.62	0.80 0.75 0.82	0.25 0.29 0.33	0.45 0.38 0.54			
		ΔT					0.24 0.21 0.24	0.20 0.16 0.20	0.43 0.44 0.43
		R	/	0.78	0.67	**0.91**			
2	**Matterhorn I**	T	**0.94 0.94 0.96**	0.72 0.74 0.62	**0.93 0.93** 0.86	**0.95** 0.89 **0.94**			
		ΔT					0.64 0.56 0.84	**0.98 0.99 0.93**	0.77 0.78 0.77
		R	/	0.22	0.02	0.17			
3	**Matterhorn II**	T	0.80 0.49 0.75	**0.97 0.94 0.97**	**0.95 0.92 0.95**	**0.96 0.96 0.98**			

		ΔT					0.33 0.27 0.64	0.24 0.35 0.20	0.20 0.23 0.24
		R	0.65	0.35	0.18	0.18			
4	**Mont Pelà**	*T*	0.26 0.17 0.55	0.27 0.29 0.27	0.12 0.13 0.12	***<0.09 <0.09 <0.09***			
		ΔT					0.25 0.21 0.29	0.29 0.15 0.42	0.83 0.69 0.85
		R	0.72	0.80	0.68	<0.08			
5	**Matterhorn III**	*T*	**0.94 0.93 0.97**	0.78 0.74 0.80	0.76 0.76 0.75	0.71 0.72 0.69			
		ΔT					0.75 0.83 0.62	0.84 0.74 **0.93**	**0.94 0.97** 0.89
		R	/	0.18	0.27	0.41			
6	**Rocciamelone I**	*T*	0.88 0.35 **>0.94**	0.49 0.45 0.63	0.55 0.57 0.58	0.85 0.85 0.85			
		ΔT					0.21 0.12 0.45	0.67 0.41 0.78	0.86 0.67 **0.93**
		R	/	0.05	0.19	0.20			
7	**Matterhorn IV**	*T*	**0.98 0.94 0.96**	**0.93 0.94 0.90**	**0.93 0.91 0.91**	0.81 0.78 0.76			
		ΔT					0.64 0.56 0.84	0.58 0.54 0.69	0.80 0.78 0.84
		R	0.15	0.70	0.70	0.47			
8	**Rocciamelone II**	*T*	**>0.94** 0.85 **>0.94**	0.65 0.65 0.69	**>0.94 >0.94 >0.94**	**>0.94 >0.94 >0.94**			

		ΔT					0.25 0.27 0.11	0.59 0.70 0.74	0.83 0.88 0.87
		R	/	0.40	0.63	0.36			
9	**Belvedere**	*T*	**>0.96 >0.96 >0.96**	**>0.93 >0.93 >0.93**	0.89 **0.90 0.90**	0.81 0.82 0.81			
		ΔT					0.63 0.71 0.79	0.72 0.80 0.62	0.43 0.47 0.56
		R	/	/	0.54	0.40			
10	**Tré-la-Tête**	*T*	0.88 0.61 **>0.95**	0.70 0.59 0.70	0.48 0.57 0.48	0.66 0.63 0.67			
		ΔT					0.13 0.21 0.17	0.79 0.55 **0.93**	0.75 0.67 0.87
		R	0.46	0.63	0.79	**0.95**			
11	**Punta Patrì Nord**	*T*	0.21NA NA	***<0.09*** NA NA	0.31 NA NA	0.36 NA NA			
		ΔT					0.81NA NA	0.79 NA NA	***0.07*** NA NA
		R	0.37	0.73	0.61	0.55			
12	**Crammont**	*T*	**0.92 >0.95 0.93**	**>0.95 >0.95 >0.95**	0.30 0.31 0.37	0.66 0.63 0.67			
		ΔT					0.22 0.13 0.22	0.59 0.67 0.59	**0.94 0.94 0.94**
		R	/	0.87	0.51	**0.91**			
13	**Val Formazza**	*T*	0.28 0.32 0.74	0.60 0.68 0.38	0.50 0.67 0.56	0.38 0.35 0.33			

		ΔT					0.23 ***0.05*** 0.89	0.67 0.59 0.65	0.18 0.14 0.42	
		R	0.31	0.21	0.58	0.46				
14	**Monviso**	*T*	0.25 0.31 0.15	0.57 0.32 0.55	0.46 0.43 0.43	0.85 0.86 0.56				
		ΔT					0.15 0.29 0.24	0.36 0.69 0.11	0.57 0.53 0.69	
		R	/	/	0.19	0.50				
15	**Mont Rouge Peuterey**	*T*	0.83 0.77 0.84	0.77 0.75 0.82	0.67 0.80 0.69	0.83 0.83 0.83				
		ΔT					0.59 0.34 0.31	0.84 0.76 0.63	0.46 0.58 0.66	
		R	/	0.64	0.38	0.36				
16	**Matterhorn V**	*T*	0.84 0.80 0.88	0.83 0.80 **0.91**	**0.93 0.93 0.93**	0.88 0.87 0.88				
		ΔT					0.83 **0.91** 0.64	0.35 0.45 0.30	0.34 0.39 0.34	
		R	/	0.71	0.62	0.34				
17	**Melezet**	*T*	0.67 0.75 0.34	0.18 0.22 0.20	0.27 0.30 0.28	0.14 0.13 0.18				
		ΔT					0.72 0.74 0.86	0.72 **0.90** 0.31	**0.90 0.95** 0.72	
		R	/	0.12	0.62	0.29				
18	**Punta Tre Amici**	*T*	***<0.04*** 0.37 ***0.07***	0.38 0.53 0.27	0.39 0.57 0.29	0.75 0.75 0.60				

		ΔT					0.19 0.75 0.19	***0.03*** 0.19 ***0.07***	***0.04***	
		R	0.15	0.46	0.36	0.76				
19	**Gressoney-Saint-Jean**	*T*	0.81 0.76 0.83	0.53 0.49 0.61	0.74 0.73 0.74	***<0.09 <0.09 <0.09***				
		ΔT					0.77 0.73 0.76	0.76 0.80 0.77	0.63 0.74 0.69	
		R	/	**0.99**	**0.92**	0.51				
Eastern Italian Alps										
20	**Latemar**	*T*	0.83 0.76 0.59	0.64 0.78 0.54	***<0.06*** 0.16 ***<0.04***	0.12 0.48 ***0.06***				
		ΔT					0.83 0.66 0.68	0.80 0.61 0.78	0.84 0.74 0.64	
		R	0.13	0.45	0.82	0.61				
21	**San Vito di Cadore**	*T*	***0.09 <0.05 0.09***	***<0.05 <0.05 <0.05***	***<0.05 <0.05 <0.05***	0.46 0.48 0.37				
		ΔT					0.29 0.57 0.13	0.58 0.44 0.50	0.77 0.78 0.86	
		R	0.50	0.35	0.51	0.30				
22	**Colcuc**	*T*	0.83 0.67 **>0.95**	0.43 0.42 0.30	0.42 0.31 0.52	0.24 0.16 0.28				
		ΔT					0.88 0.87 0.89	0.79 0.52 **0.94**	**0.97 0.96 0.94**	
		R	0.15	0.22	0.45	0.20				

23	**Ivigna**	*T*	NA 0.27 ***<0.03***	NA 0.78 0.20	NA 0.50 0.28	NA 0.37 0.38				
		ΔT					NA 0.87 ***0.04***	NA 0.16 ***0.01***	NA 0.14 ***0.09***	
		R	/	0.24	0.2	0.23				
24	**Torre Trephor**	*T*	0.21 0.33 0.46	0.77 0.86 0.67	0.17 0.29 0.15	***0.09*** 0.13 0.11				
		ΔT					***0.04 0.08*** 0.21	***0.02 0.02 0.02***	0.15 0.11 0.33	
		R	0.20	0.63	0.28	<0.05				
25	**Cima Dodici I**	*T*	0.42 0.41 0.58	0.45 0.46 0.46	0.31 0.34 0.20	***<0.05 <0.05 <0.05***				
		ΔT					0.47 0.34 0.81	0.19 0.20 0.16	0.80 0.78 0.70	
		R	0.83	0.36	0.38	<0.05				
26	**Forcella dei Ciampei**	*T*	NA 0.41 0.84	NA 0.69 0.61	NA 0.65 0.26	NA 0.44 0.15				
		ΔT					NA 0.18 **0.98**	NA 0.21 0.24	NA 0.60 0.78	
		R	/	0.21	0.17	0.33				
27	**Monte Pelmo**	*T*	0.82 0.71 0.80	0.57 0.49 0.72	0.78 0.67 0.84	0.27 0.20 0.19				
		ΔT					0.72 0.67 0.40	0.78 0.80 0.58	0.76 0.84 0.51	
		R	/	0.56	0.14	0.17				

28	**Thurwieser**	*T*	NA 0.88 **>0.91**	NA 0.52 0.62	NA 0.77 0.45	NA 0.51 0.41				
		ΔT					NA **0.95 0.97**	NA 0.89 **0.90**	NA 0.78 0.72	
		R	/	0.12	0.2	0.23				
29	**Monte Castelin**	*T*	0.87 0.53 0.74	0.63 0.55 0.62	0.61 0.56 0.42	0.51 0.43 0.45				
		ΔT					0.58 0.25 0.70	0.78 0.40 0.86	0.61 0.63 0.35	
		R	/	0.67	0.37	0.15				
30	**Tofana di Rozes**	*T*	0.27 0.53 0.12	***0.01*** 0.14 ***0.09***	0.21 0.18 0.13	0.47 0.36 0.40				
		ΔT					**0.98 0.98** 0.80	0.81 0.87 0.60	0.55 0.68 0.38	
		R	/	0.69	0.28	0.31				
31	**Monte Pelf**	*T*	0.82 0.84 0.66	0.81 0.75 0.82	0.71 0.55 0.69	0.22 0.14 0.15				
		ΔT					0.36 0.32 0.36	0.51 0.51 0.51	0.52 0.62 0.52	
		R	0.17	0.06	0.37	0.08				
32	**Cima Dodici II**	*T*	**>0.95 >0.95 0.93**	0.86 **0.91** 0.81	**0.91** 0.85 **0.93**	0.58 0.47 0.43				
		ΔT					0.82 0.65 0.82	**0.91** 0.74 **0.92**	0.79 0.67 0.77	
		R	/	/	0.13	<0.05				

33	**Cima Una**	*T*	0.50 0.68 0.45	0.53 0.73 0.44	0.54 0.70 0.41	0.31 0.40 0.17				
		ΔT					0.89 0.72 0.87	0.66 0.63 0.54	0.35 0.71 0.22	
		R	/	0.26	0.40	0.56				
34	**Cima Canali**	*T*	0.49 0.45 0.57	0.28 0.26 0.13	0.83 0.81 0.72	0.75 0.78 0.80				
		ΔT					**0.93** 0.66 **0.95**	**0.91** 0.70 **0.92**	0.52 0.46 0.46	
		R	0.05	**0.96**	0.74	**0.92**				
35	**Cima Undici**	*T*	**>0.95** 0.89 **0.93**	0.89 0.86 0.81	0.55 0.47 0.64	0.58 0.49 0.82				
		ΔT					0.53 0.36 0.83	0.76 0.55 0.80	0.85 0.70 0.88	
		R	/	0.15	0.52	0.74				
36	**Plattkofel**	*T*	NA 0.42 0.54	NA ***0.08*** 0.28	NA ***<0.05 <0.05***	NA 0.27 0.47				
		ΔT					NA **0.93** 0.44	NA **0.96 0.90**	NA **0.91** 0.65	
		R	0.06	**0.98**	**0.97**	0.61				
37	**Euringer**	*T*	NA 0.57 0.16	NA 0.49 0.40	NA 0.44 0.16	NA 0.64 0.61				
		ΔT					NA 0.74 0.62	NA 0.33 0.21	NA 0.55 ***0.08***	
		R	/	0.77	0.69	0.54				

38	**Sass Maor**	*T*	0.36 0.37 0.55	0.23 0.09 0.18	0.19 0.81 0.21	0.89 0.84 0.73					
		ΔT					**0.94 0.98 0.94**	0.75 **0.91** 0.75	0.20 0.31 0.20		
		R	/	/	0.10	0.11					
39	**Sorapiss**	*T*	0.44 0.20 0.53	0.83 0.73 **0.90**	0.70 0.61 0.73	0.83 0.83 0.83					
		ΔT					0.17 0.13 0.26	0.16 0.13 0.20	***0.04 0.03*** 0.11		
		R	0.51	0.59	0.29	0.34					
40	**Monte Civetta**	*T*	0.55 0.68 0.63	**0.90** 0.83 **0.91**	**>0.95** 0.89 **>0.95**	**0.91** 0.69 **>0.95**					
		ΔT					0.57 0.31 0.57	0.15 0.32 0.15	0.51 0.50 0.51		
		R	/	0.66	0.59	0.40					
41	**Antelao**	*T*	0.31 0.40 0.30	0.60 0.63 0.60	0.76 0.75 0.85	0.69 0.52 0.82					
		ΔT					0.50 0.24 0.50	0.13 ***0.08*** 0.13	***0.05 0.06 0.05***		
		R	0.78	0.80	0.76	0.70					

Table B-2 Synthetic characterization of case studies and possible processes leading to slope failure. Number (No.) and location of case studies are the same as in Table 1. Climate anomaly: type of anomaly associated to rockfall occurrence: ST: short-term temperature anomaly; LT: long-term temperature anomaly; WT: widespread temperature anomaly; RT: precipitation anomaly -at the weekly range or longer- without or in association to temperature anomalies; NO: no anomaly; positive temperature anomaly ($P(V) \geq 1-\alpha/2$) are indicated as + while negative temperature anomaly ($P(V) \leq \alpha/2$) are indicated as -; the coexistence of both anomalies is indicated as ±. Season: season of occurrence of rockfalls: W (winter), SP (spring), S (summer), A (autumn). Elevation: Range of elevation z of rockfall niche (m a.s.l.): L ($1500 \leq z < 2400$); M ($2400 \leq z < 3300$); H ($3300 \leq z \leq 4200$). Volume: volume of detached rock (m^3): small-volume (S, $10^2 \leq$ volume $< 10^4$) and large-volume (L, $10^4 \leq$ volume $< 10^6$) events. Permafrost: expected permafrost occurrence in the detachment zone: A (permafrost in nearly all conditions), C (mostly in cold conditions), F (only in very favourable conditions), N (no permafrost).

No.	Location	Climate anomaly	Season	Elevation	Volume	Permafrost	Presence of ice/snow	Hypothesized processes leading to slope failure
1	Brenva	RT	W	H	L	A	In the detachment area, ice-snow debris with fragmented rocks and supraglacial sediments have been observed, along with huge ice blocks (Barla et al. 2000)	Several shear discontinuities and tension cracks have been observed in the rock mass, forming a sliding surface in the bedrock (Barla et al., 2000). Exceptional precipitation in the months preceding the event may have caused the onset of high water pressure in the rock joints. As in Magnin et al. (2015a), active layer depth is maximum in October, because of thermal inertia. One of the main effect of snow cover on ground temperature is thermal insulation, which starts playing a major role when snow cover is around 50 cm depth (Gruber and Hoelzle, 2008). As we

								can also notice in Figure 6 in Magnin et al. (2015a), the surface refroze in October, but the complete refreezing of the active layer occur some months later, depending on the aspect and year, due to thermal inertia processes. As can be seen in Magnin et al. (2015a) and Gruber and Hoelzle (2008), this process occur in the first meters of the surface. The combination of these two processes (i.e., warm propagation from the rockwall surface to depth and frost penetration inside the slope during the winter) may has been responsible for further groundwater pressure increase, leading finally to failure.
2	Matterhorn I	WT+	S	H	S	A	Ice has been observed in the detachment area (Deline et al., 2011)	Permafrost thaw (Deline et al., 2011)
3	Matterhorn II	WT+	S	H	S	A	Massive ice exposed in the scar (Deline et al., 2011)	Permafrost thaw (Deline et al., 2011)
4	Mont Pelà	LT-	S	L	S	N		Rain on snow. The negative LT anomaly at the quarterly scale may have preserved the

								snowpack until mid-summer. The addition of snow melting to rain may have caused the slope failure.
5	Matterhorn III	ST+	S	H	-	A		Melting of winter snowpack due to a sudden temperature rise in the days (1-6) preceding the failure.
6	Rocciamelone I	ST+	S	M	-	A		No proposed explanation
7	Matterhorn IV	WT+	S	H	-	A	Ice and melt water have been observed in the rock joints (Deline et al., 2011)	Permafrost thaw (Deline et al., 2011)
8	Rocciamelone II	WT+	W	M	L	A		No proposed explanation
9	Belvedere	WT+	SP	H	L	A	Probable ice and snowmelt at the surface (Huggel et al., 2010)	According to Huggel et al. (2010), even if air temperature at the niche must have been well below 0°C in the days preceding the rockfall, the intense solar radiation might have caused snow and ice melting. Besides the triggering factor, the predisposing conditions for this failure relate to the rapid evolution

								undergone by the eastern face of the Monte Rosa massif since the late 90s: in particular, this rockfall occurred two years after a huge icefall that detached just below this rockfall niche (Tamburini et al., 2013).
10	Tré-la-Tête	RT+	S	H	L	A	Ice has been observed in the detachment zone (Deline et al. 2008)	Exceptional precipitation at the quarterly scale may have caused the onset of high water pressure in the rock slope. The sudden increase of T_{max} in the days (1-3) preceding the event may have caused the melting of an early snowfall, triggering slope failure. Deline et al. (2008) relate the occurrence of rockfalls to permafrost degradation in a fractured rock mass, so favoring the percolation of snowmelt along joints.
11	Punta Patrì Nord	ST-	S	H	L	A	Melt water coming from ice lens uncovered by the rockfall has been observed (Deline et al., 2011)	Freezing of water springs along the slope, blocking the seepage of water from the permafrost thaw through the rock mass: the build-up of high water pressure may have caused the collapse of the rock mass.
12	Crammont	RT+	W	M	L	F	Snow was present (Deline et al., 2011)	No proposed explanation about the event trigger. Deline et al. (2013) relate the occurrence of this rockfall to permafrost

							degradation, based on the presence of seepage water in the scar after the collapse, in spite of negative air temperatures.
13	Val Formazza	ST-	SP	L	L	N	Freezing of water springs along the slope and consequent blockage of snowmelt water seepage through the rock mass: the high water pressure caused by the blockage of the water flow may have caused the collapse of the rock mass.
14	Monviso	NO	S	M	S	C	No detected anomaly
15	Mont Rouge Peutery	NO	S	M	-	F	No detected anomaly
16	Matterhorn V	WT+	S	H	-	A	Permafrost thaw
17	Melezet	ST+	SP	L	S	N	Accelerated snow melt due to sudden temperature increase
18	Punta Tre Amici	ST-	A	H	L	A	Freezing of water springs along the slope, blocking the seepage of water from the permafrost thaw through the rock mass: the build-up of high water pressure may have

							caused the collapse of the rock mass (Fischer et al., 2013).
19	Gressoney-Saint-Jean	RT-	SP	L	S	N	Snow melt of an exceptionally deep snow pack. The amount of water released by snowmelt may have been particularly relevant because of the combination of a cold temperature anomaly at the quarterly scale with extraordinary precipitations in the month before the event, resulting in a deep snowpack.
20	Latemar	LT-	S	M	-	C	Snow melt of an exceptionally deep snow pack. The amount of water released by snowmelt may have been particularly relevant because of the combination of a cold temperature anomaly at the quarterly scale with extraordinary precipitations in the month before the event, resulting in a deep snowpack.
21	San Vito di Cadore	WT-	A	M	S	F	Freezing of water springs along the slope and consequent blockage of water seepage through the rock mass: the high water pressure caused by the blockage of the water flow may have caused the collapse of the

							rock mass.
22	Colcuc	ST+	SP	L	S	N	Accelerated snow melt due to sudden temperature increase
23	Ivigna	ST-	SP	L	-	N	Freezing of water springs along the slope and consequent blockage of snowmelt water seepage through the rock mass: the high water pressure caused by the blockage of the water flow may have caused the collapse of the rock mass.
24	Torre Trephor	WT-	SP	L	-	N	Freezing of water springs along the slope and consequent blockage of snowmelt water seepage through the rock mass: the high water pressure caused by the blockage of the water flow may have caused the collapse of the rock mass.
25	Cima Dodici I	LT-	S	M	-	C	Rain on snow. The negative LT anomaly at the quarterly scale may have preserved the snowpack until the date of the event. The addition of snow melting to rain may have caused the slope to fail.
26	Forcella dei	ST+	S	L	S	N	Accelerated snowmelt due to sudden

	Ciampei							temperature increase the day of the event.
27	Monte Pelmo	NO	S	M	-	C		No detected anomaly
28	Thurwieser	ST+	S	H	L	A	Few ice blocks have been found in the debris (Sosio et al., 2008).	Accelerated permafrost thaw due to sudden temperature increase in the days (1-3) preceding the event.
29	Monte Castelin	NO	A	L	-	N		No detected anomaly
30	Tofana di Rozes	ST±	S	M	-	F		Rapid melting of an early snowfall. Temperature suddenly raised in the day of the event, following extraordinarily low temperatures and heavy precipitation in the week before the event.
31	Monte Pelf	NO	SP	L	-	N		No detected anomaly
32	Cima Dodici II	WT+	S	M	L	C		Rapid snowmelt caused by extraordinarily high temperatures in the month and in the days preceding the event.
33	Cima Una	NO	A	M	L	C	Any ice or water on the failure surface have	No detected anomaly

							been observed (Viero et al., 2013).	
34	Cima Canali	RT+	S	M	S	F		Heavy precipitations in the week and in the months preceding the event. No proposed explanation for the trigger.
35	Cima Undici	ST+	S	M	S	C		No proposed explanation
36	Plattkofel	RT±	S	M	S	C	The break off surface was partially covered by an ice-debris mixture (Deline et al., 2011)	Rapid melting of an early snowfall. Temperature suddenly raised the day of the event, following extraordinarily low temperatures and heavy precipitation in the month before the event.
37	Euringer	ST-	S	L	S	F		Freezing of water springs along the slope and consequent blockage of snowmelt water seepage through the rock mass: the high water pressure caused by the blockage of the water flow may have caused the collapse of the rock mass.
38	Sass Maor	ST±	W	L	-	F		No proposed explanation
39	Sorapiss	ST±	A	M	S	C		Freezing of water springs along the slope and consequent blockage of water seepage

							through the rock mass: the high water pressure caused by the blocking of the water flow may have caused the collapse of the rock mass.
40	Monte Civetta	WT+	A	M	L	C	Warm temperatures allowed precipitations to fall as rain rather than as snow in the week and month before the event.
41	Antelao	ST-	A	L	-	F	Freezing of water springs along the slope and consequent blockage of water seepage through the rock mass: the high water pressure caused by the blocking of the water flow may have caused the collapse of the rock mass.

References

Akbari, H., Matthews, H. D. and Seto, D.: The Long-term Effect of Increasing the Albedo of Urban Areas, Environ. Res. Lett., 7(2), 24004, doi:10.1088/1748-9326/7/2/024004, 2012.

Allamano, P. and Claps, P.: Precipitation measurement errors at high-elevation sites in the Italian Alps, in: EGU General Assembly Conference Abstracts, 12, 11287, 2010.

Allamano, P., Croci, A. and Laio, F.: Toward the camera rain gauge, Water Resources Research, 51(3), 1744-1757, 2015.

Allen, S. and Huggel, C.: Extremely warm temperatures as a potential cause of recent high mountain rockfall, Global Planetary Changes, 107, 59–69 [online] Available from: http://www.sciencedirect.com/science/article/pii/S0921818113001112, 2013.

Allen, S. K., Cox, S. C. and Owens, I. F.: Rock avalanches and other landslides in the central Southern Alps of New Zealand: a regional study considering possible climate change impacts, Landslides, 8(1), 33–48, doi:10.1007/s10346-010-0222-z, 2010.

Arnfield, A. J.: Two decades of urban climate research: A review of turbulence, exchanges of energy and water, and the urban heat island, Int. J. Climatol., 23(1), 1–26, doi:10.1002/joc.859, 2003.

ARPA Piemonte: Evento meteopluviometrico del 26–28 aprile 2009, 2009.

ARPA Piemonte Banca dati meteorologica (1990), http://www.arpa.piemonte.it/, last access: 14 August 2013.

Auer, I., Bohm, R., Jurkovic, A., Lipa, W., Orlik, A., Potzmann, R., Schoner, W., Ungersbock, M., Matulla, C., Briffa, K., Jones, P., Efthymiadis, D., Brunetti, M., Nanni, T., Maugeri, M., Mercalli, L., Mestre, O., Moisselin, J. M., Begert, M., Muller-Westermeier, G., Kveton, V., Bochnicek, O., Stastny, P., Lapin, M.,

Szalai, S., Szentimrey, T., Cegnar, T., Dolinar, M., Gajic-Capka, M., Zaninovic, K., Majstorovic, Z. and Nieplova, E.: HISTALP - historical instrumental climatological surface time series of the Greater Alpine Region, Int. J. Climatol., 27, 17–46, doi:10.1002/joc.1377, 2007.

Barla, G., Dutto, F., and Mortara, G.: Brenva glacier rock avalanche of 18 January 1997 on the Mount Blanc range, northwest Italy, Landslide News, 13, 2–5, 2000.

Beniston, M.: Mountain weather and climate: A general overview and a focus on climatic change in the Alps, Hydrobiologia, 562, 3–16, doi:10.1007/s10750-005-1802-0, 2006.

Bennie, J., Davies, T. W., Duffy, J. P., Inger, R. and Gaston, K. J.: Contrasting trends in light pollution observed night time lights, Nature, 4(3789), 1–6, doi:10.1038/srep03789, 2014.

Berkeley Earth, 2016, http://berkeleyearth.org/data/, last access: 18 December 2016.

Boeckli, L., Brenning, a., Gruber, S. and Noetzli, J.: Permafrost distribution in the European Alps: Calculation and evaluation of an index map and summary statistics, Cryosphere, 6(c), 807–820, doi:10.5194/tc-6-807-2012, 2012.

Bovo, S., Carenzo, G., Cattaneo, M., Debrando, V., Faletto, C. and Gandino, E.: La valanga di ghiaccio del Monviso - Il contributo delle reti di monitoraggio della Regione Piemonte nell'interpretazione dell'evento, Neve e Valanghe, 11:6–13, 1990.

Brunetti, M., Lentini, G., Maugeri, M., Nanni, T., Auer, I., Bohm, R. and Schoner, W.: Climate variability and change in the Greater Alpine Region over the last two centuries based on multi-variable analysis, Int. J. Climatol., 29, 2197–2225, doi:10.1002/joc.1857, 2009.

Brunetti, M. T., Peruccacci, S., Antronico, L., Bartolini, D., Deganutti, A. M., Gariano, S. L., Iovine, G., Luciani, S., Luino, F., Melillo, M., Palladino, M. R., Parise, M., Rossi, M., Turconi, L., Vennari, C., Vessia, G., Viero, A. and Guzzetti, F.: Catalogue of rainfall events with shallow landslides and new rainfall thresholds in Italy, in Engineering Geology for Society and Territory - Volume 2: Landslide Processes, pp. 1575–1579., 2015.

Cardinali, M., Ardizzone, F., Galli, M., Guzzetti, F. and Reichenbach, P.: Landslides triggered by rapid snow melting: the December 1996-January 1997 event in Central Italy, Proc. EGS Plinius Conf. Held, (January), 439–448, 2000.

Cauwels, P., Pestalozzi, N. and Sornette, D.: Dynamics and spatial distribution of global nighttime lights, EPJ Data Sci., 3, 2, doi:10.1140/epjds19, 2014.

Ceola, S., Laio, F. and Montanari, A.: Satellite nighttime lights reveal increasing human exposure to floods worldwide, Geophys. Res. Lett., 41(20), 7184–7190, doi:10.1002/2014GL061859, 2014.

Ceola, S., Laio, F. and Montanari, A.: Human-impacted waters: New perspectives from global high-resolution monitoring, Water Resour. Res., 51(9), 7064–7079, doi:10.1002/2015WR017482, 2015.

Chand, T. R. K., Badarinath, K. V. S., Elvidge, C. D. and Tuttle, B. T.: Spatial characterization of electrical power consumption patterns over India using temporal DMSP-OLS night-time satellite data, Int. J. Remote Sens., 30(3), 647–661, doi:10.1080/01431160802345685, 2009.

Chen, X. and Nordhaus, W. D.: Using luminosity data as a proxy for economic statistics, , 108(21), doi:10.1073/pnas.1017031108, 2011.

Chiarle, M., Iannotti, S., Mortara, G. and Deline, P.: Recent debris flow occurrences associated with glaciers in the Alps, Glob. Planet. Change, 56, 123–136, 2007.

Chiarle, M. and Mortara, G.: Geomorphological impact of climate change on alpine glacial and periglacial areas, Interpraevent, 2, 111–122, 2008.

Chiarle, M., Paranunzio, R., Laio, F., Nigrelli, G. and Guzzetti, F.: Recent slope failures in the Dolomites (Northeastern Italian Alps) in a context of climate change, in: EGU General Assembly Conference Abstracts, 16, 4017, 2014.

Collins, B. D. and Stock, G. M.: Rockfall triggering by cyclic thermal stressing of exfoliation fractures, Nature Geoscience, 2016.

Corumluoglu, O. and Asri, I.: The effect of urban heat island on Izmir's city ecosystem and climate, Environ. Sci. Pollut. Res., 22(5), 3202–3211, doi:10.1007/s11356-014-2874-z, 2015.

Cui, Y., Xu, X., Dong, J. and Qin, Y.: Influence of Urbanization Factors on Surface Urban Heat Island Intensity: A Comparison of Countries at Different Developmental Phases, , doi:10.3390/su8080706, 2016.

Davies, M. C. R., Hamza, O. and Harris, C.: The effect of rise in mean annual temperature on the stability of rock slopes containing ice-filled discontinuities, Permafr. Periglac. Process., 12, 137–144, doi:10.1002/ppp.378, 2001.

Deline, P., Arattano, M., Chiarle, M., Cremonese, E., Giordano, M., Guilietto, W., Gruber, S., Jaillet, S., Morra Di Cella, U., Mortara, G., Noetzli, J., Pau, R., Ravanel, L., Rabatel, A., Pogliotti, P., Ravello, M., Tamburini, A., Vagliasindi, M. and Voyat, I.: The relation of permafrost degradation and slope instabilities in high-Alpine steep rockwalls (Mont blanc massif and Matterhorn) : the research project PERMAdataROC, Eur. Geosci. Union, Gen. Assem. 2007, 9(i), 2007.

Deline, P., Kirkbride, M. P., Ravanel, L. and Ravello, M.: The Tré-la-Tete rockfall onto the Lex Blanche Glacier, Mont Blanc Massif, Italy, in September 2008, Geogr. Fis. e Din. Quat., 31(2), 251–254, 2008.

Deline, P., Chiarle, M., Curtaz, M., Kellerer-Pirklbauer, A., Lieb, G. K., Mayr, V., Mortara, G., and Ravanel L.: Chapter 3: Rockfalls, in: Hazards related to permafrost and to permafrost degradation, PermaNET project, state-of-the-art report 6.2, edited by: Schoeneich, P., Dall'Amico, M., Deline, P., and Zischg, A., online publication ISBN 978-2-903095-59-8, 67-105, 2011.

Deline, P., Broccolato, M., Noetzli, J., Ravanel, L. and Tamburini, A.: The December 2008 Crammont Rock avalanche, Mont Blanc Massif Area, Italy, in Landslide Science and Practice: Global Environmental Change, vol. 4, pp. 403–408., 2013.

Dutto, F. and Mortara, G.: Rischi connessi con la dinamica glaciale, Geografia Fisica Dinamica Quaternaria, 85–99, 1992.

Dutto, F., Godone, F. and Mortara, G.: L'écroulement du glacier supérieur de Coolidge (Paroi nord du Mont Viso, Alpes occidentales)., Rev. géographie Alp., 79, 7–18, 1991.

Elvidge, C. D., Sutton, P. C., Ghosh, T., Tuttle, B. T., Baugh, K. E., Bhaduri, B. and Bright, E.: A global poverty map derived from satellite data, Comput. Geosci., 35(8), 1652–1660, doi:10.1016/j.cageo.2009.01.009, 2009.

Environmental Protection Agency, U.: Reducing Urban Heat Islands: Compendium of Strategies - Urban Heat Island Basics, , 1–22, 2008.

Esposito, S., Beltrano, M. C., De Natale, F., Di Giuseppe, E., Iafrate, L., Libertà, A., Parisse, B. and Scaglione, M.: Atlante italiano del clima e dei cambiamenti climatici, , 2014, 2014.

Fall, S., Niyogi, D., Gluhovsky, A., Pielke, R. A., Kalnay, E. and Rochon, G.: Impacts of land use land cover on temperature trends over the continental United States: Assessment using the North American Regional Reanalysis, Int. J. Climatol., 30(13), 1980–1993, doi:10.1002/joc.1996, 2010.

Falvey, M. and Garreaud, R. D.: Regional cooling in a warming world: Recent temperature trends in the southeast Pacific and along the west coast of subtropical South America (1979-2006), J. Geophys. Res. Atmos., 114(4), 1–16, doi:10.1029/2008JD010519, 2009.

FAOClim-NET: Agroclimatic database management system, 2016, http://geonetwork3.fao.org/climpag/agroclimdb_en.php, last access: 10 June 2016.

Fischer, L., Amann, F., Moore, J. R. and Huggel, C.: Assessment of periglacial slope stability for the 1988 Tschierva rock avalanche (Piz Morteratsch, Switzerland), Eng. Geol., 116, 32–43, doi:10.1016/j.enggeo.2010.07.005, 2010.

Fischer, L., Eisenbeiss, H., Kääb, A., Huggel, C. and Haeberli, W.: Monitoring topographic changes in a periglacial high-mountain face using high-resolution DTMs, Monte Rosa East Face, Italian Alps, Permafr. Periglac. Process., 22, 140–152, 2011.

Fischer, L., Purves, R. S., Huggel, C., Noetzli, J. and Haeberli, W.: On the influence of topographic, geological and cryospheric factors on rock avalanches and rockfalls in high-mountain areas, Nat. Hazards Earth Syst. Sci., 12, 241–254, doi:10.5194/nhess-12-241-2012, 2012.

Fischer, L., Huggel, C., Kääb, A. and Haeberli, W.: Slope failures and erosion rates on a glacierized high-mountain face under climatic changes, Earth Surf. Process. Landforms, 38, 836–846, doi:10.1002/esp.3355, 2013.

Fitzsimons, S. J. and Veit, H.: Geology and Geomorphology of the European Alps and the Southern Alps of New Zealand Geology and Geomorphology of the European Alps and the Southern Alps of New Zealand, Mt. Res. Dev. , 21(4), 340–349, 2001.

Gallo, K. P., McNab, a. L., Karl, T. R., Brown, J. F., Hood, J. J. and Tarpley, J. D.: The Use of NOAA AVHRR Data for Assessment of the Urban Heat Island Effect, J. Appl. Meteorol., 32(5), 899–908, doi:10.1175/1520-0450(1993)032<0899:TUONAD>2.0.CO;2, 1993.

Gariano, S. L. and Guzzetti, F.: Landslides in a changing climate, Earth-Science Rev., doi:10.1016/j.earscirev.2016.08.011, 2016.

GISS Surface Temperature Analysis (GISTEMP), 2016, http://data.giss.nasa.gov/gistemp/, last access: 9 July 2016.

Gobiet, A., Kotlarski, S., Beniston, M., Heinrich, G., Rajczak, J. and Stoffel, M.: 21st century climate change in the European Alps-A review, Sci. Total Environ., 493, 1138–1151, doi:10.1016/j.scitotenv.2013.07.050, 2014.

Govi, M. and Sorzana, P. F.: Landslide susceptibility as a function of critical rainfall amount in Piedmont Basin (North-Western Italy), Studia Geomorphologica Carpatho-Balcanica, 14, 43-61, 1980.

Govi, M., Pasuto, A., Silvano, S. and Siorpaes, C.: An example of a low-temperature-triggered landslide, Eng. Geol., 36(1–2), 53–65, doi:10.1016/0013-7952(93)90018-8, 1993.

Groisman, P. Y. and Legates, D. R.: The accuracy of United States precipitation data, Bulletin of the American Meteorological Society, 75(2), 215-227, 1994.

Gruber, S. and Haeberli, W.: Permafrost in steep bedrock slopes and its temperatures-related destabilization following climate change, J. Geophys. Res. F Earth Surf., 112, 2007.

Gruber, S., Hoelzle, M. and Haeberli, W.: Permafrost thaw and destabilization of Alpine rock walls in the hot summer of 2003, Geophys. Res. Lett., 31, doi:10.1029/2004GL020051, 2004a.

Gruber, S., Hoelzle, M. and Haeberli, W.: Permafrost thaw and destabilization of Alpine rock walls in the hot summer of 2003, Geophys. Res. Lett., 31, 4, doi:10.1029/2004gl020051, 2004b.

Guzzetti, F., Peruccacci, S., Rossi, M. and Stark, C. P.: The rainfall intensity-duration control of shallow landslides and debris flows: an update, Landslides, 5, 3–17, doi:10.1007/s10346-007-0112-1, 2008.

HadCRUT4, 2016, https://crudata.uea.ac.uk/cru/data/temperature/, last access: 30/01/2016.

Haeberli, W., Gärtner-Roer, I., Hoelzle, M., Paul, F. and Zemp, M.: Glacier Mass Balance Bulletin No. 10 (2006–2007), World Glacier Monit. Serv. Zurich, Switz., 2009.

Hansen, J., Sato, M., Ruedy, R., Lo, K., Lea, D. W. and Medina-Elizade, M.: Global temperature change, Proc. Natl. Acad. Sci., 103(39), 14288–14293, doi:10.1073/pnas.0606291103, 2006.

Hansen, J., Ruedy, R., Sato, M. and Lo, K.: Global surface temperature change, Rev. Geophys., 48(4), RG4004, doi:10.1029/2010RG000345.1.INTRODUCTION, 2010.

Harris, C., Arenson, L. U., Christiansen, H. H., Etzemuller, B., Frauenfelder, R., Gruber, S., Haeberli, W., Hauck, C., Holzle, M., Humlum, O., Isaksen, K., Kaab, A., Kern-Lutschg, M. A., Lehning, M., Matsuoka, N., Murton, J. B., Nozli, J., Phillips, M., Ross, N., Seppala, M., Springman, S. M. and Muhll, D. V: Permafrost and climate in Europe: Monitoring and modelling thermal, geomorphological and geotechnical responses, Earth-Science Rev., 92, 117–171, doi:10.1016/j.earscirev.2008.12.002, 2009.

Hausfather, Z., Menne, M. J., Williams, C. N., Masters, T., Broberg, R. and Jones, D.: Quantifying the effect of urbanization on u.s. Historical climatology network temperature records, J. Geophys. Res. Atmos., 118(2), 481–494, doi:10.1029/2012JD018509, 2013.

Howard, L.: The climate of London: deduced from meteorological observations made in the metropolis and at various places around it (Vol. 2), Harvey and Darton, J. and A. Arch, Longman, Hatchard, S. Highley [and] R. Hunter, 1833.

Huang, Q., Yang, X., Gao, B., Yang, Y. and Zhao, Y.: Application of DMSP/OLS nighttime light images: A meta-analysis and a systematic literature review, Remote Sens., 6(8), 6844–6866, doi:10.3390/rs6086844, 2014.

Huggel, C., Salzmann, N., Allen, S., Caplan-Auerbach, J., Fischer, L., Haeberli, W., Larsen, C., Schneider, D. and Wessels, R.: Recent and future warm extreme events and high-mountain slope stability., Philos. Trans. A. Math. Phys. Eng. Sci., 368, 2435–2459, doi:10.1098/rsta.2010.0078, 2010.

Imhoff, M. L., Lawrence, W. T., Stutzer, D. C. and Elvidge, C. D.: A technique for using composite DMSP/OLS "city lights" satellite data to map urban area, Remote Sens. Environ., 61(3), 361–370, doi:10.1016/S0034-4257(97)00046-1, 1997.

Imhoff, M. L., Zhang, P., Wolfe, R. E. and Bounoua, L.: Remote sensing of the urban heat island effect across biomes in the continental USA, Remote Sens. Environ., 114(3), 504–513, doi:10.1016/j.rse.2009.10.008, 2010.

IPCC: Climate Change 2007 - The Physical Science Basis: Working Group I Contribution to the Fourth Assessment Report of the IPCC (Climate Change 2007), 2007.

IPCC: Climate Change 2014: Impacts, Adaptation and Vulnerability - Contributions of the Working Group II to the Fifth Assessment Report., Clim. Chang. 2014 Impacts, Adapt. Vulnerability - Contrib. Work. Gr. II to Fifth Assess. Rep., 1–32, 2014.

Isotta, F. A., Frei, C., Weilguni, V., Perčec Tadić, M., Lassegues, P., Rudolf, B., ... and Munari, M.: The climate of daily precipitation in the Alps: development and analysis of a high- resolution grid dataset from pan- Alpine rain- gauge data, International Journal of Climatology, 34(5), 1657-1675, 2014.

Jomelli, V., Pech, V. P., Chochillon, C. and Brunstein, D.: Geomorphic variations of debris flows and recent climatic change in the French Alps, Clim. Change, 64, 77–102, doi:10.1023/b:clim.0000024700.35154.44, 2004.

Jones, P. D., Groisman, P. Y., Coughlan, M., Plummer, N., Wang, W. C. and Karl, T. R.: Assessment of urbanization effects in time series of surface air temperature over land, Nature, 347(6289), 169–172, doi:10.1038/347169a0, 1990.

Kääb, A., Huggel, C., Barbero, S., Chiarle, M., Cordola, M., Epifani, F., Haeberli, W., Mortara, G., Semino, P. and Tamburini, A.: Glacier hazards at Belvedere Glacier and the Monte Rosa east face, Italian Alps: processes and mitigation, in Interpraevent, vol. 1, pp. 67–78., 2004.

Kääb, A., Chiarle, M., Raup, B. and Schneider, C.: Climate change impacts on mountain glaciers and permafrost, Glob. Planet. Change, 56, vii–ix, 2007.

Kalnay, E. and Cai, M.: Impact of urbanization and land-use change on climate, Nature, 423(May), 528–531, doi:10.1038/nature01649.1., 2003.

Kassomenos, P. A. and Katsoulis, B. D.: Mesoscale and macroscale aspects of the morning Urban Heat Island around Athens, Greece, Meteorol. Atmos. Phys., 94(1–4), 209–218, doi:10.1007/s00703-006-0191-x, 2006.

Kirchner, M., Faus-Kessler, T., Jakobi, G., Leuchner, M., Ries, L., Scheel, H. E. and Suppan, P.: Altitudinal temperature lapse rates in an Alpine valley: Trends and the influence of season and weather patterns, Int. J. Climatol., 33, 539–555, doi:10.1002/joc.3444, 2013.

Krautblatter, M., Funk, D. and Günzel, F. K.: Why permafrost rocks become unstable: a rock–ice-mechanical model in time and space, Earth Surface Processes and Landforms, 38(8), 876-887, 2013.

Lawrimore, J. H., Menne, M. J., Gleason, B. E., Williams, C. N., Wuertz, D. B., Vose, R. S. and Rennie, J.: An overview of the Global Historical Climatology Network monthly mean temperature data set, version 3, J. Geophys. Res. Atmos., 116(19), 1–18, doi:10.1029/2011JD016187, 2011.

Libertino, A., Sharma, A., Lakshmi, V. and Claps, P.: A global assessment of the timing of extreme rainfall from TRMM and GPM for improving hydrologic design. Environmental Research Letters, 11(5), 054003, 2016.

Magnin, F., Deline, P., Ravanel, L., Noetzli, J. and Pogliotti, P.: Thermal characteristics of permafrost in the steep alpine rock walls of the Aiguille du Midi (Mont Blanc Massif, 3842 m asl), The Cryosphere, 9(1), 109-121, 2015a.

Magnin, F., Brenning, A., Bodin, X., Deline, P. and Ravanel, L.: Modélisation statistique de la distribution du permafrost de paroi: application au massif du Mont Blanc, Géomorphologie: relief, processus, environnement, 21(2), 145-162, 2015b.

Magnin, F., Krautblatter, M., Deline, P., Ravanel, L., Malet, E. and Bevington, A.: Determination of warm, sensitive permafrost areas in near-vertical rockwalls and evaluation of distributed models by electrical resistivity tomography, Journal of Geophysical Research: Earth Surface, 120(5), 745-762, 2015c.

Manconi, A. and Giordan, D.: Landslide failure forecast in near-real-time. Geomatics, Natural Hazards and Risk, 7(2), 639-648, 2016.

Manconi, A., Picozzi, M., Coviello, V., De Santis, F. and Elia, L.: Real-time detection, location, and characterization of rockslides using broadband regional seismic networks, Geophys. Res. Lett., doi:10.1002/2016GL069572, 2016.

Marchi, L. and Tecca, P. R.: Magnitudo delle colate detritiche nelle Alpi Orientali Italiane, Geoing. Ambient. e Mineraria, 33, 79–86, 1996.

Marconcini, M., Metz, A., Esch, T. and Zeidler, J.: Global urban growth monitoring by means of SAR data, in: Geoscience and Remote Sensing Symposium (IGARSS), 2014 IEEE International, IEEE, pp. 1477-1480, 2014.

McCarthy, M. P., Best, M. J. and Betts, R. A.: Climate change in cities due to global warming and urban effects, Geophys. Res. Lett., 37(9), 1–5, doi:10.1029/2010GL042845, 2010.

McSaveney, M. and Massey, C.: Did radiative cooling trigger New Zealand's 2007 Young River landslide?, in: Landslide Science and Practice, vol. 4, pp. 347–353, 2013.

McSaveney, M. J.: Recent rockfalls and rock avalanches in Mount Cook National Park, New Zealand, in Catastrophic landslides: effects, occurrence and mechanisms: Boulder, Colorado, Geological Society of America Reviews in Engineering Geology, vol. XV, pp. 35–70., 2002.

Mercalli, L. and Berro, D. C.: Atlante climatico della Valle d'Aosta (Vol. 2). SMS, 2003.

Merlone, A., Lopardo, G., Sanna, F., Bell, S., Benyon, R., Bergerud, R. A., ... and Cappella, A.: The MeteoMet project–metrology for meteorology: challenges and results, Meteorological Applications, 22(S1), 820-829, 2015.

Mortara, G. and Giuliano, M.: La colata detritica del 7 settembre 2008 nel bacino glaciale della Torre di Castelfranco, in: Mortara G, Tamburini A (eds): Il ghiacciaio del Belvedere e l'emergenza del lago Effimero. Edizioni Societa` Meteorologica Subalpina, Castello Borello, Bussoleno, pp 135–139, 2009.

Mortara, G. and Palomba, M.: Il Ghiacciaio Superiore di Coolidge (Monviso) a venti anni dal crollo del 6 luglio 1989, Nimbus 53–54:30–31, 2009.

Mortara, G. and Tamburini, A.: Il ghiacciaio del Belvedere e l'emergenza del lago Effimero, Edizioni Societa` Meteorologica Subalpina, Castello Borello, Bussoleno, 2009.

Mortara, G., Dutto, F. and Godone, F.: Effetti degli eventi alluvionali nell'ambiente proglaciale. La sovraincisione della morena del Ghiacciaio del Mulinet (Stura di Valgrande, Alpi Graie), Geogr. Fis. Dinam. Quat, 18, 295–304, 1995.

Mveyange, A.: Night lights and regional income inequality in Africa, World Bank, 2015.

Nel·lo, O., López, J., Martín, J. and Checa, J.: Energy and urban form. The growth of European cities on the basis of night-time brightness, Land use policy, 61, 103–112, doi:10.1016/j.landusepol.2016.11.007, 2017.

Nigrelli, G., Lucchesi, S., Bertotto, S., Fioraso, G. and Chiarle, M.: Climate variability and Alpine glaciers evolution in Northwestern Italy from the Little Ice Age to the 2010s, Theor. Appl. Climatol., 122(3), 595–608, doi:10.1007/s00704-014-1313-x, 2014.

Nigrelli, G., Fratianni, S., Zampollo, A., Turconi, L. and Chiarle, M.: The altitudinal temperature lapse rates applied to high elevation rockfalls studies in the Western European Alps, Theoretical and Applied Climatology, 1-13. 2017.

NOAA - Data access - Land Based Station Data, 2016, https://www.ncdc.noaa.gov/data-access/land-based-station-data, last access: 9 September 2016.

NOAA - Earth Observation Group, Version 4 DMSP-OLS Nighttime Lights Time Series, 2015a, http://ngdc.noaa.gov/eog/dmsp/downloadV4composites.html, last access: 21 December 2015.

NOAA National Centers for Environmental Information, State of the Climate: Global Analysis for Annual 2014, 2015b, http://www.ncdc.noaa.gov/sotc/global/201413, last access: 12 January 2017.

Noetzli, J., Hoelzle, M. and Haeberli, W.: Mountain permafrost and recent Alpine rock-fall events: a GIS-based approach to determine critical factors, Permafrost, 2, 827–832, 2003.

Noetzli, J., Huggel, C., Hoelzle, M. and Haeberli, W.: GIS-based modelling of rock-ice avalanches from Alpine permafrost areas, in Computational Geosciences, vol. 10, pp. 161–178., 2006.

Oke, T. R.: The energetic basis of the urban heat island, Q. J. R. Meteorol. Soc., 108(455), 1–24, doi:10.1002/qj.49710845502, 1982.

Paranunzio, R. and Laio, F.: Analysis of the effect of soil anthropization on air temperature in the Mediterranean area based on nightlights, 2016/5-085, MedClivar 2016, 26-30 September 2016, Athens, 2016.

Paranunzio, R., Laio, F., Nigrelli, G. and Chiarle, M.: A method to reveal climatic variables triggering slope failures at high elevation, Nat. Hazards, 76(2), 1039–1061, doi:10.1007/s11069-014-1532-6, 2015.

Paranunzio, R., Laio, F., Chiarle, M., Nigrelli, G. and Guzzetti, F.: Climate anomalies associated to the occurrence of rockfalls at high-elevation in the Italian Alps, Nat. Hazards Earth Syst. Sci., 16(9), 2085-2106, 2016.

Parker, D. E.: Urban heat island effects on estimates of observed climate change, Wiley Interdiscip. Rev. Clim. Chang., 1(1), 123–133, doi:10.1002/wcc.21, 2010.

Peng, S., Piao, S., Ciais, P., Friedlingstein, P., Ottle, C., Bréon, F. M., Nan, H., Zhou, L. and Myneni, R. B.: Surface urban heat island across 419 global big cities, Environ. Sci. Technol., 46(2), 696–703, doi:10.1021/es2030438, 2012.

Peterson, T. C., Gallo, K. P., Lawrimore, J., Owen, T. W., Huang, A. and McKittrick, D. a.: Global rural temperature trends, Geophys. Res. Lett., 26(3), 329–332, doi:10.1029/1998GL900322, 1999.

Peterson, T. C., Owen, T. W., Nesdis, N., Climatic, N. and Carolina, N.: Urban Heat Island Assessment: Metadata Are Important, J. Clim., 18(14), 2637–2646, doi:10.1175/JCLI3431.1, 2005.

Ravanel, L. and Deline, P.: Climate influence on rockfalls in high-Alpine steep rockwalls: The north side of the Aiguilles de Chamonix (Mont Blanc massif) since the end of the "Little Ice Age," The Holocene, 21, 357–365, doi:10.1177/0959683610374887, 2011.

Ravanel, L., Allignol, F., Deline, P., Gruber, S. and Ravello, M.: Rock falls in the Mont Blanc Massif in 2007 and 2008, Landslides, 7(4), 493–501, doi:10.1007/s10346-010-0206-z, 2010.

Rohde, R., Muller, R., Jacobsen, R., Perlmutter, S., Rosenfeld, A., Wurtele, J., ... and Mosher, S.: Geostatistics : Berkeley Earth Temperature Averaging Process, Geoinfor. Geostat.: An Overview, 13, 20-100, 2013.

Saez, J. L., Corona, C., Stoffel, M. and Berger, F.: Climate change increases frequency of shallow spring landslides in the French Alps, Geology, 41, 619–622, 2013.

Santamouris, M.: Heat Island Research in Europe: The State of the Art, Adv. Build. Energy Res., 1(1), 123–150, doi:10.1080/17512549.2007.9687272, 2007.

Santamouris, M., Cartalis, C., Synnefa, A. and Kolokotsa, D.: On the impact of urban heat island and global warming on the power demand and electricity consumption of buildings—A review, Energy Build., 98, 119–124, doi:10.1016/j.enbuild.2014.09.052, 2015.

Schär, C., Vidale, P. L., Lüthi, D., Frei, C., Häberli, C., Liniger, M. A. and Appenzeller, C.: The role of increasing temperature variability in European summer heatwaves., Nature, 427, 332–336, doi:10.1038/nature02300, 2004.

Small, C., Pozzi, F. and Elvidge, C. D.: Spatial analysis of global urban extent from DMSP-OLS night lights, Remote Sens. Environ., 96(3–4), 277–291, doi:10.1016/j.rse.2005.02.002, 2005.

Sosio, R., Crosta, G. B. and Hungr, O.: Complete dynamic modeling calibration for the Thurwieser rock avalanche (Italian Central Alps), Eng. Geol., 100(1–2), 11–26, doi:10.1016/j.enggeo.2008.02.012, 2008.

Soto Gómez, A. J., Di Baldassarre, G., Rodhe, A. and Pohjola, V. A.: Remotely sensed nightlights to map societal exposure to hydrometeorological hazards, Remote Sens., 7(9), 12380–12399, doi:10.3390/rs70912380, 2015.

Stocker, T. F., Qin, D. and Platner, G. K.: Climate Change 2013: The Physical Science Basis, Work. Gr. I Contrib. to Fifth Assess. Rep. Intergov. Panel Clim. Chang. Summ. Policymakers (IPCC, 2013), 2013.

Stoffel, M., Tiranti, D. and Huggel, C.: Climate change impacts on mass movements - Case studies from the European Alps., Sci. Total Environ., 493, 1255–66, doi:10.1016/j.scitotenv.2014.02.102, 2014.

Tamburini, A., Villa, F., Fischer, L., Hungr, O., Chiarle, M. and Mortara, G.: Slope instabilities in high-mountain rock walls. Recent events on the Monte Rosa east face (Macugnaga, NW Italy), in Landslide Science and Practice: Spatial Analysis and Modelling, vol. 3, pp. 327–332., 2013.

Tran, H., Uchihama, D., Ochi, S. and Yasuoka, Y.: Assessment with satellite data of the urban heat island effects in Asian mega cities, Int. J. Appl. Earth Obs. Geoinf., 8(1), 34–48, doi:10.1016/j.jag.2005.05.003, 2006.

Turconi, L., Kumar De, S., Tropeano, D. and Savio, G.: Slope failure and related processes in the Mt. Rocciamelone area (Cenischia Valley, Western Italian Alps), Geomorphology, 114, 115–128, doi:10.1016/j.geomorph.2009.06.012, 2010.

UIPO, Annali idrologici, Parte prima. Ufficio Idrografico del Po, Parma, 1913-1994.

Viero, A., Furlanis, S., Squarzoni, C., Teza, G., Galgaro, A. and Gianolla, P.: Dynamics and mass balance of the 2007 Cima Una rockfall (Eastern Alps, Italy), Landslides, 10(4), 393–408, doi:10.1007/s10346-012-0338-4, 2013.

Weber, S., Beutel, J., Faillettaz, J., Hasler, A., Krautblatter, M. and Vieli, A.: Quantifying irreversible movement in steep, fractured bedrock permafrost on Matterhorn (CH), The Cryosphere, 11(1), 567, 2017.

Wickham, C., Rohde, R., Muller, R. A., Wurtele, J., Curry, J., Groom, D., Jacobsen, R., Perlmutter, S., Rosenfeld, A. and Mosher, S.: Influence of Urban Heating on the Global Temperature Land Average using Rural Sites Identified from MODIS Classifications, Geoinformatics Geostatistics An Overv., 1(2), 1–6, doi:10.4172/2327-4581.1000104, 2013.

WMO (World Meterological Organization): Guide to climatological practices (WMO-No. 100), 3rd Edn., Geneva, Switzerland, 180 pp., 2011.

Zemp, M., Haeberli, W., Hoelzle, M. and Paul, F.: Alpine glaciers to disappear within decades?, Geophys. Res. Lett., 33, doi:10.1029/2006GL026319, 2006.

Zemp, M., Paul, F., Hoelzle, M. and Haeberli, W.: Glacier Fluctuations in the European Alps, 1850-2000, Darkening Peaks Glacier Retreat, Sci. Soc., 152, 2008.

Zemp, M., Frey, H., Gärtner-Roer, I., Nussbaumer, S. U., Hoelzle, M., Paul, F., ... and Bajracharya, S.: Historically unprecedented global glacier decline in the early 21st century, Journal of Glaciology, 61(228), 745-762, 2015.

Zhou, L., Dickinson, R. E., Tian, Y., Fang, J., Li, Q., Kaufmann, R. K., Tucker, C. J. and Myneni, R. B.: Evidence for a significant urbanization effect on climate in China., Proc. Natl. Acad. Sci. U. S. A., 101(26), 9540–9544, doi:10.1073/pnas.0400357101, 2004.

Zhou, Y., Smith, S. J., Zhao, K., Imhoff, M., Thomson, A., Bond-Lamberty, B., Asrar, G. R., Zhang, X., He, C. and Elvidge, C. D.: A global map of urban extent from nightlights, Environ. Res. Lett., 10(5), 54011, doi:10.1088/1748-9326/10/5/054011, 2015.